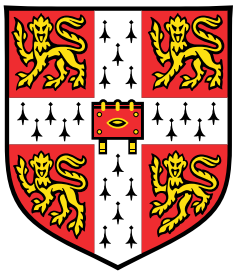

Novel waveguides for terahertz quantum cascade lasers

Adam Klimont

Department of Physics
University of Cambridge

This dissertation is submitted for the degree of
Doctor of Philosophy

Trinity Hall

March 2019

Moim dziadkom.

Declaration

I hereby declare that except where specific reference is made to the work of others, the contents of this dissertation are original and have not been submitted in whole or in part for consideration for any other degree or qualification in this, or any other university. This dissertation is my own work and contains nothing which is the outcome of work done in collaboration with others, except as specified in the text and Acknowledgements. This dissertation contains fewer than 65,000 words including appendices, bibliography, footnotes, tables and equations and has fewer than 150 figures.

Adam Klimont
March 2019

Acknowledgements

I would like to acknowledge the financial support of the Engineering and Physical Sciences Research Council, the Schiff Fund, the Semiconductor Physics Group, and Trinity Hall.

Thanks go to my supervisors, Dr. Harvey Beere and Prof. Dave Ritchie, for the willingness to share their knowledge and give advice whenever I needed it. I am also indebted to Dr. Yuan Ren and Dr. Riccardo Degl'Innocenti for training, helpful discussions, and research ideas.

Thank you to my collaborators in Leeds and Pisa, who were very kind to offer their time and expertise when the lab equipment was not working in the Cavendish. Special thanks to Dr. Dave Ellis, who was substantial in fixing those tools.

I am deeply grateful to Prof. Jan Misiewicz from Wrocław University of Technology, whose support made it possible for me to come to Cambridge.

Special thanks to all the friends I have made during my time at the university. Dave, Rob, and Ugo — thank you for making my time in the THz corner fun and thought provoking.

I have a wonderful family, who support me in everything I do. Thank you for believing in me. Ewa, your love, patience, and support were much more than I could ask for.

Publications

Line-defect photonic crystal terahertz quantum cascade laser
Klimont A., Ottomaniello A., Degl'Innocenti R., Masini L., Bianco F., Wu Y., Shah Y. D., Ren Y., Jessop D. S., Tredicucci A., Beere H. E., and Ritchie D. A., Optics Express, submitted

Fast terahertz imaging using a quantum cascade amplifier
Ren Y., Wallis R., Jessop D. S., Degl'Innocenti R., **Klimont A.**, Beere H. E., and Ritchie D. A., Applied Physics Letters, **107**, 011107 (2015)

Efficient coupling of double-metal terahertz quantum cascade lasers to flexible dielectric-lined hollow metallic waveguides
Wallis R., Degl'Innocenti R., Jessop D. S., Ren Y., **Klimont A.**, Shah Y. D., Mitrofanov O., Bledt C. M., Melzer J. E., Harrington J. A., Beere H. E. and Ritchie D. A., Optics Express **23** (20), 26276-26287 (2015)

A hybrid plasmonic waveguide terahertz quantum cascade laser
Degl'Innocenti R., Shah Y. D., Wallis R., **Klimont A.**, Ren Y., Jessop D. S., Beere H. E. and Ritchie D. A., Applied Physics Letters, **106**, 082101 (2015)

Single mode terahertz quantum cascade amplifier
Ren Y., Wallis R., Shah Y. D., Jessop D. S., Degl'Innocenti R., **Klimont A.**, Kamboj V., Beere H. E. and Ritchie D. A., Applied Physics Letters **105**, 141102 (2014)

Conferences

Low-threshold, single-mode defect line terahertz quantum cascade laser
Klimont A., Degl'Innocenti R., Masini L., Shah Y. D., Ren Y., Jessop D. S., Tredicucci A., Beere H. E., and Ritchie D. A., CLEO, San Jose, US, 2016

Fast Terahertz Imaging using a Quantum Cascade Amplifier up to 20,000 pps
Ren Y., Wallis R., Jessop D. S., Degl'Innocenti R., **Klimont, A.**, Beere H. E., Ritchie, D. A., 27th International Symposium on Space Terahertz Technology, Nanjing, China, 2016

A hybrid plasmonic waveguide for improved beam profile from terahertz quantum cascade lasers
Degl'Innocenti R., **Klimont A.**, Shah, Y. D., Wallis R., Ren Y., Jessop D. S., Beere H. E., and Ritchie D. A., The 13th International Conference on Intersubband Transitions in Quantum Wells, Vienna, 2015

Self-mixing imaging using a terahertz quantum cascade amplifier
Wallis R., Ren Y., Degl'Innocenti R., Jessop D. S., **Klimont A.**, Beere H. E., and Ritchie D. A., 40th International Conference on Infrared, Millimeter, and Terahertz waves (IRMMWTHz), Hong Kong, 2015

High Gain Terahertz Quantum Cascade Amplifier
Wallis R., Ren Y., Shah Y. D., Jessop D. S., Degl'Innocenti R., **Klimont A.**, Kamboj V., Beere H. E. and Ritchie D. A., 2015 CLEO Europe, Munich, 2015

A Hybrid Plasmonic Waveguide Terahertz Quantum Cascade Laser
Degl'Innocenti R., Shah Y. D., Wallis R., **Klimont A.**, Ren Y., Jessop D. S., Beere H. E., and Ritchie D. A., CLEO Europe, Munich, 2015

Terahertz quantum cascade amplifier
Ren Y., Wallis R., Shah Y. D., Jessop D. S., Degl'Innocenti R., **Klimont A.**, Kamboj V., Beere H. E., and Ritchie D. A., 26th International Symposium on Space Terahertz Technology, Cambridge MA, US, 2015

Beam cleaning in terahertz quantum cascade lasers by coupling to flexible polystyrene/silver coated hollow waveguides
Wallis R., Degl'Innocenti R., Jessop D. S., Ren Y., **Klimont A.**, Shah Y. D., Mitrofanov O., Bledt C. M., Melzer J. E., Harrington J. A., Beere H. E., Ritchie D. A., CLEO Europe, Munich, 2015

Abstract

Since their first demonstration in 2002, terahertz (THz) quantum cascade lasers (QCLs) have proven to be one of the most reliable sources of this type of radiation. Advances have been made in increasing maximum operating temperature, shaping the beam and tuning the frequency and bandwidth. Waveguide engineering has been a particular area of interest due to the large wavelength of the THz radiation ($> 100\,\mu$m). This thesis introduces several improvements related to THz QCL waveguide technology.

We begin by describing the THz radiation range, its applications and available sources. We then focus on the theoretical framework used to describe and design QCLs. We also review the two main waveguides employed in THz QCLs: the surface plasmon (SP) and the metal-metal (MM) waveguides. We outline the main fabrication steps for both waveguides.

Firstly, a novel photonic crystal-based QCL is presented. It comprises a defect line in a triangular lattice of active region (GaAs/AlGaAs) pillars embedded in a polymer matrix. The defects are made of pillars larger than the lattice pillars. Lasing is possible in this device on specific frequency levels (defect modes) within the band gap of the photonic crystal. Emitted frequency can be finely tuned by changing the size of the pillars in the lattice. A non-linear QCL geometry (a 90° junction), which allows for arbitrary emission direction, is also presented. Such waveguides may play an important role in integrated THz circuits.

Secondly, a new hybrid plasmonic waveguide for THz QCL is presented. It employs a polymer, benzocyclobutene (BCB), which solidifies upon heating and acts as a bonding agent. This waveguide serves as an alternative to MM and allows for arbitrarily thick metal deposition below the active region. Simulations are presented with an aim to explain the observed beam shape. For two different active regions and different thicknesses of bottom gold layer, a full light-current-voltage, spectral, and far-field characterisation is presented. The BCB-bonded device may be another element crucial in developing integrated THz elements on chip as it is more flexible than the rigid, substrate-based MM waveguide fabrication.

Thirdly, another novel concept of a THz QCL waveguide is presented, which employs etched pockets in the substrate directly below the active region. The air pockets allow for reducing the bottom plasmon layer doping and improving the ratio between the mode overlap

(with the gain medium) and waveguide loss. The process development is presented, as well as simulations corroborating the hypothesis that this device has a potential to outperform surface plasmon waveguides.

Finally, potential applications of this work are discussed and suggestions are made for further work that could be done to improve the presented concepts.

Table of contents

List of figures

List of tables

Nomenclature

Acronyms / Abbreviations

4QW	Four quantum well (design)
AR	active region
BCB	benzocyclobutene
BtC	bound-to-continuum (design)
cw	continuous wave
FF	far-field
FWHM	full width at half maximum
LIV	light-current-bias
MM	metal-metal (waveguide)
PhC	photonic crystal
QCL	Quantum Cascade Laser
SP	single plasmon (waveguide)

Chapter 1

Introduction

1.1 Sources of THz radiation

THz radiation, loosely defined as 0.3-10 THz (see Figure 1.1), remains one of the least developed spectral ranges in terms of convenient radiation sources. Although many attempts have been made to invent such a source, most of these devices suffer from various drawbacks, e.g. low output power, lack of tunability, large size, and instability over time. The examples of THz devices currently available are Schottky diode multipliers[1] and Gunn oscillators[2], and down- or up-converting nonlinear devices[3]. Electronic devices (such as Schottky and Gunn diodes) only approach the lower end of the THz spectrum ($f < 1\,\mathrm{THz}$), whereas photonic devices are usually limited by the very small energy differences involved in generating THz radiation ($2\,\mathrm{THz} \simeq 8\,\mathrm{meV}$), and the upper end of the spectrum ($f > 10\,\mathrm{THz}$) is available for them. Free electron lasers cover the THz range, but they are impractical due to their size and price.

THz radiation has several appealing applications. Firstly, they do not carry enough energy to ionise atoms in human tissue, thus non-invasive medical imaging is one of the most prevalent expectations about THz. Indeed, research has been done on imaging cancer[5] with promising results. Secondly, THz (or *sub-millimetre*) has been useful in astronomy, specifically in spectroscopy. The conditions on the orbit are more forgiving for THz sources (lower temperatures if not pointing towards the Sun, "natural" vacuum), therefore the technology has been already incorporated there, most notably in ESA's Herschel space observatory. Other interesting applications include gas sensing, high-speed telecommunication, security screening or detection of dangerous substances. For a detailed review, see Reference [6].

A major obstacle for using THz sources in uncontrolled environments is the radiation's absorption by water vapour. In the 1-2 THz range, the absorption coefficient in air varies between 10^{-1} and $10^{2}\,\mathrm{m}^{-1}$[7]. Realistic applications are therefore limited to short distances

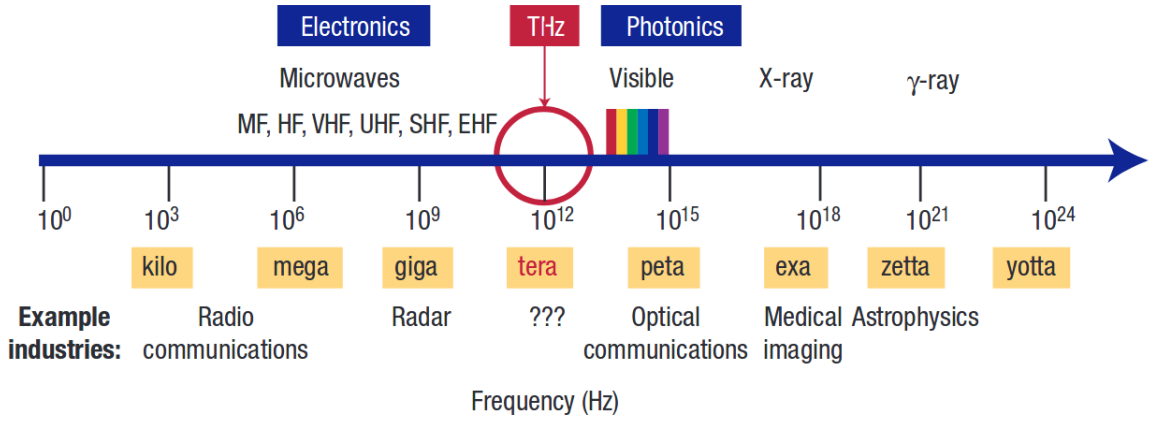

Fig. 1.1 The position of THz in the electromagnetic spectrum. Reproduced from Reference [4].

(e.g. skin cancer detection), space (where no water vapour is present), or controlled environments, such as nitrogen-filled chambers. Long-distance telecommunication with THz on Earth is difficult to imagine.

1.2 Quantum cascade lasers

The first theoretical description of gain in a superlattice was published by Kazarinov and Suris in 1971[8], following the article by Esaki and Tsu[9] in which the authors predicted formation of band structure minizones in a semiconductor heterostructure with many alternating wells and barriers. In their paper Kazarinov and Suris predicted the generation of electromagnetic waves as a result of intersubband transitions in quantum wells. Because such a device would be unipolar, transition energies would not be limited by the band gap of the used material. This would enable designing of structures emitting radiation of much longer wavelengths than those of conventional semiconductor lasers. The original proposal was later shown to have practical limitations. It was based on undoped wells and barriers, where electrons injected into the superlattice would form space charge domains, causing electrical instability.

Because of technological limits the fabrication of such structures was impossible until the late 1980s, when Molecular Beam Epitaxy (MBE) allowed semiconductor growth control with nanometre precision. In 1986 fabrication of a unipolar laser was suggested again by Capasso *et al.*[10] and in 1988 by Liu[11]. In 1994 Faist *et al.* demonstrated the first Quantum Cascade Laser (QCL), emitting in the mid-infrared region ($\lambda \simeq 4.3\,\mu m$)[12]. They introduced the doped injector/collector region which served as a reservoir of electrons and solved the electrical instability problem.

For several years after the initial demonstration, QCLs were limited to mid-infrared radiation (wavelengths approximately between 2 and 20 µm). THz operation was achieved in 2001 by incorporating GaAs/AlGaAs material system matched to GaAs substrates, as well as inventing the Surface Plasmon (SP) waveguide[13]. The first THz QCL's emission was centred at 4.4 THz (63 µm). As of late 2018, THz QCL operate in the region between 1.2 THz[14] and 4.9 THz[15]. The maximum operating temperature is approximately 200 K[16] in pulsed mode, and 129 K in continuous wave (cw) operation[17]. The most powerful THz QCLs emit more than 2 W power in pulsed mode[18], and 0.23 W in cw[19]. The broadest bandwidth demonstrated spans more than an octave, from 1.64 THz to 3.35 THz[20].

Band structure designs of QCLs can differ significantly, but some features are common for all of them. A diagram of the conduction band in a QCL is shown in Figure 1.2. The structure consists of two semiconductor materials which create wells and barriers. The same sequence is repeated 50-200 times, thus one electron can take part in multiple transitions, hence the name *cascade*. Two regions are marked on the diagram. *Injector* is a set of electronic states which collect carriers from the lower lasing level $|1\rangle$ of a previous *active region* and inject them into the upper lasing level $|2\rangle$ in the next *active region*. The injector and active regions usually comprise several wells and barriers. The barrier *i* is called the *injection barrier* and plays a crucial role in electron transport into the upper lasing level. Population inversion is

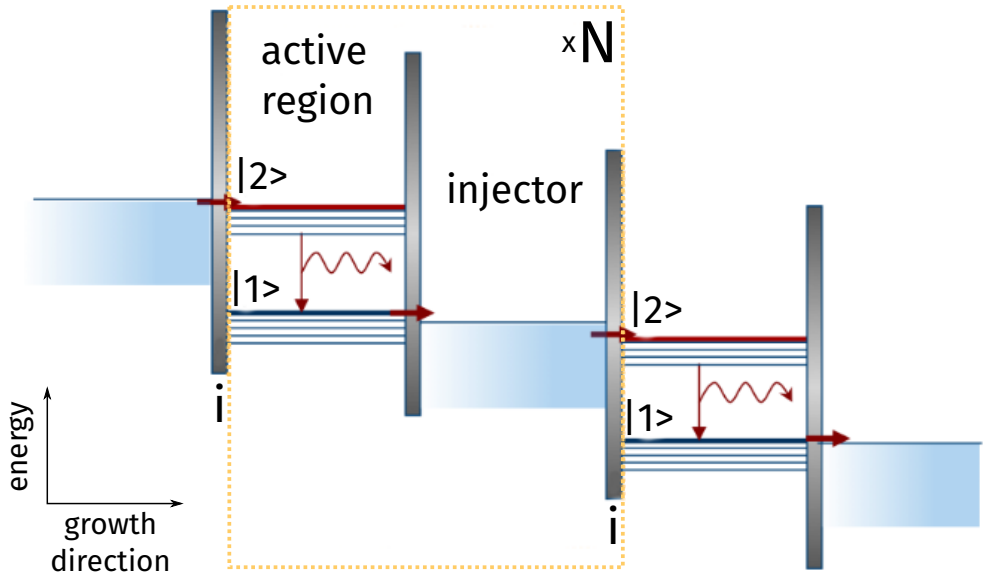

Fig. 1.2 Schematic diagram of the conduction band in a QCL. $|1\rangle$ and $|2\rangle$ are lower and upper lasing levels, respectively. The radiative transition is marked with a wavy arrow. The region within the dashed rectangle (active region and injector) is one period of a QCL active region, usually repeated 50-200 times.

achieved by means of fast depopulation of the lower state and relatively long lifetime of the upper state. Both conditions are achieved by adjusting the width (material thickness) and height (material composition) of the wells and barriers. The depopulation of the lower state usually involves scattering mechanisms, e.g. LO phonon scattering. Note that in this thesis (in line with QCL literature) we use the term *active region* (AR) to describe the whole series of wells and barriers repeated N times, as opposed to the specific well of one period of the superlattice.

Electronic transport in QCL has been extensively studied and reported in literature. For a simplified rate equation model of the active region see e.g. Reference [21]. Other notable models of transport include the density matrix[22], Monte Carlo[23], and non-equilibrium Green's function (NEGF) approaches[24].

1.3 Active Regions

The design of QCL active regions is guided by maximising the gain and the population inversion between radiative states, minimising the current flow via non-radiative channels, and reducing absorption and scattering. The conduction band structure can be calculated using Schrödinger's and Poisson's equations[25].

Several designs of the active region have been demonstrated to work in THz QCLs. The designs include chirped superlattice, bound-to-continuum (BtC), resonant phonon, and various mixed approaches[26]. In Chapter 2, we describe devices comprising the BtC design, which was first reported in the THz by Scalari *et al.*[27]. In this AR, multiple adjacent quantum wells are coupled to create energy minibands. See the diagram on the left of Figure 1.3. The radiative transition occurs between a bound state in between the minibands (2), and the top of the next miniband (1). The transition is diagonal in real space, which suppresses the coupling between the injector state (*inj*) and the lower lasing state (1). BtC design allows for high output power at low temperatures[28] and low threshold current densities[29], but they do not achieve high operating temperatures[30]. Two example BtC designs reported in literature are reproduced in Figure 1.4. The QCL presented by Barbieri *et al.*[31] (left) had a centre frequency of 2.9 THz, and the laser presented by *et al.*[29] (right) was centred at 2.0 THz. The latter design was used to fabricate devices for this thesis.

Another notable AR design is the resonant phonon (RP), first presented by Williams *et al.*[32] (see Figure 1.3, right). The lower lasing state tunnels into a state in an adjacent, wide quantum well, and that state is depopulated by means of longitudinal optical (LO) phonon scattering. The efficiency and temperature independence of the depopulation scheme contributed to the design's success in high operating temperature THz QCLs[33].

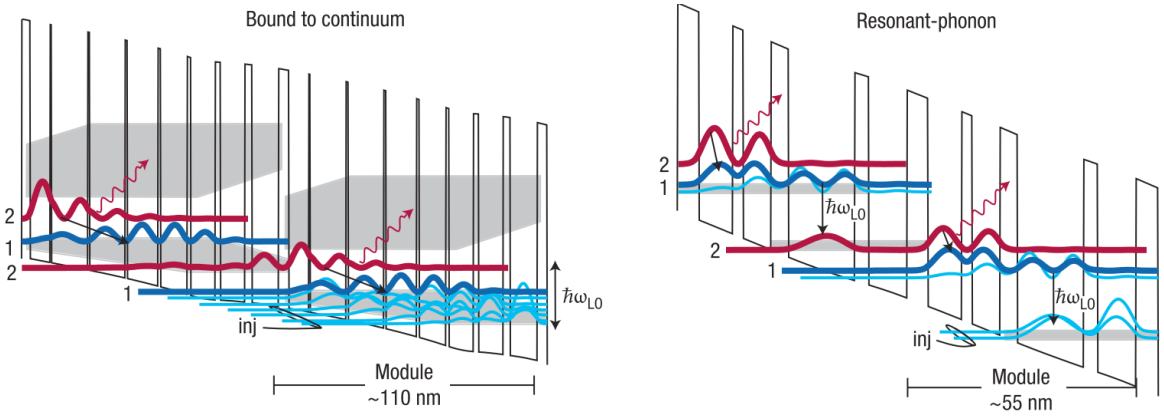

Fig. 1.3 Band diagrams of two popular types of THz QCL active regions. Energy is plotted on the vertical axis, and the horizontal axis corresponds to distance in the direction of MBE growth. Red and blue curves represent energy levels taking part in radiative transitions. Shaded regions represent bands of other electronic levels. **Left**: Bound-to-continuum design. **Right**: Resonant phonon design. Reproduced from Williams[26].

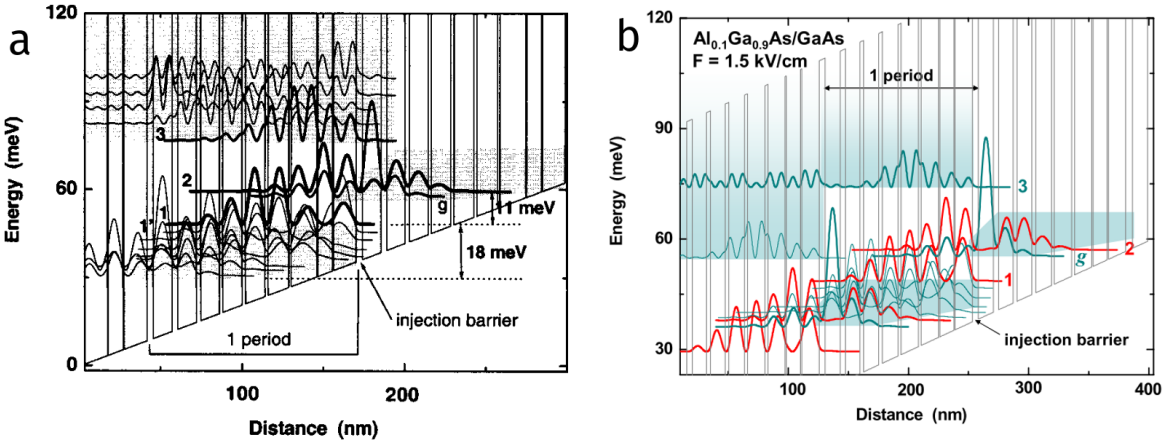

Fig. 1.4 Band diagrams of two BtC THz QCLs realised in the Semiconductor Physics group. 2 and 1 are upper and lower lasing states, respectively. Both designs comprise a miniband below the lower lasing level, allowing the electrons to relax into the injector state. **a**: Design by Barbieri *et al.*[31], lasing at $\sim 2.9\,\mathrm{THz}$. **b**: Design by Worrall *et al.*[29], lasing at $\sim 2.0\,\mathrm{THz}$.

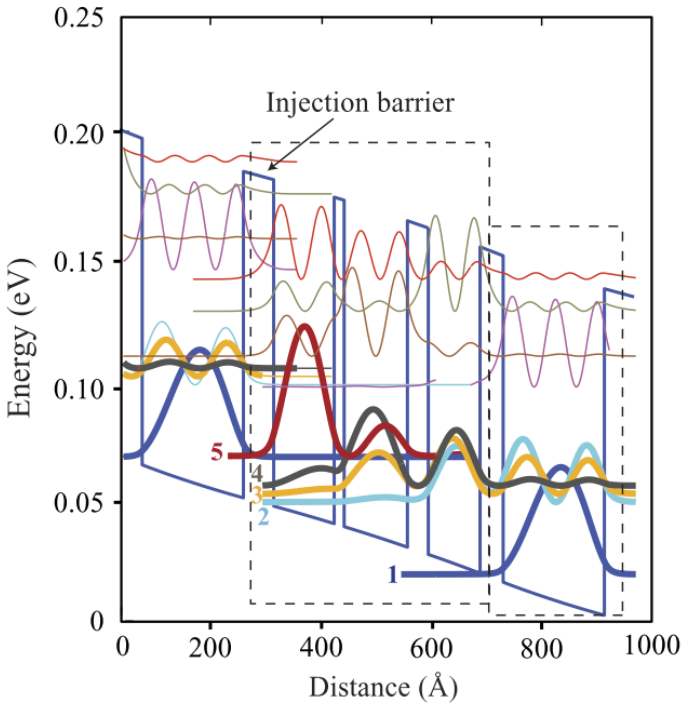

Fig. 1.5 Band diagram of the 4 quantum well design, used in devices in Chapter 3. Reproduced from Amanti *et al.*[30].

Several devices presented in Chapter 3 incorporate an AR which is a combination of the two aforementioned approaches. The so-called 4 quantum well (4QW) QCL, demonstrated by Amanti *et al.*[30], is shown schematically in Figure 1.5. The design based on a diagonal radiative transition between a bound state (5 in Figure 1.5) and two states in the next quantum well (3 and 4), which are in turn coupled to another state (2) and depopulated via LO phonons onto the injector (1). This design has been successful due to its wide bandwidth (resulting from the doublet of lower lasing states), and good temperature performance ($\sim 150\,\mathrm{K}$) due to fewer quantum wells in the active region period.

1.4 Waveguides

Waveguide design is crucial for efficient extraction and propagation of THz radiation in a QCL. In mid-infrared QCLs dielectric claddings are used to confine the optical mode in the AR. However, in order to do it efficiently, the cladding thickness must be of the order of the wavelength of the emitted radiation[21]. For THz QCLs, the 100 µm-thick GaAs layers would need to be grown on top of the laser, which is impractical, if not impossible to achieve.

Moreover, the claddings are doped in order to provide carriers to the laser, and a thick doped layer would introduce significant losses which are proportional to λ^2. For these reasons, THz QCLs employ a different approach, namely plasmonic waveguides.

A surface plasmon is an oscillation of the electric field at the boundary of two materials with opposite dielectric function signs, e.g. metal and semiconductor. The maximum intensity of the oscillation occurs at the boundary, and it decays exponentially in both materials. This is a result of TM mode continuity condition of $\vec{H}_x$ and $\frac{1}{\varepsilon_i}\frac{\partial \vec{H}_x}{\partial y}$, where y is the direction of growth[21]. In THz QCLs, the surface plasmon mode is the least lossy one. Figure 1.6 shows the decay of the surface plasmon on a metal-semiconductor interface.

The quality of a waveguide is defined by the threshold gain:

$$g_{th} = \frac{\alpha_m + \alpha_w}{\Gamma}, \tag{1.1}$$

where Γ is the overlap of the mode with the AR:

$$\Gamma = \frac{\int_{AR} \vec{E}^2 dV}{\int_{-\infty}^{\infty} \vec{E}^2 dV}. \tag{1.2}$$

In equation 1.1, α_m are mirror losses stemming from the QCL-air impedance mismatch, and α_w represents waveguide losses which comprise two phenomena: Drude losses due to free carriers, and intersubband absorption of radiation in the AR. Waveguide losses and overlap can be engineered, which we will demonstrate in Chapter 3. In THz QCLs, two

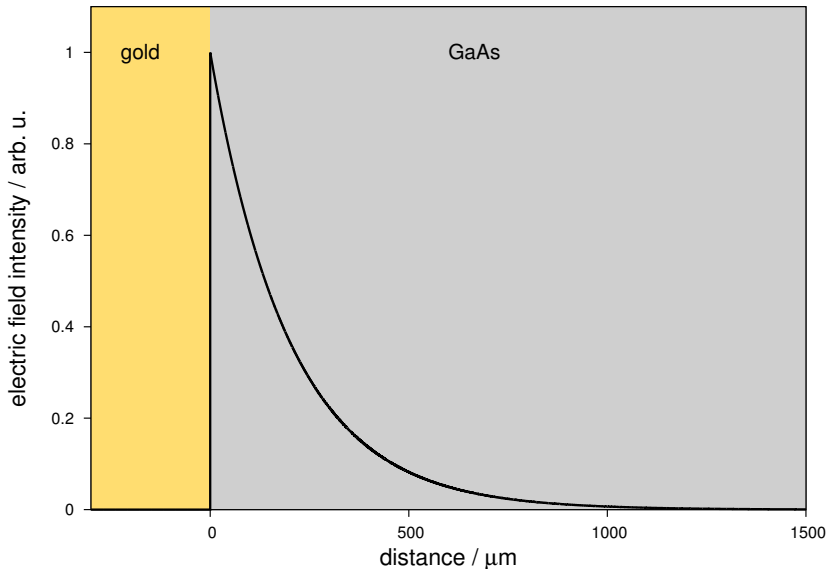

Fig. 1.6 The decay of a surface plasmon mode on a metal-semiconductor interface.

different waveguides based on surface plasmons are routinely used: the surface (single) plasmon (SP), and metal-metal (MM). In this work, we will also present a waveguide based on a series of defects in a photonic crystal (a defect line QCL). Photonic crystals will be discussed in detail in Chapter 2.

1.4.1 Single Plasmon

A single plasmon (SP) waveguide is fabricated by deposition of a metal layer on top of the doped GaAs layer above the AR stack. At the bottom, the AR is bounded by a strongly doped *quasi-plasmonic* GaAs layer with a low negative dielectric constant. A plasmon mode is generated on its boundary, but it is much weaker than the one sustained on the metal-semiconductor junction on the top of the laser. Simulated mode in a SP waveguide is shown in Figure 1.7. Most of the mode leaks into the substrate, which results in a low overlap (approx. 0.3), but the waveguide losses are relatively low as well, on the order of $10\,\mathrm{cm}^{-1}$. QCLs embedded in this type of waveguide are the record holders for the output power[34].

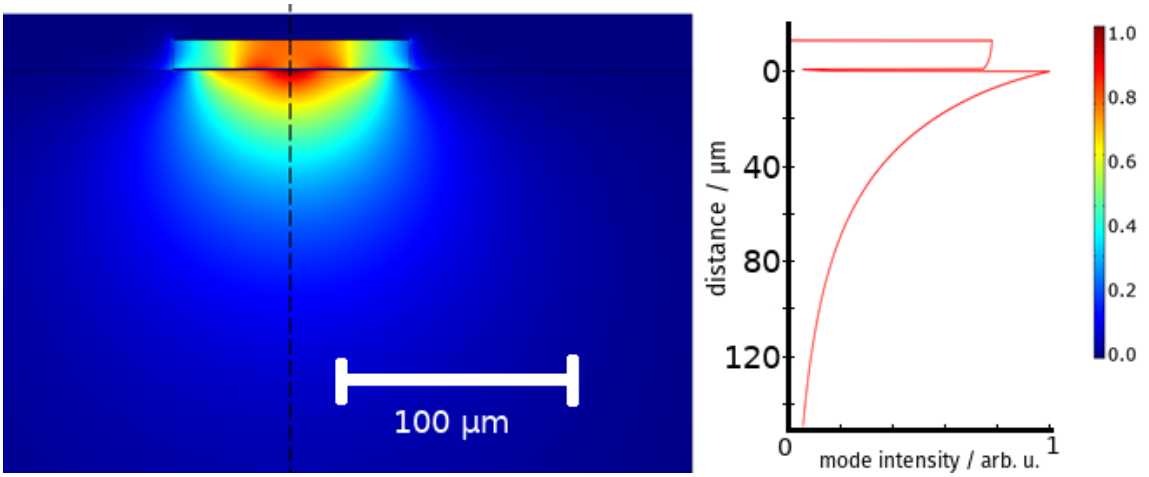

Fig. 1.7 Normalised electric field of the dominant mode in a SP waveguide. On the right, the cross section of the field is shown along the dashed line in the surface plot. The overlap of the mode with the AR is 30%.

1.4.2 Metal-Metal

A metal-metal (MM) waveguide, sometimes called double-metal, confines the optical mode on both sides of the AR with a metal layer. Simulated mode in a MM waveguide is shown in Figure 1.8. Fabrication of these waveguides requires an additional step, which is described

below in Section 1.5.3. With such a strong confinement, the overlap factor is close to 1. On the other hand, the losses introduced by the gold layer below the AR are more than twice as high as in SP ($\alpha_w \simeq 20\,\mathrm{cm}^{-1}$). The gold layer at the bottom also improves thermal conductivity, which allows for more efficient cooling, hence the highest operating temperatures are achieved with MM devices[33, 16, 35]. One drawback of MM is low power efficiency due to very high impedance mismatch on laser facets, resulting from the ridge thickness (10-15 µm) being much lower than the wavelength (100-200 µm).

Due to greater sub-wavelength confinement in the AR and increased impedance mismatch at the facet, the MM emission is more divergent (beam width often greater than 50°), and tends to exhibit multi-lobe patterns. SP beam, on the other hand, is relatively less divergent (emission width less than 30°), and exhibits a quasi-Gaussian pattern with one prominent lobe. See Figure 1.17 in Section 1.6 for exemplar results of far-field patterns from the two waveguides.

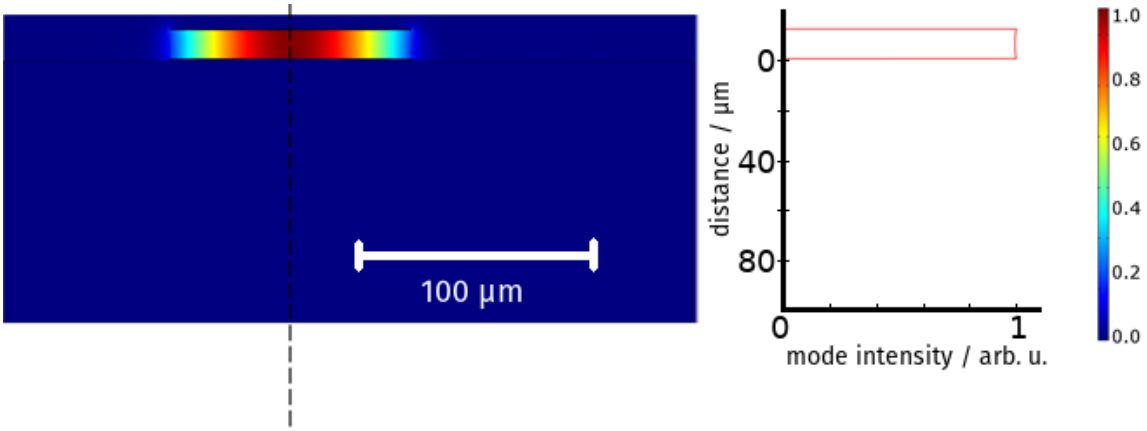

Fig. 1.8 Normalised electric field of the dominant mode in a MM waveguide. On the right, the cross section of the field is shown along the dashed line in the surface plot. The overlap of the mode with the AR is 99%.

1.5 Fabrication

1.5.1 MBE wafer growth

Most THz QCL heterostructures are currently grown by Molecular Beam Epitaxy (MBE). An MBE tool comprises an ultra-high vacuum chamber, with a sample holder inside, and effusion cells around the chamber. Each of the cells contains elemental material of a very high purity. For the GaAs/AlGaAs material system, those are gallium, arsenic, and aluminium. During the

growth process, a GaAs substrate is placed on the heated holder (600-650 °C). The effusion cells are also heated to control the speed of the atoms incident on the substrate. Typical growth rates are 0.1-1 monolayer/s. The composition of the output material is controlled by opening and closing shutters in front of the cells. In such a system, layers of well defined semiconductor alloys can be grown with subnanometre precision[36].

A typical cascade structure is shown schematically in Figure 1.9. The starting point for QCL growth is a (100) GaAs 500 µm thick wafer. After a 250 µm buffer layer of GaAs, 300 nm of $Al_{0.5}Ga_{0.5}As$ are deposited, which serve as an etch-stop in MM processing. The next layer is $\sim$ 700 nm thick GaAs doped with silicon at 1-2 $\times$ 10^{18} cm^{-3}. Its function is twofold: firstly, it serves as an electrical contact in a fabricated device; secondly, in single plasmon devices it gives rise to a quasi-plasmon. The next layers are the core of a QCL: these are repeated sequences of quantum wells and barriers consisting of GaAs and AlGaAs. The fraction of aluminium and gallium varies between designs. For the BtC design used in this work, we used $Al_{0.1}Ga_{0.9}As$, and for the 4QW AR we used $Al_{0.15}Ga_{0.85}As$. The number of repeats usually varies from 50 to 200. Each repeated sequence consists of 5-10 layers a few nanometers thick. At least one of these is silicon doped. The total thickness of the AR varies from 5 to 15 µm. Finally, 80-200 nm of highly doped (5 $\times$ 10^{18} cm^{-3}) GaAs are grown. This layer provides the top electrical contact.

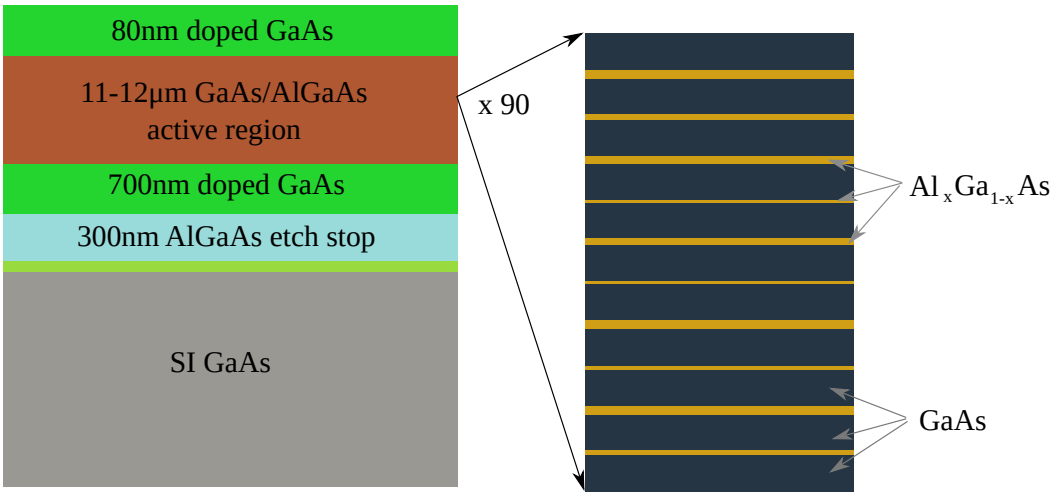

Fig. 1.9 Diagram of a typical MBE grown QCL structure (not to scale). To the right, the AR is shown schematically.

1.5.2 Single plasmon processing

Consecutive steps of QCL sample processing are schematically shown in Figure 1.10. From the MBE-grown substrate 5 mm × 6 mm chips are cleaved, each of which contains three laser ridges when the fabrication is finished.

Photoresist (usually Shipley S1828) is spun on a sample, which is then aligned under a microscope and an appropriate pattern is defined on it using the UV photolithography technique. The first aligned pattern is the laser ridge. Its dimensions are approximately $3-5\,\text{mm} \times 200-250\,\mu\text{m}$. The ridge is then etched in $1:8:40$ $H_2SO_4 : H_2O_2 : H_2O$ solution, which yields the etch rate of about $0.8\,\mu\text{m/min}$ and a side wall slope of 45°. The etch depth is based on the thickness of the AR, such that 300-400 nm of bottom GaAs layer is left unetched.

The next step is to define the bottom contacts on the sides of the ridge. The lithography is performed with a slight modification (always used when developing a pattern is followed by metal evaporation): after exposure to UV light, the chip is dipped in chlorobenzene for 3 to 5 minutes before development. The top layer of the photoresist hardens, creating an undercut profile, which allows for easier *lift-off* after metal evaporation. After developing an appropriate pattern, 100 nm of AuGeNi (88:12:5 by molecular weight) are evaporated and then lifted off in acetone. Annealing at 450 °C is carried out on the sample in order for the alloy to spike down through several hundred nanometres of the underlying GaAs. An ohmic contact is formed instead of a Schottky junction, which provides effective carrier transport through the structure.

The final lithography and evaporation steps lead to the deposition of an overlayer of titanium (15 nm) and gold (100 nm). Its function is twofold: it facilitates wire bonding of the device and sustains the plasmon on top of the laser ridge.

After depositing the aforementioned layers, the back side of the sample is mechanically ground in order to thin the host GaAs substrate. It improves the thermoconductive properties, which are essential for heat sinking when the device is mounted. Then a back side Ti/Au evaporation is carried out to facilitate soldering the device onto a copper block with indium, and to prevent diffusion of indium into the substrate. An image of a device processed with aforementioned steps is shown in Figure 1.11. Mounted lasers are then wire-bonded to Au-coated pads to provide electrical contact in experiments. Figure 1.12 shows SEM images of fully processed SP QCLs.

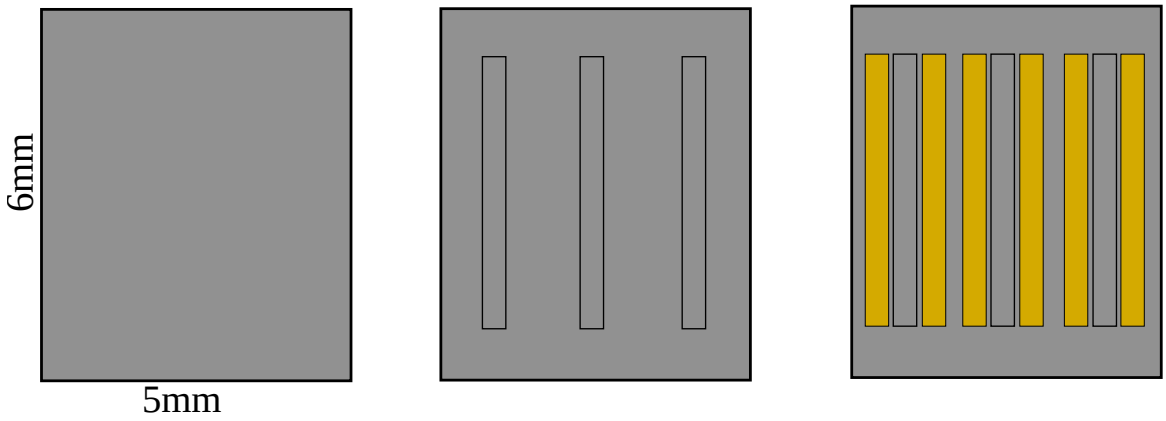

(a) cleaved chip

(b) mesas defined and etched

(c) AuGeNi bottom contacts evaporated

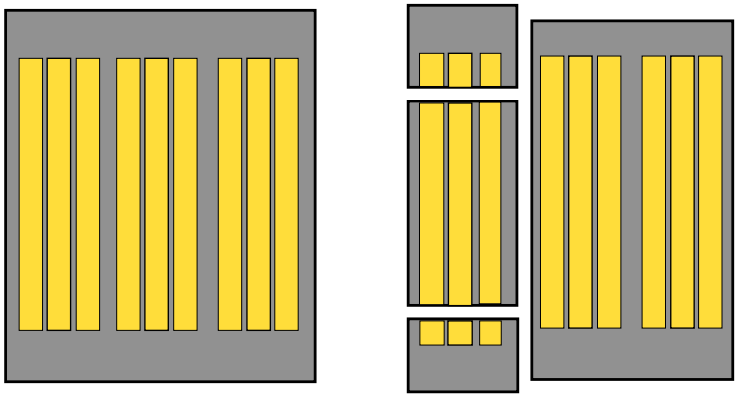

(d) TiAu overlayer evaporated

(e) ridge cleaved

Fig. 1.10 The main steps in the processing of single plasmon QCLs

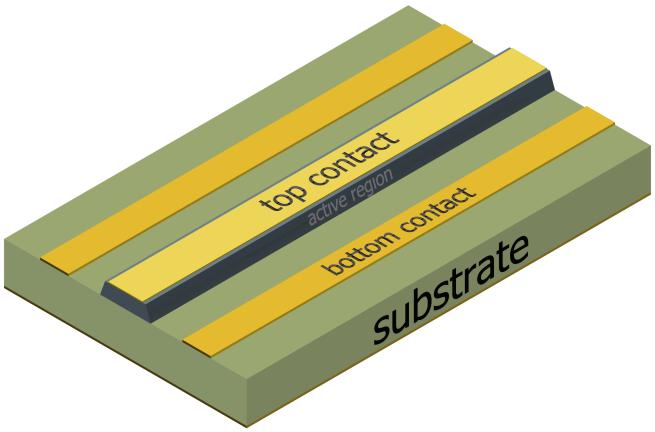

Fig. 1.11 Image of a single plasmon QCL after cleanroom processing.

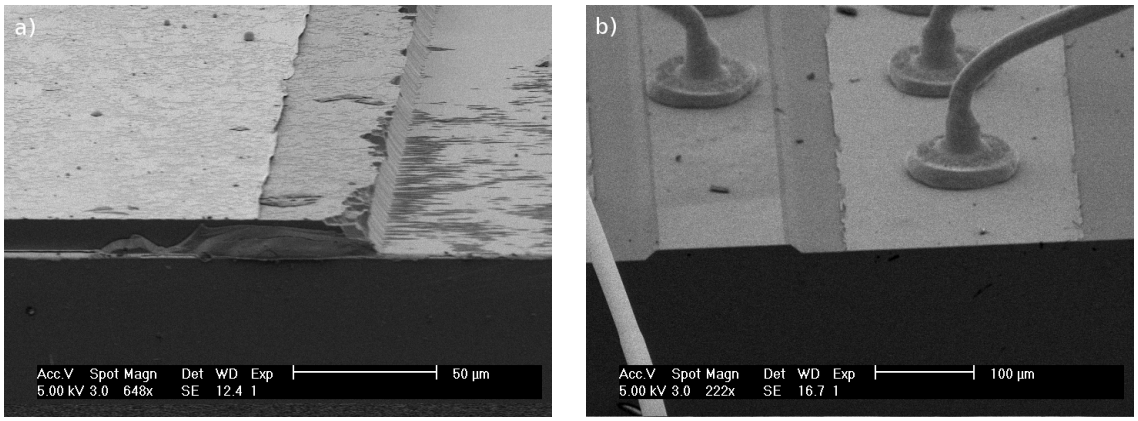

Fig. 1.12 SEM images of a mounted SP QCL. **a)** a close-up of the facet and the etched ridge (mesa) of the laser. Notice the walls of the mesa are not perpendicular to the bottom surface, which is the result of wet etching. The brighter layer on the top is the evaporated gold. **b)** laser ridge (left, narrower) and bottom contact (right, wider) wire-bonded with thin golden wires. Each wire can withstand a current of about 0.7 A.

1.5.3 Metal-Metal fabrication

MM processing starts with cleaving an MBE wafer and an n^+ highly doped GaAs wafer. Both chips are then cleaned and prepared for titanium and gold (Ti/Au) evaporation. A thin (15 nm) adhesion layer of Ti is evaporated, followed by a long evaporation of Au. At least 500nm are required by the subsequent steps. Once covered with gold, the two chips are thermocompressively bonded for 15 min, at 320°, with a force of 7.5 kN.

The following steps are shown in Figure 1.13. First, the chip is mechanically polished in order to remove the majority (about 300 µm) of the substrate GaAs. Then, an etch solution of citric acid ($C_6H_8O_7$) is prepared. The solid form of the acid is dissolved in water in 1g:1ml proportion. The prepared solution is then mixed with H_2O_2 in 1:5 ratio (H_2O_2: citric acid). The citric etch solution normally etches GaAs at a rate of about 0.3 µm/min and AlGaAs about 120 times slower, essentially terminating at the AlGaAs *etch stop* layer.

When the substrate is etched away, the sample is put in hydrofluoric acid (HF), which selectively etches AlGaAs, but does not remove doped GaAs underneath. Once this is done, the chip is immersed in 1:8:80 $H_2SO_4 : H_2O_2 : H_2O$ solution for 1 minute, which is sufficient to dissolve the GaAs layer. The sample is then ready for laser ridge definition.

Laser ridges can be etched either in a dry reactive ion etching (RIE) process or a wet sulphuric acid etch. When wet etching method is chosen, a layer of Ti/Au is defined and evaporated as in the SP processing. The ridges are then etched in sulphuric acid solution until the metal layer below is reached. Another Ti/Au photolithography/evaporation/lift-off sequence is carried out to define 3 stripes of metal: one on top of the ridge, two on the sides. They facilitate wire bonding to the top of the laser, and to the bottom metal layer. When dry

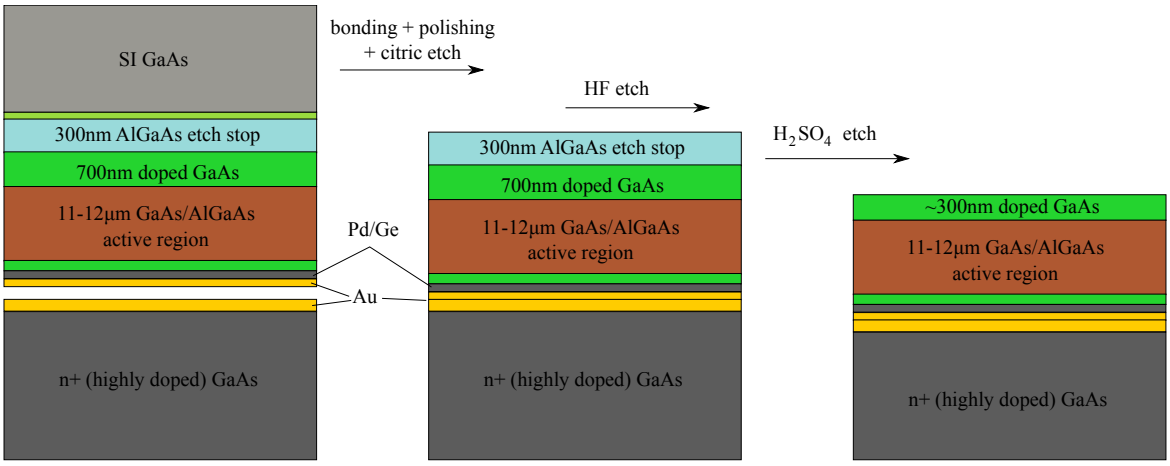

Fig. 1.13 Thermocompression bonding, polishing and etching steps of metal-metal fabrication process.

etching is the preferred technique, the metal etch mask needs to be thicker ($> 300\,\text{nm}$), as the process is longer and etches away the mask as well as the semiconductor material. We used a sacrificial layer of nickel (100 nm) on top of the ridges, which was removed in the RIE process. Dry etching is described in more detail in Section 2.4 in the next chapter.

1.6 Experimental methods

In this work we used three characterisation methods for QCLs: light-current-voltage (LIV) measurement, far-field collection, and spectral measurement. Figure 1.14 shows the experimental setup for all three measurements.

A slow modulation generator is used to gate the laser operation and send the reference frequency (9 Hz for a Golay cell, 330 Hz for a bolometer) to the lock-in amplifier. A function generator (pulser) powers the laser with a frequency of 10-150 kHz and adjustable duty cycle (rectangular signal). To measure the current passed to the device, a current probe is connected between the pulser and the laser. The electric signal is received by an oscilloscope connected to a computer.

In case of the LIV and far-field measurements, the detector used was always a Golay cell with a Winston cone at the front. A Golay cell consists of an infrared-absorbing material surrounded by gas. The material absorbs radiation and heats up the gas, which in turn

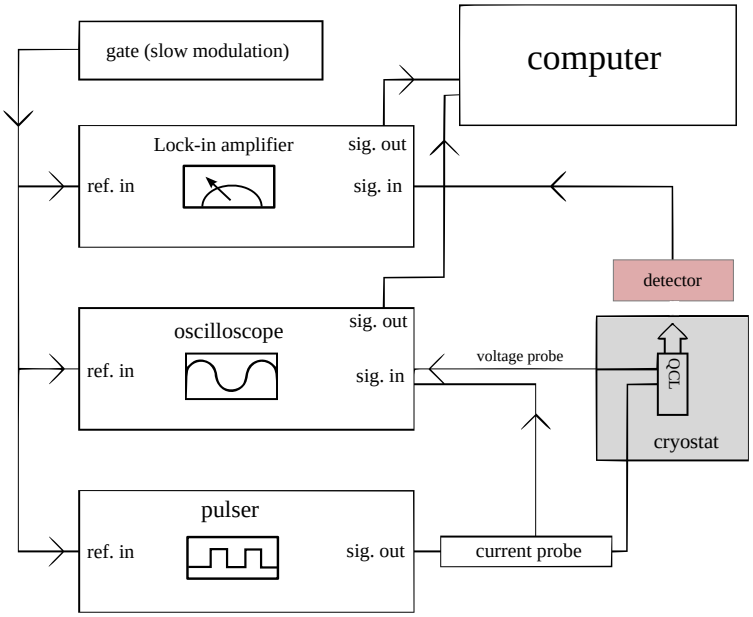

Fig. 1.14 Experimental setup for LIV measurement.

deforms a membrane inside the detector. This deformation is detected by a photodiode. During LIV measurements, the detector was placed in front of the laser.

Figure 1.15 shows the result of a typical LIV experiment. First ($J = 0 - 70\,\mathrm{A\,cm^{-2}}$), the slope of the current-voltage (IV) curve is steep, when the Schottky barrier on top of the laser ridge needs to be overcome. Pre-threshold parasitic (non-lasing) current ensues ($J = 70 - 450\,\mathrm{A\,cm^{-2}}$) until the discrete electron levels in adjacent quantum wells align. Then we see the onset of lasing, and the IV slope is appreciably flatter ($J = 450 - 650\,\mathrm{A\,cm^{-2}}$). The output power peaks just before the electronic levels misalign again, and the IV curve becomes steep again ($J > 650\,\mathrm{A\,cm^{-2}}$) — efficient current channels have been shut.

For far-field characterisation, we used an aperture (1-2 mm in diameter) at the front of the Golay cell, and a motorised stage to move the detector vertically and horizontally. See Figure 1.16 for a schematic diagram of this setup. The vertical movement followed one axis (z), whereas the horizontal movement followed the circumference of a circle with the centre at the laser's facet (θ) or the horizontal axis (x). Figure 1.17 shows typical far-field beam patterns for QCLs employing MM (left) and SP (right) waveguides. The MM beam width is much more divergent (beam width more than 70° compared to 30° in SP), and exhibits multiple lobes, as opposed to one clear maximum from the SP device.

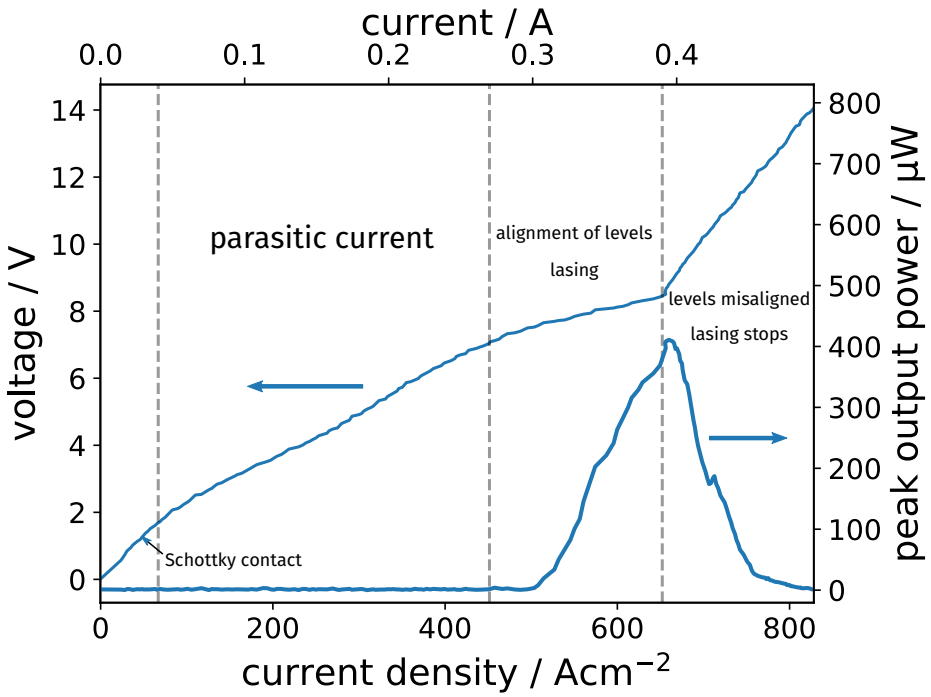

Fig. 1.15 A typical light-current-voltage measurement results of a THz QCL (4QW design in a MM waveguide). Dashed vertical lines separate four stages of QCL operation.

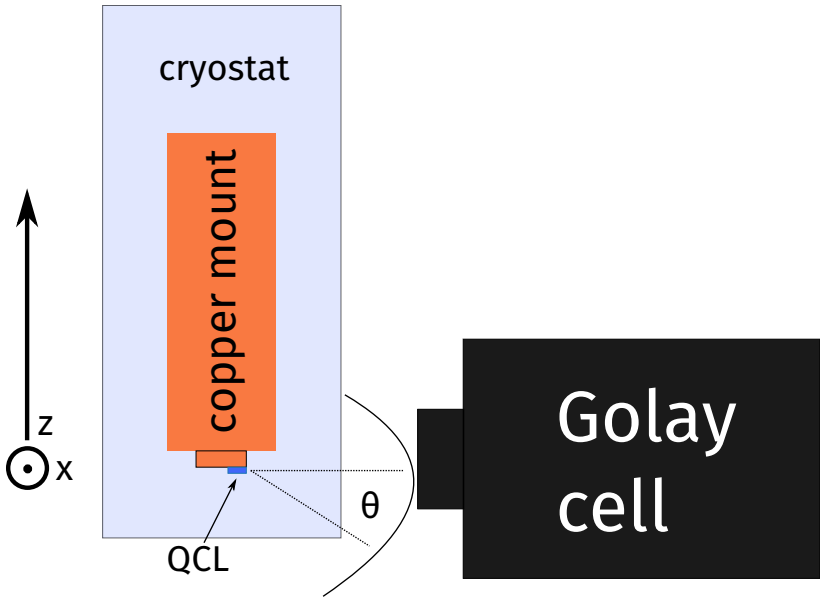

Fig. 1.16 Far-field measurement setup. The QCL is mounted upside down in a cryostat. The Golay cell, with an aperture in front of it, is mounted on a motorised stage. The detector can be moved up and down the z axis, as well as around the laser (θ).

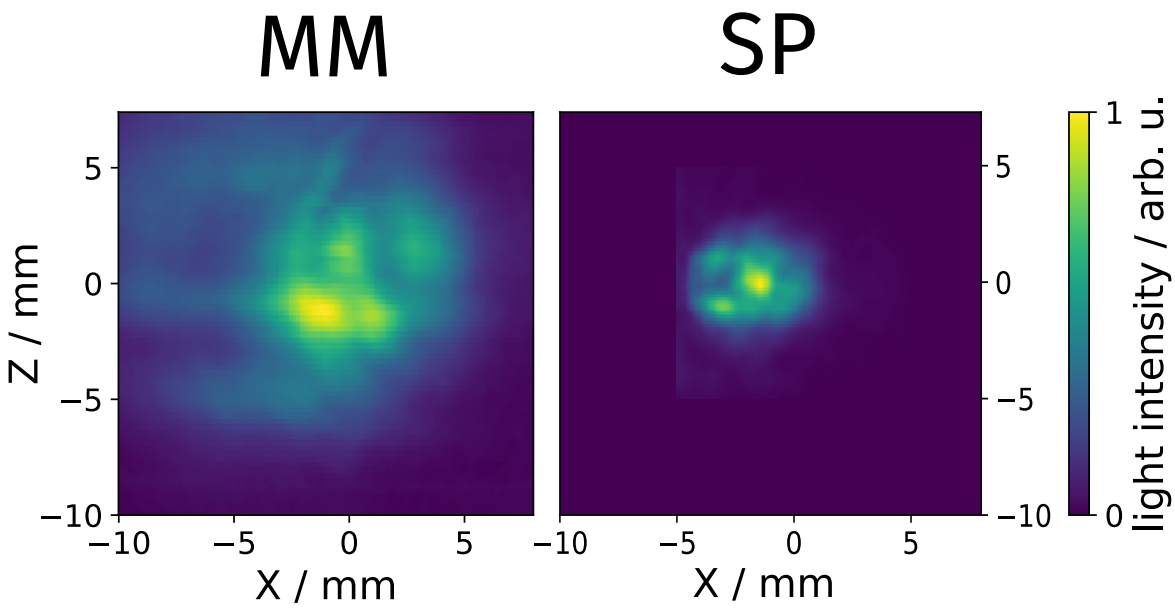

Fig. 1.17 Far-field emission from a typical MM QCL (left) and SP QCL (right), taken at 11 mm from laser facets, with a 1.5 mm aperture in front of a Golay cell. Due to much higher impedance mismatch, MM is more divergent.

For spectral measurements, we used a Bruker Fourier transform infrared spectrometer (FTIR) in between the laser and the detector (liquid helium cooled silicon bolometer). The laser was placed directly in front of the spectrometer. After reflecting from FTIR's set of mirrors, the output beam passed through a high density polyethylene (HDPE) window and was collected in the bolometer with a Winston cone. The resolution of this experimental setup in the THz range was $0.25\,\mathrm{cm}^{-1}$ ($\simeq 7.5\,\mathrm{GHz}$). Figure 1.18 shows exemplar spectral data from a 4QW device. Due to two lower lasing states there are two separate emission regions around 2.6 THz and 2.95 THz. Within those regions, laser ridge geometry gives rise to regularly-spaced Fabry-Pérot peaks.

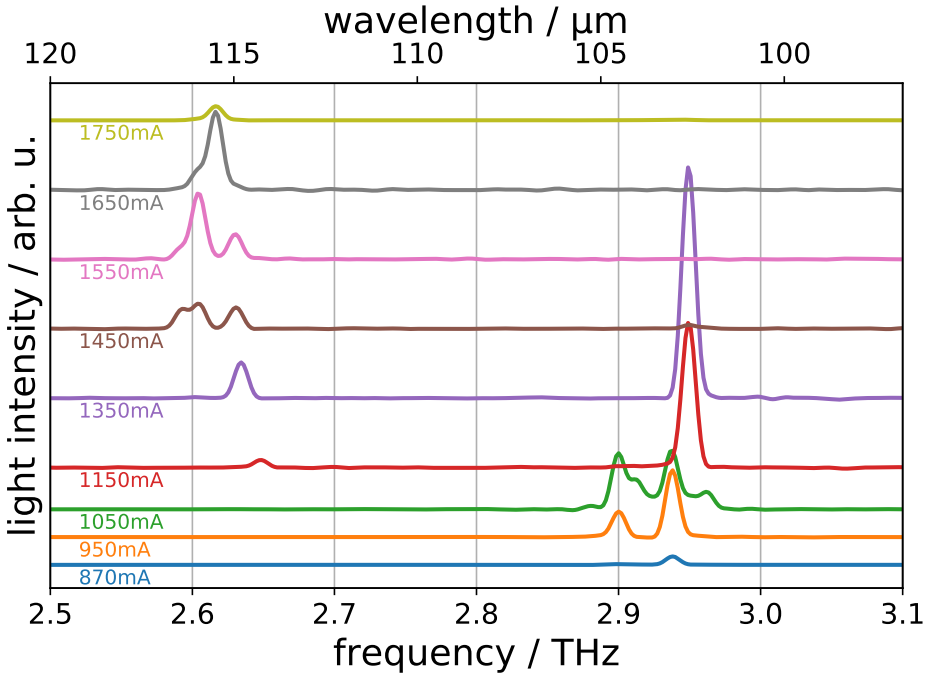

Fig. 1.18 Typical spectra of a 4QW THz QCL. Two radiative transitions give rise to two distinct emission frequencies, around 2.6 THz and 2.95 THz. Within those two regions, regularly-spaced Fabry-Pérot peaks can be seen.

1.7 Thesis overview

This thesis has the following structure. In Chapter 2 we demonstrate, for the first time, a defect line THz QCL. The design is inspired by previous reports on photonic crystals in laser devices. We describe design and fabrication of pillars of AR material in a triangular lattice, with bigger pillars (defects) forming a line. We present a low threshold, frequency tunable, and single-mode operation of THz QCLs. We discuss the benefits of this system, including

engineerable output direction, and its usage as a platform for studying the slow light and Purcell effects.

In Chapter 3, we explore another alternative waveguide, namely the hybrid benzocyclobutene (BCB)-metal THz QCL. In this approach, thermocompression bonding is replaced by BCB curing, which allows for more flexibility in waveguide design. We begin by reporting the proof-of-concept work done in our group. By fabricating and characterising more hybrid waveguides, we address the questions which the initial report raised: what is the origin of seemingly better output beam pattern, what is the optimal metal thickness of a hybrid MM laser, and whether the approach is transferable to other active region designs.

In Chapter 4, another novel waveguide is presented, namely the "air pocket QCL". It is an alternative to SP waveguides, with trenches etched at the bottom of the substrate. The pockets are designed to push the mode back into the AR, which increases mode overlap and allows for lower doping of the bottom plasmon layer (thus reducing loss). Such waveguide can improve the threshold gain and temperature performance of THz QCLs.

Each of the chapters is concluded with discussion of obtained results. A chapter about possible future research enabled by our work concludes this thesis.

Chapter 2

Defect line QCL

2.1 Introduction

Some of the most attractive applications for QCLs are in the fields of spectroscopy[3], sensing[37], and imaging[3]. Often these applications require radiation sources with well defined, single mode operation. Typical QCLs however have a gain bandwidth of $\sim 200\,\mathrm{GHz}$. In the standard ridge geometry of QCLs (where the ridges are a few millimetres long), this results in multi-mode, Fabry-Pérot lasing. Traditionally, single mode operation in QCLs has been achieved by embedding them in frequency selective structures, such as distributed feedback resonators. See References [38] and [39] for examples of such devices.

The concept of using frequency selective patterns in QCLs was extended by employing photonic crystals (PhCs). PhCs were first used in mid-infrared, surface emitting QCLs by Colombelli *et al.*[40]. The authors etched a hexagonal pattern of holes in the AR and obtained single mode surface emission from the device. Note that this work was done at much higher frequencies than THz QCLs ($f \simeq 35\,\mathrm{THz}$, or equivalently $\lambda \simeq 8\,\mu\mathrm{m}$), therefore the dimensions involved were small (etch depth 2-3 μm, and hole radius of the order of 1 μm). Dunbar *et al.*[41] first used PhC in the context of THz QCLs. The authors surrounded the facets of a standard QCL ridge with a PhC lattice and used it as a frequency filter for the laser output. This addition was successful and the emitted light was single mode (around 3.6-3.8 THz).

Our approach is inspired by subsequent work in embedding QCL AR material in a photonic lattice. Zhang *et al.*[42] etched a triangular lattice of AR pillars and spun benzocyclobutene (BCB) in between them. They placed a metal contact on top of the pillars (see Figure 2.1, top row) in order to apply bias across the AR. The authors sought to exploit the slow light effect emerging on the photonic band edges, where the mode dispersion (and therefore group velocity) is low. Lower group velocity results in stronger light-matter

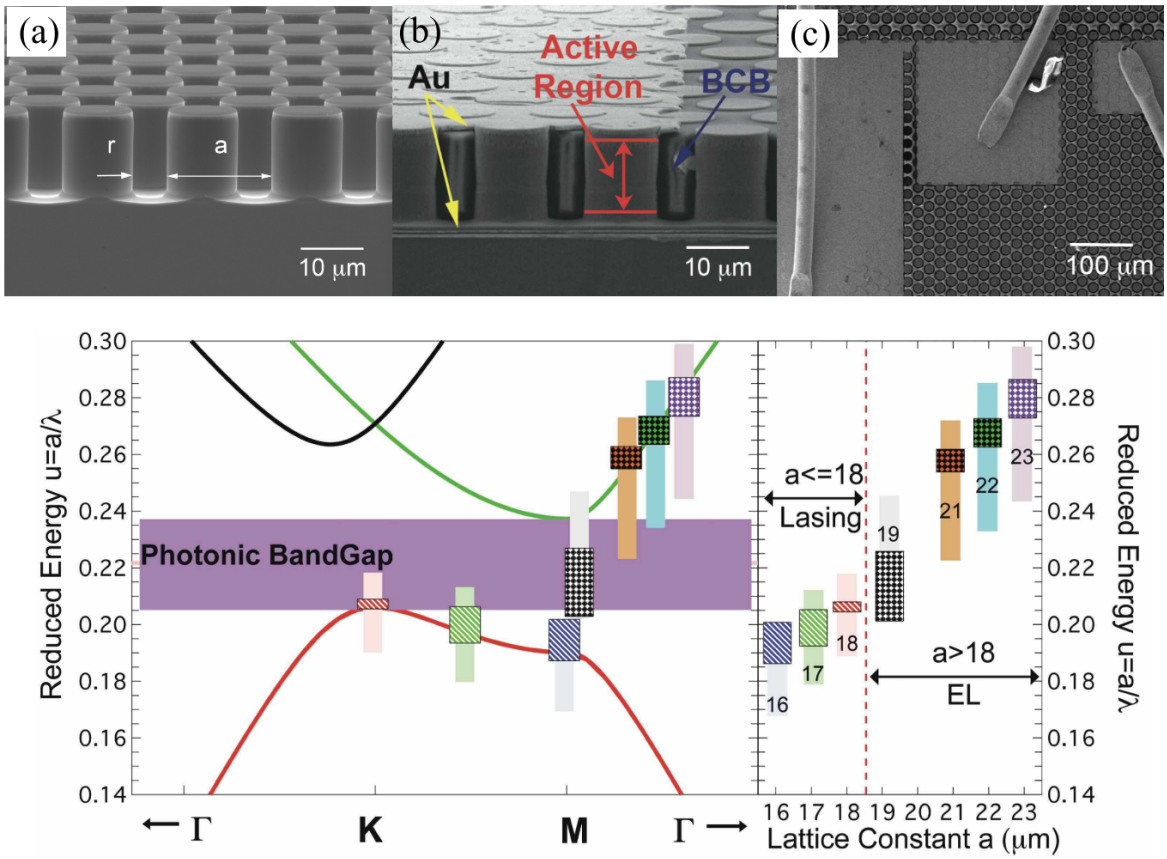

Fig. 2.1 **Top**: SEM pictures of the PhC QCL presented by Zhang *et al.*[42]. GaAs pillars are embedded in planarised BCB. **Bottom**: Calculated band structure (left) and measured frequency of lasing and electroluminescence of PhC lasers. Devices with lattice constant $a \leq 18\,\mu m$ lased at the band edge and exhibited single mode operation. Reproduced from Ref. [42].

interaction in the AR. They fabricated devices with lattice constant varying from 16 μm to 23 μm. Observed lasing and electroluminescence frequencies agreed well with Plane Wave Expansion calculations of the photonic band edges. The authors also observed a reduction in threshold current density of up to 17% compared to MM lasers.

In a more recent report, Benz and others[43] also demonstrated an active PhC QCL in a triangular lattice of pillars. They suspended the pillars in air by adding another thermocompressive bonding step, where they attached a wafer to already etched pillars. This allowed for a higher contrast between the pillars and the surroundings ($n_{pillar}/n_{medium} = 3.6$, as opposed to 2.3 for BCB), and thus a stronger confinement of the optical mode to the pillars. Again, the lattice was uniform, without any defects (see Figure 2.2a). Reported devices lased on the band edges of the photonic structure, similarly to those in Reference [42]. The output was single mode, and lasing frequencies were tunable with lattice parameters.

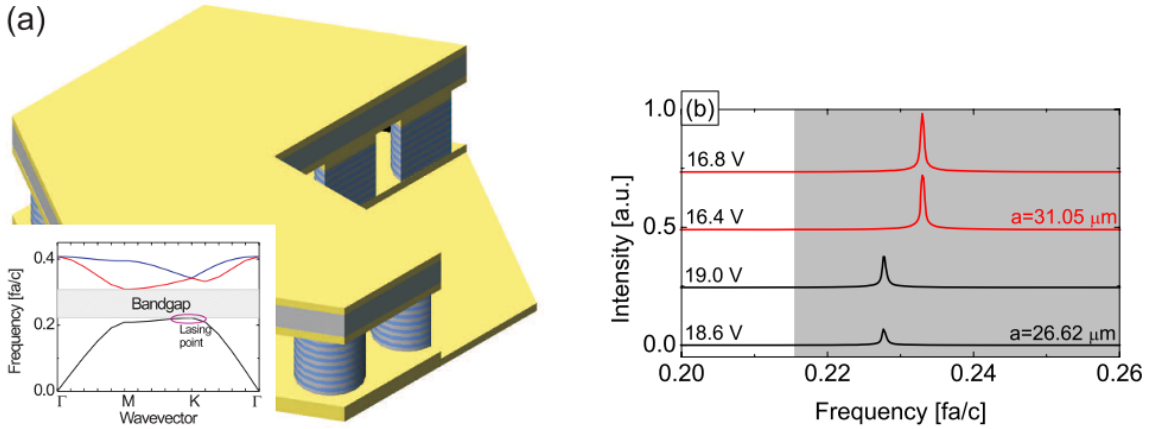

Fig. 2.2 **a**: A 3D drawing of the PhC QCLs fabricated by Benz *et al.*[43]: a triangular lattice of pillars surrounded by air. Inset: calculated photonic band structure in the first Brillouin zone of the lattice. **b**: Emission spectra of two devices with different lattice constants. The lasers emit single modes, close to the band edge. Reproduced from Ref. [43].

For other work exploring the use of PhCs and QCLs, see References [44–49].

The PhCs in this work are similar to those in the works of Zhang[42] and Benz[43] insofar as they exploit a triangular lattice of GaAs pillars. However, our aim was to concentrate QCL modes in a line of defects, i.e. a series of bigger pillars. Line defects have been extensively studied in the near infrared, see for example Baba *et al.*[50], and Notomi *et al.*[51]. However, the dimensions of PhCs are proportional to the wavelengths involved, therefore fabrication of such systems for THz radiation is much easier. The features are of the order of tens of microns, as opposed to submicron sizes required in the near infrared. The defect line design was chosen for several reasons. Firstly, it benefits from the PhC band structure properties, allowing for single mode tunability across the gain bandwidth of the active medium. Secondly, unlike the previous demonstrations of PhC QCLs, it is directional. Moreover, the lasing direction can be engineered by introducing bends in the waveguide. Additionally, defect modes lead to lower current density (compared to conventional QCLs) due to their ultra-flat dispersion. This is crucial in environments with limited electrical power, such as heterodyne receivers on satellites[52]. Finally, by reporting working defect lines, we hope that they will be used as a platform to study the nature of optical effects such as slow light, Purcell enhancement, and cavity pulling, similarly to short wavelength defect lines[50]. In summary, the goal of this work was to use a novel PhC design to fabricate THz QCLs which are single mode, widely tunable by fabrication, have low current threshold, and whose output direction can be engineered. To the best of our knowledge, this is the first realisation of a defect line THz QCL.

This chapter has the following structure: in Section 2.2 we will introduce the concept of photonic crystals and summarise equations and approximations used to describe them quantitatively. Section 2.3 is aiming to explain, with numerical simulation results, why we chose certain design parameters. In 2.4, we briefly discuss how PhC fabrication is different from standard QCL processing. Section 2.5 comprises experimental results and their discussion: 2.5.1 focuses on light-current-voltage characteristics and current density reduction, 2.5.2 on spectral measurements, and 2.5.3 on mode profiles. We then briefly discuss our initial experiments with T-shaped defect lines in Section 2.6. The chapter ends with conclusions in Section 2.7.

2.2 Photonic crystals

Photonic crystals (PhCs) are periodic structures comprising regions of high and low refractive index. This periodicity allows certain optical modes to propagate through the crystal without scattering, analogously to electrons in solids with crystalline periodicity. The eigenvalue problem for electromagnetic waves in a periodic potential has the following form:

$$\nabla \times \left(\frac{1}{\varepsilon(\vec{r})} \nabla \times \vec{H}(\vec{r}) \right) = \left(\frac{\omega}{c} \right)^2 \vec{H}(\vec{r}), \tag{2.1}$$

where $\vec{H}(\vec{r})$ is the magnetic field, $\varepsilon(\vec{r})$ is the dielectric function, ω is the angular frequency of the field, and c is the speed of light in vacuum. This equation can be rewritten in a form which looks more like a traditional eigenvalue equation:

$$\hat{\Theta}\vec{H}(\vec{r}) = \left(\frac{\omega}{c} \right)^2 \vec{H}(\vec{r}). \tag{2.2}$$

The above equation is called the **master equation**. It is derived from Maxwell equations, under several assumptions:

- The structure of the material does not vary in time.
- There are no currents in the material.
- The material is isotropic.
- The field strengths are small enough for the displacement field to be linearly proportional to the electric field ($\vec{D}/\varepsilon_0 = \varepsilon\vec{E}$).

It should be noted that the second assumption (no currents) is not true in QCLs. However, we assume that the charge in QCLs does not significantly perturb the simplified eigenproblem,

especially that the current flows in less than a half of the structure (form factor is below 0.5). Authors of References [42, 43] did not account for this discrepancy either. For the detailed derivation of the master equation, as well as an excellent description of photonic crystals, see Joannopoulos *et al.*[53].

By solving Equation 2.1 we obtain harmonic modes with real frequencies, which propagate in the PhC. In the context of defects, it is useful to refer to the variational principle, which dictates the change in mode frequency after introducing a small perturbation:

$$\Delta\omega \simeq -\frac{\omega}{2}\frac{\int d^3\vec{r}\Delta\varepsilon(\vec{r})|\vec{E}(\vec{r})|^2}{\int d^3\vec{r}\varepsilon(\vec{r})|\vec{E}(\vec{r})|^2}, \tag{2.3}$$

where ω and $\vec{E}$ are the angular frequency and the electric field for the unperturbed dielectric function ε. The minus sign implies that an increase in the dielectric function lowers the mode frequency, and the change is proportional to the fraction of field intensity ($\int \varepsilon|\vec{E}|^2$) in the perturbed regions[53].

One consequence of a discrete translational symmetry of a system is that electromagnetic waves can be described as Bloch states, labelled by a wave vector $\vec{k}$:

$$\vec{H}_{\vec{k}}(\vec{r}) = e^{i\vec{k}\cdot\vec{r}}\vec{u}_{\vec{k}}(\vec{r}), \tag{2.4}$$

where $\vec{u}_{\vec{k}}(\vec{r})$ is a function with the same periodicity as the lattice, i.e. $\vec{u}_{\vec{k}}(\vec{r}) = \vec{u}_{\vec{k}}(\vec{r}+\vec{R})$ for all lattice vectors $\vec{R}$. The wave vector can be expanded as

$$\vec{k} = k_1\vec{b}_1 + k_2\vec{b}_2 + k_3\vec{b}_3, \tag{2.5}$$

where $\vec{b}_{1,2,3}$ are the reciprocal vectors of the lattice. In a periodic system, the wave vector $\vec{k}$ is a conserved quantity.

Inserting the Bloch state (Equation 2.4) into the master equation (Equation 2.1) gives rise to continuous functions $\omega_n(\vec{k})$, which inform us about the band structure of the crystal, n being the band index. Careful study of the band structure will guide the design of the defect line QCLs described in Section 2.3.

All band structures and other simulations in this chapter were obtained using MIT Photonic Bands (MPB) open-source package[54]. The software takes in the geometry and material parameters as arguments, and numerically computes the eigenvectors and eigenvalues of the master equation. The results were postprocessed using NumPy[55] and Matplotlib[56] Python packages.

We approximate our PhC QCLs as two dimensional systems. This is due to the metal layers on top and the bottom of the AR. In systems with mirror symmetry (in our case,

$\hat{z} = -\hat{z}$), optical modes can be classified into two polarisations: TE (the electric field is perpendicular to $\hat{z}$ axis) and TM (the magnetic field is perpendicular to $\hat{z}$ axis)[53]. Selection rules in QCLs restrict the radiative transitions to TM polarisation, therefore we will be preoccupied with this class of modes.

There are many possible configurations of PhCs structure, such as hexagonal, square or triangular lattices. We chose to work with the latter because it offers a wider TM gap for the same index contrast compared to other configurations.

The lattice vectors of the triangular lattice are (see Fig. 2.3a):

$$\vec{a}_1 = a\left[\frac{1}{2}, \frac{\sqrt{3}}{2}\right], \qquad \vec{a}_2 = a\left[\frac{1}{2}, -\frac{\sqrt{3}}{2}\right] \tag{2.6}$$

where a is the lattice constant. The reciprocal lattice vectors are then:

$$\vec{b}_1 = 2\pi/a[1, \sqrt{3}], \qquad \vec{b}_2 = 2\pi/a[1, -\sqrt{3}] \tag{2.7}$$

The reciprocal lattice of a triangular system is also a triangular lattice (see Figure 2.3b). This figure also depicts the main symmetry points $(\Gamma, \mathrm{M}, \mathrm{K})$ of the irreducible Brillouin zone.

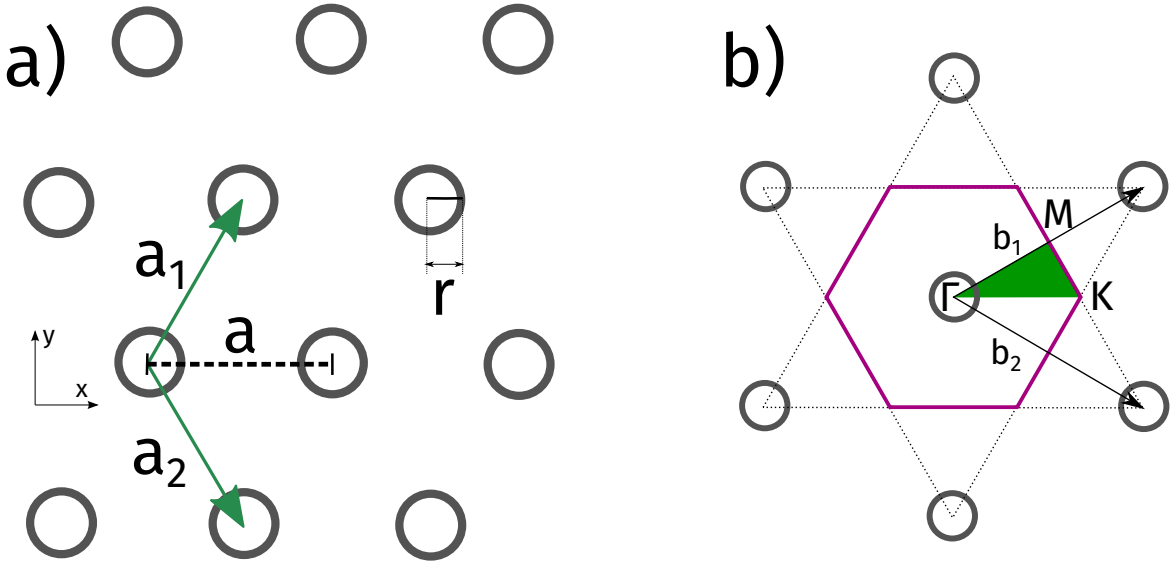

Fig. 2.3 **a)** Triangular lattice of pillars. $\mathbf{a}_1$ and $\mathbf{a}_2$ are lattice vectors. $\mathbf{a}_2$ has a length of a (the lattice constant). r is the pillar diameter. **b)** Reciprocal of the triangular lattice. b_1 and b_2 are the reciprocal basis vectors. The violet hexagon represents the first Brillouin zone, and the right triangle its irreducible part. Three main symmetry points are marked as Γ, M, and K.

The optical properties of PhCs depend on its geometry and the refractive index contrast between constituent materials. We chose to work with GaAs/AlGaAs QCLs surrounded by BCB, therefore $n_{pillars}$ is set to 3.6, and $n_{medium} = 1.55$. See Figure 2.4 for two examples of photonic band diagrams, calculated for the aforementioned material system, with $a = 44\,\mu m$. On the left diagram, $r = 0.23a \simeq 10\,\mu m$, and on the right $r = 0.41a \simeq 18\,\mu m$. The diagrams are restricted to TM polarisation. The first three photonic bands are plotted. In between them, there is a region where no modes are allowed to exist in the system. This is the photonic band gap. Its position and width are crucial for the design of our devices, as we aim to create defect modes within the gap. In general, the photonic bandgap of the triangular lattice is bigger for higher refractive index contrast between pillar materials and the surrounding medium. The diagram on the left shows the maximum band gap attainable for the chosen material system and geometry ($\Delta f \simeq 0.57\,THz$). For bigger pillars (Figure 2.4, right), the gap is much narrower ($\Delta f \simeq 0.11\,THz$). The first (blue) band has been traditionally called the *dielectric* band, because the modes comprising it are concentrated in high refractive index regions of the system. The second band (orange) is called the *air* band.

Unless stated otherwise, we will be using relative units rather than absolute ones, following the reasoning from Ref. [53]: if we expand or contract the photonic crystal by a factor of s, the band will change proportionally. Therefore pillar radii are stated relative to the lattice constant ($r = 0.25a$ in Figure 2.4), and so are frequencies ($\omega_{relative} = \omega a/2\pi c$). We also use the **gap-to-midgap** ratio or the **relative width** to quantify band gaps. The relative width is defined as $\Delta\omega/\omega_m$, where ω_m is the frequency at the middle of the gap. For the optimal structure on the left of Figure 2.4, $\Delta\omega/\omega_m \simeq 0.3$. For the $r = 0.41a$ system, $\Delta\omega/\omega_m \simeq 0.08$.

Others have successfully realised a triangular lattice surrounded by air, which maximises the band gap (the relative gap width is approx. 50%), but fabrication of pillars suspended in air is challenging[43]. Figure 2.5 illustrates the trade-off between the contrast and gap width. Using BCB as a medium results in $n_{pillars}/n_{medium} = \simeq 2.3$, which allows for a bandgap relative width of 30% with pillar features in the micrometre range, as will be shown below. The dashed line in Figure 2.5 corresponds to the band gap shown on the left of Figure 2.4.

The frequencies of the bands in a photonic crystal depend on the ratio of pillar radii to the lattice constant. The first step of device design was to identify the ratio for which the band gap is the widest and how quickly it shrinks around the optimal ratio. Wider band gaps give more flexibility in terms of defect mode design, and they increase the confinement of the defect modes[53]. Figure 2.6 shows the size of the first band gap as a function of r/a. Because of our chosen operating frequency ($\sim 2\,THz$), we are interested in the first band gap, which occurs between the first (*dielectric*) and second (*air*) photonic bands. More gaps

may appear between higher order photonic bands. The maximum relative width of the first bandgap is approximately 30% and it occurs at $r \simeq 0.23a$. This point corresponds to the dashed line in Figure 2.5, and the left diagram in Figure 2.4. We decided to increase the ratio to 0.25 in our devices. This allows for fabricating bigger features than for $r = 0.23a$, and does not introduce a significant band gap penalty (the gap at $r = 0.25a$ is approximately 29%).

2.3 Defect line

With the refractive index ratio set to 2.3 and the ratio between the pillar radius and the lattice constant set to 0.25, we explore the available defect modes. A defect is a perturbation of the photonic crystal in the form of a missing pillar, or a pillar of different radius than that of lattice pillars. In this work, defect is defined as a pillar with a **larger** radius than the lattice pillars. Such a defect can sustain optical modes with frequencies within the band gap of the PhC and with TM polarisation (i.e. with the same polarisation as the THz QCL output). Defects smaller than the lattice pillars can also confine optical modes, but the volume of the active region in the device would then be much smaller, so we did not explore this setup.

In order to investigate available defect modes, we modelled a single GaAs pillar with a bigger radius surrounded by the triangular lattice, with parameters as discussed above. Surrounding the defect with 2 periods of the PhC lattice (creating a *supercell*) is enough to confine the mode in a defect[57]. Periodic boundary conditions were set in the simulation, to reflect the fact that we are dealing with a defect line.

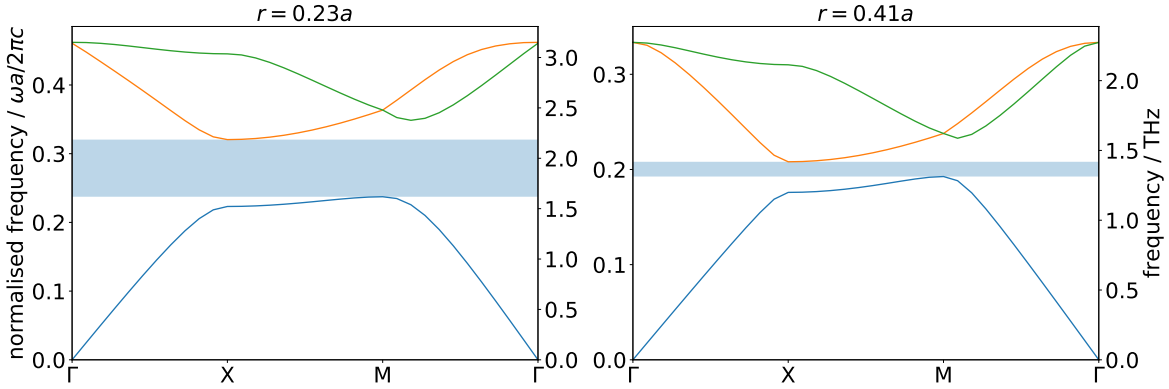

Fig. 2.4 Exemplar TM band diagrams for a triangular lattice ($a = 44\,\mu$m) of GaAs pillars (**left**: $r = 0.23a \simeq 10\,\mu$m, **right**: $r = 0.41a \simeq 18\,\mu$m), surrounded by BCB. A TM band gap (filled region) emerges between the top of the *dielectric* band (blue), and the bottom of the *air* band (orange). For $r = 0.23a$, the band gap has the maximum width ($\Delta\omega/\omega_m \simeq 0.3$). For $r = 0.41a$, the gap is much narrower ($\Delta\omega/\omega_m \simeq 0.08$).

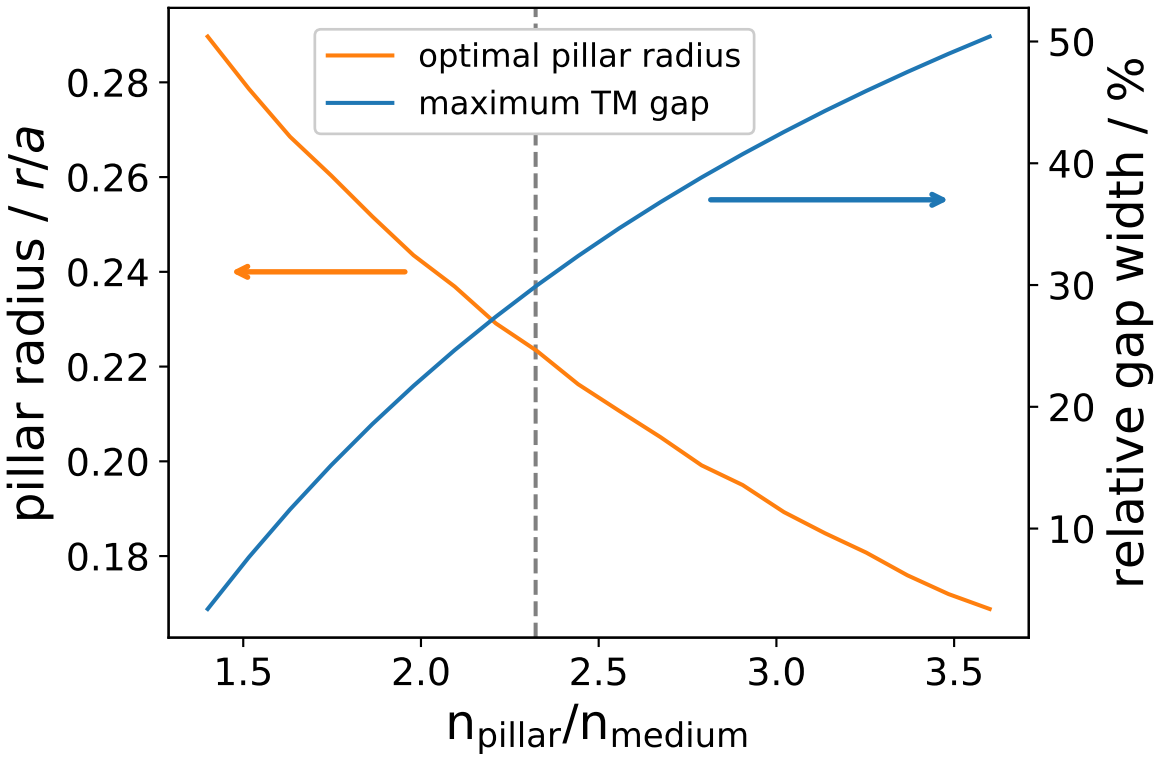

Fig. 2.5 Maximum bandgap width (blue) and corresponding pillar radius (orange) for different values of refractive index contrast between the pillars and the surrounding medium. The bandgap is maximised (and the optimal radius minimised) for $n_{medium} = 1$, i.e. when the pillars are surrounded by air. For a GaAs-BCB system (marked by the dashed line), the optimal pillar radius is $r = 0.23a$, and the maximum relative gap is 30%.

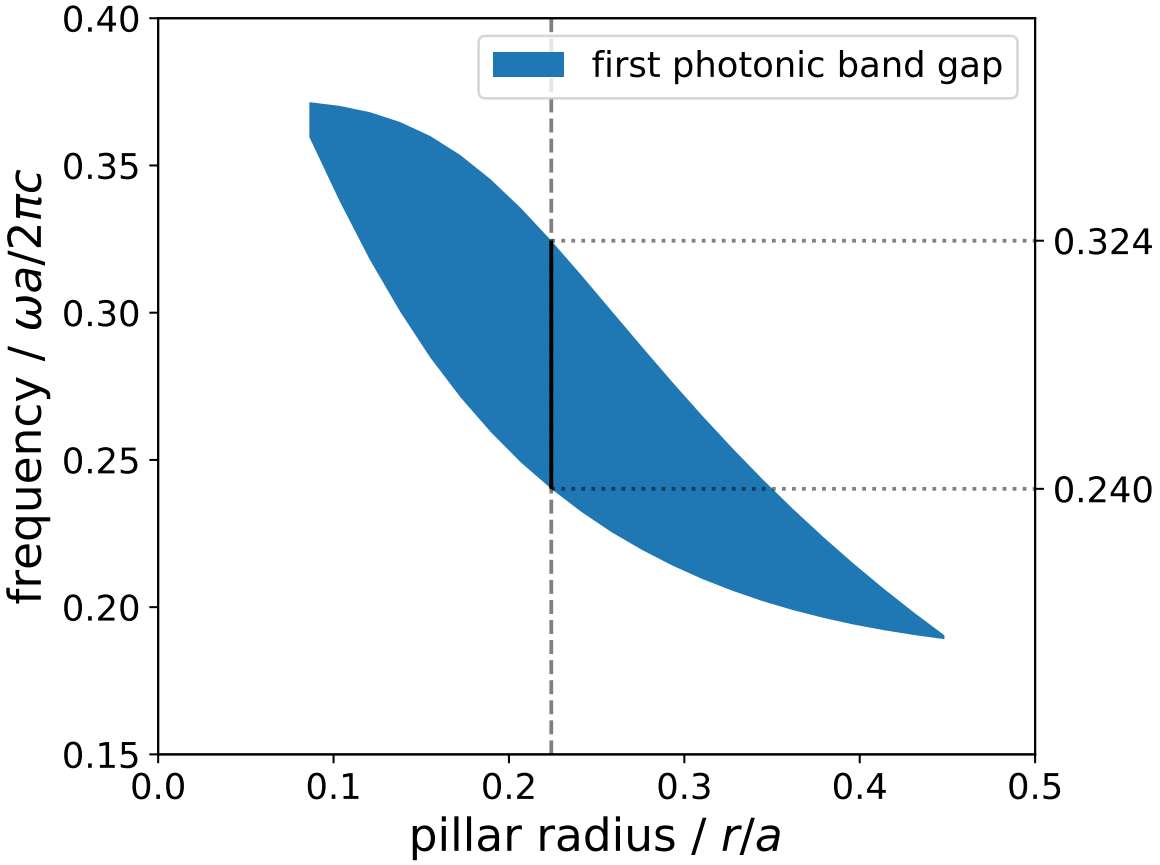

Fig. 2.6 Photonic TM band gap width as a function of pillar radius for the triangular lattice. The gap starts opening at $r = 0.1a$, is maximised for $r = 0.23a$ (30% relative width), and closes at $r = 0.45a$. The right y-axis shows the top and the bottom of the band gap at $r = 0.23a$.

For defect radius (R) between $0.25a$ (the size of the lattice pillars) and $0.7a$ (the limit of keeping pillars separate), four defect modes emerge, two of which are degenerate. See Figure 2.7 for electric field plots of the modes, and Figure 2.8 for the relation between the defect radius and frequencies of the modes. We define the fraction of the electromagnetic energy in the defect as the overlap:

$$\Gamma = \frac{\int_{\text{defect}} \varepsilon \|E\|^2}{\int_{\text{supercell}} \varepsilon \|E\|^2}, \tag{2.8}$$

where the integration in the numerator is over the defect pillar area only, and the denominator is over the whole supercell, ε is the dielectric constant and $\|E\|$ is the norm of the electric field.

The mode spanning the widest range of defect radii is the dipole, which is degenerate due to PhC symmetry. Its overlap with the defect is 0.32. At $R \simeq 0.55a$, the quadrupole mode appears, which has four lobes in the defect, and is also doubly degenerate. Its overlap with the defect is 0.63. At $R \simeq 0.6a$, two additional modes appear. The first is the hexapole, with the lowest overlap of all modes (0.25), and finally the monopole. The latter is in fact a superposition of higher-order modes (the true monopole appears for defect radii smaller than the lattice pillars), but it does have a single peak in the defect. The overlap of the monopole is 0.66. Our goal was to design and fabricate devices which would allow either the monopole or the quadrupole to be excited, in order to exploit the effects of mode concentration in the active medium (more on this in Section 2.5.1, which focuses on light-current-voltage characteristics).

A defect in the photonic lattice which is bigger than the lattice pillars will in general pull modes down from the air band. This is a consequence of the variational principle for PhCs, which dictates that increasing the effective refractive index of optically active media leads to lowering of the frequencies, as explained in Section 2.2. For a triangular lattice with the previously determined favourable ratio of $r/a = 0.25$, Figure 2.8 shows the normalised frequency of all defect modes in the band gap. The plot shows the wide tunability range of our system. The defect frequency can be chosen from a range of 0.5 THz just by changing the defect size. It is worth noting that because of the scaling properties of PhC, the entire THz region (1-10 THz) could be covered by pillars with sizes of the order of micrometers, which is entirely possible with current photolithography and etching tools.

For the active region, we chose to work with a 2 THz BtC design developed by our group[29]. It exhibits a bandwidth of ~ 100 GHz, threshold current density of 130-200 A cm^{-2}, and a maximum operating temperature of 77 K in pulsed mode. Most importantly, the AR nominal centre frequency is 2 THz, which will define the PhC physical dimensions. For

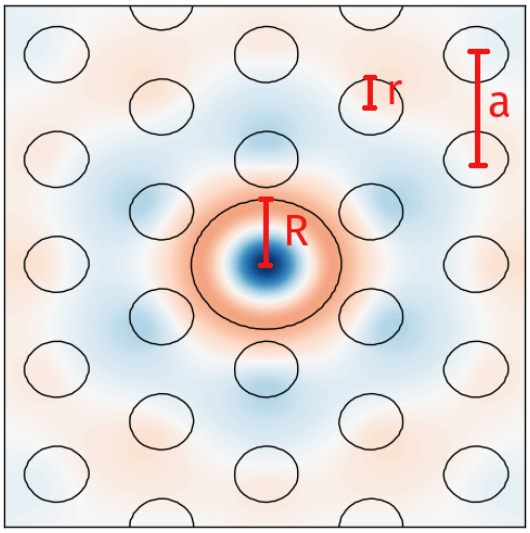

(a) Monopole. The overlap with the defect is 0.66. This mode appears in the $R = 0.6 - 0.7a$ range. a (lattice constant), r (small radius), and R (defect radius) are shown in red.

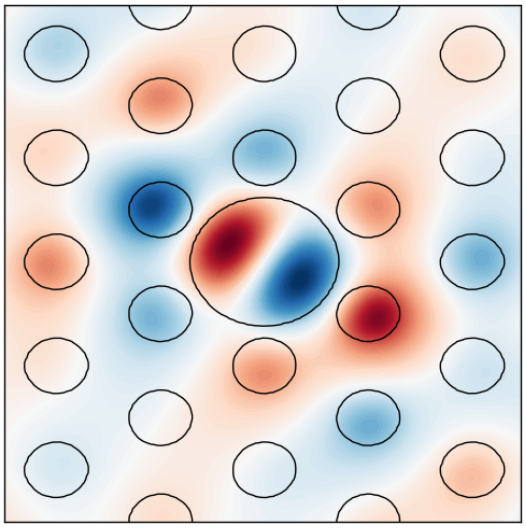

(b) Dipole. The overlap with the defect is 0.32. This mode appears in the whole range ($R = 0.25 - 0.7a$), and it is doubly degenerate due to its symmetry.

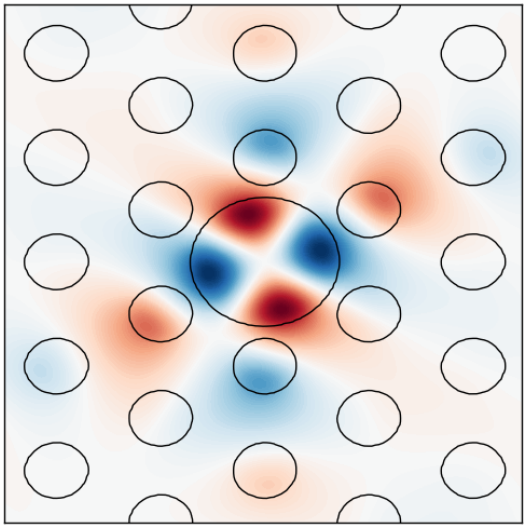

(c) Quadrupole. The overlap with the defect is 0.63. This mode appears in the $R = 0.55 - 0.7a$ range, and it is doubly degenerate due to its symmetry.

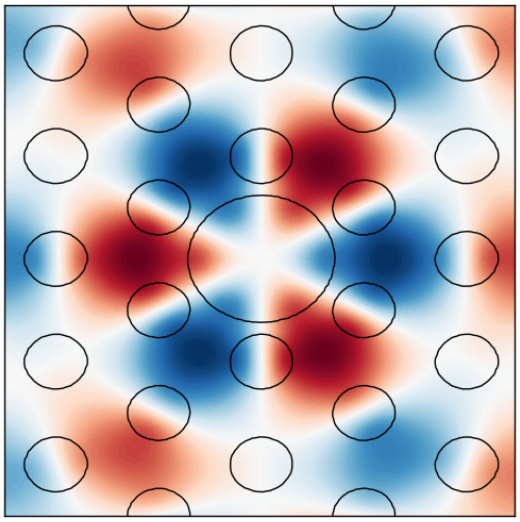

(d) Hexapole. The overlap with the defect is 0.25. This mode appears in the $R = 0.6 - 0.7a$ range.

Fig. 2.7 Profiles of the four optical modes allowed in the defects. Normalised E field is shown in each of the plots.

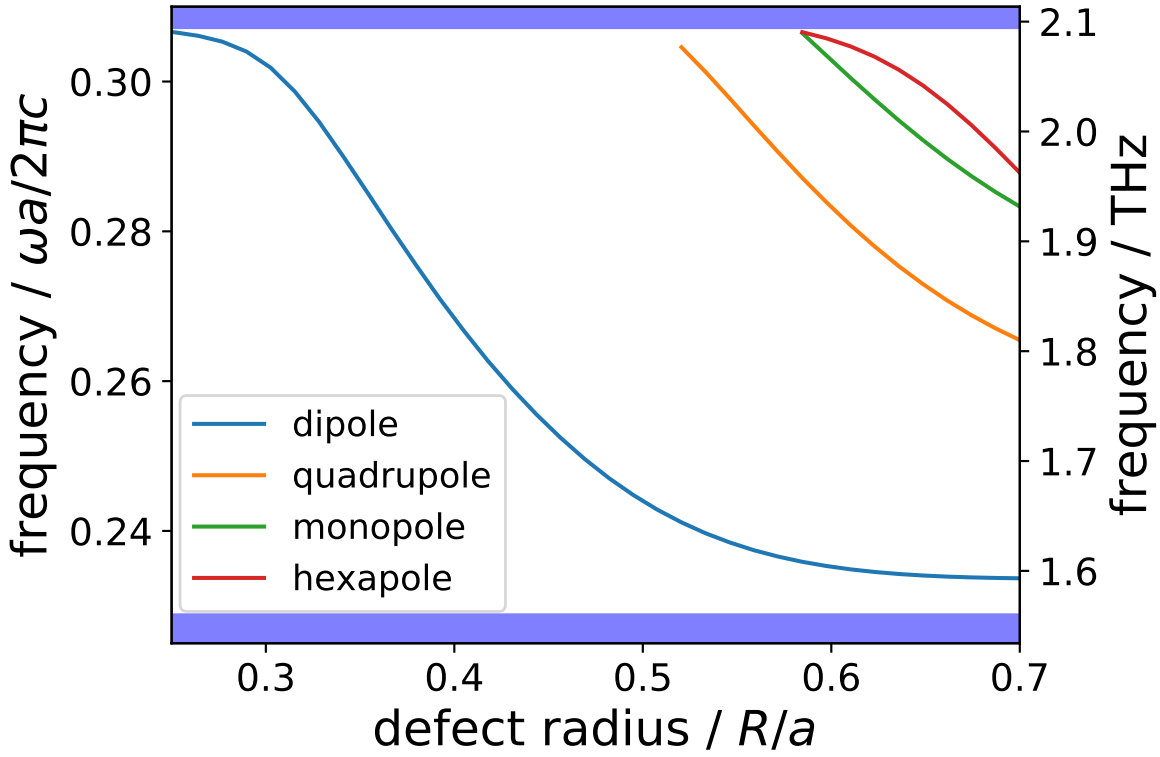

Fig. 2.8 Optical modes in the band gap vs. defect radius. The dipole (blue) exists throughout the whole range ($R = 0.25a - 0.7a$), the quadrupole (orange) exists from $R = 0.55a$ to $R = 0.7a$. The hexapole (red) and the monopole (green) are sustained from $R = 0.6a$ to $R = 0.7a$. Filled regions mark the optical bands. The right vertical axis shows absolute frequencies for $a = 44\,\mu\text{m}$, which was used for several devices presented below. The simulation was run for small pillar radius $r = 0.25a$.

large defect radius $R > 0.6a$ (maximising the overlap with the AR), the modes close to 2 THz are the monopole, the quadrupole, and the hexapole. Frequencies between 2-3 THz are particularly interesting in gas spectroscopy. Many molecules exhibit vibrational and rotational resonances in this frequency range. The bandwidth of this AR ($\sim$ 100 GHz) is wide enough to test mode selectivity with standard laboratory equipment.

The defect line geometry provides an opportunity to explore the so-called *slow light effect*. It arises from very low group velocity (v_g) of the optical modes propagating along the line. We can vary v_g by changing the distance between consecutive defects in the line.

The theory for analysing structures such as the defect line was laid out by Yariv *et al.*[58]. The authors call such structures *coupled-resonator optical waveguides* or CROWs. They use the tight-binding model analogy from condensed matter physics to show that in coupled cavities (such as PhC defects), the group velocity v_g of the optical modes is proportional to the coupling factor between the cavities. For weakly coupled cavities v_g can be low, which leads to an increase in the effective refractive index, which in turn leads to a higher electromagnetic field concentration: *the small group velocity of the CROW band can result in a large optical field with only a modest amount of power flux*[58]. This so-called *slow light effect* should enhance the gain in the defect line by concentrating the mode in the AR material, and consequently reduce J_{th}.

We chose to fabricate PhC QCLs with three different levels of coupling: D5 (weakest coupling), D3, and D1 (strongest coupling). In Figure 2.9 we show SEM images of the three types. In the experimental section (2.5) we group the results by coupling type, and then compare all three. Following Ref.[58], we expect the weakly coupled lines to exhibit the biggest reduction in J_{th}. D1 devices should in turn be the most powerful, since there is more AR material overlapping with the mode. Quantifying this effect is beyond the scope of this thesis, and we will analyse it qualitatively instead.

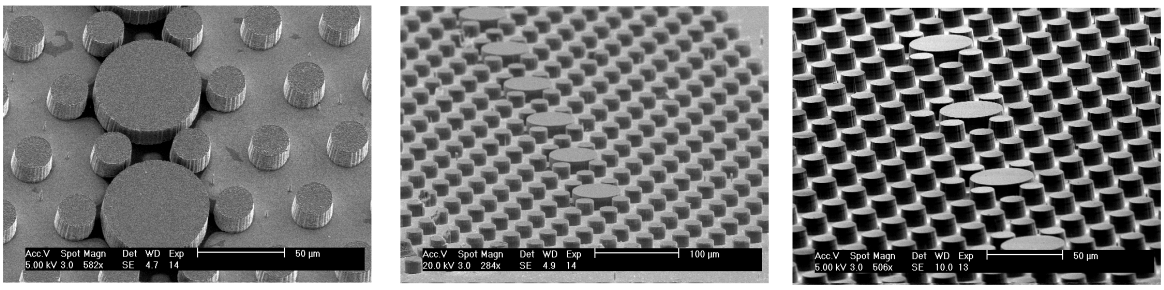

Fig. 2.9 SEM images of three different defect lines. **Left**: D1, where the defects are separated by one row of small pillars. **Middle**: D3, where the defects are separated by three rows of small pillars. **Right**: D5, where the defects are separated by five rows of small pillars.

Another effect observed in laser cavities is the Purcell enhancement[59], which affects the local density of states of photons inside a microcavity. Walther *et al.*[60] proposed it as a way to reduce radiative emission lifetimes and thus decrease J_{th}. The enhancement is proportional to $\frac{(\lambda/n)^3}{V}$, where λ is the free space wavelength of the optical mode, n is the refractive index of the cavity material, and V is the volume of the cavity. Substituting the values for the defects ($\lambda \simeq 155\,\mu m$, $n = 3.6$, $V = \pi \cdot (30\,\mu m)^2 \cdot 14\,\mu m$), the ratio is around 2. This suggests the reduction in radiative lifetimes could be measurable. In order to quantify Purcell effect in the defect line, one should cleave the device so that only one pillar is left, which is entirely possible. A more profound exploration of the Purcell enhancement is beyond the scope of this work, but we suggest that defect line QCLs could serve as a platform to study this phenomenon.

2.4 Fabrication

In order to fabricate defect line QCLs, a 2 THz BtC wafer (V305) was thermocompressively bonded to a n+ doped substrate wafer with gold as a bonding layer. The substrate side of the QCL wafer was then mechanically polished and etched in citric acid solution, as described in Section 1.5.3 about MM processing. Pillar patterns were defined on samples with optical photolithography and thermal evaporation. Layers of titanium (10 nm), gold (500 nm), and nickel (100 nm) were evaporated to serve as the etching mask. Nickel acted as a sacrificial layer in the etching process. Ni is harder and slower to etch than gold, but the etches were very long (2-3 h), so all of the Ni was etched away and only a layer of Ti and Au was left.

The PhC was dry etched in a JLS Designs RIE80 tool, using $SiCl_4$: Ar process gases in 6:10 sccm proportion (see Figure 2.11a). Etch duration was limited to approximately 3 h, in order not to exceed the chamber temperature of 40 °C. At higher temperatures we observed a deterioration in the surface roughness, as well as a slower etch rate. The initial, long etch of 150-180 min was preceded by a 15-20 h evacuation of the chamber, to reduce the pressure below 0.1 mTorr (13 mPa). After the first etch, samples were removed from the chamber, and inspected with a surface profilometer and an optical microscope. If more etching was required, the sample was put back into the RIE chamber, which was then evacuated for approximately 2 h, until the pressure dropped below 0.3 mTorr (40 mPa). For shorter etch duration, slightly higher pressure than for the initial etch resulted in acceptable quality. The average etch ratio was $\sim 100\,nm/min$.

We observed some variability in the slope of the pillar walls. Figure 2.10 illustrates the limits of wall angle range. On the left, a device with 83° slope is shown. On the right, a vertical wall can be seen. In the simulations in the previous section, we assumed the pillars to

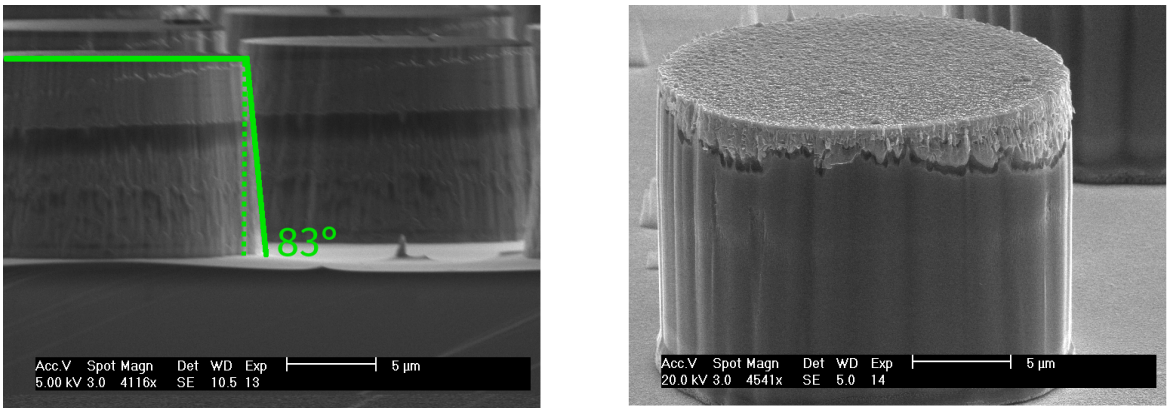

Fig. 2.10 Two limits of pillar wall verticality. **Left**: A pillar with a wall incline of 83°. **Right**: A pillar with vertical walls.

have the same radius at the base and at the top. A 83° wall would lead to a base approximately 3 µm wider than the top. The pillars should therefore be thought of as having an effective radius. This will affect frequency selectivity, which we discuss in Section 2.5.2.

Next, BCB was spun in between the pillars and cured (Figure 2.11b). The spinning and curing process was repeated until the BCB layer was at least as thick as the pillars ($\sim 14\,\mu$m, see Figure 2.11c). Usually, 3 repeats of the spinning and curing process were enough to cover the pillars. The detailed description of BCB processing is described in the next chapter, in Section 3.3. In order to remove excess BCB and flatten its surface, the samples were plasma etched in $O_2 : CHF_3$ (30:20 sccm) atmosphere (Figure 2.11d). Subsequently, a top contact layer of Ti/Au (10/300 nm) was thermally evaporated (Figure 2.11e). Finally, the lasers were cleaved and mounted on copper blocks. It is especially difficult to achieve repeatability in facet cleaving, which greatly affects the output power and beam quality.

Some of the fabrication was done in house, and some (when the RIE tool was not available) by Luca Masini at the Scuola Normale Superiore in Pisa.

2.4.1 Failure modes

It should be noted that the fabrication yield for PhC QCLs was approximately 30%. Here we will discuss some of the most common fabrication failure modes, illustrated in Figure 2.12.

The lithography and lift-off process is more sensitive to imperfections than in the case of standard ridge fabrication. The features are finer — for the small pillars, circles with a $\sim 11\,\mu$m radius need to be defined and developed. Figure 2.12a shows an optical microscope image of poorly defined features. Jagged pillar edges during lithography propagated in the etch direction in the RIE, as seen in Figure 2.12b. These imperfections were not always

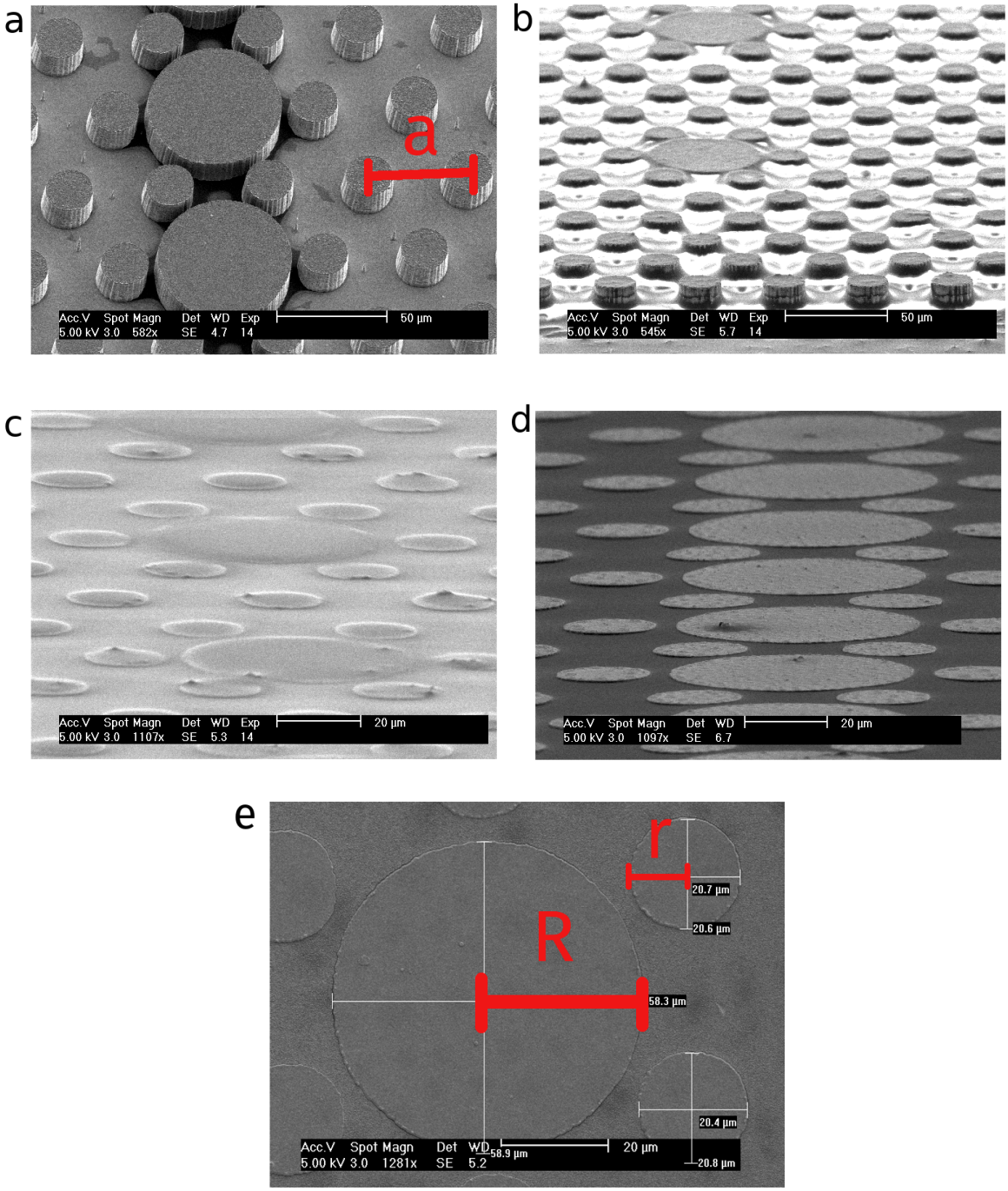

Fig. 2.11 SEM images of consecutive defect QCL processing stages. **a**: After dry etching. The pillar height is approximately $\sim 14\,\mu m$. A layer of Ti/Au remains on top of the pillars. Lattice constant **a** is marked in red. **b**: After the first BCB layer spinning and curing. The pillars are not fully covered yet. **c**: After final BCB spinning and curing. The pillars are fully covered with the polymer. **d**: After several rounds of $O_2 : CHF_3$ etch. The BCB surface is flat and the tops of the pillars are exposed. **e**: After evaporating the top contact. All pillars are connected with a layer of Ti/Au. Defect radius **R**, and lattice pillar radius **r** are marked in red.

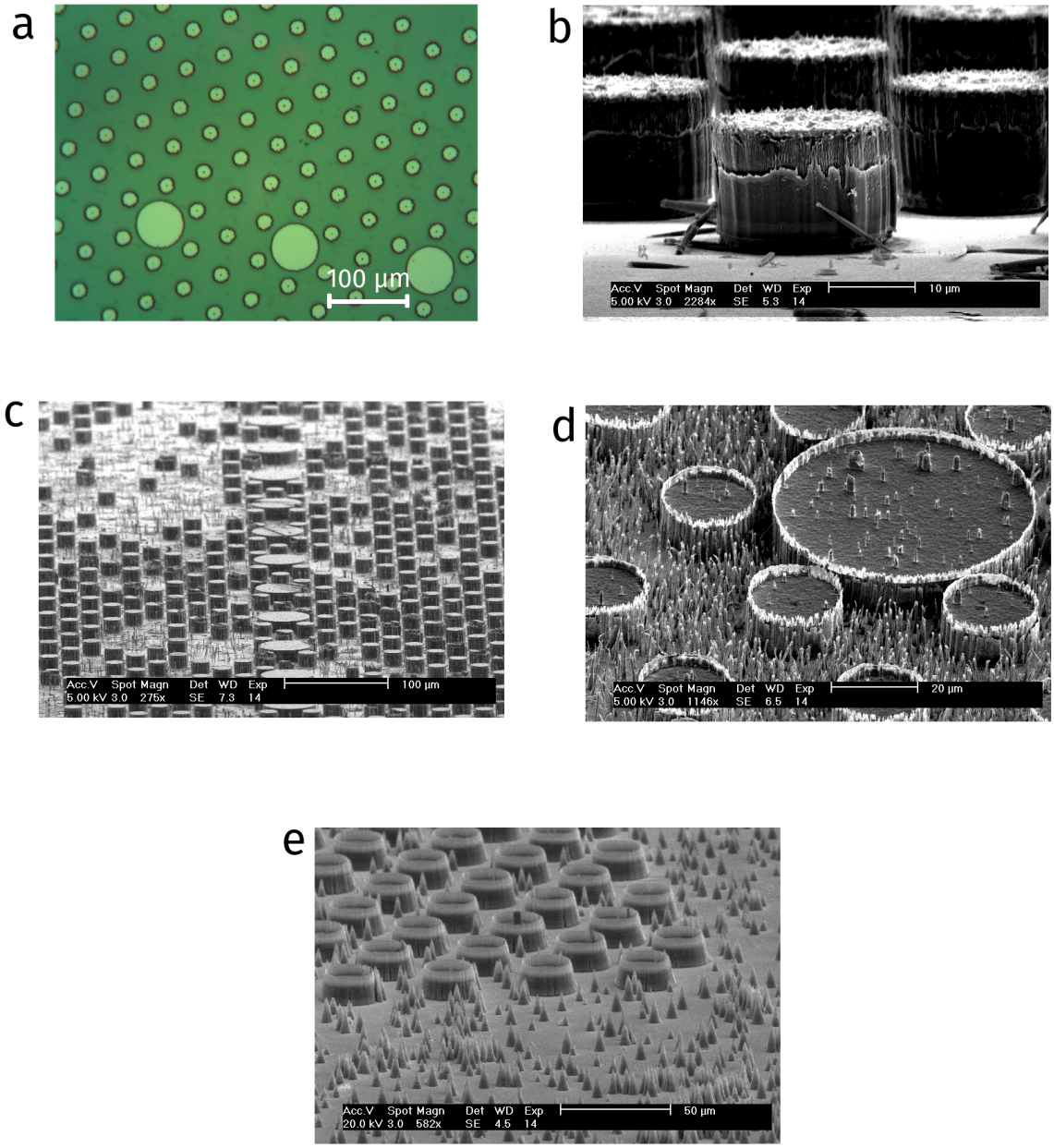

Fig. 2.12 Common defect QCL fabrication failure modes. **a**: Poorly defined photolitography features and **b**: their effect on pillar wall smoothness. **c**: The result of uneven evaporation and lift-off — part of the mask detached during etching and pillars were not formed. **d**: *Grassing*. The QCL material was not etched uniformly, and many spikes remained on the surface. **e**: *Grassing*, as well as a mask which had been etched before the desired pillar height was reached.

clearly visible after lithography, therefore we assume that some of the working devices did not have smooth vertical walls.

Metal lift-off was another important step which affected the RIE outcomes. Figure 2.12c shows a device for which lift-off looked normal during optical microscope inspection, but clearly part of the pillar mask did not adhere to the surface strongly enough. It detached early during the dry etch, and this resulted in missing pillars.

Dry etching in the RIE chamber was the step in the defect QCL fabrication with the highest failure rate. We spent approximately 3 months on system calibration and test etches (approx. 30 samples). Despite the efforts to keep the chamber conditions the same for each defect sample, the process failed about 30% of the time. In our opinion, there were two main reasons for the variability. Firstly, the state of the samples going into the chamber was not always identical. The evaporation or lift-off quality could vary, as well as the cleanliness of the sample. Secondly, the gas mixture that we used is very corrosive, and the chamber had to be cleaned every other day. It is possible that the cleaning quality was not always the same, and some residues from previous processes remained in the chamber. Two example RIE failure modes are shown in Figure 2.12d and e. In the first SEM picture, chamber contamination (either from a previous process or from low quality evaporation) caused heavy *grassing*. In the second image, another sample with "grass" is shown. Additionally, the mask on this sample had been etched before the desired pillar height was reached.

2.5 Experimental results

2.5.1 Light-current-voltage characteristics

In order to present the light-current-voltage (LIV) characteristics of defect QCLs, we must first discuss how to calculate current density in PhC lasers, which is a non-trivial task[49]. BCB is an electrical insulator, therefore the current only passes through the pillars, but the non-uniform electromagnetic field affects electronic transport. Perhaps the most intuitive method of calculating J is to divide the current (as read by a current probe) by the total area of pillars in a device, thus assuming that the flow is approximately uniform across pillars. We will use this method in the presented plots unless stated otherwise.

An alternative method of current density estimation, used by Zhang *et al.*[42], is to align current-voltage (IV) curves of photonic devices with those of reference MM lasers. Their AR exhibited a distinct feature in electronic transport before J_{th}, which served as an aligning anchor for the two curves. Unfortunately, the BtC AR used in this work did not have any prominent features. Instead, we aligned the slopes of two devices (PhC and

reference MM) pre-threshold. In most cases, J_{th} calculated with this method was similar to the area estimation method ($\pm 20\%$, except for two devices, S2 and S8, where the IV method resulted in a 50-100% higher J_{th}). This method is illustrated in Figure 2.13, with S2 and the reference laser. IV-based current estimation resulted in $J_{th} = 150\,\mathrm{A\,cm^{-2}}$, which was 35% lower than the reference MM ($J_{th} = 230\,\mathrm{A\,cm^{-2}}$). Area-based current estimation resulted in $J_{th} = 95\,\mathrm{A\,cm^{-2}}$, which was a 59% reduction compared to MM. As explained earlier, we expected the current reduction to be correlated with coupling strength due to the slow light effect, i.e. $J_{th}(D5) < J_{th}(D3) < J_{th}(D1)$.

Because the BCB, which surrounds the PhC pillars, is a worse thermal conductor than GaAs, we expected the maximum operating temperature of the defect lasers to be lower than that of the reference MM laser. Dow, the BCB manufacturer, reports the polymer's thermal conductivity to be $0.29\,\mathrm{W\,m^{-1}\,K^{-1}}$ at 297 K. GaAs conductivity varies with temperature, and in the 10-100 K range it takes values between 1000 and $4000\,\mathrm{W\,m^{-1}\,K^{-1}}$[61].

The effective lasing volume of defect line QCLs is much smaller than in conventional MM lasers. The defects only constitute approximately 10% of the total volume of the device above the bonding metal layer. Additionally, the BCB/GaAs facets are not as well-defined as in ridge lasers, potentially reducing output power. We therefore expected that MM lasers would be at least one order of magnitude more powerful. The effect of varying the defect coupling is difficult to quantify. On the one hand, strongly coupled defect lines (D1) have

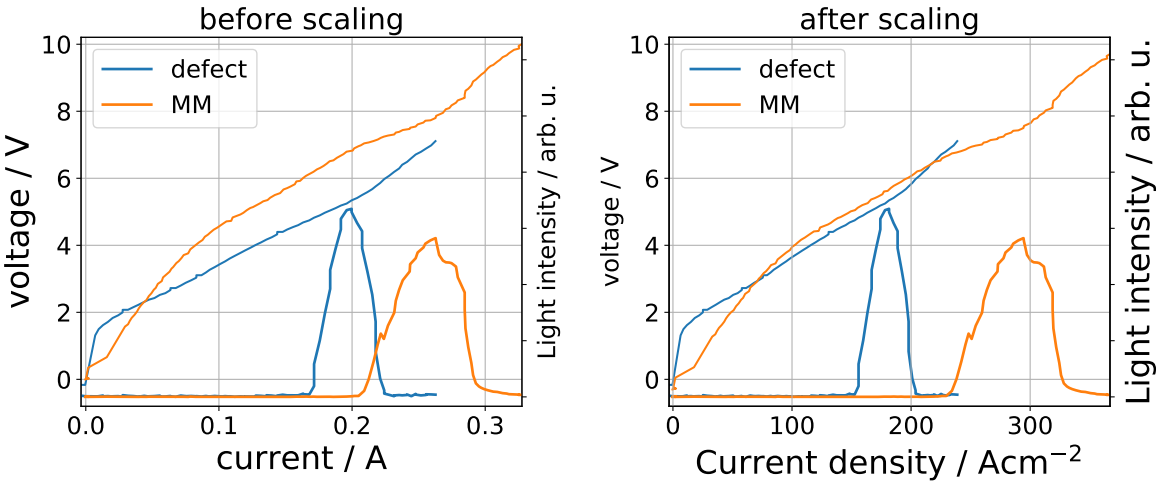

Fig. 2.13 **Left**: LIV data for S2 defect QCL and the MM reference device. **Right**: J_{th} estimated from IV curves of defect (S2) and MM devices. The two pre-threshold slopes are aligned by changing the effective area of the defect QCL. This leads to an estimation of $J_{th} = 150\,\mathrm{A\,cm^{-2}}$, which is 35% lower than the reference ($J_{th} = 230\,\mathrm{A\,cm^{-2}}$). The bias voltage of the defect laser was shifted by 0.3 V for easier visual alignment. The light intensity is not to scale (MM's output is 50× more powerful).

more active material than D3 and D5, potentially resulting in higher power output. On the other hand, the slow light effect is stronger in weakly coupled defect lines (D5), and should enhance the output. We expected that these subtle differences would be overshadowed by fabrication variability.

Figure 2.14 shows LIV characteristics of the reference MM device, fabricated from the same AR as the defect lasers, into a 1 mm × 85 µm ridge. Whenever possible, we cleaved the PhC devices to a similar length. The reference device attained a maximum operating temperature of 70 K, $J_{th} = 230\,\mathrm{A\,cm^{-2}}$, and the peak output power of 120 µW. Below we present the LIV characterisation of the nine fabricated devices, grouped by the coupling strength, i.e. the distance between the defect pillars. We will compare the results at the end of this section. All of the devices were measured in pulsed mode at 100 kHz. We found 30% to be the optimal duty cycle for these lasers (good signal to noise ratio without decreasing T_{max}). We therefore measured most of the devices at 30%, except for S3 and S8, which worked optimally at 5% DC, possibly due to thermal management issues. Table 2.1 lists all

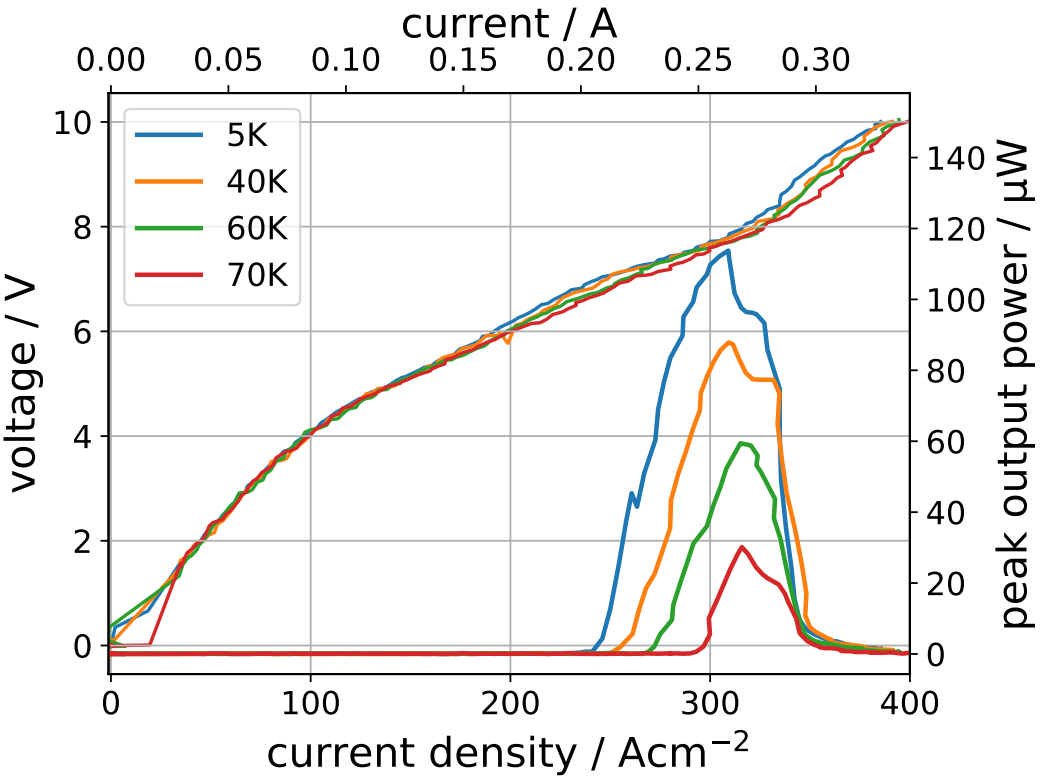

Fig. 2.14 LIV characteristics of the reference MM device. The laser was measured in pulsed mode, with 100 kHz pulses and 5% duty cycle, with a Golay cell detector. The threshold current density of this device at 5 K is 220 $\mathrm{A\,cm^{-2}}$, and it lases up to 70 K.

Table 2.1 All defect line devices reported in this thesis along with their nominal parameters and measured properties. *Type* pertains to the coupling strength (number of small pillars between defects), R is the nominal defect radius, a is the nominal lattice constant. Nominal small pillar radius was set to $0.25a$ in all devices.

sample	type	R (μm)	a (μm)	J_{th} (area) ($\mathrm{A\,cm^{-2}}$)	J_{th} (IV) ($\mathrm{A\,cm^{-2}}$)	peak power (μW)
MM				230		115
S1	D5	30	44	115	140	0.7
S2	D5	30	44	95	150	3.0
S3	D5	27	42	135	160	22
S4	D3	31	46	190	150	2.8
S5	D3	30	44	120	170	29
S6	D3	31	46	215	170	0.8
S7	D1	31	46	125	160	6.8
S8	D1	30	44	100	210	3.0
S9	D1	30	44	170	185	9.0

devices reported in this section, along with their nominal parameters, measured threshold current density, and output power.

D5

Figures 2.15–2.17 show LIV characteristics of three D5 defect line QCLs characterised in this work: S1, S2, and S3.

Maximum operating temperature was lower than MM in the defect devices, with S1 attaining $\mathrm{T_{max}} = 25\,\mathrm{K}$, S2 attaining $\mathrm{T_{max}} = 50\,\mathrm{K}$, and S3 attaining $\mathrm{T_{max}} = 60\,\mathrm{K}$, compared to MM's $\mathrm{T_{max}} = 70\,\mathrm{K}$.

All three devices had a narrower dynamic range than the MM reference (for which the range was $120\,\mathrm{A\,cm^{-2}}$). S1 emission spanned $20\,\mathrm{A\,cm^{-2}}$, S2 spanned $30\,\mathrm{A\,cm^{-2}}$, and S3 spanned $70\,\mathrm{A\,cm^{-2}}$. This, in addition to a smooth rise and fall of all defect peaks, already hints at single mode emission.

The peak output power from D5 defect devices was 0.7 μW (S1), 3 μW (S2), and 22 μW (S3), i.e. approximately 1-2 orders of magnitude lower than the reference MM. S3 had a different defect size ($R = 27\,\mu\mathrm{m}$) than S1 and S2 ($R = 30\,\mu\mathrm{m}$, see Table 2.1), which could lead to a stronger mode confinement. However, this would not account for an order of magnitude difference. We attribute it instead to the fabrication quality, the control of which is an area for future improvement.

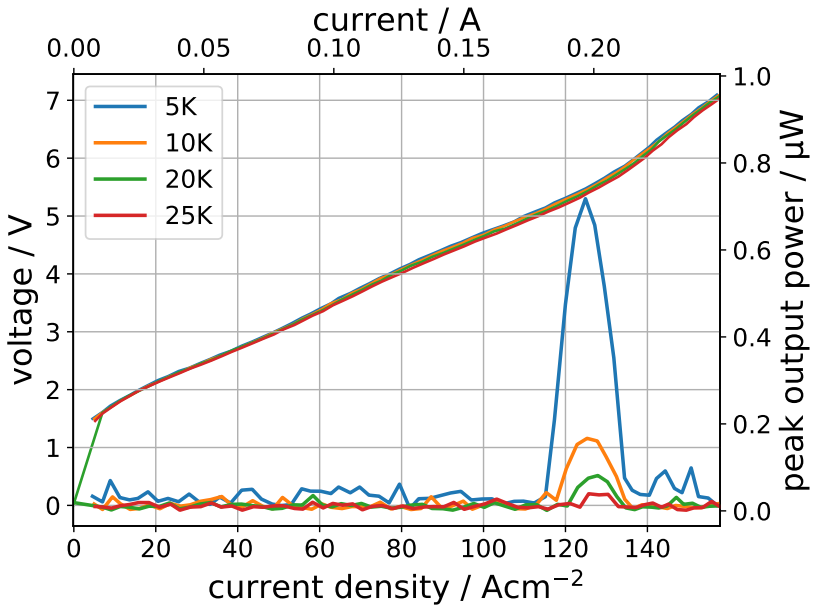

Fig. 2.15 LIV characteristics of S1 defect QCL. The laser was measured in pulsed mode, with 100 kHz pulses and 30% duty cycle, with a Golay cell detector. The threshold current density of this device at 5 K (estimated using the total area of pillars) is 115 A cm^{-2}, and it lases up to 25 K.

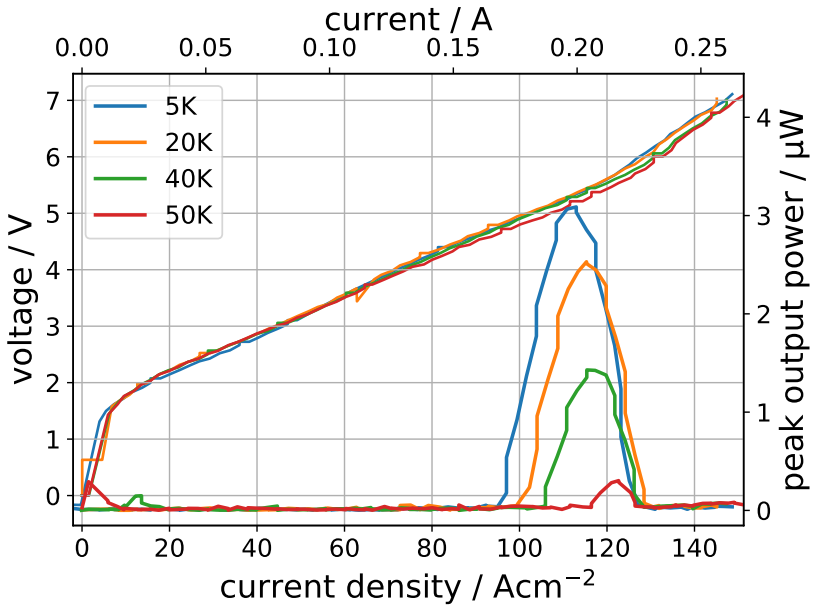

Fig. 2.16 LIV characteristics of S2 defect QCL. The laser was measured in pulsed mode, with 100 kHz pulses and 30% duty cycle, with a Golay cell detector. The threshold current density of this device at 5 K (estimated using the total area of pillars) is 95 A cm^{-2}, and it lases up to 50 K.

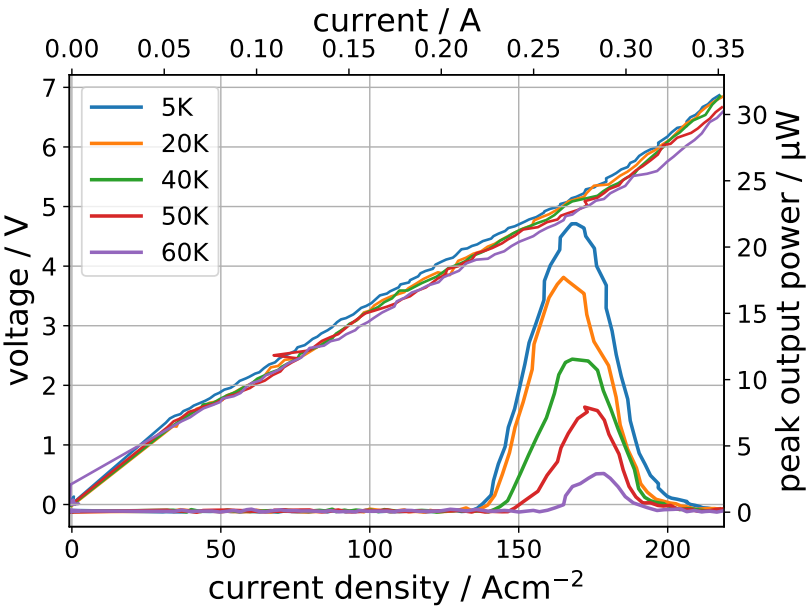

Fig. 2.17 LIV characteristics of S3 defect QCL. The laser was measured in pulsed mode, with 100 kHz pulses and 5% duty cycle, with a Golay cell detector. The threshold current density of this device at 5 K (estimated using the total area of pillars) is 135 A cm^{-2}, and it lases up to 60 K.

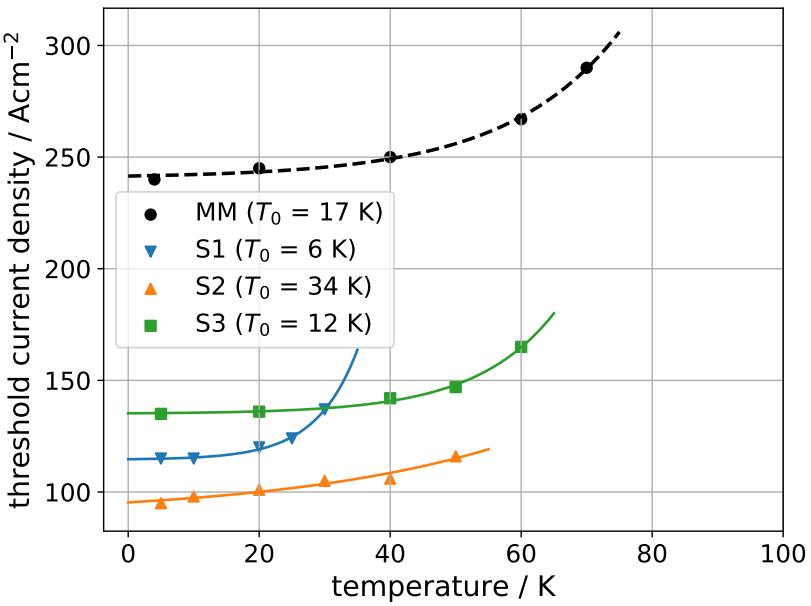

Fig. 2.18 J_{th} of D5 devices (colour) and the reference MM QCL (black). Defect QCL J_{th} was estimated using the pillar area method. The lines are fitted to $J_{th} = J_0 + A \cdot \exp T/T_0$. Defect line QCLs exhibit lower J_{th} than the MM throughout the operating temperature range.

Threshold current density was reduced in all D5 devices, compared to the MM reference. Using the effective area estimation, the reduction at 5 K was 48% (S1), 57% (S2), and 39% (S3). J_{th} calculated using the LIV alignment method was reduced by 37% (S1), 32% (S2), and 28% (S3). As shown in Figure 2.18, the reduction prevailed throughout the operating temperature range of all defect QCLs. J_{th} in this figure was obtained using the effective area estimation. Solid curves correspond to the least squares fit of $J_{th} = J_0 + A \cdot \exp T/T_0$.

D3

Figures 2.19–2.21 show LIV characteristics of three D3 defect line QCLs characterised in this work: S4, S5, and S6.

Maximum operating temperature was lower than MM in two D3 defect devices. S4 attained $T_{max} = 35\,K$, and S6 attained $T_{max} = 55\,K$. S5 however lased up to $T_{max} = 70\,K$, the same as the reference MM. It also turned out to be the most powerful device. S5 therefore exemplifies the higher end of what is attainable using our fabrication techniques in terms of performance.

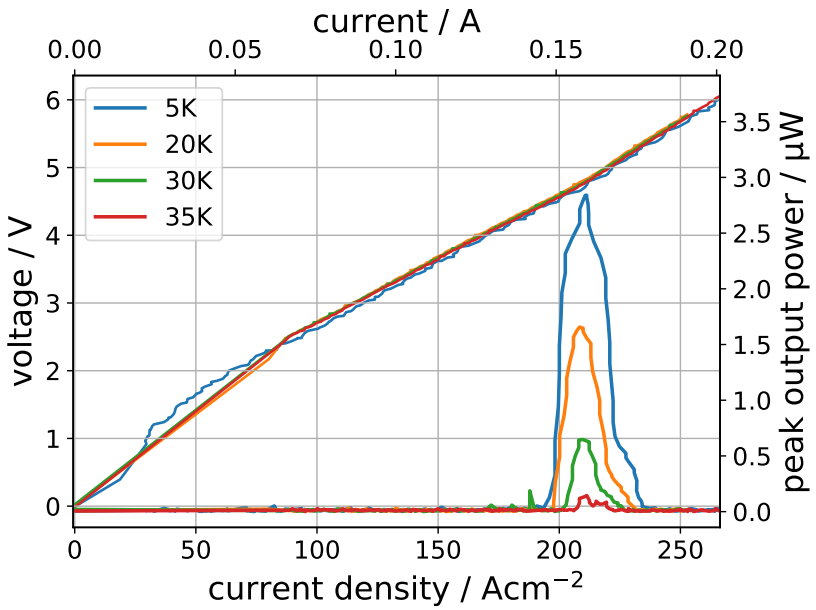

Fig. 2.19 LIV characteristics of S4 defect QCL. The laser was measured in pulsed mode, with 100 kHz pulses and 30% duty cycle, with a Golay cell detector. The threshold current density of this device at 5 K (estimated using the total area of pillars) is 190 A cm^{-2}, and it lases up to 35 K.

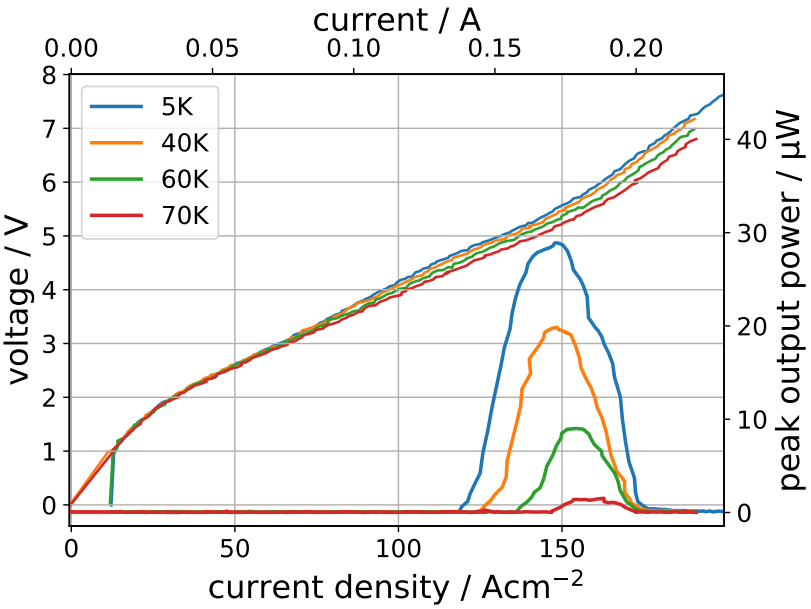

Fig. 2.20 LIV characteristics of S5 defect QCL. The laser was measured in pulsed mode, with 100 kHz pulses and 30% duty cycle, with a Golay cell detector. The threshold current density of this device at 5 K (estimated using the total area of pillars) is 120 A cm^{-2}, and it lases up to 70 K.

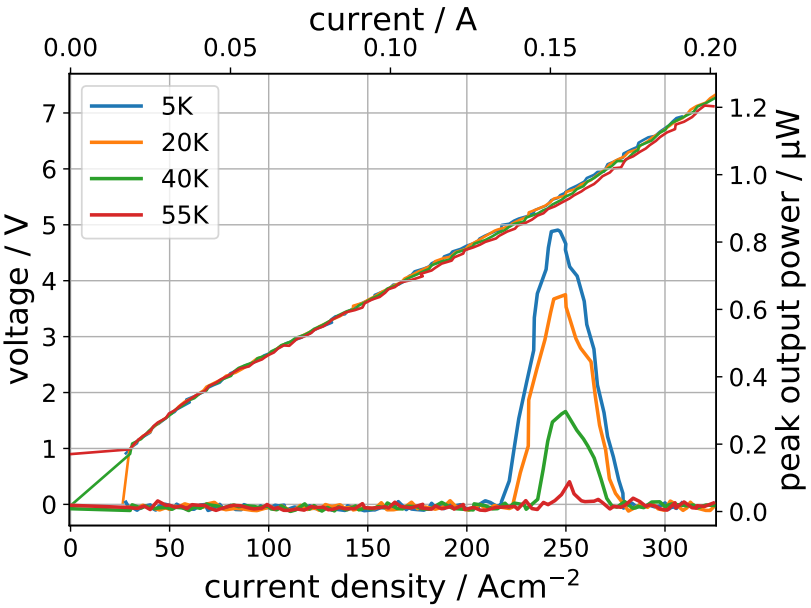

Fig. 2.21 LIV characteristics of S6 defect QCL. The laser was measured in pulsed mode, with 100 kHz pulses and 30% duty cycle, with a Golay cell detector. The threshold current density of this device at 5 K (estimated using the total area of pillars) is 215 A cm^{-2}, and it lases up to 55 K.

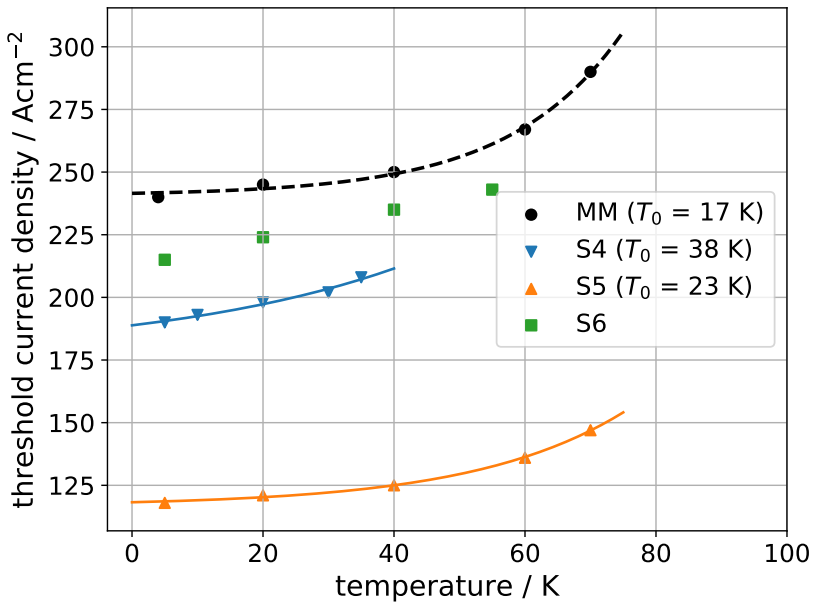

Fig. 2.22 J_{th} of D3 devices (colour) and the reference MM QCL (black). Defect QCL J_{th} was estimated using the pillar area method. The lines are fitted to $J_{th} = J_0 + A \cdot \exp T/T_0$. We were unable to calculate fitting parameters for S6, which exhibited linear dependency of J_{th} vs. T. Defect line QCLs exhibit lower J_{th} than the MM throughout the operating temperature range.

All three devices had a narrower dynamic range than the MM reference (120 A cm^{-2}). S4 emission spanned 40 A cm^{-2}, S5 spanned 50 A cm^{-2}, and S6 spanned 60 A cm^{-2}. Similar to D5, the shape of the intensity peaks did not suggest multi-mode emission.

The peak output power from D3 defect devices was 2.8 µW (S4), 29 µW (S5), and 0.8 µW (S3), i.e. approximately 1-2 orders of magnitude lower than the reference MM. These values are of the same order as for D5, and we again attribute their variability to the fabrication process. Threshold current density was reduced in all D3 devices, compared to the MM reference. Using the effective area estimation, the reduction at 5 K was 14% (S4), 45% (S5), and 2% (S6). J_{th} calculated using the LIV alignment method was reduced by 32% (S4), 23% (S5), and 23% (S6). Figure 2.22 shows J_{th} vs. T throughout the operating temperature range. S5 exhibited a similar threshold reduction to D5 devices. J_{th} of S6 did not show the typical exponential behaviour, and we were unable to get good fitting parameters for the threshold formula $J_{th} = J_0 + A \cdot \exp T/T_0$. S6, along with S4, showed a more modest reduction in current density than other defect devices. This could be caused by worse thermal management compared to other defect line lasers.

D1

Figures 2.23–2.25 show LIV characteristics of three D1 defect line QCLs characterised in this work: S7, S8, and S9.

Maximum operating temperature was lower in the defect devices, with S7 attaining $T_{max} = 40\,K$, S8 attaining $T_{max} = 50\,K$, and S9 attaining $T_{max} = 60\,K$, compared to MM's $T_{max} = 70\,K$.

Again, all three devices had a narrower dynamic range than the MM reference ($120\,A\,cm^{-2}$). S7 emission spanned $30\,A\,cm^{-2}$, S8 spanned $20\,A\,cm^{-2}$, and S9 spanned $50\,A\,cm^{-2}$. S7 exhibited a sharp feature in its emission peak, which could be an indication of multi-frequency emission. Unfortunately, we were unable to measure S7's spectrum due to the spectrometer's unavailability.

The peak output power from D1 defect devices was 6.8 µW (S7), 3 µW (S8), and 9 µW (S9), i.e. approximately 1-2 orders of magnitude lower than the reference MM.

Threshold current density was reduced in all D1 devices, compared to the MM reference. Using the effective area estimation, the reduction at 5 K was 43% (S7), 55% (S8), and 23% (S9). J_{th} calculated using the LIV alignment method was reduced by 27% (S7), 5% (S8), and 16% (S9). As shown in Figure 2.26, the reduction prevailed throughout the operating

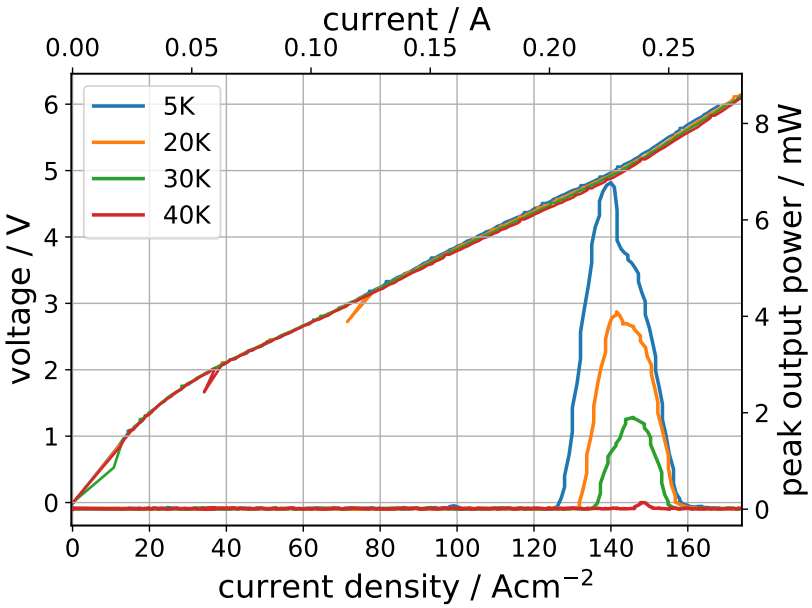

Fig. 2.23 LIV characteristics of S7 defect QCL. The laser was measured in pulsed mode, with 100 kHz pulses and 30% duty cycle, with a Golay cell detector. The threshold current density of this device at 5 K (estimated using the total area of pillars) is $125\,A\,cm^{-2}$, and it lases up to 40 K.

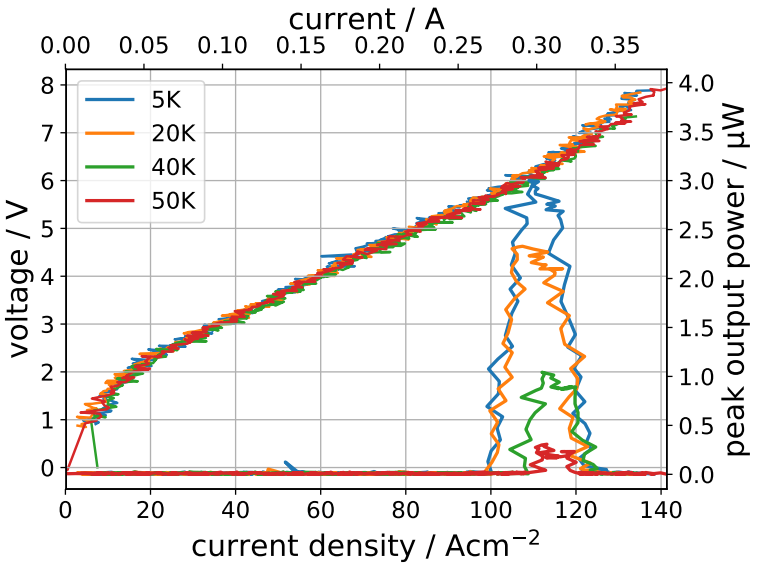

Fig. 2.24 LIV characteristics of S8 defect QCL. The laser was measured in pulsed mode, with 100 kHz pulses and 5% duty cycle, with a Golay cell detector. The threshold current density of this device at 5 K (estimated using the total area of pillars) is 100 A cm^{-2}, and it lases up to 50 K. The noise in the current signal is due to intermittent problems with the current probe and/or the power supply.

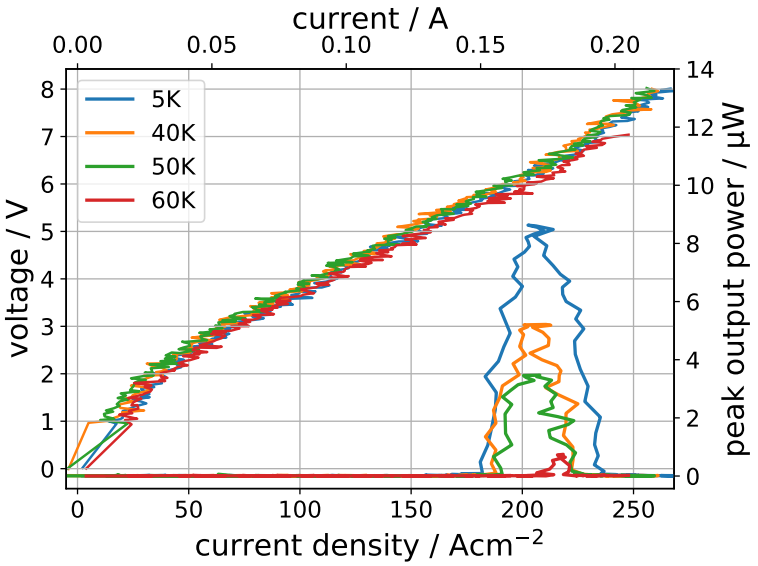

Fig. 2.25 LIV characteristics of S9 defect QCL. The laser was measured in pulsed mode, with 100 kHz pulses and 30% duty cycle, with a Golay cell detector. The threshold current density of this device at 5 K (estimated using the total area of pillars) is 170 A cm^{-2}, and it lases up to 60 K. The noise in the current signal is due to intermittent problems with the current probe and/or the power supply.

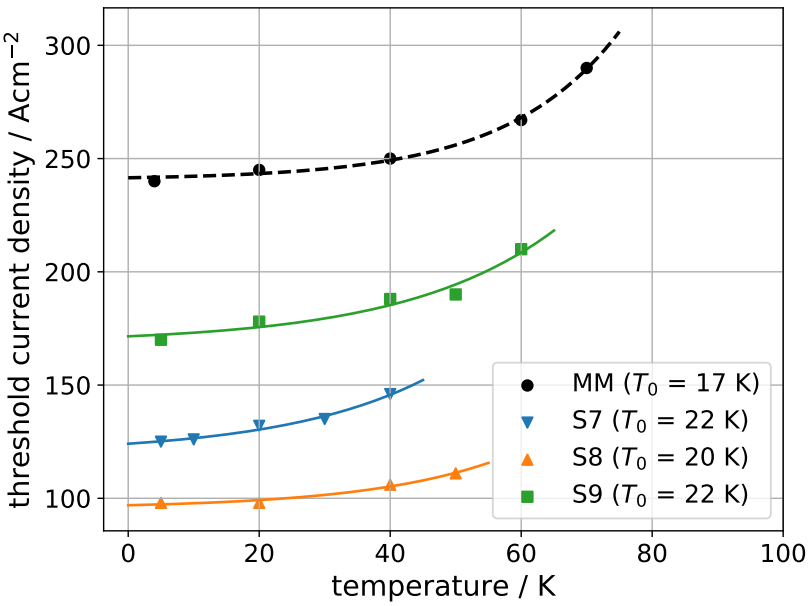

Fig. 2.26 J_{th} of D1 devices (colour) and the reference MM QCL (black). Defect QCL J_{th} was estimated using the pillar area method. The lines are fitted to $J_{th} = J_0 + A \cdot \exp T/T_0$. Defect line QCLs exhibit lower J_{th} than the MM throughout the operating temperature range.

temperature range of all D1 defect QCLs. The fitting parameter T_0 in all three devices was similar to that of the reference QCL ($T_0(\mathrm{MM}) = 17\,\mathrm{K}$). This is in line with the expectation that PhC lasers with closely spaced defects should have the most similar characteristics to traditional waveguide QCLs.

Comparing D5, D3, and D1

All defect devices exhibited a lower J_{th} than the reference MM sample. This, along with frequency selectivity, was the main goal of this work. See Figure 2.27 for all values of J_{th} at 5 K, using both area and IV estimation method. The reduction varied from 2% (S6, area estimation method) to 57% (S2, area estimation method). A 20% to 40% reduction was typical, using both methods of current density estimation. See also Table 2.1, which includes all measured devices along with their properties and performance.

The slow light effect should lead to higher J_{th} reduction in weakly coupled PhC QCLs. Indeed, when using the values from IV approximation of threshold current density, D5 QCLs had on average the lowest threshold ($150\,\mathrm{A\,cm^{-2}}$), followed by D3 ($163\,\mathrm{A\,cm^{-2}}$), and D1 ($185\,\mathrm{A\,cm^{-2}}$). However, this trend was not confirmed when using values approximated with the area of the devices. There, the lowest average threshold current density was still in D5

(115 A cm^{-2}), but it was followed by D1 (132 A cm^{-2}), and D3 samples had on average the highest $J_{th} = 175$ A cm^{-2}.

Unsurprisingly, the peak emitted power in all defect lasers was lower than in the reference MM, where $P_{peak} = 115\,\mu W$. The power ranged from 0.7 µW in S1 (Figure 2.15) to 29 µW in S5 (Figure 2.20).

As mentioned at the beginning of this section, the power should increase with coupling strength (i.e. D5 less powerful than D1) due to lower defect density. On the other hand it should decrease with coupling strength due to the weaker slow light phenomenon. In order to adjust for the first factor, we divided the peak power by the number of defects in each device and plotted the data in Figure 2.28. Indeed, power per defect was correlated with coupling strength; it was 1.4 µW on average for D5, 1.1 µW for D3, and 0.38 µW for D1. However, average peak power of D3 and D5 was skewed by two powerful devices: S5 and S3, respectively. More experiments are required to confirm the dependency between defect coupling and power.

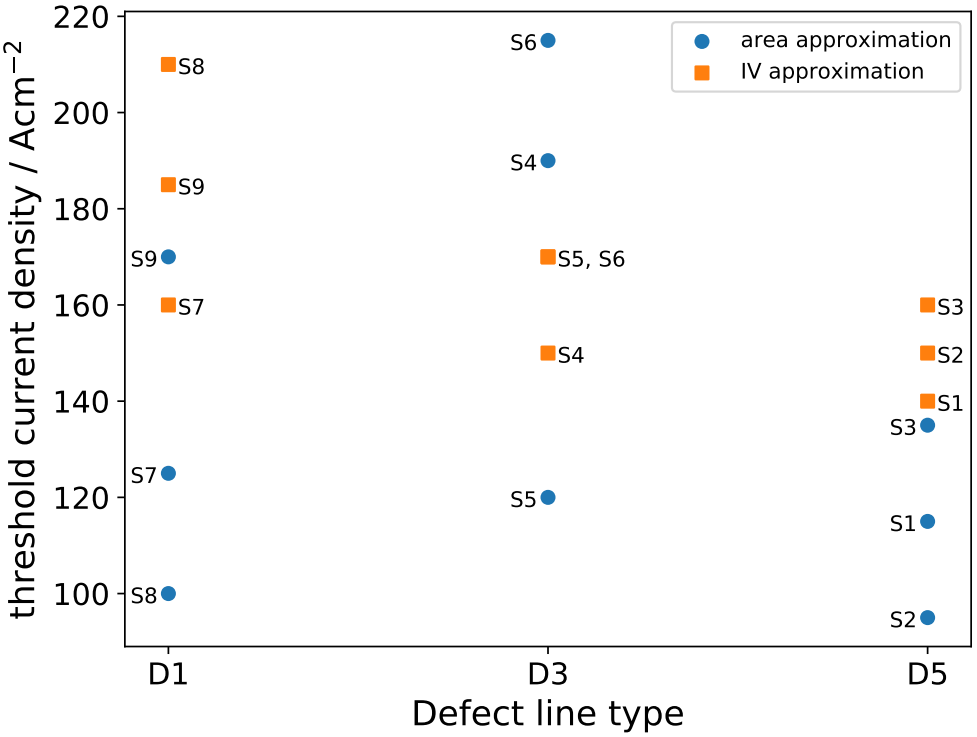

Fig. 2.27 Threshold current density for defect lines with varying coupling between individual cavities. Blue circles are the values approximated with the area of the pillars, and the orange squares are the values approximated by comparing IV curves with the reference MM device.

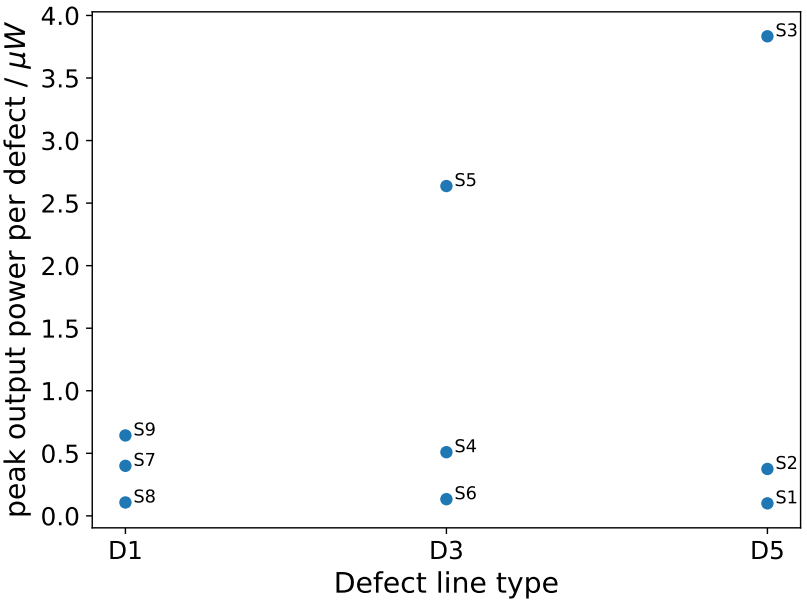

Fig. 2.28 Peak power of all defect devices, sorted by defect line coupling strength (the distance between defect pillars). The output of each device is divided by the number of defect pillars on it. On average, power per pillar was the lowest for D1 lasers, and the highest for S5 devices.

2.5.2 Spectral measurements

We obtained spectral data in order to test two phenomena predicted by PhC theory. Firstly, all defect QCLs should emit single frequency. Secondly, that frequency should depend on the defect radius, and we should be able to engineer it with precise fabrication. To this end, we made devices with different defect radii, as seen in Table 2.1. One device (S3) had $R \simeq 0.643a$, five devices (S1, S2, S5, S8, and S9) had $R = \simeq 0.682a$, and three devices (S4, S6, and S7) had $R = \simeq 0.674a$. Unfortunately, we were unable to perform spectral measurements of the latter three devices, partly due to their low output power, and partly due to the limited spectrometer availability. Figure 2.29 shows the relationship between R and defect modes, with the fabricated devices' R marked with dashed lines. The plot on the left represents the five devices with bigger R, and the plot on the right shows the simulation for smaller R defect. Note that due to scaling properties of PhCs, the only difference between the two plots is the absolute frequency scale on the right. We were expecting the devices to emit frequencies close to the intersections of the dashed lines with the mode lines.

We measured the samples with Bruker Fourier Transform Infrared spectrometer (FTIR) and a QMS liquid helium cooled bolometer. The spectral resolution of the tool is $0.25\,\mathrm{cm}^{-1}$ (7.5 GHz). We set the pulsing frequency (10-100 kHz) as low and the duty cycle (30%-50%)

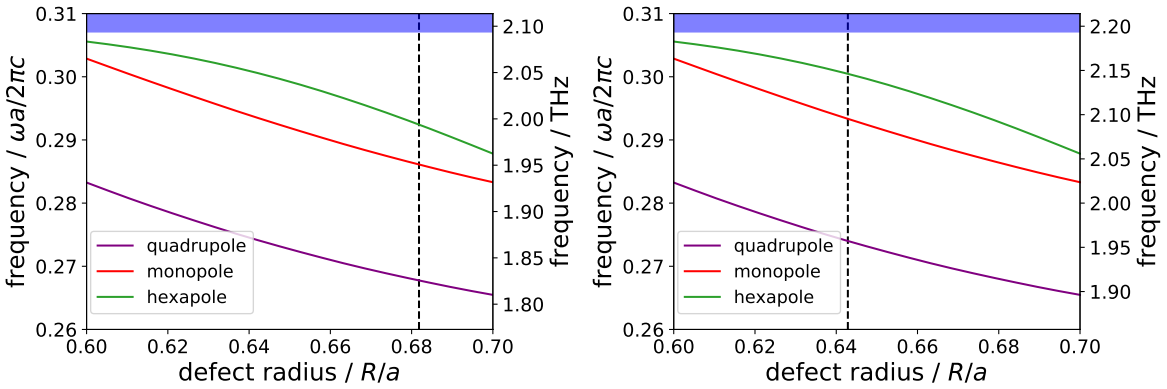

Fig. 2.29 Optical modes in the band gap vs. defect radius, zoomed in on the area of interest. On the **left**, we simulated devices S1, S2, S5, S8, and S9. On the **right**, the simulation for S3 is shown. Due to scaling properties of PhCs, the plots are identical, except for the absolute frequency axis. Defect radius R of the fabricated devices is marked with dashed lines. We were expecting to see lasing at their intersections with optical modes.

as high as possible for each laser, in order to get the best signal. Neither of these parameters affects the emitted frequency in QCLs.

The reference MM laser, shown in Figure 2.30, exhibits three Fabry-Pérot peaks centred at 1.93 THz and an overall bandwidth of 100 GHz. This is commensurate with the results in the original paper[29]. The QCL shows a minimal frequency blue-shift at higher bias values. In each of the defect QCL spectral plots, we overlaid two lines and filled regions around them. The lines correspond to two simulated mode frequencies, the quadrupole (purple), and the monopole (red). For clarity, we omitted the hexapole, because it was outside of the lasers' bandwidth. The filled regions represent the fabrication uncertainty. Their limits correspond to simulations with the pillar radius 2% lower/higher than the nominal value. This is commensurate with our observations of pillar walls (see Section 2.4), where we concluded that there could be as much as 3 µm difference in diameter between the base and the top of the defect pillars (which have a nominal diameter of approximately 60 µm).

The frequency spectrum of S2 defect QCL is shown in Figure 2.31. It was measured at 10 kHz and 30% DC. It exhibits a single intensity peak throughout the dynamic range, centred at 1.96 THz. It shifted to 1.97 THz at the upper limit of operating bias (6.2 V). The emitted frequency is in excellent agreement with the simulated monopole mode.

The frequency spectrum of S3 defect QCL is shown in Figure 2.32. It was measured at 100 kHz and 50% DC. It exhibits a single intensity peak throughout the dynamic range, centred at 1.91 THz. This is the only measured defect QCL with a smaller defect radius ($R = 0.643a$). The emitted frequency is below the simulated quadrupole. The only lower frequency defect mode, the dipole, is further away (centred around 1.7 THz) than the quadrupole. It is

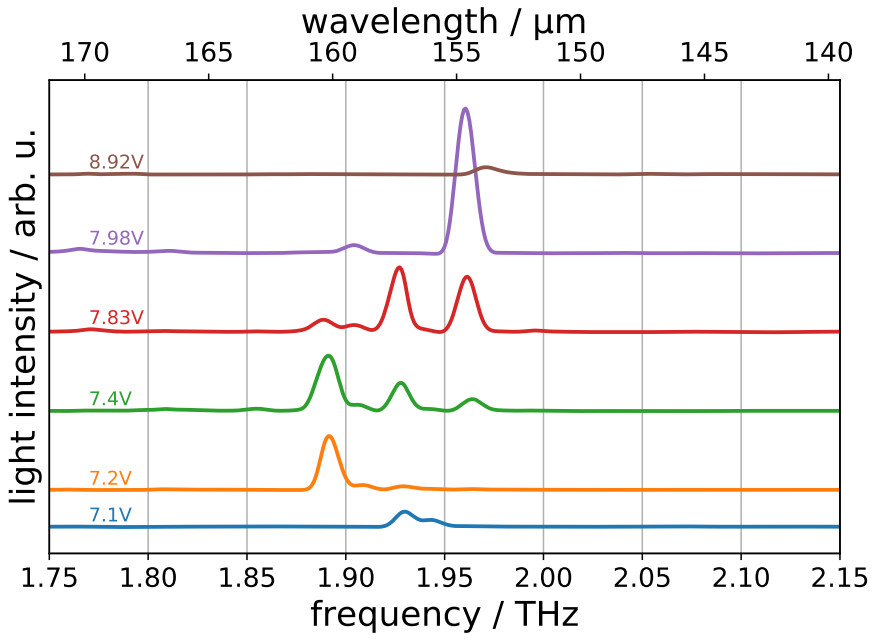

Fig. 2.30 Measured frequency spectrum of the reference MM QCL. It exhibits three distinct Fabry-Pérot peaks, and the overall bandwidth is approximately 100 GHz, centred at 1.93 THz.

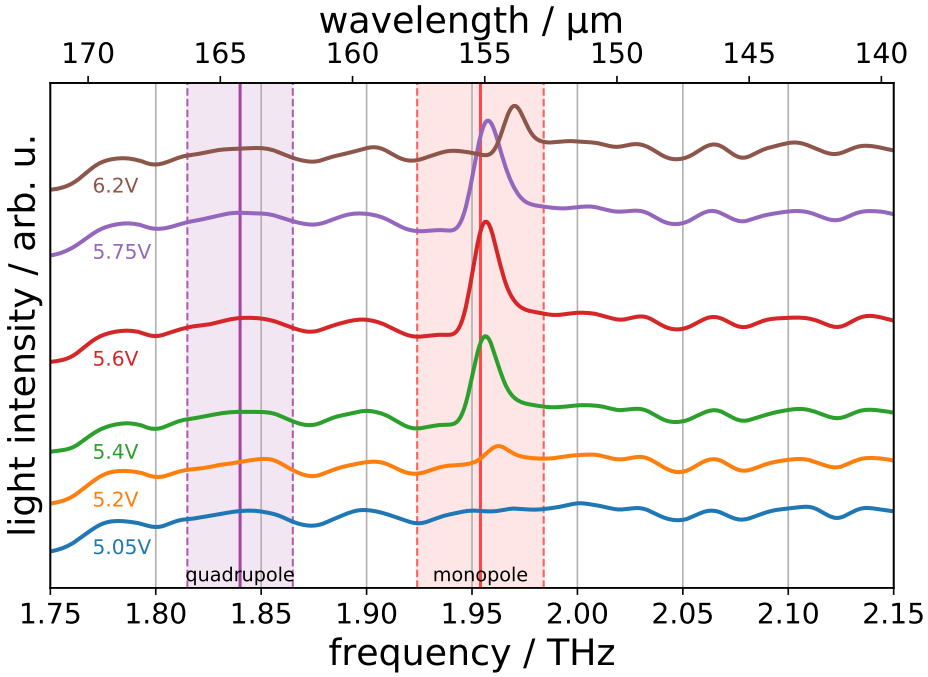

Fig. 2.31 Measured frequency spectrum of S2 defect QCL. It exhibits a single intensity peak throughout the dynamic range, centred at 1.96 THz, shifted to 1.97 THz at the high bias end of the range.

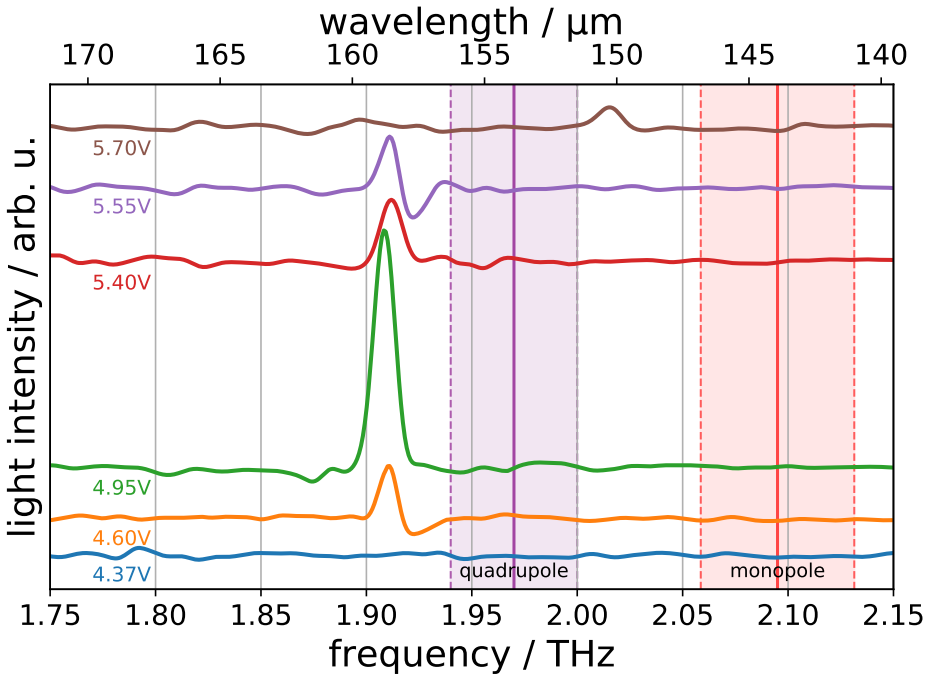

Fig. 2.32 Measured frequency spectrum of S3 defect QCL. It exhibits a single intensity peak throughout the dynamic range, centred at 1.91 THz.

therefore possible that the effective size of the defect is about 5% larger than the nominal value. This would shift the quadrupole close to the measured frequency.

The frequency spectrum of S5 defect QCL is shown in Figure 2.33. It was measured at 100 kHz and 55% DC. It is the only measured sample which emits multiple frequencies, at 1.88 THz, 1.91 THz, and 2.01 THz for high bias. This could be caused by fabrication imperfections — if individual defect pillars have different radii, they can support distinct optical modes. The mode at 1.91 THz is approximately 4 times more powerful than the 1.88 THz mode. The frequencies do not match the nominal dimensions of defects. It appears that the features could be approximately 5% smaller than the nominal values. This would shift the quadrupole close to the lower measured frequencies (the double peak), and the monopole to the higher one.

The frequency spectrum of S8 defect QCL is shown in Figure 2.34. It was measured at 10 kHz and 30% DC. It exhibits a single intensity peak throughout the dynamic range, centred at 1.97 THz. The emitted frequency is in good agreement with the simulated monopole mode.

The frequency spectrum of S9 defect QCL is shown in Figure 2.35. It was measured at 100 kHz and 50% DC. It exhibits a single intensity peak throughout the dynamic range, centred at 1.89 THz. This frequency is exactly in between the simulated modes. If the defects

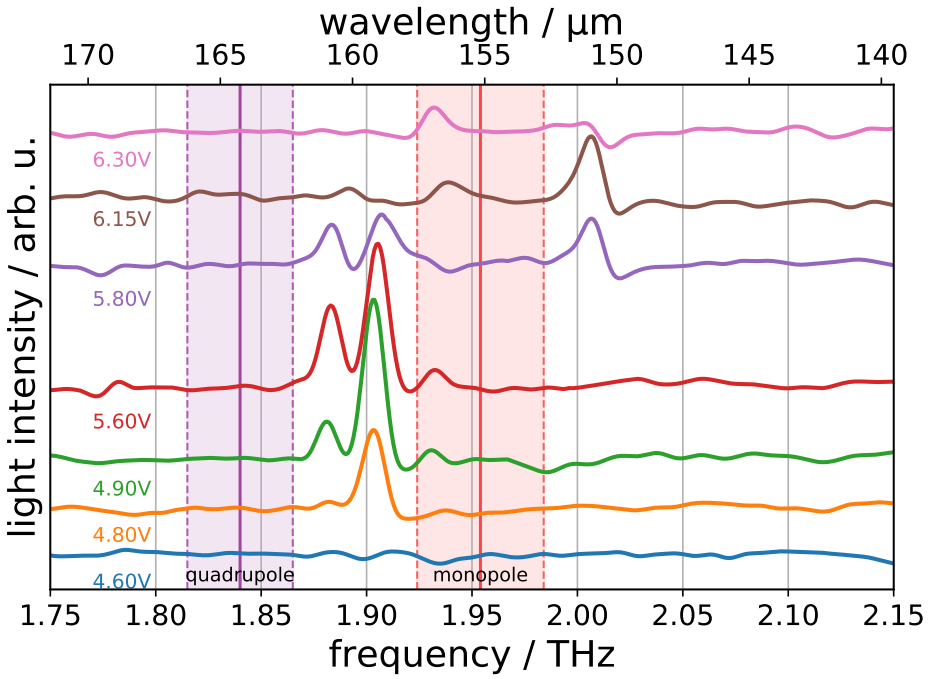

Fig. 2.33 Measured frequency spectrum of S5 defect QCL. It exhibits two intensity peaks at 1.88 THz and 1.9 THz for the most of the dynamic range, and a third peak at 2.01 THz at the high bias end of the range.

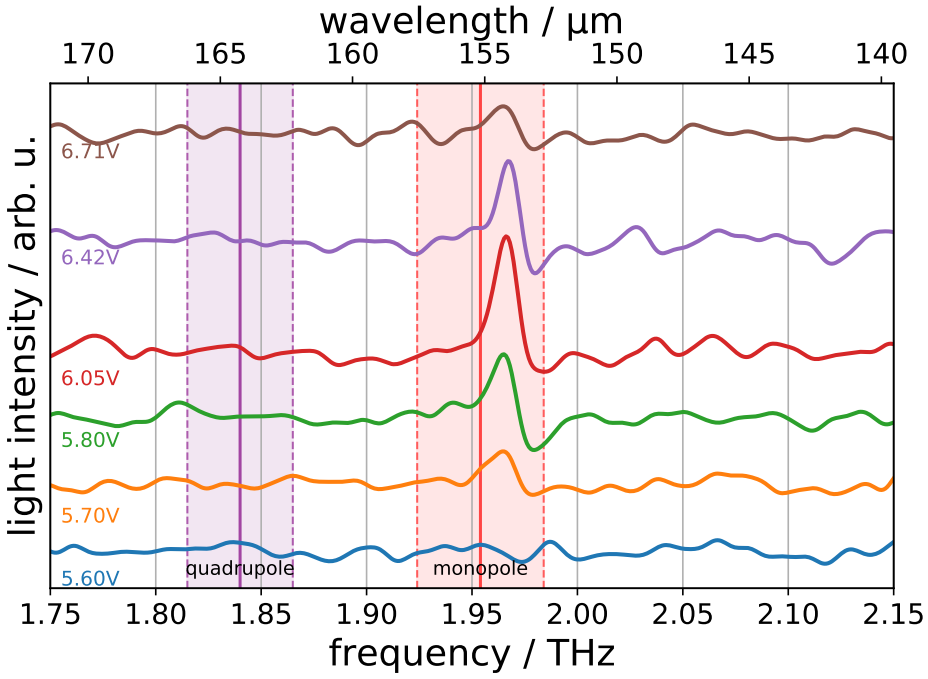

Fig. 2.34 Measured frequency spectrum of S8 defect QCL. It exhibits a single intensity peak at 1.97 THz throughout the dynamic range.

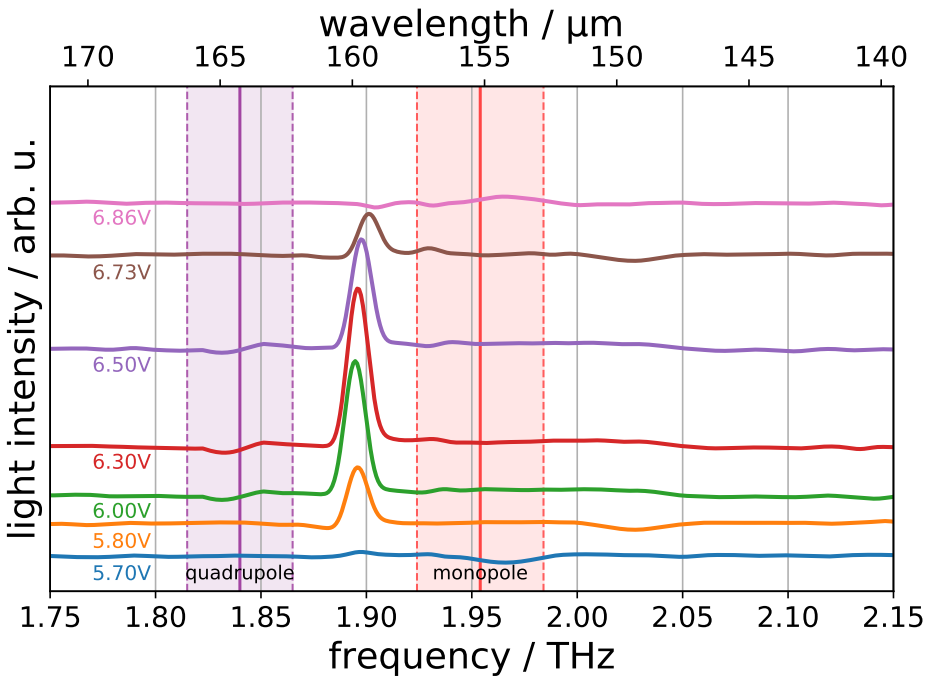

Fig. 2.35 Measured frequency spectrum of S9 defect QCL. It exhibits a single intensity peak throughout the dynamic range, centred at 1.89 THz.

had a 5% smaller radius, it would agree with the simulated quadrupole. If the defects were 5% larger, the spectrum would agree with the simulated monopole.

Figure 2.36 shows a summary of all spectral measurements along with theoretical calculations. The green filled region represents the bandwidth of the reference MM QCL. The black bars show the full measured width of the defect spectra. Violet and red lines represent theoretical defect mode frequencies for quadrupole and monopole modes, respectively. The violet and red filled regions, and the dashed lines limiting them, represent the fabrication uncertainty of 2% in the defect radius, as in the individual plots above.

In summary, we measured the spectra of five defect QCLs, and compared them to MPB simulations. Four devices (S2, S3, S8, and S9), emitted a single frequency mode. This suggests that defect lines are indeed good candidates for frequency-selective waveguides in QCLs. Two of the devices (S2 and S8) exhibited lasing at the predicted frequency. The other two (S3 and S9) emitted frequencies which matched simulations of devices with a 5% difference between nominal and real dimensions.

It should be noted that the discrepancies between numerical simulations of the frequencies and the measured quantities are most likely due to fabrication imperfections. With the dry etching method used (RIE), it was not possible to ensure the pillars' radii were equal to the nominal values. As mentioned in the fabrication section, many pillars were truncated cones,

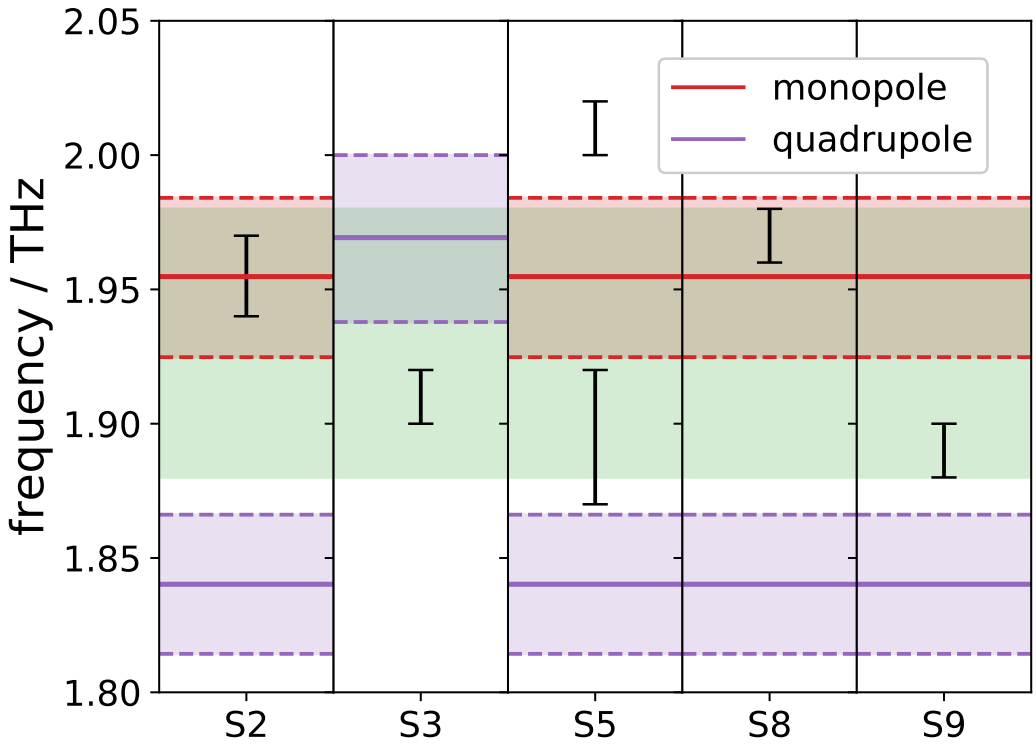

Fig. 2.36 Summary of spectral measurements. The green filled region represents the bandwidth of the reference MM QCL. Black brackets show the full width of emission from individual devices. The purple and red lines correspond to calculated frequencies of defect modes. Solid horizontal lines mark the frequencies for nominal defect dimensions (as measured on the optical mask). Dashed horizontal lines show the tolerance intervals for defects and lattice pillars radii $\pm$ 2%, to account for fabrication imperfections. Devices S2 and S8 show emission within the simulated range, whereas S3, S5, and S9 are outside of the range, suggesting bigger differences in fabrication.

with the radius at the base bigger than at the top. In the 2D approximation in the simulations, where pillars were cylinders of infinite height, it was not possible to accurately reflect this geometry. Nevertheless, all working devices lased at frequencies within 5% of the modelled one. In order to have more control over the radius of the devices, we suggest using a more precise (and faster) dry etching tool, such as an inductively coupled plasma (ICP) machine.

2.5.3 Beam profile

Defect line QCLs have more complex facets than MM QCLs. Instead of a vertically cleaved AR ridge, it is a mix of BCB and partially cleaved lattice pillars (we took care not to cleave any of the defect pillars). Such non-uniformity adds to the usual impedance mismatch at the air-QCL interface, therefore we did not expect the beam pattern to be less divergent than in a typical MM. The aim of this section is to show that albeit highly divergent, defect QCLs are directional, i.e. they do not emit laterally. Directionality, along with the unique properties of photonic crystals, would allow for defect QCL waveguides to emit at arbitrary angles. In all measurements reported below, lasers were driven at 100 kHz. They were measured in pulsed mode, at 30% duty cycle, except for S7, which we were able to measure at 50%DC for a better signal to noise ratio. All measurements were taken at 5 K.

The exemplary MM far-field pattern from Chapter 1 is shown again in Figure 2.37 for comparison. It shows a beam width of approximately 40°. The emission has one central peak at ($\theta = -3°, z = -1\,\text{mm}$) (at the intersection of the dashed lines), and two weaker maxima at ($\theta = 3°, z = -1.5\,\text{mm}$) and at ($\theta = -1°, z = 2\,\text{mm}$). Figure 2.38 shows the beam pattern of S2 defect line QCL 30 mm from the facet. It is the only measurement that we took at 30 mm from the facet instead of 16 mm, because a thinner cryostat window was not available at the time. As a consequence, the measurement is noisy, with a signal to noise ratio of approximately 5. The emission in the horizontal direction spans less than 20°, and less than 20 mm ($< 40°$) in the vertical direction. Overall, the beam pattern is narrower than in the example MM laser. The emission is not centred, with three maxima at ($\theta = 2°, z = -3\,\text{mm}$), ($\theta = 2°, z = 5\,\text{mm}$), and ($\theta = 8°, z = 5\,\text{mm}$). Figure 2.39 shows the beam pattern of S3 defect line QCL 16 mm from the facet. The emission in the horizontal direction spans 60°, and 8 mm (25°) in the vertical direction. It exhibits three emission peaks, at ($\theta = 5°, z = -2.5\,\text{mm}$), ($\theta = 22°, z = -2.5\,\text{mm}$), and ($\theta = 47°, z = -2.5\,\text{mm}$). The three peaks had similar intensity. This laser only emitted to one side of the ridge (only positive angles), which suggests asymmetric features near the facet.

Figure 2.40 shows the beam pattern of S5 defect line QCL 16 mm from the facet. The emission in the horizontal direction spans more than 100°, and 10 mm (32°) in the vertical

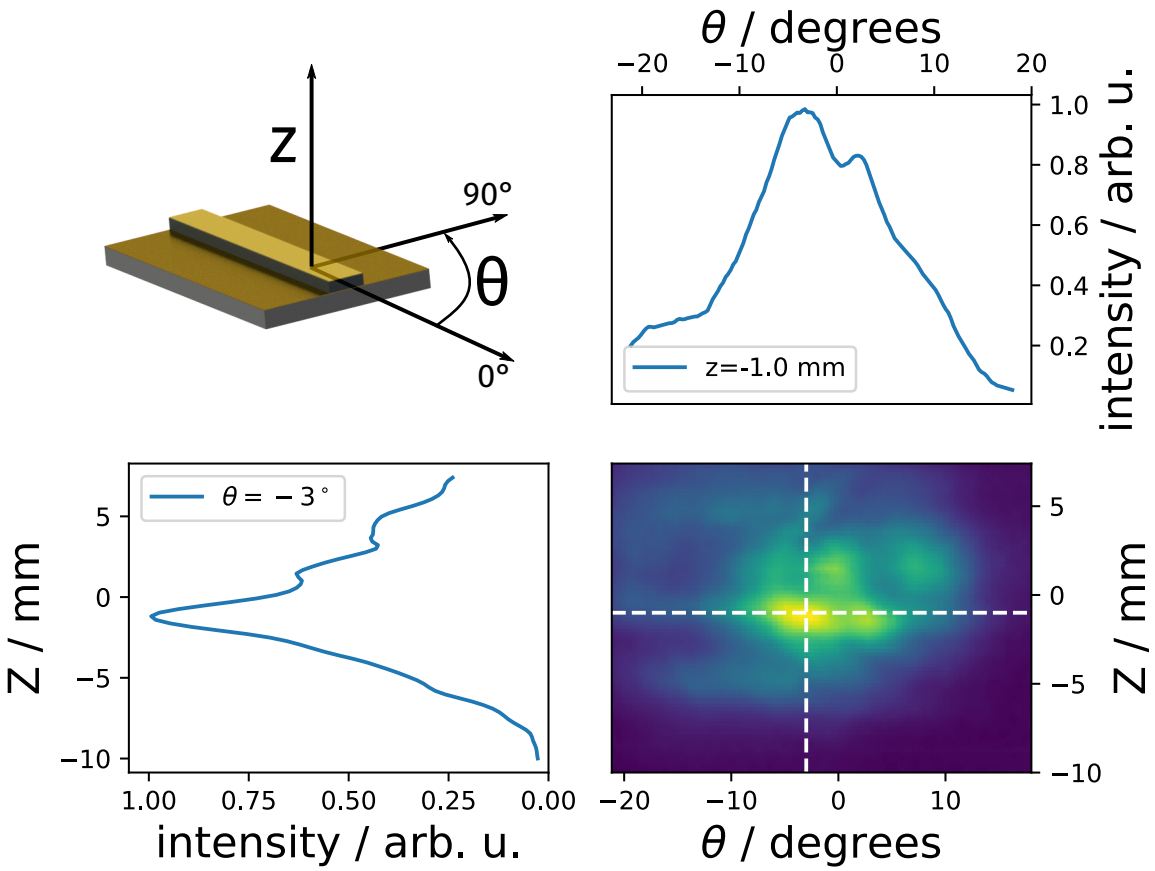

Fig. 2.37 Far-field beam intensity pattern from a MM QCL. Laser orientation is shown in the top left. Two cross-sectional plots of normalised intensity are shown on the top and the left of the 2D intensity plot. The beam is approximately 40° wide, with several maxima near the centre.

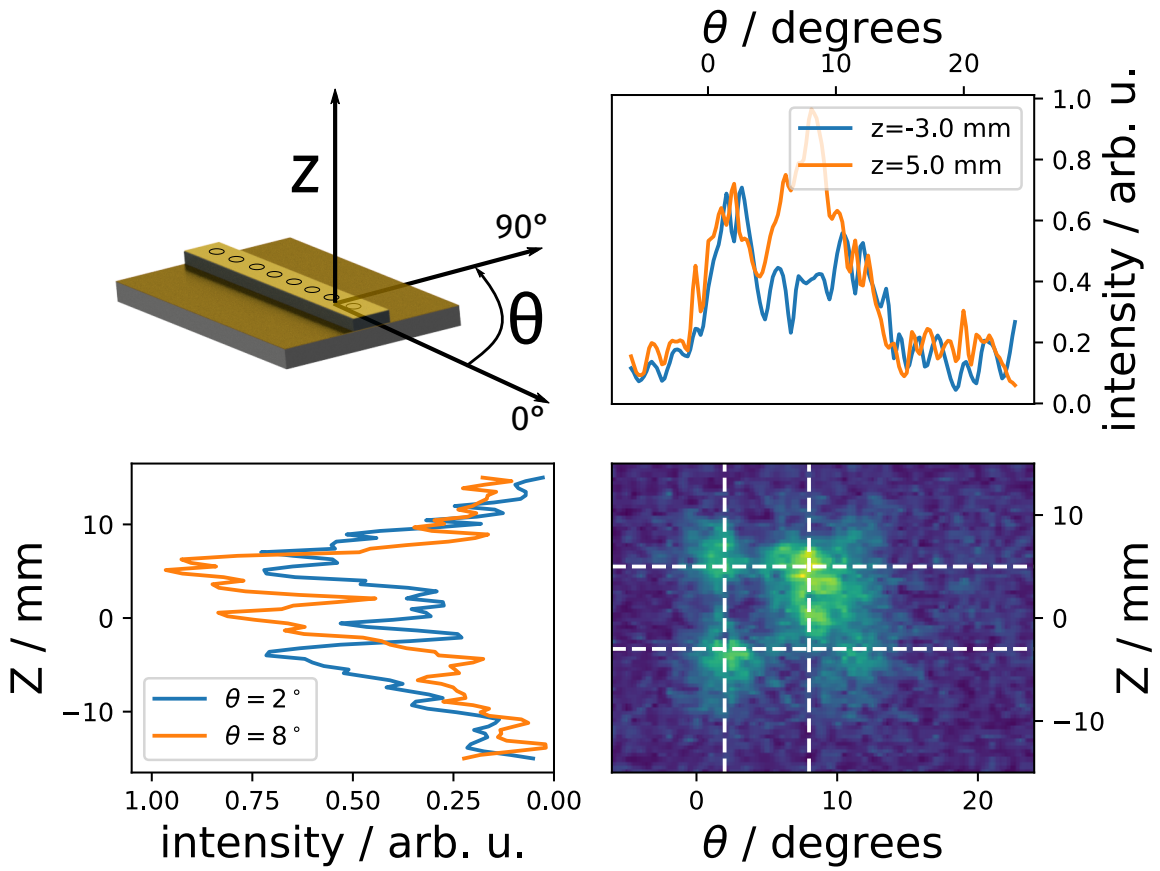

Fig. 2.38 **Left**: Defect QCL position with respect to the detector. **Right**: Measured beam intensity from S2 defect QCL at 5.53 V bias. The Golay cell detector (with a 2 mm aperture in front) was placed 30 mm from the facet. The beam spanned 20 mm (40°) in the vertical direction and 20° horizontally.

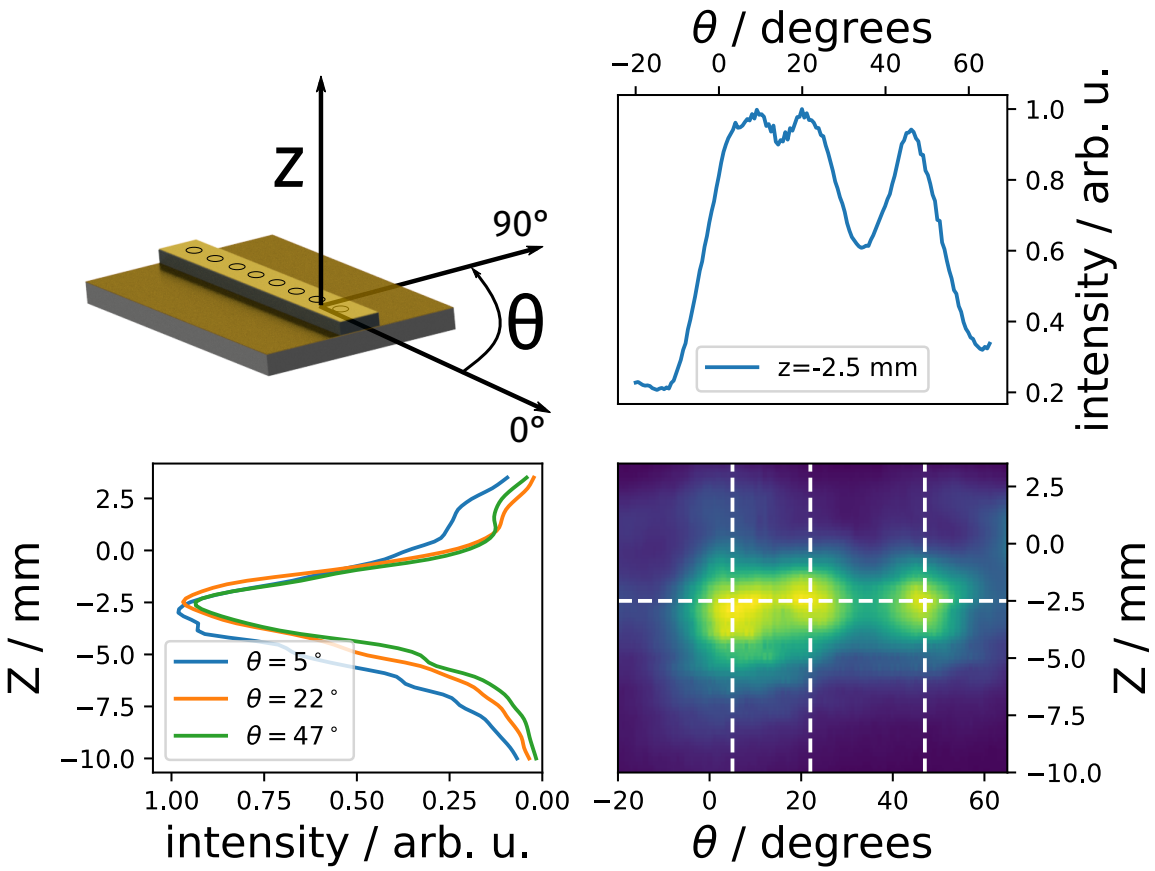

Fig. 2.39 **Left**: Defect QCL position with respect to the detector. **Right**: Measured beam intensity from S3 defect QCL at 5.2 V bias. The Golay cell detector (with a 2 mm aperture in front) was placed 16 mm from the facet. The beam spanned 8 mm (25°) in the vertical direction and 60° horizontally.

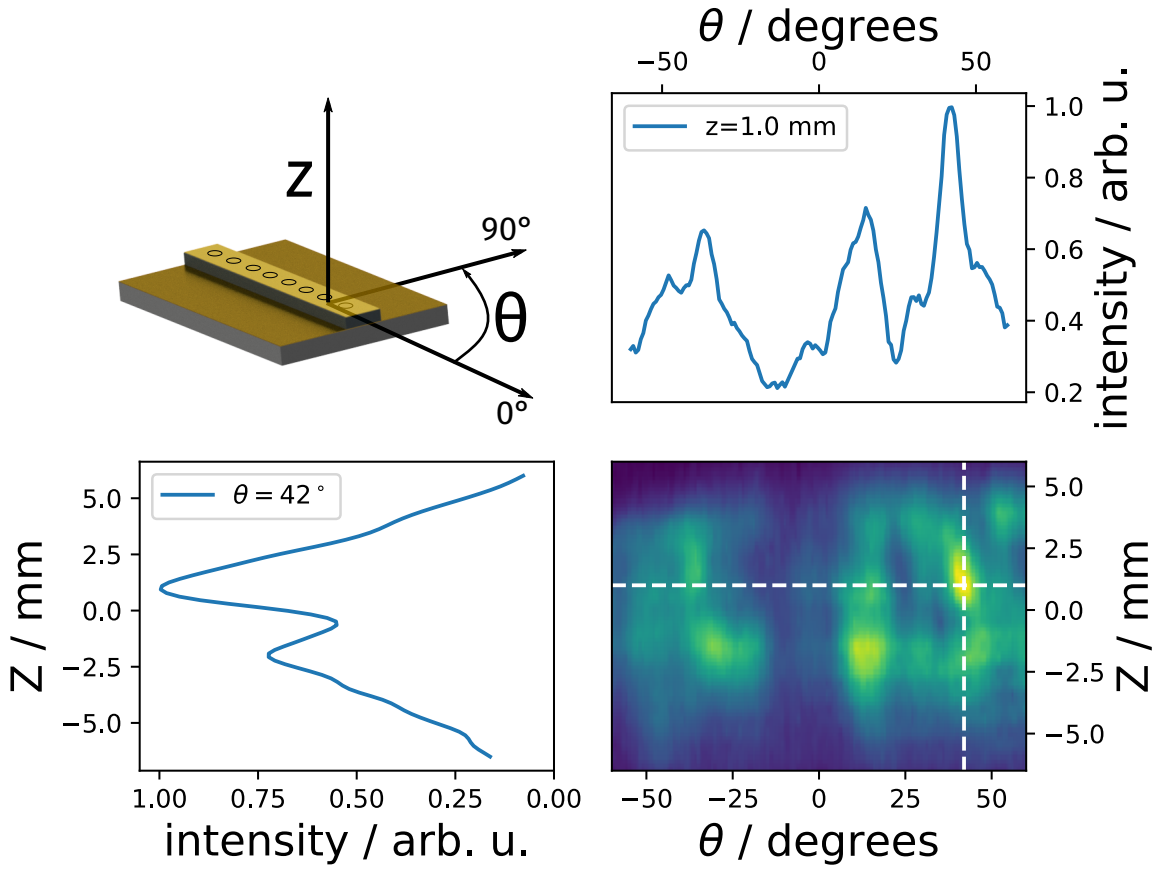

Fig. 2.40 **Left**: Defect QCL position with respect to the detector. **Right**: Measured beam intensity from S5 defect QCL at 5.45 V bias. The Golay cell detector (with a 2 mm aperture in front) was placed 16 mm from the facet. The beam spanned 10 mm in the vertical direction and more than 100° horizontally.

direction. It is very dispersive and exhibits multi-lobe behaviour. There are two strongest maxima, at $(\theta = 42°, z = 1\,\text{mm})$, and $(\theta = 20°, z = -2\,\text{mm})$.

Figure 2.41 shows the beam pattern of S7 defect line QCL 16 mm from the facet. The emission in the horizontal direction spans more than 60°, and 6 mm (20°) in the vertical direction. Two maxima with approximately the same intensity can be distinguished at $(\theta = 36°, z = -0.5\,\text{mm})$, and $(\theta = 46°, z = -0.5\,\text{mm})$.

Albeit dispersive, emission from defect line QCLs *is* directional. There was no signal from the devices beyond 65° from the facets, as shown in the far-field plots. Because the lattice pillars on the sides of the defects act as a photonic mirror, there is no lateral emission from the devices. The angular width of the output could be improved with an external element such as a silicon lens. This configuration suggests an interesting way to investigate QCLs in future: create an *arched* defect line, which would follow the circumference of a

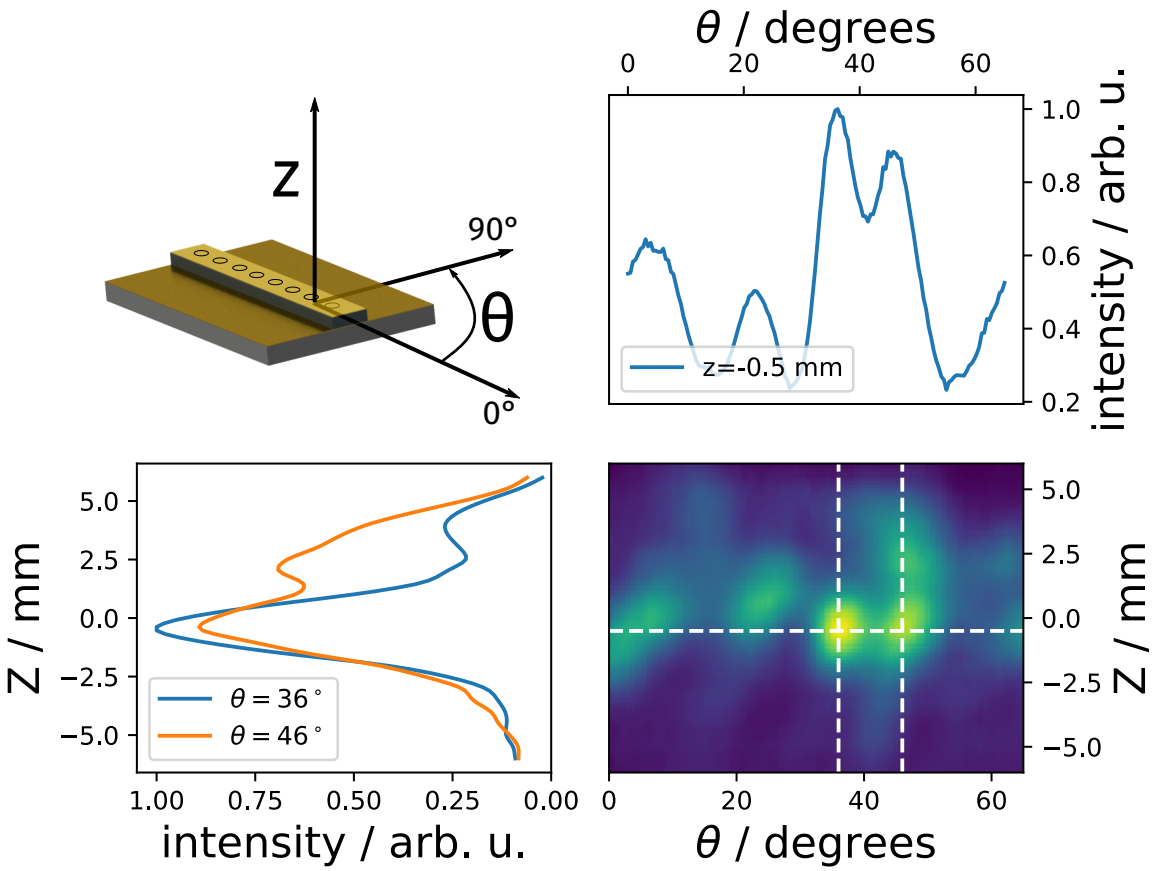

Fig. 2.41 **Left**: Defect QCL position with respect to the detector. **Right**: Measured beam intensity from S7 defect QCL at 5.08 V bias. The Golay cell detector (with a 2 mm aperture in front) was placed 16 mm from the facet. The beam spanned 16 mm in the vertical direction and more than 60° horizontally.

circle. It could prove useful in integrated THz circuits, where changes in light direction must currently be dealt with by means of mirrors.

2.6 Planar waveguide with defect line architecture

The properties of photonic crystals allow us to part with the traditional, straight-line design of QCLs, and introduce waveguide angles. To this end, we designed a T-shaped defect line, with a different defect radius in each of the three branches. There were 5 rows of pillars in between the defects, as in the D5 defect line devices. The design is shown in Figure 2.42. We will call this type of device the T defect henceforth. The goal of this experiment was to see whether the QCL lases from all three ends, whether it lases at different frequencies, and whether there are differences in the output intensity from all facets. This work was only a proof-of-concept. The full study of the system was beyond the scope of this thesis due to time constraints.

We fabricated two identical devices according to the procedure described in Section 2.4, using the same BtC AR as in the straight defect line. The top contact was continuous, we therefore biased the whole structure during the measurements.

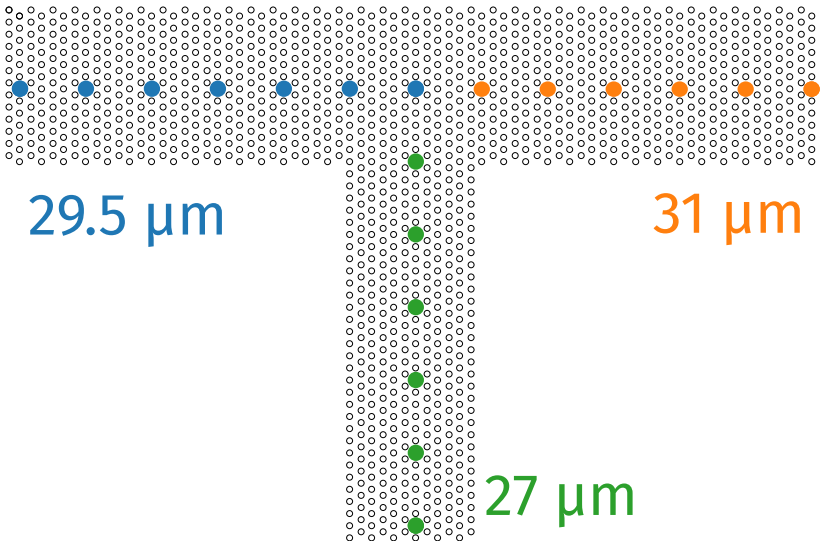

Fig. 2.42 Design of the T defect optical mask. The radii of the defect pillars are given beside each of the branches. Lattice constant $a = 44\,\mu\text{m}$ and lattice pillar $r = 11\,\mu\text{m}$ across the device.

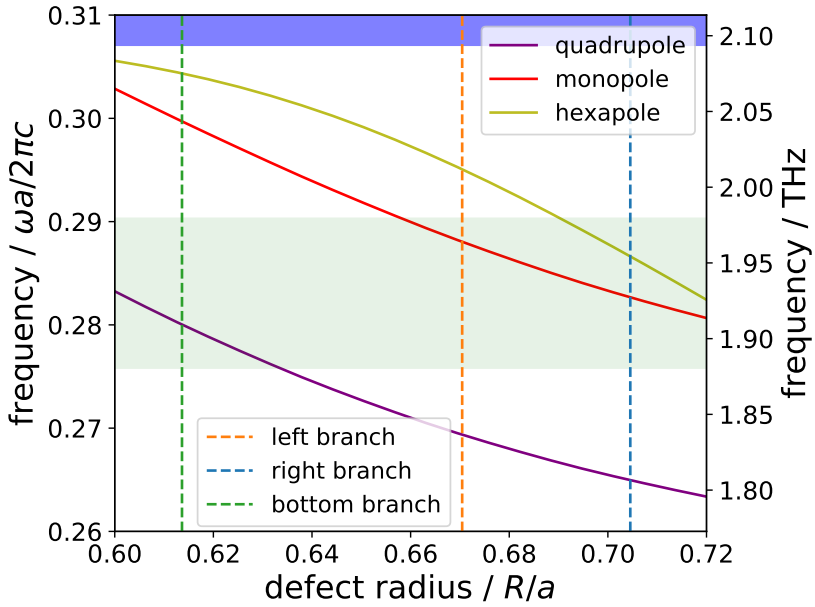

Fig. 2.43 Simulated optical mode frequencies vs. defect radius. The solid lines represent the simulated modes. Vertical lines mark the nominal defect radii of each of the T branches. The filled green region represents the bandwidth of the reference MM QCL. The filled region at the top marks the band edge. Each of the T branches should be able sustain modes with a frequency at the intersection of dashed and solid lines within the green region.

2.6.1 Spectral characteristics

The simulated frequency vs. defect radius plot is shown again in Figure 2.43. This time we added three dashed lines marking the R of each of the three branches of the T defect, and a filled area to represent the bandwidth of the reference MM QCL. The intersections of the solid and dashed lines within the filled region are frequencies which should be sustained in individual branches. In the bottom branch ($R \simeq 0.61a$), only the quadrupole lies within the bandwidth of the AR at 1.91 THz. In the left branch ($R \simeq 0.67a$), only the monopole should be allowed at 1.96 THz. In the right branch ($R \simeq 0.705a$) two modes are allowed, namely the hexapole (1.955 THz) and the monopole (1.925 THz).

The spectra of sample S10 are shown in Figure 2.44. It comprises four plots: three detailed measurements of each of the T branches, and a combined plot of all three branches. In the plots for individual branches we also marked the simulated defect mode frequencies (and 2% fabrication tolerance), as in the previous spectral plots. For clarity, we only plotted the simulated mode closest to the emitted frequency. Spectral measurements of both T defects were carried out by Andrea Ottomaniello at the University of Pisa (our FTIR was not available at the time).

S10 T defect was pulsed at 100 kHz and 30% DC. It showed single mode operation throughout the dynamic range, from all sides of the device. Its lasing peak was centred at 1.925 THz, matching the quadrupole in the bottom ($R = 27\,\mu m$) branch, and the monopole in the right ($R = 31\,\mu m$) branch. Outputs from all branches had the same frequency. The slight red shift visible in the right branch is below the resolution of the FTIR (~ 0.008 THz). This result suggests that there is one dominating mode (the monopole or the quadrupole), which propagates in all defect pillars. It is possible that the differences between nominal defect radii were reduced during fabrication, and the effective radius in three branches is similar. However, it is the left branch (where no simulated modes match) which outputs the most signal. It is approximately two times more powerful than the bottom branch, and three times more powerful than the right branch (we will quantify it more precisely with LIV measurements below). The differences in power depend very much on the quality of the facets, so it could be that the left end of S10 is less absorptive than the other two.

The spectra of sample S11 are shown in Figure 2.45. It was pulsed at 100 kHz and 30% DC. It showed one stronger emission peak (centred at 1.985 THz) throughout the dynamic range, and a weaker peak centred at 1.975 THz, appearing between 760 to 880 mA. The simulated monopole in the left ($R = 29.5\,\mu m$) branch is the closest to the two emitted frequencies. The output from the left branch is however the least powerful, approximately 5 times weaker than the right branch, and almost two times weaker than the bottom branch. Without results from separately biased branches it is difficult to ascertain the origin of the emitted frequency.

We disproved the initial hypothesis that each branch would allow only one frequency and filter out the others. Instead, the same mode propagated in all branches, with intensities of the same order of magnitude. In S10, the left branch output was approximately twice as powerful as in the right branch. In S11, the right branch was the most powerful, and the intensity of the output beam was approximately five times that of the left branch. Such differences in intensity could be caused by the quality of individual defects and facets.

The reason for the same spectral output from all sides is unclear. However, given that the pillars were dry etched with an RIE tool, the sizes could be a few microns off from the nominal values. Moreover, the pillars are not perfectly cylindrical, but they are wider at the bottom, forming partial cones. They may allow several closely spaced frequencies to compete, and the observed spectra are the result of the dominant mode propagating in all branches.

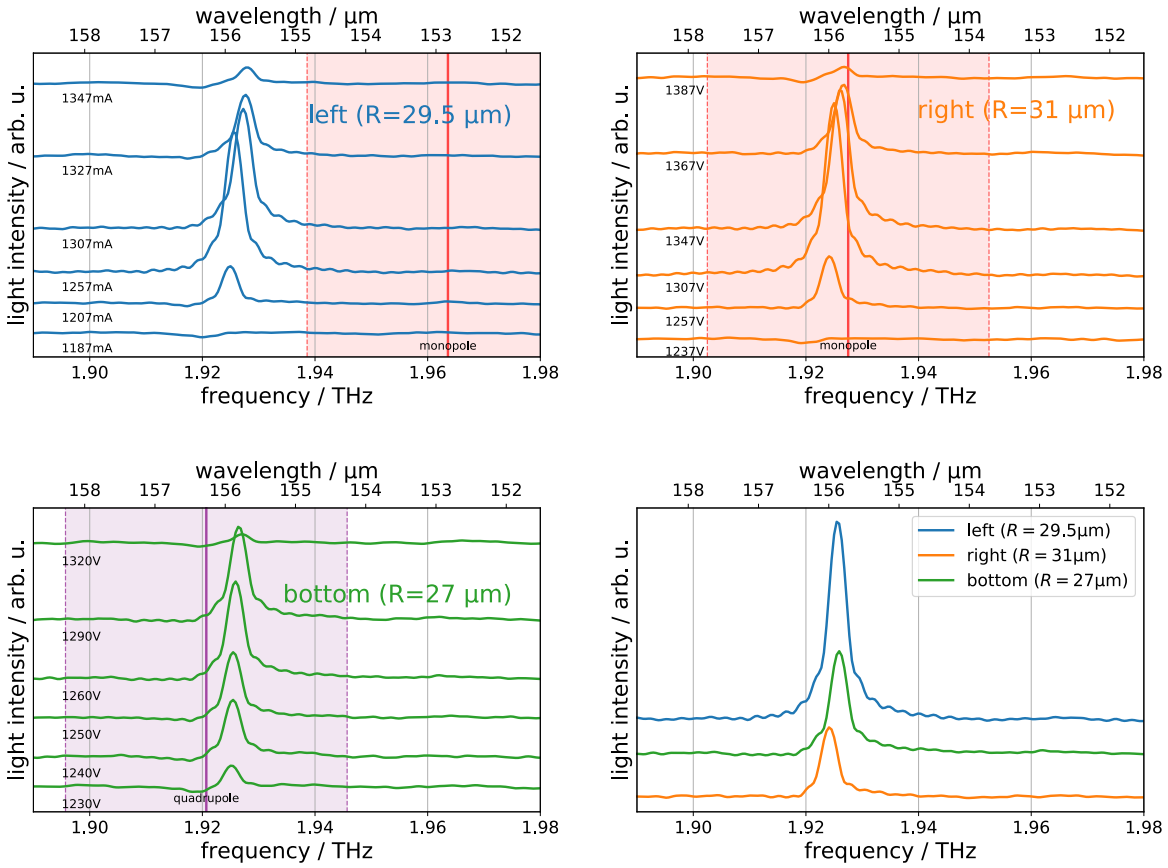

Fig. 2.44 Measured frequencies of each of T branches in S10. The solid lines and filled regions represent the simulated modes closest to the measured frequency. The bottom right plot shows the output of all three branches at 1260 mA. All branches emitted the same frequency, centred at 1.925 THz.

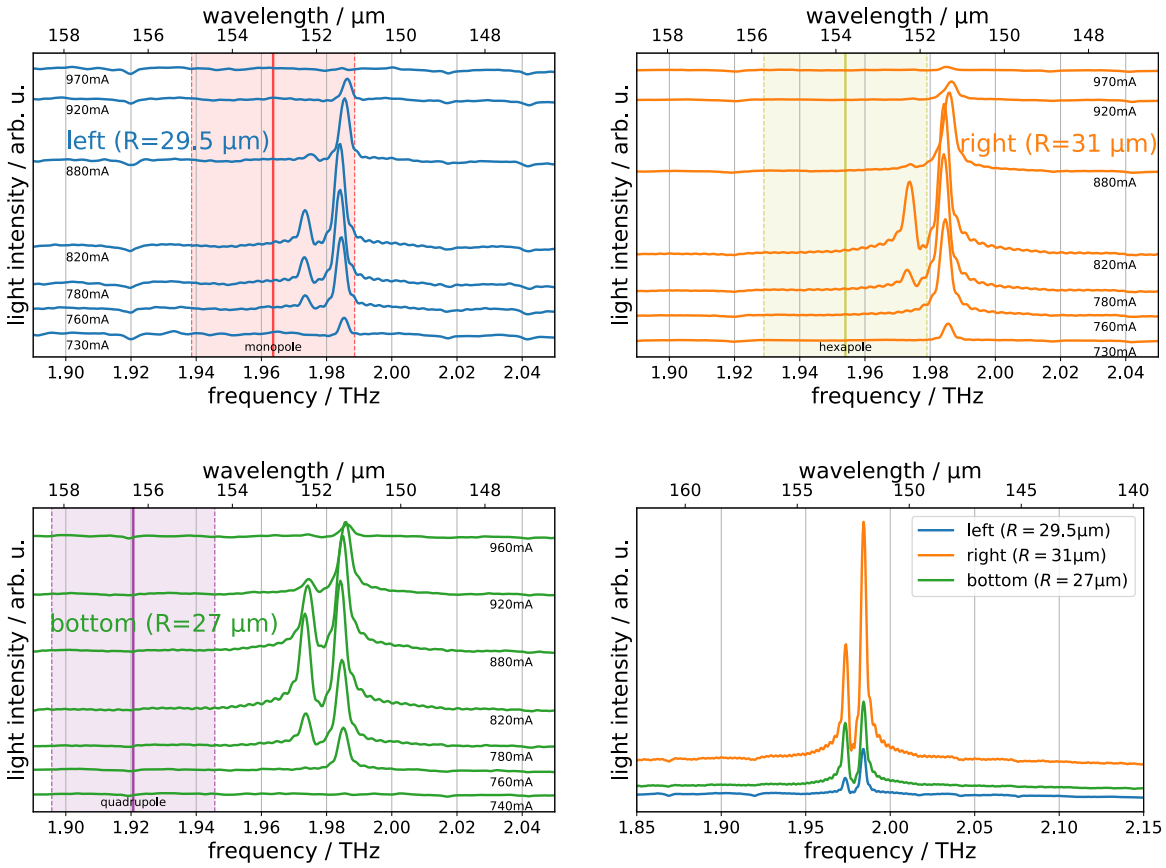

Fig. 2.45 Measured frequencies of each of T branches in S11. The solid lines and filled regions represent the simulated modes closest to the measured frequencies. The bottom right plot shows the output of all three branches at 820 mA. All three branches exhibited two emission peaks, centred at 1.985 THz and 1.975 THz.

2.6.2 Light-current-voltage characteristics

To complement the spectral data, we carried out full LIV characterisation of the T defects. Figure 2.46 shows the LIV of the first device, S10. On the left, we plotted the output from each of the T branches at 5 K. The device was pulsed at 100 kHz and 40% DC. The left branch emitted the most power (0.2 µW), followed by the bottom branch (0.13 µW), and the right branch (0.05 µW). This is commensurate with intensities from FTIR measurements. The data confirm that the emission from all branches has the same dynamic range. S10 showed lasing at an unusually low bias (peak at 3 V), which suggests very good electrical contact. On the right of Figure 2.46 we plotted LIV from the left ($R = 29.5\,\mu m$) branch. The higher peak power (0.3 µW) is due to a better alignment in this measurement. S10 lased up to 30 K, which is similar to some of the defect line QCLs. We did not expect the operating temperature to be high. As explained earlier, heat extraction is more difficult from pillars surrounded by BCB than from ridge lasers. In T defects, there is even more active material to extract the heat from than in the line defect QCLs.

Figure 2.47 shows the LIV of S11. On the left, we plotted the output from each of the T branches at 9 K (we used an almost empty liquid Helium dewar and were unable to reach 5 K). The device was pulsed at 100 kHz and 30% DC. The right branch emitted the most power (1.5 µW), followed by the bottom branch (0.5 µW), and the left branch (0.25 µW). This is commensurate with intensities from FTIR measurements. The data confirm that the emission from all branches has the same dynamic range. The operating bias was similar to

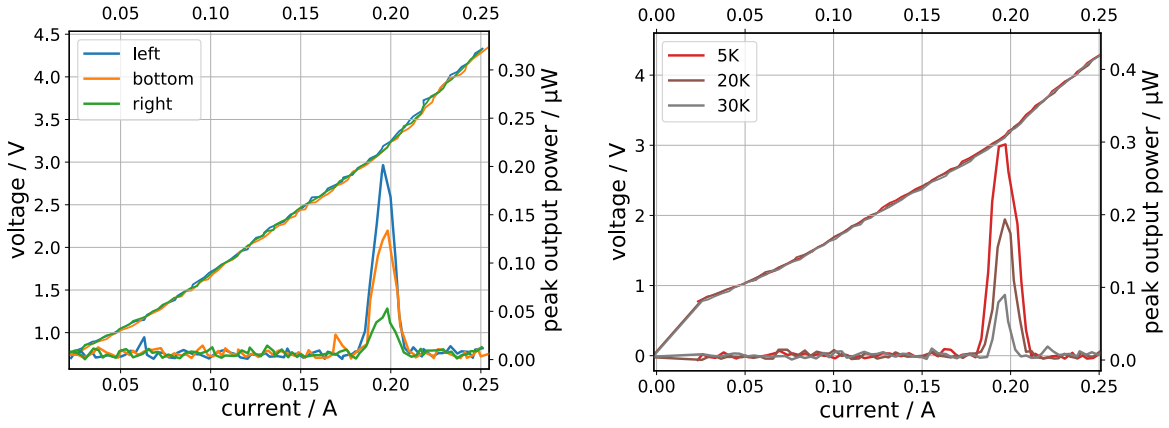

Fig. 2.46 LIV of S10 T defect. **Left**: the output from each of the T branches. The left branch ($R = 29.5\,\mu m$) emits 0.2 µW, the bottom branch ($R = 27\,\mu m$) emits 0.13 µW, and the right branch ($R = 31\,\mu m$) emits 0.05 µW. **Right**: temperature sweep of the output from the left branch. $T_{max} = 30\,K$.

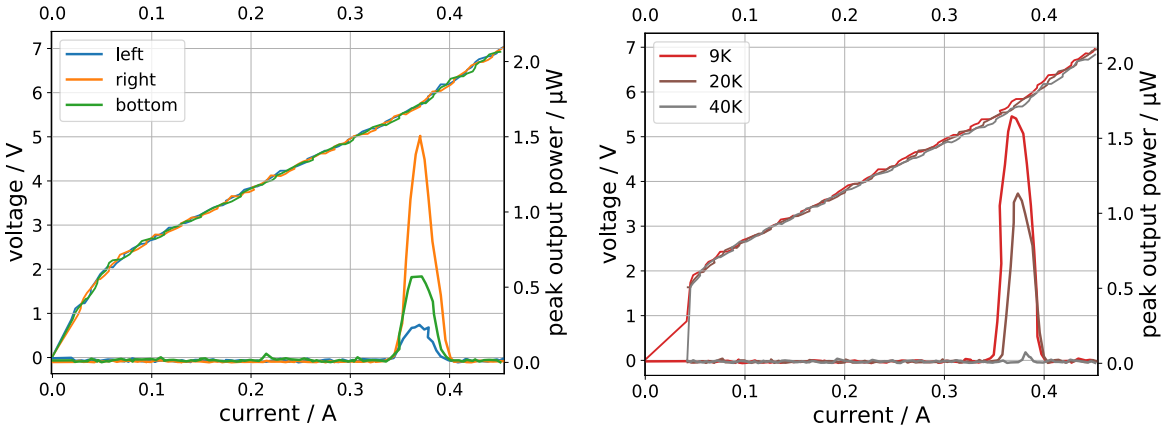

Fig. 2.47 **Left**: the output from each of the T branches. The right branch ($R = 31\,\mu m$) emits 1.5 µW, the bottom branch ($R = 27\,\mu m$) emits 0.6 µW, and the left branch ($R = 29.5\,\mu m$) emits 0.25 µW. **Right**: temperature sweep of the output from the right branch. $T_{max} = 40\,K$.

defect line QCLs (peak at 5.5 V). On the right of Figure 2.47 we plotted LIV from the right ($R = 31\,\mu m$) branch. It lased up to 40 K.

The emitted power from T defects is lower than most of the defect line QCLs. This could be caused by more demanding thermal management of T defects. Besides, if the defect radii differ between the branches (like they were designed), some of the defects would attenuate the mode rather than enhancing it.

The most interesting observation is that all facets emit radiation. This means that we can create defect devices not only as straight lines (which is a limitation of traditional QCLs), but also in bent or angled waveguides. This could prove beneficial in integrated THz systems, obviating the need for optical elements (such as mirrors) to reflect the output beam. Future work in this area should involve fabricating defect waveguides with the same defect size throughout the device and bends at different angles, as described in Ref. [58]. Modes with different symmetry (hexapole, quadrupole, etc.) should only propagate efficiently through bends aligned with their symmetry planes, therefore such experiments could shed more light on which modes exactly propagate in defect PhC.

2.7 Conclusions

In this chapter, we presented defect line THz QCLs based on a triangular lattice photonic crystal. Previous work on photonic crystals in QCLs was described. We explained where our approach was similar (processing, triangular lattice design), and where it was different

(defect line instead of uniform lattice). We noted that this, to the best of our knowledge, is the first demonstration of a defect line QCL.

We outlined the theory of calculating optical mode profiles in PhCs following Joannopoulos *et al.*[53]. We put this theory into practice using MPB software, and used numerical simulations to design our devices. The pillar (instead of hole) lattice, the lattice constant, pillar-to-lattice-constant ratio, and the defect size — these parameters all came out as optimal in simulations. Our goal was to fabricate low-threshold, tunable, single-mode, and directional QCLs. The motivation was two-fold. Firstly, such lasers are sought after in spectroscopy and sensing, especially in low-power environments. Secondly, such systems might prove useful in studying phenomena leading to current density reduction, namely the slow light effect and Purcell enhancement. We designed defect lines with varying coupling strength between defects in order to study these effects. We also explained the fabrication steps involved in making defect line QCLs, which were a result of careful processing optimisation.

We then presented experimental results from 11 defect devices and 1 reference MM QCL. The threshold current density was consistently lower in defect QCLs than in the reference, highlighting the role of slow light effect. The maximum operating temperature was, with one exception, lower than in MM QCL. We explained this by lower thermal conductivity of BCB than that of GaAs. The output power of our devices was also lower, because the effective volume of the gain medium was an order of magnitude smaller than in MM.

Out of 5 defect line QCLs whose spectra we measured, only one was not a single mode device. The others were indeed frequency selective, although the exact match with numerical calculations of expected frequencies was achieved only in 2 devices. We attribute this to the uncertainty in size and non-uniformity of the fabricated pillars.

We also presented far-field beam profiles from 4 defect devices. We concluded that they were indeed directional, as there was no lateral emission from the defect lines. However, the shape of the beam was highly divergent. This is a consequence of complex facets, including partially cleaved GaAs pillars and BCB. This could be alleviated by incorporating focusing elements such as silicon lenses or hollow waveguides.

Finally, we explored another novel QCL design, a T-shaped defect line. The defect radius was different in each branch of the T. The aim was to demonstrate that such waveguides could lift the straight line constraint from traditional, ridge QCLs, and could be engineered to lase in multiple directions. We measured spectral output from each of the branches in two T-shaped QCLs, and proved that the devices lased in all three directions. Single-mode operation was only achieved in one of the devices. More work on mode selectivity is required, especially by fabricating devices with one defect size throughout.

In summary, we designed, fabricated and characterised a novel QCL waveguide based on photonic crystal defect line. We achieved the design goals: frequency tunability, single mode operation, low current density, and directionality. We presented a system that can be further studied for its applications in spectroscopy, and in integrated circuits (due to its engineered directionality). The defect line THz can also serve as a platform to study fundamental effects such as slow light and Purcell enhancement.

Chapter 3

BCB bonded THz QCLs

3.1 Introduction

In Degl'Innocenti *et al.*[62] we reported a new, hybrid waveguide for THz QCLs. It comprises a polymer, benzocyclobutene (BCB), layer between the bottom metal layer and the substrate. Its main purpose was to serve as a more flexible alternative to metal-metal thermocompression bonding used routinely for MM QCLs. The MM bonding technique requires specialised equipment (wafer bonder) and requires the metal layers on bonded wafers to be approx. 0.5 µm thick each for the bond to be mechanically stable. BCB bonding only requires tools used in other steps of QCL processing (thermal evaporators, spinner, annealer) and allows for the bottom metal layers to be arbitrarily thick. This in turn opens the way for experimentation with QCLs in which the optical mode extends below the AR. BCB is a low-loss THz material with $\alpha \simeq 10\,\mathrm{cm}^{-1}$ [63]. This, and the polymer's malleability, could enable the development of integrated THz circuits with other optical elements, such as interferometers, coupled to QCLs. The BCB waveguides reported in Ref. [62] achieved comparable temperature performance to MM waveguides. They also exhibited a Gaussian-like beam pattern, which is more useful for QCL applications than the typical divergent MM beam (see Figure 3.9), but the origin of this is not completely understood. The purpose of this work is to develop a fabrication process with higher yield, investigate the beam profile, extend the concept of a hybrid waveguide to an AR design with high maximum operating temperature (4 Quantum Well bound-to-continuum QCL first reported in Ref. [30]) as well as thicker ridges (15.6 µm instead of $\sim 11\,\mu\mathrm{m}$), in order to test the robustness of the waveguide design.

Several concepts have been reported aiming to improve the beam pattern emitted by QCLs (i.e. reduce divergence or make the beam more Gaussian). Amongst them are a third-order grating[39] and photonic crystals[48]. See Figure 3.1 and 3.2 for key results from these studies. Amanti *et al.*[39] (Fig. 3.1) reported a MM QCL with a grating etched deep

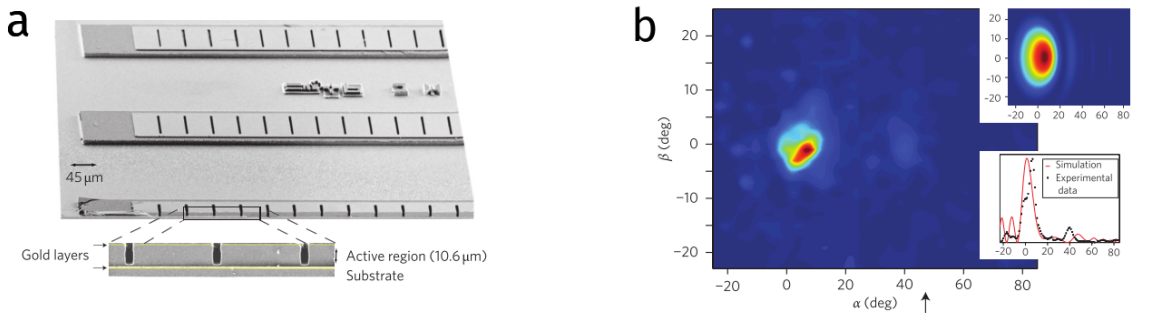

Fig. 3.1 **a:** SEM image of a third-order distributed feedback QCL. The grating was etched down into the AR with a period of approx. 40 µm. **b:** Measured far-field emission of the laser above. The full beam width is approx. 10°. The inset in the top right shows a simulated far-field pattern. Reproduced from Ref. [39].

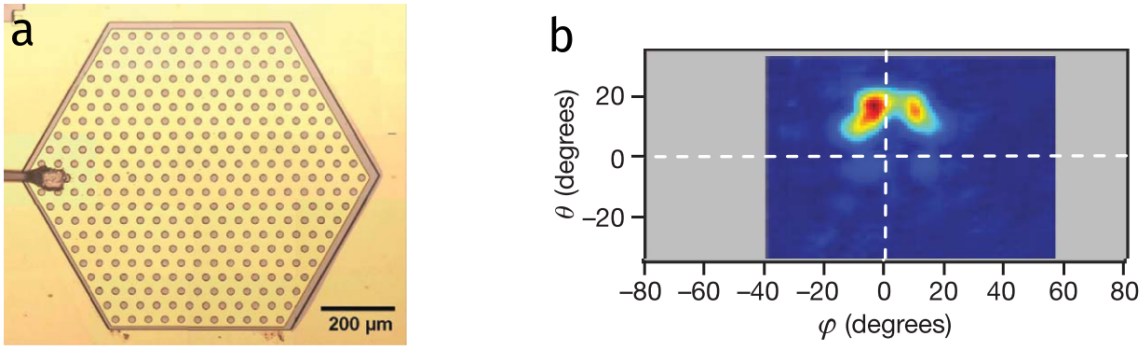

Fig. 3.2 **a:** Microscope image of a surface-emitting QCL patterned with a photonic crystal on the top contact. **b:** Measured far-field emission of the laser above. The full beam width is approx. 30°. Reproduced from Ref. [48].

(∼ 10 µm) into the AR across the top metal contact. The grating was resonant with the third order Bragg condition. Each grating acted as a phased linear source, resulting in a narrow beam (∼ 10° full beam width) emitted from the surface. Chassagneux *et al.*[48] (Fig. 3.2) demonstrated a photonic crystal QCL, where the photonic structure was defined by patterning the top contact only. They showed that by changing the boundary conditions of the laser structure from reflecting (top metal covering the whole structure) to absorbing (a strip of the doped GaAs layer left on the edges), the emission beam changed from non-directional to narrow (approx. 30° full beam width).

These approaches are inherently frequency selective and therefore not compatible with broadband applications of QCLs. Approaches which are not frequency selective include incorporating an external lens[64] or a hollow waveguide[65] at the QCL facet. See Figures 3.3 and 3.4 for key results from these studies. By attaching a hyperhemispherical silicon lens

Figures from previous work on THz QCLs with silicon lenses removed for copyright reasons. See Lee et al.[64].

Fig. 3.3 **a:** A picture of a QCL with a silicon lens attached in front of its facet. **b:** Measured far-field emission of the laser above. The beam width is approx. 10°. Reproduced from Ref. [64].

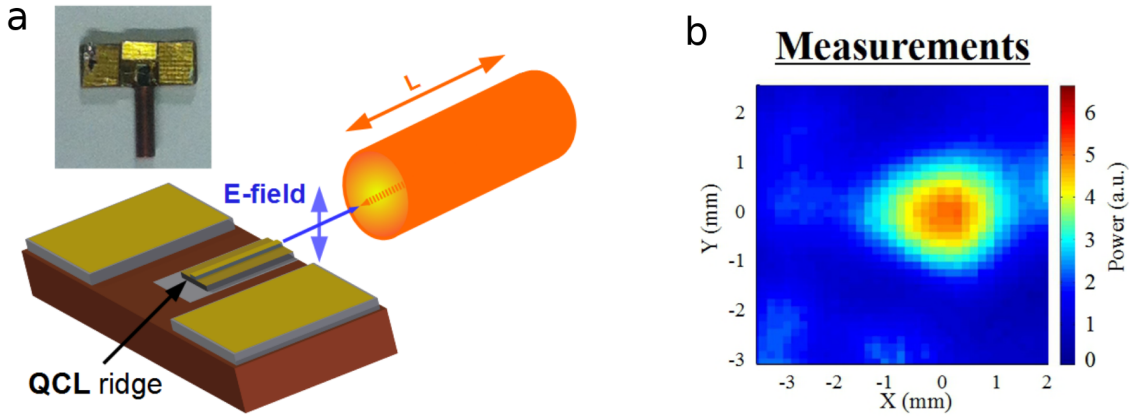

Fig. 3.4 **a:** A picture and a diagram of a QCL with a hollow copper waveguide attached. **b:** Measured far-field emission of the laser above, taken at 22 mm from the laser facet. The beam width is approx. 30°. Reproduced from Ref. [65].

(3 mm diameter, 1.62 mm length) to a facet of a MM QCL, Lee *et al.*[64] were able to reduce the highly divergent MM output into a beam with FWHM $\simeq 5°$ (Figure 3.3). Degl'Innocenti *et al.*[65] also used a standard MM QCL as a source, but attached a hollow copper waveguide (7 mm inner diameter, 7-11 mm length) to the front facet (Figure 3.4). When aligned properly (with $\sim$10-20 µm precision), the authors found the divergence of the beam to be lower ($\sim 11°$ full beam width) than that of a silicon lens QCL used by them as a reference sample ($\sim 20°$ full beam width). These two configurations cited above require precise alignment of the external elements (10s of µm) and are therefore not easily reproducible. All approaches mentioned above rely on traditional MM thermocompressive wafer bonding, which sets the minimum thickness of the gold or copper layer below the active region to hundreds of nanometers, therefore introducing very high reflectivity and impedance mismatch at the facet.

BCB has already been used in several semiconductor devices. Zhang *et al.*[42] used it as a filling medium for the space between cylindrical columns of a photonic crystal lattice. It allowed for the deposition of a top contact connecting all the columns. We also used BCB as a filling medium to fabricate defect line lasers described in Chapter 2. Christiaens *et al.*[66] used it for wafer bonding of microring resonators, lasers and LEDs, and demonstrated good quality and stability of the BCB bond. BCB was chosen for its "excellent thermomechanical stability over time, no detectable outgassing at room temperature, low processing temperatures, lower than fusion bonding, and a fairly simple processing scheme that only requires basic cleanroom equipment"[66]. Guarino *et al.*[67] used BCB as a bonding agent for lithium niobate film-based devices. They found that the BCB properties reduced the role of surface defects and improved the reproducibility of fabrication.

The hybrid waveguide discussed in this chapter bears some resemblance to the slot waveguide. Contrary to the conventional waveguides employed in telecommunications, the slot waveguide confines light in a low refractive index region sandwiched between high refractive index materials. First demonstrated in the infrared[68], slot waveguides were subsequently extended into the THz[69, 70]. Light is confined in such structures due to the discontinuity of the normal component of the electric field at the interface of the high refractive index material[71]. Figure 3.5 shows the electric field distribution in a slot made of BCB surrounded by GaAs, i.e. the materials used in the hybrid QCL waveguide (BCB layer in between AR and substrate, both made of GaAs). The main difference between this slot geometry and hybrid QCL are the metal and doped layers above the BCB in the latter. The overlap of the mode with the narrow slot in Figure 3.5 is 40%, and the mode intensity in the slot is more than twice as high as in the surrounding area.

This chapter has the following structure: in Section 3.2 the physical properties of BCB are described. In Section 3.3 the fabrication process of the hybrid waveguide is outlined. A summary of the results from Ref. [62], where a bound-to-continuum (BtC) BCB-bonded QCL was reported, follows in Section 3.4. In Section 3.5 we further discuss the fabrication process and the improvements we have made to it in order to increase yield. We also list all the devices fabricated for this work. Section 3.6 contains COMSOL simulation results of the mode profile in BCB-bonded devices. In Section 3.7 the results of BCB QCL measurements (light-current-voltage curves, far-field plots, threshold current density analysis and absolute power figures) are presented. The chapter finishes with conclusions and suggestions for future work in Section 3.8.

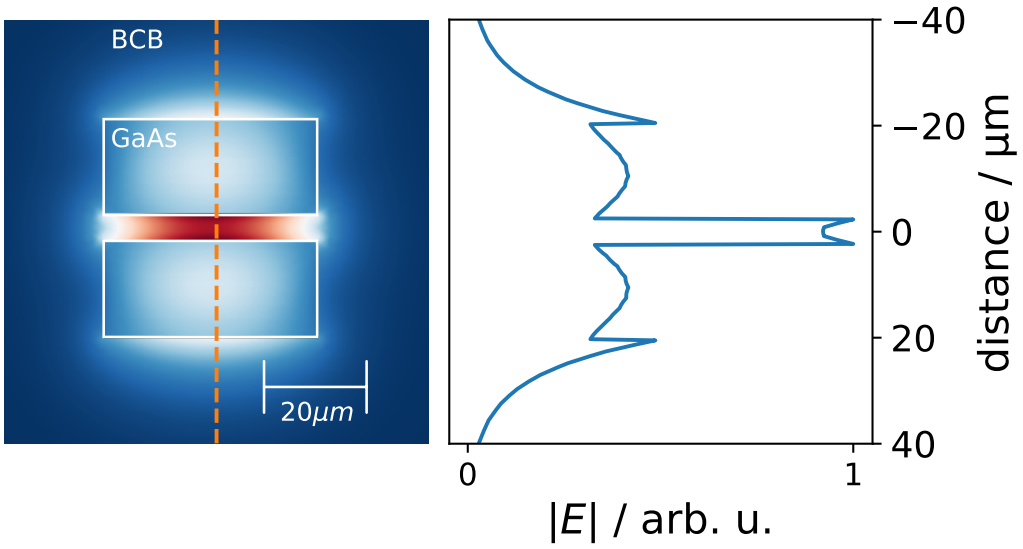

Fig. 3.5 A traditional slot waveguide simulation using BCB in the gap and GaAs around it. The width of the slot is 5 µm. The plot on the right shows electric field intensity along the vertical dashed line on the left, through the centre of this geometry.

3.2 BCB properties

BCB is a low-loss material in the THz spectral region. Its optical properties have been measured by Fourier transform infrared spectroscopy and reported in Ref. [63] as $\varepsilon_1 = 2.49$ and $\tan\delta \simeq 0.11$ at $f = 3\,\text{THz}$. The loss tangent is defined as

$$\tan\delta = \frac{\omega\varepsilon_2 + \sigma}{\omega\varepsilon_1}, \tag{3.1}$$

where ω is the angular frequency, ε_1 and ε_2 are the real and imaginary part of the dielectric constant, respectively, and σ is conductivity. For dielectrics such as BCB it is a reasonable assumption that the conductivity $\sigma \simeq 0$, therefore $\tan\delta = \varepsilon_2/\varepsilon_1$. From this, we can calculate $\varepsilon_2 = 0.0274$. In order to quantify losses we use the following equations:

$$\varepsilon_1 = n^2 - \kappa^2, \tag{3.2}$$

$$\varepsilon_2 = 2n\kappa, \tag{3.3}$$

where n and κ are the real and imaginary part of the refractive index, respectively. At 3 THz they evaluate to $n \simeq 1.578$ and $\kappa \simeq 8.68 \times 10^{-3}$. Finally, the loss is defined as

$$\alpha = \frac{4\pi\kappa}{\lambda}. \tag{3.4}$$

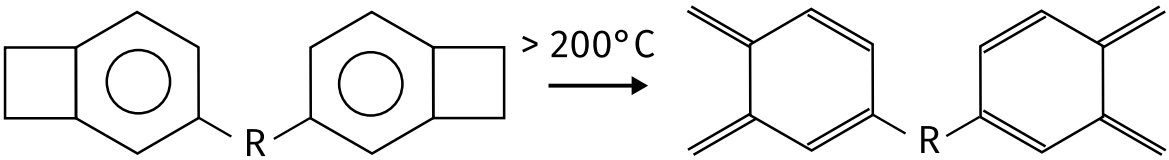

Fig. 3.6 BCB polymerisation reaction. At temperatures above 200 °C, cyclobutene undergoes a conrotatory ring-opening action, forming o-xylylene polymer.

At 3 THz, $\alpha \simeq 10\,\mathrm{cm}^{-1}$. This value is of the same order as the losses in the doped regions of typical THz QCL active regions and four orders of magnitude lower than the loss in the bottom plasmon layer at the bottom of a SP waveguide (where $\kappa \simeq 10^2$).

BCB comes in the form of partially polymerised solution. Polymerisation is purely thermal. Cyclobutene undergoes a conrotatory ring-opening reaction, forming o-xylylene[72] (see Figure 3.6). It is fully polymerised in a nitrogen environment at 250 °C[73]. At this point it is mechanically stable.

3.3 Fabrication

In this section we will describe the fabrication process of BCB waveguides until the point where it converges with the MM processing procedure, which was outlined in Section 1.5.3.

We start with two cleaved chips: one from the QCL AR wafer and one from a semi-insulating GaAs wafer. The size of the chips varied from $10\,\mathrm{mm} \times 10\,\mathrm{mm}$ to $20\,\mathrm{mm} \times 20\,\mathrm{mm}$ depending on the available material. Subsequently, a metal layer is evaporated on the QCL wafer in an Edwards thermal evaporator (Figure 3.7a). First a wetting layer of titanium is evaporated (10–15 nm) and then a layer of gold with the desired thickness. The base pressure of the evaporator is kept at 2×10^{-7} mbar. The evaporation rate is kept at $\sim 0.2\,\mathrm{nm/s}$ and it is constantly monitored with a quartz crystal monitor.

BCB spinning on both chips follows (Figure 3.7b). After the samples are cleaned with acetone and isopropanol, they are mounted on glass slides and put onto a vacuum spinner. A layer of adhesion promoter (AP3000) is spun for 50 s at 3000 rpm. Immediately after that, a layer of BCB is spun for 60 s at 5000 rpm. The samples are then baked to remove the BCB solvent at 90 °C on a hot plate for 2 h, at 120 °C for 2 h and finally at 150 °C for 15 h in an oven. This baking sequence was empirically found to result in a satisfactory flat and bubble-free layer of BCB[74].

In this first planarisation step the spun layer is cured at 210 °C for 60 min in a nitrogen environment, in order to polymerise the majority of the substance, but retain some of its malleability (Figure 3.7c). After the first curing, spinning is repeated on the AR chip,

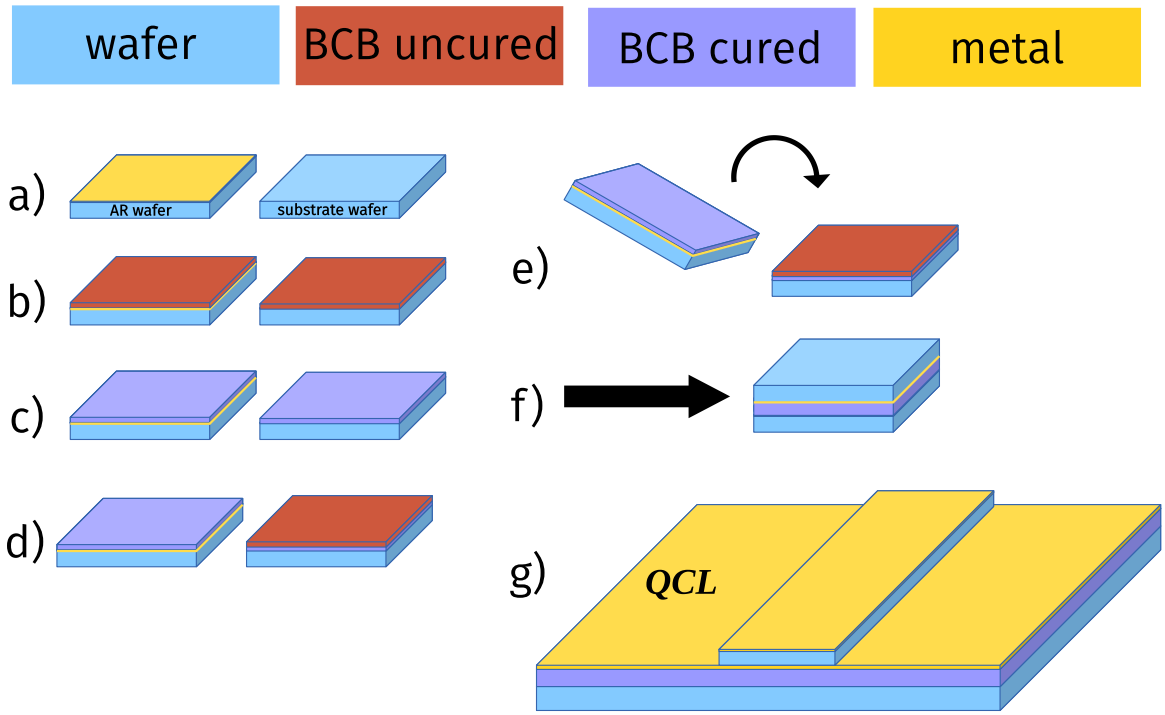

Fig. 3.7 BCB bonding process. **a)**: a layer of Au is thermally evaporated on the AR wafer. **b)**: BCB is spun on two wafers (the AR and the substrate). **c)**: BCB is cured in an annealer. **d)**: another layer of BCB is spun on the substrate wafer. **e)**: the substrate is inverted and put on top of the AR wafer. **f)**: the bonded sample is cured. **g)**: standard metal-metal processing follows (ridge etching, top metallisation).

whereas on the substrate chip AP3000 is spun and then a drop of BCB is placed on its centre without spinning (Figure 3.7d). Subsequently, the AR is inverted and carefully placed on the substrate chip (Figure 3.7e). This ensures no bubbles are formed within the BCB structure. The baking procedure is repeated, followed by the second curing at 255 °C for 60 min. After this, the two chips are bonded and the whole structure is mechanically stable (Figure 3.7f). Photolithography, liftoff, etching and cleaving (standard MM processing) follows, as described in Section 1.5.3 (Figure 3.7g).

An SEM image of a fully processed hybrid BCB waveguide is shown in Figure 3.8. On top of this image, a bond wire can be seen. This ridge was not cleaved perfectly, which can be seen in its top corners. Cleaved BCB, being a polymer rather than a crystal, is less uniform than the QCL ridge. Small imperfections (bubbles) can be seen in the BCB, especially below the left side of the laser ridge. The BCB bonding interface can be seen approximately half way between the AR and the substrate, where BCB layers change brightness.

We will now discuss our initial, published work on hybrid waveguides. We only managed to fabricate five working devices for that work, with a very low fabrication success rate. In

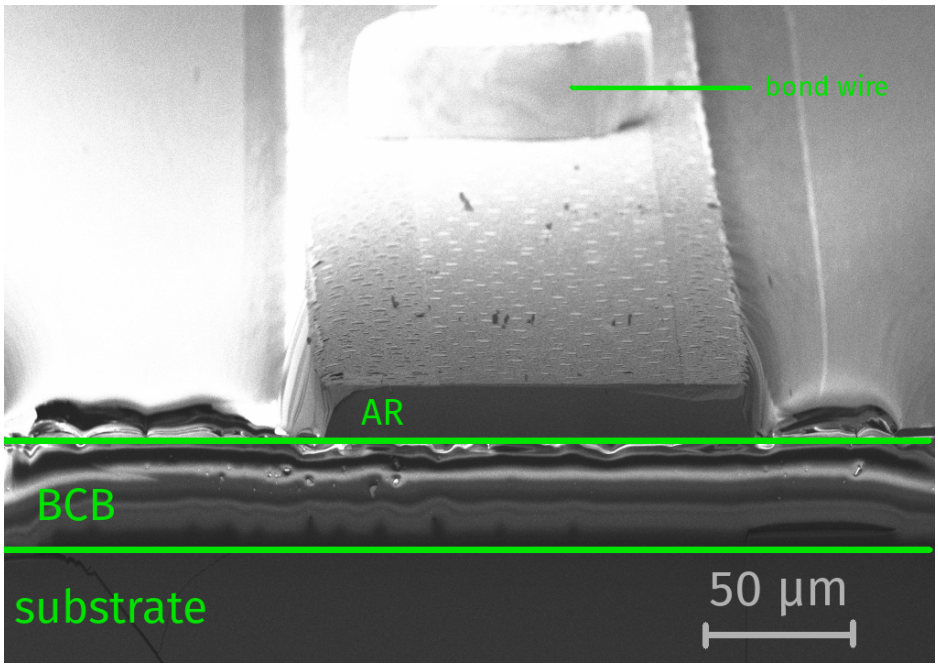

Fig. 3.8 SEM image of a fully fabricated hybrid BCB waveguide QCL, mounted on a copper block. A bond wire is visible at the top of the image. The AR ridge of this device was cleaved imperfectly, which can be seen on the top right of the facet. Some BCB imperfections (bubbles) can be seen, mostly below the left side of the ridge.

the subsequent Section 3.5, we will revisit the most important fabrication steps and discuss how we improved upon them.

3.4 Bound-to-continuum QCL initial results

We first reported the BCB hybrid waveguide QCL in Degl'Innocenti *et al.* [62]. The demonstrated lasers were based on a BtC active region designed to lase at around 2.85 THz. We fabricated devices with different thicknesses of the bottom metal layer (i.e. the one normally involved in thermocompressive bonding). The widths of the devices ranged from 120 to 140 µm and their length from 1.3 to 2.1 mm (see Table 3.1). We found the optimum thickness of gold to be between 200 and 300 nm. For this thickness, the temperature performance of the laser (T_{max} =75-95 K) was similar to that of a reference MM device (T_{max} = 85 K), while the beam pattern was much less divergent (full beam width was 35° for the 200 nm BCB device vs. 70° for MM). See Figure 3.9 for a comparison of far-field patterns. The MM QCL exhibited a typical multi-lobe behaviour, while the beam from the BCB-bonded QCL was Gaussian-like.

Table 3.1 All devices reported in Degl'Innocenti *et al.*[62], along with the gold layer thickness and ridge dimensions.

wafer	gold layer	dimensions
V706	MM	1.79 mm × 140 µm
V706	420	2.10 mm × 140 µm
V706	300	1.50 mm × 130 µm
V706	220	2.05 mm × 130 µm
V706	150	1.60 mm × 130 µm
V706	40	1.30 mm × 120 µm

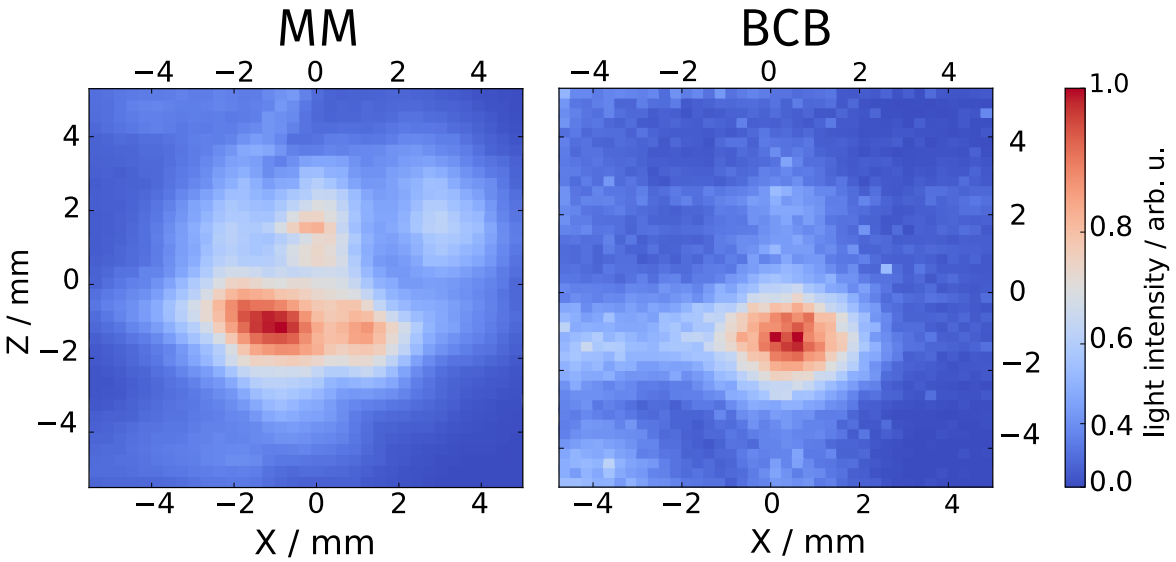

Fig. 3.9 Far-field patterns of a MM (left) and BCB-bonded (right) device, taken with a Golay cell detector (1.5 mm aperture diameter) placed 12 mm from the facets. The MM pattern is a typical, multi-lobe and divergent emission. The BCB device emits a narrow (36° full beam width), Gaussian-like beam. Each plot is normalised to its own maximum. Reproduced from Ref. [62].

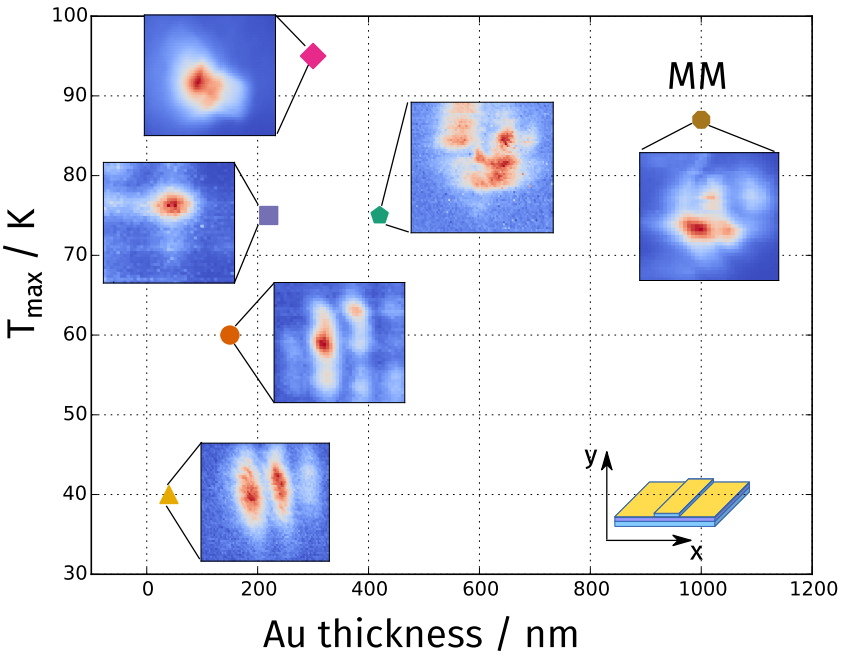

Fig. 3.10 Far-field patterns and temperature performance of BtC, BCB bonded devices. Device orientation with respect to plot axis is shown in the bottom right of the plot. The rightmost data point (brown octagon) is a reference MM QCL. Reproduced from Ref. [62].

In Figure 3.10 we reproduce the temperature performance plot from Ref. [62]. The devices with gold thickness of 200-400 nm attained similar temperature performance as the MM laser. Moreover, the 220 nm and 300 nm lasers both had a more convergent output beam. This was unexpected, as the gold layers were much thicker than the skin depth for this frequency ($\delta \simeq 55$ nm) for the mode to leak. The 300 nm laser outperformed the reference sample in terms of temperature performance (95 K vs. 85 K) and emitted a less divergent beam. Devices with the metal layer thinner than 200 nm emitted multi-lobe beams, elongated in the vertical direction, suggesting a leakage through the metal layer. In Figure 3.11, threshold current density data from Ref. [62] are shown. Except for one device (40 nm), hybrid waveguide QCLs had similar J_{th} to the MM reference. The low temperature performance of the 40 nm sample ($T_{max} = 40$ K) was attributed to the large amount of leakage of the mode from the AR into the substrate. 220 nm, 300 nm, and 420 nm samples all attained maximum operating temperatures greater than the boiling temperature of liquid nitrogen (77 K), which is desirable for QCLs which otherwise need to be cooled with liquid helium.

In this work, we will attempt to answer three important questions about the results reported above. Firstly, can fabrication yield be improved? (Section 3.5) Only five hybrid waveguide QCLs were reported in Ref. [62], out of numerous fabrication batches. The yield

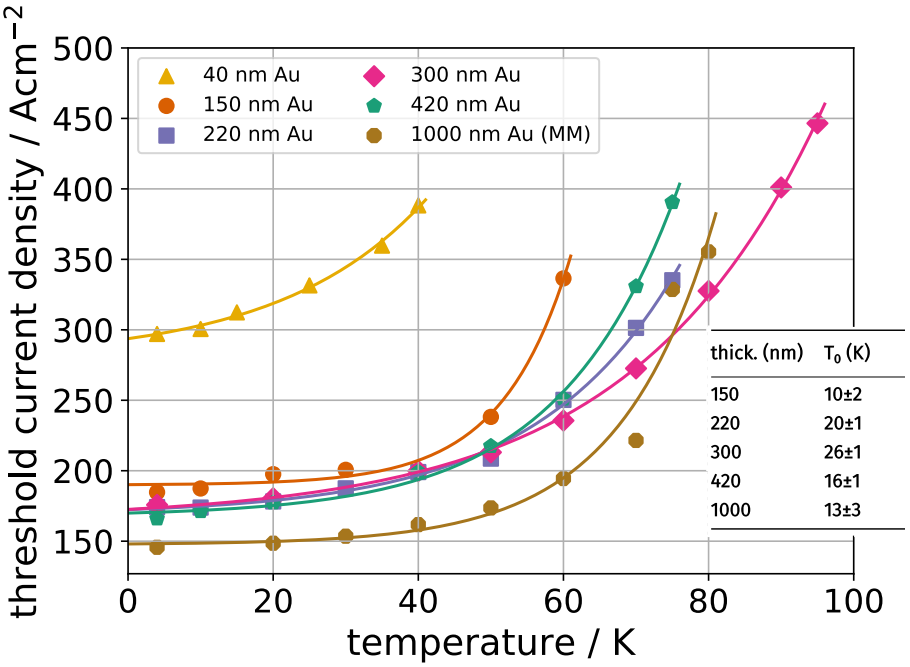

Fig. 3.11 Threshold current density of the first batch of BCB bonded devices. The solid lines are fitted as $J_{th} = J_0 + A \cdot \exp T/T_0$. The outlying 40 nm device exhibited multi-lobe output. The other BCB lasers were comparable in temperature performance to the reference MM device, with the 300 nm QCL exceeding the maximum operating temperature by 10 K. Reproduced from Ref [62].

was approximately 10-15%. Secondly, why did the reported devices show unusual far-field patterns? In Section 3.6 we will try to explain the mode leakage. Finally, is this waveguide design transferable to other QCL active regions? In Section 3.7 we replicate the results from Degl'Innocenti *et al.* using a higher T_{max} AR. The results shown in Figures 3.9, 3.10 and 3.11 will serve as a reference in our comparisons. In Section 3.7.4 we report the unpublished absolute power figures for the devices from Ref. [62] alongside the new devices fabricated for this work. In Section 3.7.3 we analyse the threshold current density and maximum operating temperature of all existing hybrid waveguide devices.

3.5 Improving fabrication yield

The laser ridges presented in Degl'Innocenti *et al.*[62] were wet etched. Etching was one of the main failure points, as the ridges would often detach from the substrate in the etching solution. This issue was addressed by switching to dry etching, and after the initial optimisation the yield was significantly improved. In Batch I (see Table 3.2) the only change

Table 3.2 All BCB bonded samples. V758, V759, V767 — ETH 4 quantum well design[30], 160 repeats of the QCL period. V773 — ETH 4 QW design, 230 repeats of the QCL period.

batch	sample	metal thickness	description
I	V773 S2	Ti/Au 10 nm/40 nm	AR peeled off while cleaving.
I	V773 S3	Ti/Au 10 nm/118 nm	AR detached from the substrate during side contacts lift-off in acetone.
I	V758 S1	Ti/Au 10 nm/130 nm	AR peeled off while cleaving.
IIa	V773 S5	Ti/Au 10 nm/60 nm	Crumbled when detaching from polishing block. No metal left on the sides of the ridge, unable to bond.
IIa	V773 S6	Ti/Au 10 nm/60 nm	Crumbled when detaching from polishing block. AR peeled off while cleaving.
IIb	V773 S7	Ti/Au 10 nm/190 nm	The ridge came off while bonding.
IIb	V773 S8	Ti/Au 10 nm/190 nm	Impossible to bond to the ridge.
IIb	V773 S9	Ti/Au 10 nm/190 nm	Visually OK, but open circuit.
IIc	V773 S10	Ti/Au 10 nm/310 nm	OK
IIc	V773 S11	Ti/Au 10 nm/310 nm	OK, but low output power.
IIc	V773 S12	Ti/Au 10 nm/310 nm	Ridge delaminated during measurement.
IId	V767 S1	Ti/Au 10 nm/60 nm	OK, but low output power.
IId	V767 S2	Ti/Au 10 nm/60 nm	Ridge delaminated during measurement.
IIIa	V767 S3	Ti/Au 10 nm/190 nm	OK
IIIa	V767 S4	Ti/Au 10 nm/190 nm	OK
IIIa	V767 S5	Ti/Au 10 nm/190 nm	OK
IIIb	V767 S6	Ti/Au 10 nm/310 nm	OK
IV	V773 S1	Cu 274 nm	Two wafers detached during mechanical polishing.
IV	V773 S4	Cu 100 nm	Two wafers detached during mechanical polishing.
IV	V758 S2	Cu 274 nm	Two wafers detached during mechanical polishing.
IV	V759 S1	Cu 274 nm	AR detached from the substrate during ridge lift-off in acetone.

we made was dry etching in an RIE tool. None of the three samples survived the process. It is difficult to pinpoint a common cause for these failures, but we suspected BCB planarisation defects to be partially responsible. The defects are usually introduced during BCB spinning.

During Batch II fabrication we inspected the samples carefully and did not see any defects (i.e. non-uniformities or bubbles in the BCB layer). Single letter suffixes in the table (a, b, c, and d) correspond to separate metal evaporation steps (different metal thickness). After that, the samples were processed together. The BCB on the first two samples (V773 S5 and S6) crumbled when detaching from the polishing block after removing the substrate. This step involves heating up the block in order to melt the crystal bond. For subsequent samples in Batch II we heated the block more slowly, taking care not to overheat the samples. All Batch IIb devices made it through to the last processing stage (wire bonding), but we failed to put bond wires on them. We inspected them under SEM and saw irregular features on their surfaces (see Figure 3.12). They were again caused by too much thermal stress, this time during dry etching. We therefore changed the etching procedure to include 2 or 3 cooling down periods. We limited etch duration to 60 min. After this change, we did not see the hardened features on the samples any more. We were able to start characterising samples from batches IIc and IId, but they were not mechanically stable. On V773 S12 and V767 S2, the ridges delaminated during measurements.

The final adjustment made for Batch III was reducing mechanical stress during substrate polishing. The speed of sand paper disk was kept below 10rpm (in previous batches, it was up to 40rpm). This batch had the best yield. We were able to characterise all four devices from Batch III.

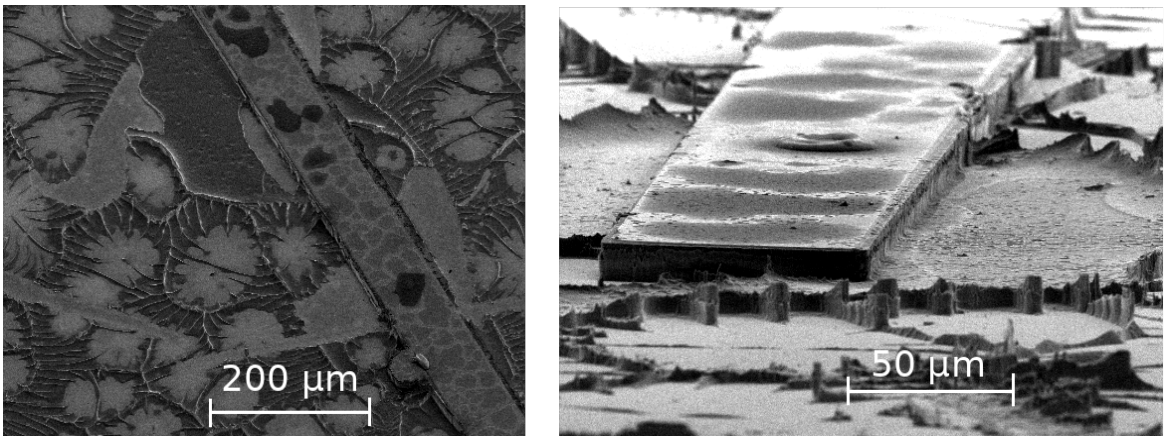

Fig. 3.12 Two views from a scanning electron microscope of a V773 sample which was exposed to too much of thermal stress during dry etching. This resulted in BCB “crumbling”.

Four of the samples (Batch IV) had a layer of copper instead of gold. Cu has been successfully used to reduce loss and improve thermal conductivity of metal cladding[75]. We tried evaporating Cu directly on to GaAs wafers in a thermal evaporator, as well as using a titanium wetting layer (not reported in the table — test GaAs samples were used only). Unfortunately, no QCL ridges were successfully fabricated from Cu-bonded samples, as they suffered from poor metal adhesion and detached during mechanical polishing. Belkin *et al.*[75] used tantalum as the intermediary adhesive layer, but an appropriate electron beam evaporator was not available at the time this work was carried out.

Some of the gold-bonded samples also detached from their substrates at various stages of processing. While this occurs with thermocompressively bonded waveguides as well, BCB might be slightly more vulnerable to this issue. The samples with very thin layers of metal (V773 S6 & S7, V767 S1 & S2) were prone to overetching and difficult to bond to in a gold wire ball bonder.

To summarise, we suggest that the following steps are crucial for fabricating BCB bonded QCLs:

1. Very careful planarisation of BCB. The introduction of imperfections such as bubbles leads to mechanical stress. These imperfections lead to failed polishing (substrate detachment) or very difficult cleaving.

2. Minimising thermal stress. On some samples BCB "bubbled up"/crumbled when they were heated on the brass block used for polishing in order to take them off.

3. Dry etching. When wet etching using H_2SO_4 solution, the active region chip is prone to detaching from the substrate.

4. When dry etching, reduce the thermal stress by splitting the process into several rounds of etching and cooling down. See Figure 3.12 for an example of an overheated device. The BCB in this case crumbled and hardened, which made it impossible to create a wire bond on the device.

3.6 Simulations and design

The aim of this section is to numerically simulate the proposed hybrid waveguide in order to investigate the Gaussian beam profile reported in Reference [62]. We begin with a summary of the Drude model, used here to calculate material properties. We then present a simplified model showing the leakage of the optical mode through a layer of metal. Finally, we show simulations of the hybrid waveguide and the modes it can sustain.

The simulations presented in this section were carried out with COMSOL Multiphysics 5.2a, and the RF module. We employed the 2D "Electromagnetic Waves, Frequency Domain" physics interface, which is used to solve for time-harmonic electromagnetic field distributions in a 2D cross-section. This uses "Mode analysis" study to find the allowed propagating modes. Scattering boundary conditions were used on the sides of the waveguide as well as on top. The bottom of the QCL waveguide was simulated as a perfect electric conductor. In the slot waveguide simulations, all boundaries were scattering. The equation solved by this interface, derived from Maxwell's equations, is of the following form:

$$\nabla \times \left(\frac{1}{\mu} \nabla \times \vec{E} \right) - \omega^2 \varepsilon_c \vec{E} = 0, \tag{3.5}$$

where μ is the vacuum permittivity, $\vec{E}$ is the electric field, ω is the angular frequency of the radiation, and ε_c is the dielectric constant of the materials.

3.6.1 Drude model

In order to calculate material properties required to carry out COMSOL simulations, we employed the Drude-Lorentz model of free electron conductivity[76]. In this model, valence electrons do not experience restoring forces and they interact with electromagnetic radiation. The equation of motion is given by

$$m_0 \frac{d^2x}{dt^2} + m_0 \gamma \frac{dx}{dt} = -eE_0 \exp(-i\omega t), \tag{3.6}$$

where m_0 is the electron mass, e is the electron charge, ω is the angular frequency of the radiation, E_0 is the electric field amplitude, and γ is the damping factor due to scattering. For damping effects, we use $\tau = \frac{1}{\gamma}$, the momentum scattering time, which can be derived from DC conductivity measurements. We use $\tau = 0.1\,\text{ps}$ for the active region, $\tau = 0.5\,\text{ps}$ for the top and bottom plasmon layers, and $\tau = 0.06\,\text{ps}$ for the metal layers[77].

Equation 3.6 leads to the following expressions for the real and imaginary parts of the dielectric constant:

$$\text{Re}(\varepsilon) = \varepsilon_{\text{opt}} \left(1 - \frac{\omega_p^2 \tau^2}{1 + \omega^2 \tau^2} \right), \tag{3.7}$$

$$\text{Im}(\varepsilon) = \frac{\varepsilon_{\text{opt}} \omega_{\text{p}}^2 \tau}{\omega(1 + \omega^2 \tau^2)}, \tag{3.8}$$

where ε_{opt} is the dielectric constant of the undoped semiconductor (12.96 for GaAs[78]), and ω_p is the plasma frequency — the frequency below which radiation is strongly reflected from

Table 3.3 Dielectric constant from Drude model used for COMSOL simulations in Chapters 3 and 4.

Material	$\mathrm{Re}(\varepsilon)$	$\mathrm{Im}(\varepsilon)$
Gold	-3×10^5	2.8×10^5
GaAs doped $5\times10^{18}\,\mathrm{cm}^{-3}$ (top plasmon)	-535	301
GaAs lightly doped $2.9\times10^{15}\,\mathrm{cm}^{-3}$ (active region)	12.55	0.045
GaAs doped $2\times10^{18}\,\mathrm{cm}^{-3}$ (bottom plasmon)	-206	120
BCB	2.56	0
GaAs undoped (substrate)	12.96	0

the material. ω_p is given by

$$\omega_p^2 = \frac{Ne^2}{\varepsilon_{\mathrm{opt}}\varepsilon_0 m^*}, \tag{3.9}$$

where N is the carrier density resulting from the doping process and m^* is the effective mass of the carriers. For gold, we assumed the carrier density of $5.9\times10^{22}\,\mathrm{cm}^{-3}$[76]. For metals, $\varepsilon_{\mathrm{opt}}$ and m^* are set to 1, as there is no need to account for the valence band or intrinsic polarisability of the bound electrons.

The substrate was simulated as a lossless material, and the doping of the active region was determined by averaging the donor density of two doped quantum wells in the BtC design used in Degl'Innocenti *et al.* [62], which resulted in $N_{\mathrm{AR}} = 2.9\times10^{15}\,\mathrm{cm}^{-3}$. See Table 3.3 for a list of parameters used to simulate a surface plasmon waveguide.

In order to simulate mode leakage through a layer of gold in Section 3.6.2, it is useful to derive the relation between the dielectric constant and conductivity. Equation 3.6 can be rewritten as

$$m_0\frac{d\vec{v}}{dt} + \frac{m_0}{\tau}\vec{v} = -e\vec{E}_0 e^{-i\omega t}. \tag{3.10}$$

On substituting $\vec{v} = \vec{v}_0 e^{-i\omega t}$ we obtain

$$\vec{v} = \frac{-e\tau}{m_0}\frac{1}{1-i\omega\tau}\vec{E}. \tag{3.11}$$

We can now use the relation between current density $\vec{j}$ and velocity

$$\vec{j} = -Ne\vec{v} = e\vec{E} \tag{3.12}$$

to derive the AC conductivity σ:

$$\sigma = \frac{\sigma_0}{1-i\omega\tau}, \tag{3.13}$$

where

$$\sigma_0 = \frac{Ne^2\tau}{m_0} \tag{3.14}$$

is the DC conductivity[76].

3.6.2 Leakage through a thin layer of gold

Given the low skin depth of gold at THz frequencies and cryogenic temperatures ($\delta \simeq 55\,\text{nm}$), it was surprising to see apparent mode leakage in the devices reported in Degl'Innocenti *et al.*[62]. In order to gain more insight into the optical properties of hybrid waveguides, it is instructive to look at a simplified model: a thin ($\leq 100\,\text{nm}$) layer of gold in between a thick piece of GaAs (400 µm thick, imitating the substrate) and a thin layer of GaAs (15 µm thick, representing the AR). See the top bar in Figure 3.13 for a schematic of this system. We used the "dielectric loss" electric field displacement model in COMSOL to simulate optical modes. This model requires pre-calculated values of the complex dielectric constant, ε_1 and

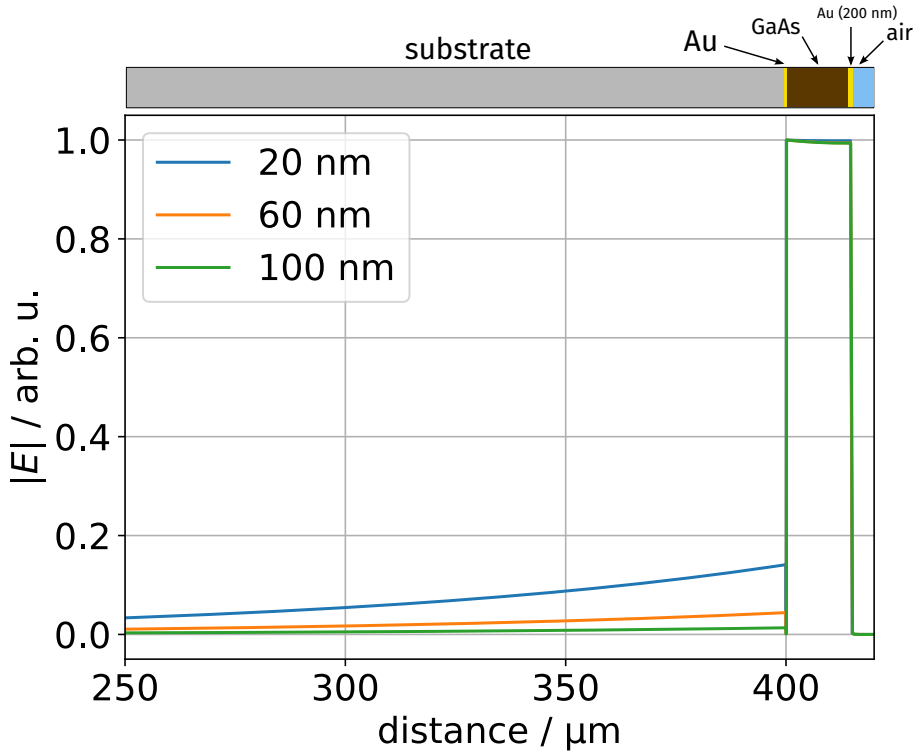

Fig. 3.13 Simulated optical mode leakage through a single layer of gold. The distance from the bottom of the geometry (the substrate) is indicated on the x axis. The blue, orange and green lines represent the mode intensity for a 20 nm, 60 nm, and 100 nm thick layer of gold, respectively.

ε_2. The choice of these parameters for gold is not trivial. Their values at THz frequencies have been published[79], but later studies showed that both the temperature and thickness of the metal layer play a significant role in determining ε and conductivity σ[80]. For example, an 85 nm thick Au layer at 77 K exhibited THz conductivity of 24 $/\mu\Omega$m. This is 12% of the bulk DC conductivity at 77 K reported in literature[81]. The reduction in conductivity with temperature is related to lower phonon scattering at low temperatures. The reduction proportional to thickness in thin films stems from temperature-independent scattering mechanisms, such as grain boundaries and defects[80]. In the following simulation we used the reported conductivity (24 $/\mu\Omega$m) to calculate the momentum scattering time τ as per equation 3.14. Then we obtained the complex dielectric constant from equations 3.7 and 3.8. These parameters were subsequently used as the input for materials in COMSOL. It should be noted that in THz QCLs the operating temperature is lower than 77 K, but published results of sub-77K measurements are not widely available to the best of our knowledge. In Ref. [80], the conductivity of gold, as well as other measured metals, was **higher** at 77 K ($\sigma_{77\,\mathrm{K}} = 24\,/\mu\Omega$m) than at 295 K ($\sigma_{295\,\mathrm{K}} = 15\,/\mu\Omega$m). Therefore our chosen value for 77 K should be viewed as the lower limit on conductivity.

We simulated three different thicknesses of the middle gold layer: 20 nm, 60 nm and 100 nm. The results are plotted in Figure 3.13. In principle, the electric field strength is attenuated by $\exp(-z/\delta)$, where $\delta = 2/\alpha$ is the skin depth. The absorption coefficient, α can be obtained from

$$\alpha = \frac{2\kappa\omega}{c}, \tag{3.15}$$

where κ is the imaginary part of the complex refractive index and is given by

$$\kappa = \frac{1}{\sqrt{2}}\left(-\varepsilon_1 + (\varepsilon_1^2 + \varepsilon_2^2)^{1/2}\right)^{1/2}. \tag{3.16}$$

Values reported in Ref. [80] result in $\delta \simeq 55$ nm at terahertz frequencies and $T = 77$ K. Figure 3.13 does not show such a strong attenuation because the simulation does not deal with a THz pulse travelling through a metal sheet. Instead, it comprises a wave confined in a subwavelength cavity, where the field strength on top of the thin metal layer is the result of many reflections. We will use the term "leakage" for the ratio between the peak field strength below the metal layer and the peak field strength in the GaAs layer. For a 20 nm layer of gold, the field strength at the bottom of the layer is 16% of that in the GaAs region, for a 60 nm Au layer it is 4.5%, and for a 100 nm gold sheet there is 1.5% leakage. However, for thicker layers the attenuation is too high for the mode to leak out into the substrate. This is evidence that either the conductivity for these films is even smaller than reported, or

there is an additional effect that determines the beam pattern, as the optimal thicknesses in Degl'Innocenti *et al.*[62] were much greater than 100 nm (namely 200-400 nm).

3.6.3 Hybrid waveguide

Subsequently, we simulated the hybrid waveguide (50 nm gold, i.e. below the skin depth of ~ 55 nm) in search of the two potentially supported optical modes: the dielectric mode and standard MM mode confined to the AR. The results are presented in Figures 3.14 (BCB mode) and 3.15 (AR mode). The geometry and material parameters are constant in both simulations: 12 µm thick and 120 µm wide AR, 15 µm thick BCB layer on top of a 400 µm wide and 100 µm thick substrate. The bottom plasmon GaAs layer (thickness 700 nm) was set to 5×10^{18} cm^{-3} doping. A 2×10^{18} cm^{-3} doped layer was positioned on the top of the AR (thickness 100 nm), and a 300 nm thick layer of gold on top of it.

The BCB mode in Figure 3.14 is concentrated in the dielectric below the AR and the metal layer. This geometry is similar to a conventional slot waveguide (see Figure 3.5), except for the layer of metal and the layer of doped GaAs on top of the dielectric in the waveguide presented in this section. The confinement of the optical mode in the BCB layer is even stronger than in the slot waveguide because the gold layer constitutes a boundary for the mode. The overlap of the mode with the BCB layer is 83%, the overlap with the substrate is 16%, and the overlap with the AR is less than 0.1%. The mode intensity in the AR attains only 0.06 of the maximum value in the BCB layer. The leakage into the substrate is smooth, as there is no metal layer in between the regions (compare to the discontinuity between GaAs

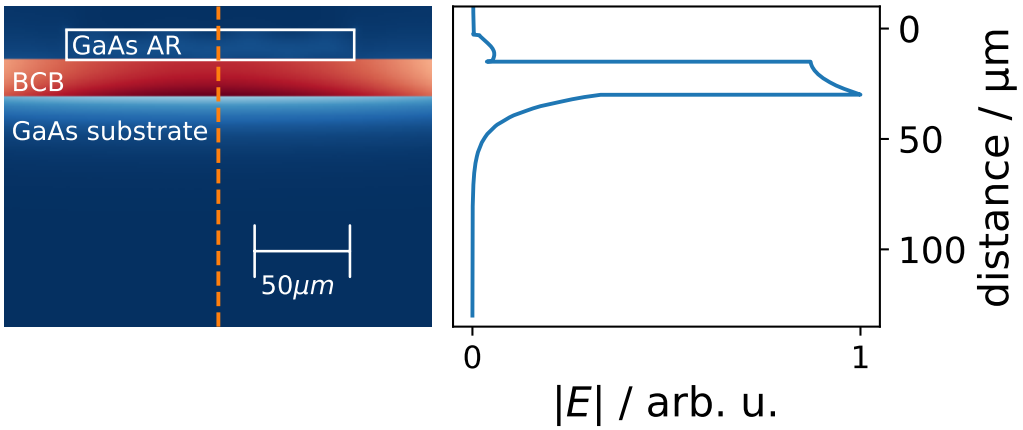

Fig. 3.14 A simulation of hybrid waveguide mode with the effective mode index close to n_{BCB} ($n_{eff} \simeq 1.6$). The overlap of the mode with the BCB region is 83%, with the substrate 16%, and with the AR less than 0.1%.

and the substrate in Figure 3.13). For comparison, the mode overlap with the AR and the substrate in a SP waveguide is approximately 30% and 70%, respectively.

In contrast to the dielectric mode discussed above, the AR mode in Figure 3.15 overlaps with the AR almost as much as the standard MM waveguide mode (98%), but there is a small amount of leakage into the BCB. The bottom gold thickness in this simulation was 50 nm, and for such a layer the leakage is small: the mode intensity on the BCB side of the metal-BCB interface is only 0.01 of the maximum in the AR, and the overlap of the mode with this region (BCB) is less than 0.5%. The rest of the mode (approximately 1.5% overlap) leaks into the substrate.

The results of the two aforementioned simulations were obtained by setting the desired effective mode index to 3.6 (AR mode) and 1.55 (BCB mode). The COMSOL solver searches for modes with n_{eff} close to the chosen value. We were unable to find a mode which would spread over the two regions more evenly (we performed this search by repeating the simulation ith desired n_{eff} between 1.55 and 3.6). Such a mode would explain the improvement in the far-field profile observed by Degl'Innocenti *et al.*[62] — the refractive index mismatch at the facets would indeed be smaller. Figure 3.16 shows the results of the hybrid waveguide simulation in the limit of **no gold** in between the AR and the BCB. The overlap of this mode with the AR is 58%, with the BCB region 38%, and with the substrate 1.5%. We postulate that in real devices the propagating optical mode is a mix (in terms of overlap with different regions) of the three modes shown in Figures 3.14, 3.15, and 3.16. Because the thin gold layer properties at temperatures below 77 K are not available (and possibly due to the limitations of the loss model used by COMSOL Multiphysics),

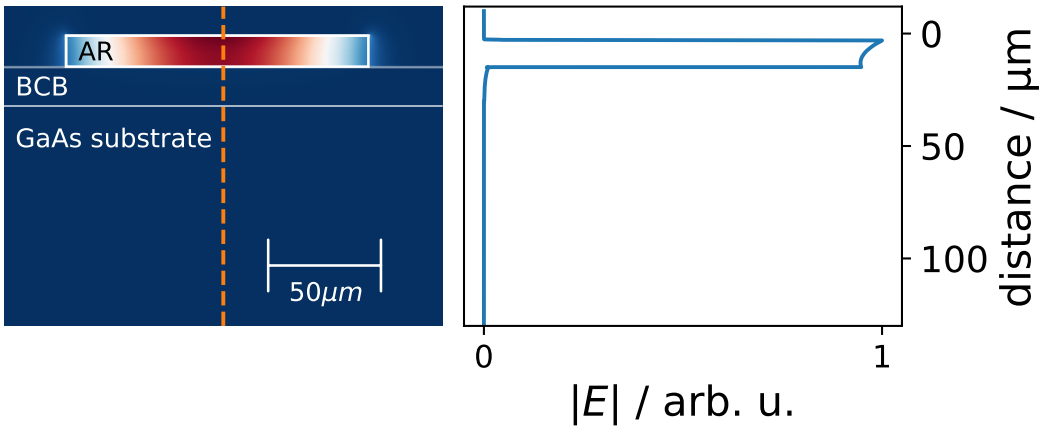

Fig. 3.15 A simulation of hybrid waveguide mode with the effective mode index close to n_{GaAs} ($n_{\text{eff}} \simeq 3.5$). The overlap of the mode with the AR is 98%, with the substrate 1.5%, and with the BCB region less than 0.5%.

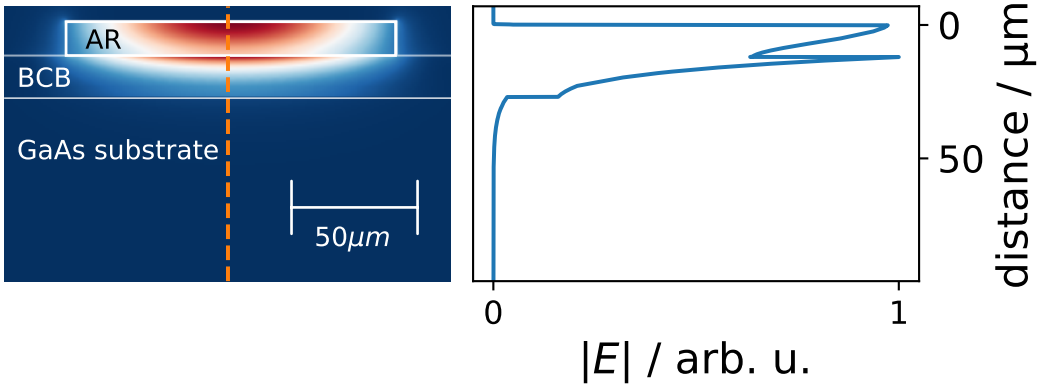

Fig. 3.16 A simulation of hybrid waveguide mode with the effective mode index in between n_{GaAs} and n_{BCB} ($n_{eff} \simeq 2.9$). The overlap of the mode with the AR is 58%, with the BCB region 38% and 1.5% with the substrate. There is no gold in between AR and BCB.

we were not able to quantitatively simulate this hybrid mode. In reality the conductivity of gold below 77 K could be higher[80]. This would lead to a higher scattering time τ (equation 3.13), which would lead to a higher $\mathrm{Im}(\varepsilon)$ (equation 3.8), which in turn would increase the absorption coefficient of the thin metal layer (equation 3.15). Then, the leakage through that layer would be even lower, and the hybrid mode more unlikely to be dominant.

In summary, we simulated a simplified (section 3.6.2) as well as the real geometry of the hybrid waveguide (this section). We saw that it is possible for the optical mode to be at least partially confined to the BCB region. The properties of gold in thin layers and very low temperatures have not been extensively described in literature yet, thus we were not able to simulate the bonding gold layer accurately. If the Drude model holds at terahertz frequencies and if thin gold film reflectivity below 77 K is indeed comparable to that reported at 77 K[80], then it is impossible for the mode to substantially leak into the BCB region and the far-field profile observed in Degl'Innocenti *et al.*[62] cannot be explained by a hybrid BCB-AR mode with low impedance mismatch at the facet.

3.7 Experimental results

3.7.1 BCB waveguide for 4QW designs

One of the aims of this work was to reproduce the results from Degl'Innocenti *et al.*[62] with a different AR design in order to examine the universality of this hybrid BCB waveguide design. We employed the 4 quantum well structure, originally developed by the ETH group[30]. This design is characterised by wide gain bandwidth (spanning more than 600 GHz) and relatively

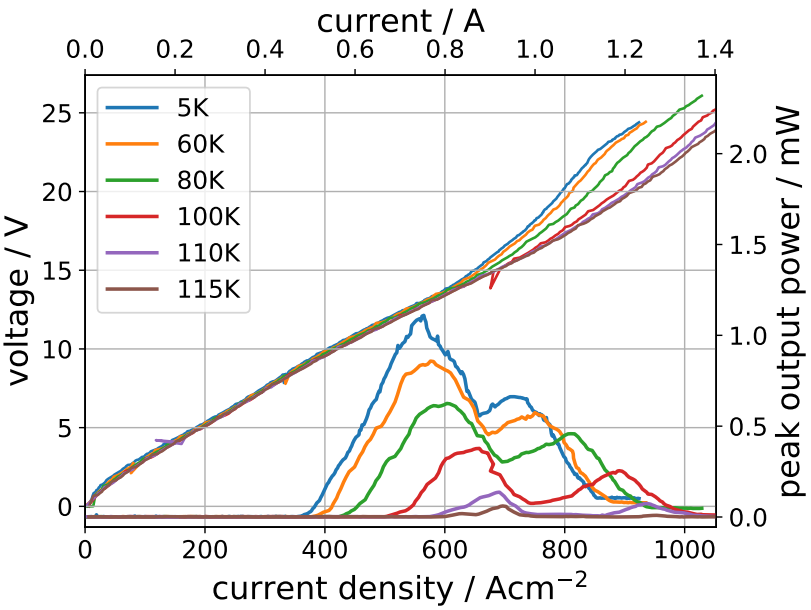

Fig. 3.17 LIV characteristics of a V767 MM device for comparison with BCB waveguides. The device was measured in pulsed mode, with 100 kHz pulses and 2% duty cycle, with a Golay cell detector. The threshold current density of this device at 5 K is 380 A cm^{-2}, and it lases up to 115 K.

high temperature operation (160 K), it therefore exhibits a broader bandwidth and higher T_{max} than the previously BCB-bonded BtC design ($\Delta g \simeq 300$ GHz and T_{max}85 K). We refer to the wafer from which the samples were fabricated as V767.

As seen in Figure 3.10, there seems to exist an optimal gold thickness for which the temperature performance is comparable with MM waveguides and the beam profile is Gaussian-like. We fabricated BCB devices with varying Ti/Au thickness: three devices with 200 nm of Ti/Au (the best beam profile in the previous study), one with 320 nm of metal (the best temperature performance), and one with 70 nm of metal (to explore the limit of extremely thin bonding layers). For reference, we also made a MM laser with approximately 1 µm (±0.1 µm) of gold below the active region.

Some data presented in this section were acquired by Yuqing Wu.

The light-current-voltage (LIV) curves for the reference MM device are shown in Figure 3.17. The threshold current density of 380 A cm^{-2} and the wide dynamic range ($\sim$ 500 A cm^{-2}) are consistent with the original paper reporting this design[30]. Its peak output power is 1.1 mW. The bimodal nature of the emission is corroborated by the spectral data shown in Figure 3.18. There is one emission region centred at 3.05 THz (showing two Fabry-Pérot peaks), and another one at 3.25 THz, showing 3 modes. The higher frequency emission is strongest around 12 V, i.e. at the top of the first peak in the LIV.

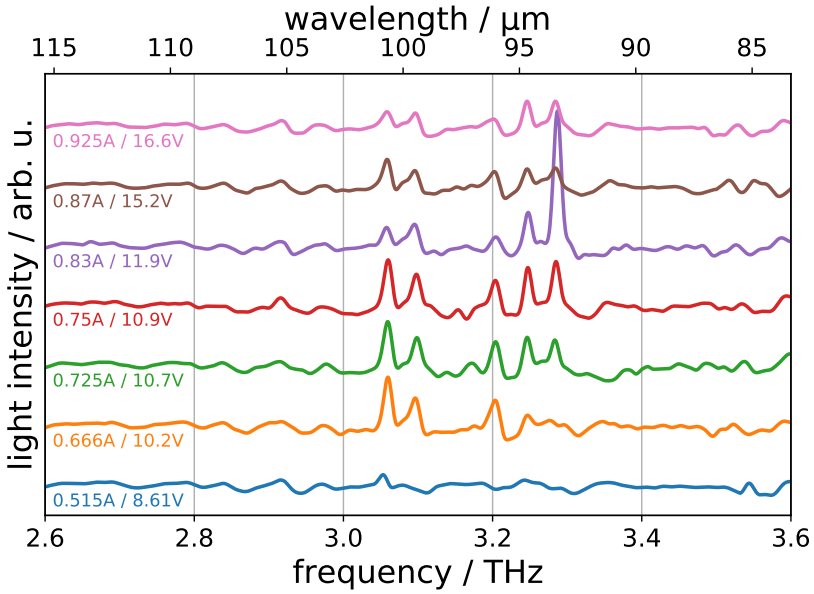

Fig. 3.18 Spectral characteristics of the V767 MM reference device for comparison with BCB waveguides. The device was measured in pulsed mode, with 100 kHz pulses and 2% duty cycle. Its emission is concentrated in two regions, one around 3.05 THz, and another around 3.25 THz.

Figure 3.19 shows the beam pattern of this MM device. It exhibits a broad, dispersive emission: FWHM = 75° in the horizontal direction and 10° vertically. There are two distinct emission maxima, at ($\theta = -7°, \phi = 0°$) and at ($\theta = 15°, \phi = 0°$).

LIV curves, spectra, and far-field patterns of the three BCB QCLs with 200 nm of metal below the AR are reported below. We refer to them as V767 S3, V767 S4, and V767 S5, consistently with Table 3.2.

LIV curves of V767 S3 are shown in Figure 3.20. This device exhibited a $J_{th} = 450\,\mathrm{A\,cm^{-2}}$, and a dynamic range of $220\,\mathrm{A\,cm^{-2}}$. Reduced dynamic range compared to the MM is corroborated by the spectral emission (Figure 3.21). The higher frequency peak (~ 3.2 THz) is only emitted around 11.3 V bias, therefore it does not contribute to a strong LIV feature. It is possible that outside of this region, the transition corresponding to this peak does not achieve gain in the hybrid BCB device. Except for this peak, the hybrid waveguide QCL emits a single mode throughout the dynamic range, centred at 3.1 THz. V767 S3 attained 0.58 mW output power at 5 K, i.e. approximately half of the power of the MM device. This is well within the typical variability of MM waveguides, where weaker output can be caused by non-optimally cleaved facets. S3's $T_{max} = 90$ K, which is 25 K lower than MM. BCB is a worse thermal conductor than GaAs, and we expected the temperature performance to be slightly worse. This will be discussed in more detail in Section 3.7.3.

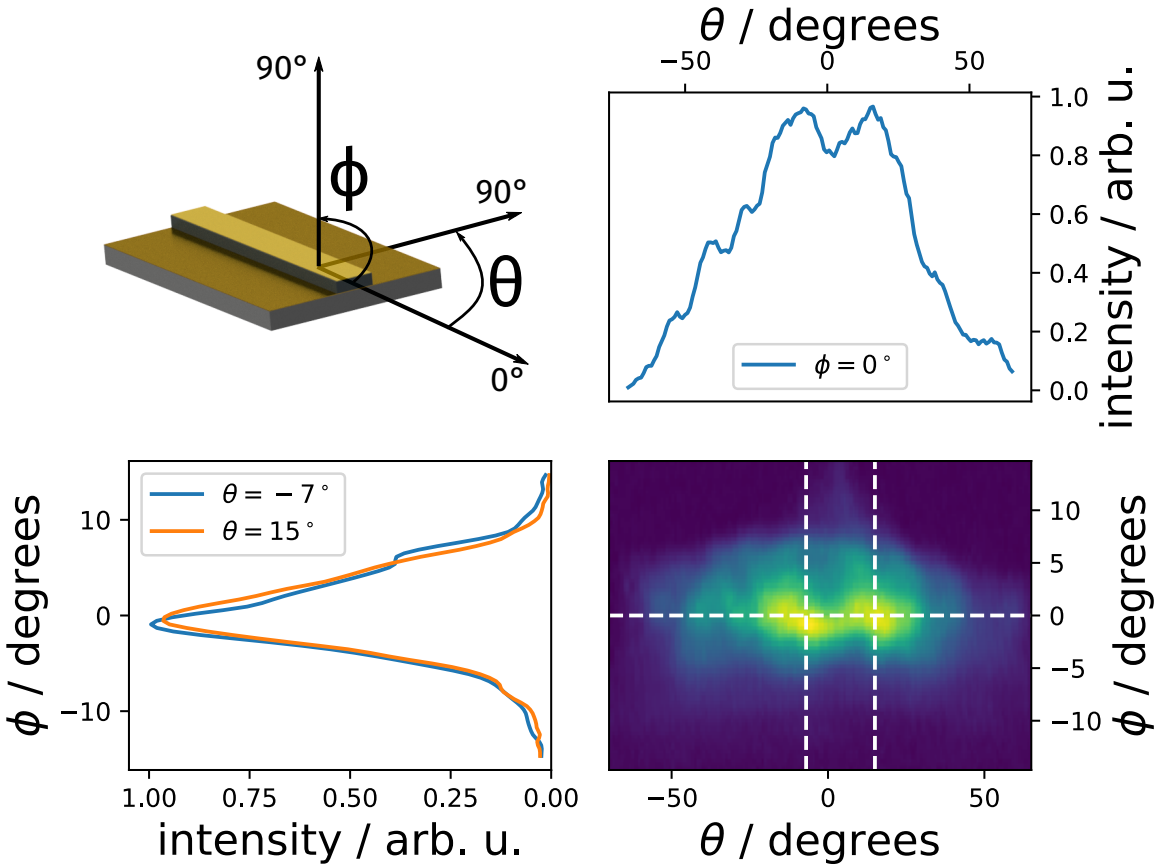

Fig. 3.19 Measured beam intensity from the reference V767 MM sample at 13.7 V bias. The Golay cell detector (with a 2 mm aperture in front) was placed at 16 mm from the facet. FWHM in the in-plane direction (θ) is 75°, FWHM in the vertical direction (ϕ) is 10°. It exhibits two maxima at ($\theta = -7°, \phi = 0°$), and ($\theta = 15°, \phi = 0°$). 1D intensity scans through the maxima are shown to the left and above the surface plot. The beam pattern in θ, with its two main peaks, exemplifies the typical MM waveguide divergence.

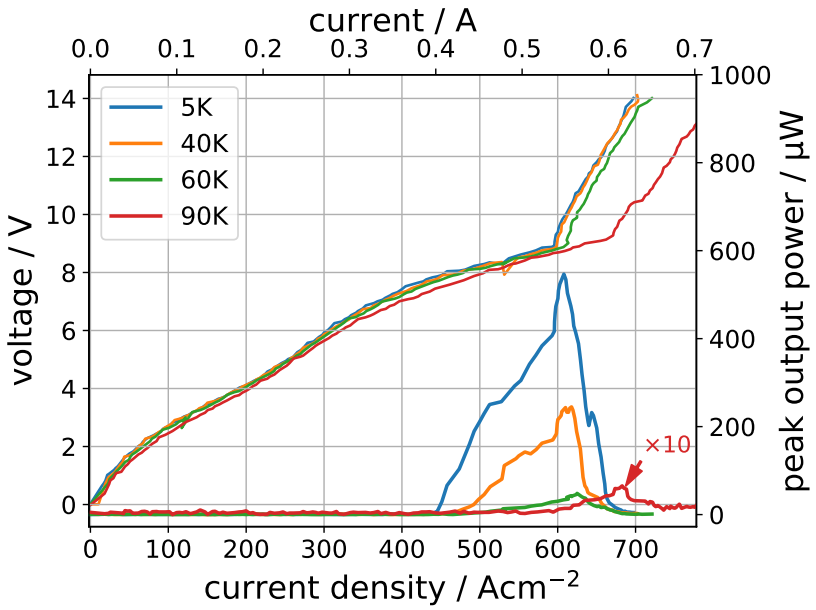

Fig. 3.20 LIV characteristics of the V767 S3 BCB 200 nm device. The hybrid waveguide QCL was measured in pulsed mode, with 10 kHz pulses and 2% duty cycle, with a Golay cell detector. The threshold current density of this device at 5 K was 450 A cm^{-2}, and it lases up to 90 K.

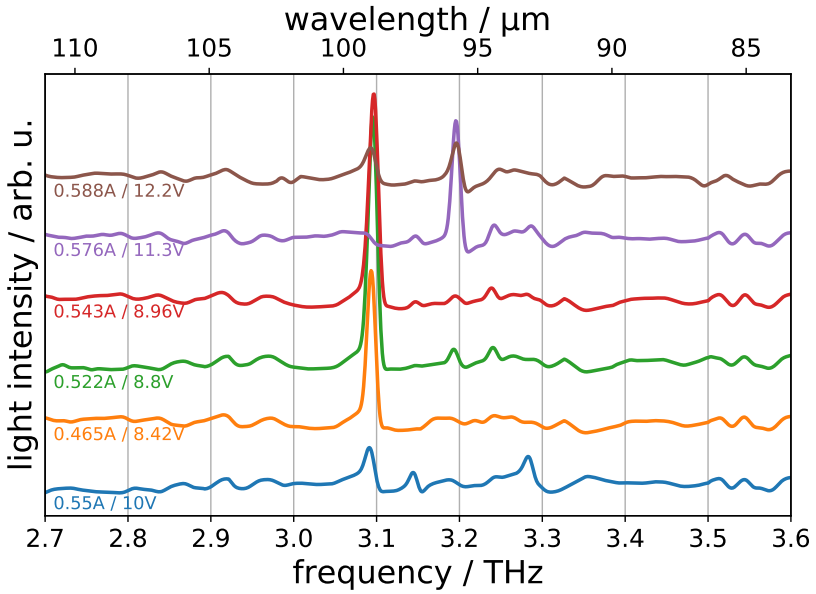

Fig. 3.21 Spectral characteristics of V767 S3 with a 200 nm metal layer. The device was measured in pulsed mode, with 10 kHz pulses and 2% duty cycle. It exhibited single mode emission at 3.1 THz until 9-10 V bias, which then changed to single emission at 3.2 THz.

Figure 3.22 shows the emission beam pattern of the S3 hybrid BCB QCL. It exhibits multi-lobe behaviour with wide emission in both angular and vertical directions. There are two prominent emission peaks, at $(\theta = 32°, \phi = 1.5°)$, and at $(\theta = 43°, \phi = 1.5°)$. The beam might have been shaped by interference effects at the boundary of the substrate, the BCB and the gold layer, although the facet roughness inspected in a scanning electron microscope was not unusual. The single plasmon-like, Gaussian emission of the optimal device from Degl'Innocenti *et al.*[62] was not reproduced in this device. As discussed in Section 3.6, we did not expect a 200 nm layer of gold to allow for a significant mode leakage, and for associated lower impedance mismatch.

LIV curves of V767 S4 are shown in Figure 3.23. This device exhibited a $J_{th} = 500\,\mathrm{A\,cm^{-2}}$, and a dynamic range of $250\,\mathrm{A\,cm^{-2}}$. It attained 0.4 mW peak output power at

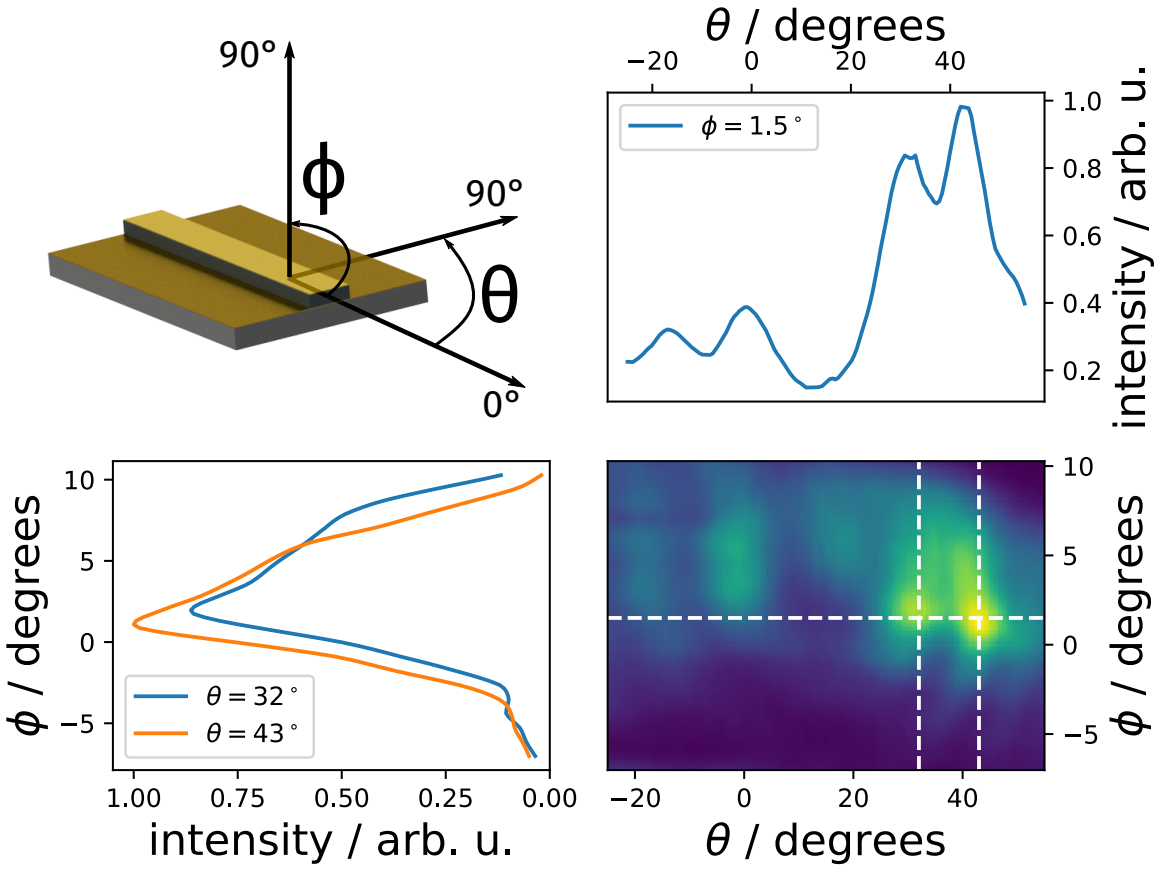

Fig. 3.22 Measured beam intensity from V767 S3 BCB sample with 200 nm thick metal layer at 10.3 V bias. The Golay cell detector (with a 2 mm aperture in front) was placed at 16 mm from the facet. In-plane (θ) emission is highly divergent. It exhibits two prominent maxima, at $(\theta = 32°, \phi = 1.5°)$, and at $(\theta = 43°, \phi = 1.5°)$. 1D intensity scans through the maxima are shown to the left and above the surface plot.

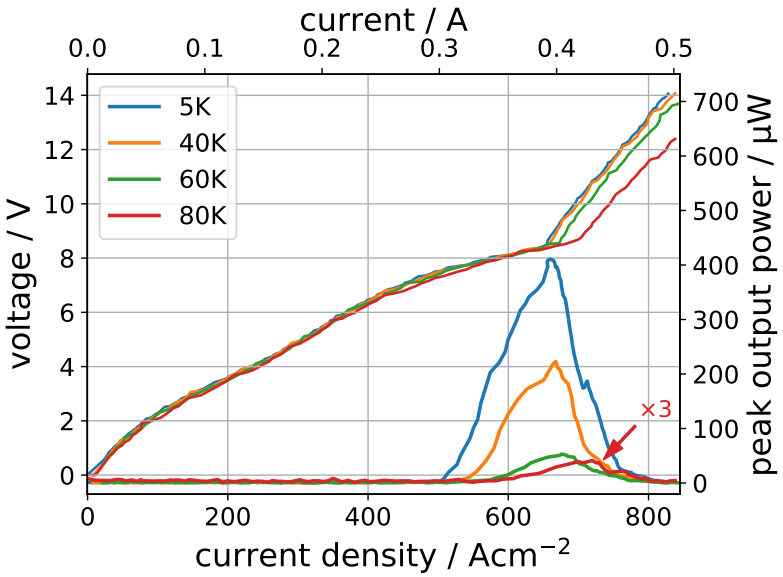

Fig. 3.23 LIV characteristics of the V767 S4 BCB 200 nm device. The hybrid waveguide QCL was measured in pulsed mode, with 10 kHz pulses and 2% duty cycle, with a Golay cell detector. The threshold current density of this device at 5 K was 500 A cm^{-2}, and it lases up to 80 K.

5 K, and a maximum operating temperature of 80 K. S4's performance was only minimally worse than that of S3, thus showing repeatability of the fabrication process. S4's spectra are shown in Figure 3.24. The 3.1 THz emission peak seen previously does not exist, and the device only emits around 3.2 THz. This was the weaker of the two modes emitted by S3, which may explain S4's poorer performance.

Figure 3.25 shows the emission beam pattern of the V767 S4 hybrid BCB QCL. It exhibits multi-lobe behaviour with wide emission in both horizontal (80°) and vertical (13°) directions. There are four prominent emission peaks, at $(\theta = 0°, \phi = 1°)$, at $(\theta = 0°, \phi = 5°)$, at at $(\theta = -35°, \phi = 1°)$, and at at $(\theta = -35°, \phi = 5°)$. Similarly to S3, this emission pattern is MM-like, indicating a strong impedance mismatch at the facets and no leakage into the BCB region of the waveguide.

LIV curves of V767 S5 are shown in Figure 3.26. This device exhibited a $J_{th} =$ 430 A cm^{-2}, and a dynamic range of 300 A cm^{-2}. It attained 0.45 mW peak output power at 5 K, and a maximum operating temperature of 90 K. S5's emission is visibly different from S3 and S4 in the LIV plot (longer operation at peak power, wider dynamic range), which is corroborated by its spectra shown in Figure 3.27. Both peaks (3.1 THz and 3.2 THz) from the reference MM are visible, as well as additional peaks at 3.3 THz and 3.4 THz. QCLs employing this design in the original paper by Amanti *et al.*[30] showed emission

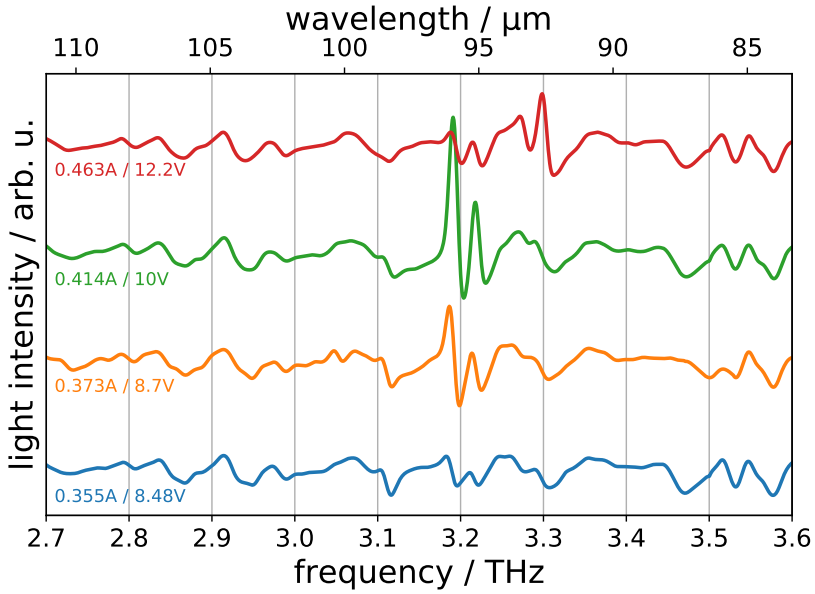

Fig. 3.24 Spectral characteristics of V767 S4 with a 200 nm metal layer. The device was measured in pulsed mode, with 10 kHz pulses and 2% duty cycle. It emitted at 3.2 THz, and possibly at 3.3 THz at high bias (> 12 V).

between 2.8 and 3.4 THz, it is therefore not surprising to see radiative transitions at those high frequencies.

Figure 3.28 shows the emission beam pattern of the V767 S5 hybrid BCB QCL. Its FWHM is 60° in the horizontal direction and 15° in the vertical direction. In contrast to S3, S4, and the reference MM, it only exhibits one prominent intensity peak at $(\theta = -29°, \phi = -2°)$. The emission is still wide, which indicates a MM-like impedance mismatch at the facet. This result suggests that, similar to MM QCLs, a cleanly cleaved facet can result in emission concentrated in one peak.

LIV curves of V767 S6 are shown in Figure 3.29. This was the only working hybrid V767 device with 320 nm of metal below the AR. This device exhibited a $J_{th} = 430\,\mathrm{A\,cm^{-2}}$, and a dynamic range of $370\,\mathrm{A\,cm^{-2}}$. It attained 0.2 mW peak output power at 5 K. S6 performed worse in terms of T_{max} (60 K) than the three 200 nm hybrid waveguides, in contrast to the original paper, where the device with 300 nm Au had the highest maximum operating temperature (95 K, which was 15 K higher than the reference MM). It is likely that the BCB layer's quality in a device, rather than the metal thickness, contributes the most to the temperature performance. The overall poorer performance of this hybrid QCL compared to 200 nm devices could be related to its high operating bias (~ 4 V higher than in previous lasers), which indicates non-optimal electrical properties of S6.

S6's spectra are shown in Figure 3.30. They exhibit two emission peaks, centred at

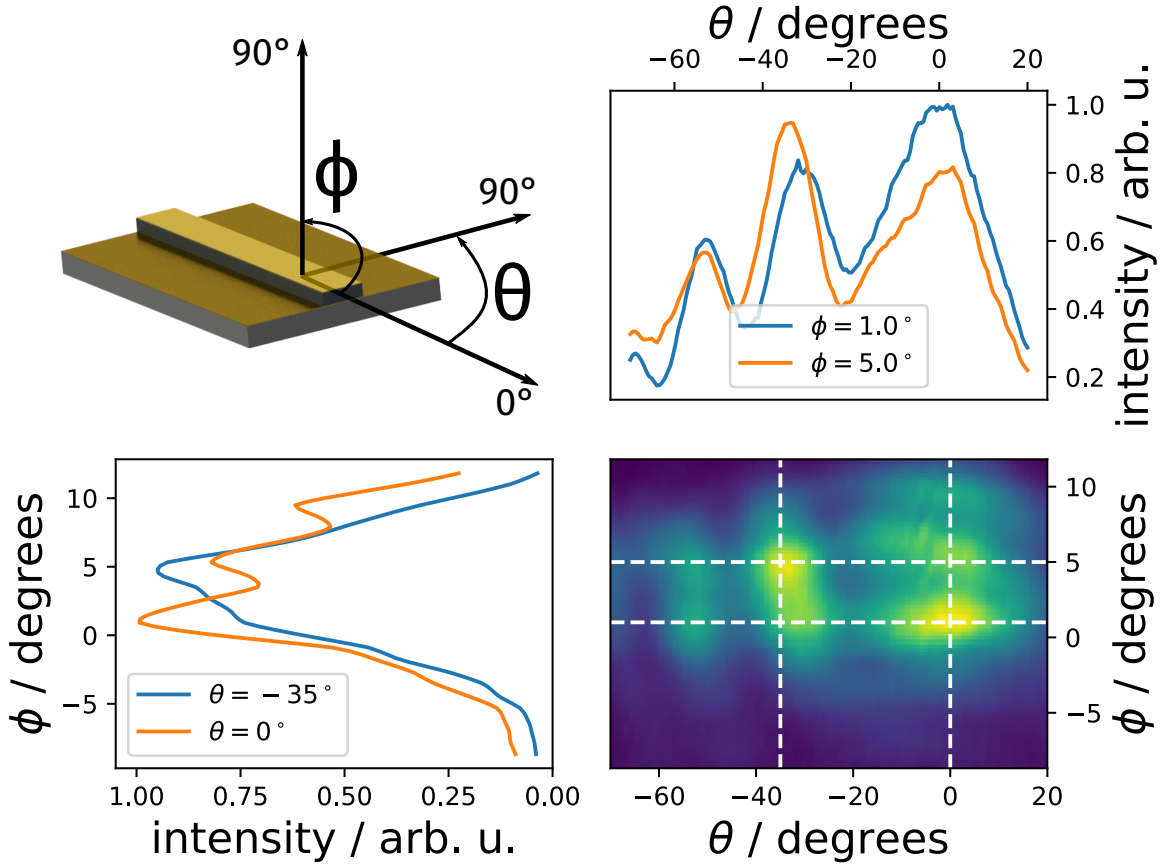

Fig. 3.25 Measured beam intensity from V767 S4 BCB sample with 200 nm thick metal layer at 9.6 V bias. The Golay cell detector (with a 2 mm aperture in front) was placed at 16 mm from the facet. There are four prominent emission peaks, at $(\theta = 0°, \phi = 1°)$, at $(\theta = 0°, \phi = 5°)$, at at $(\theta = -35°, \phi = 1°)$, and at at $(\theta = -35°, \phi = 5°)$. 1D intensity scans through the maxima are shown to the left and above the surface plot.

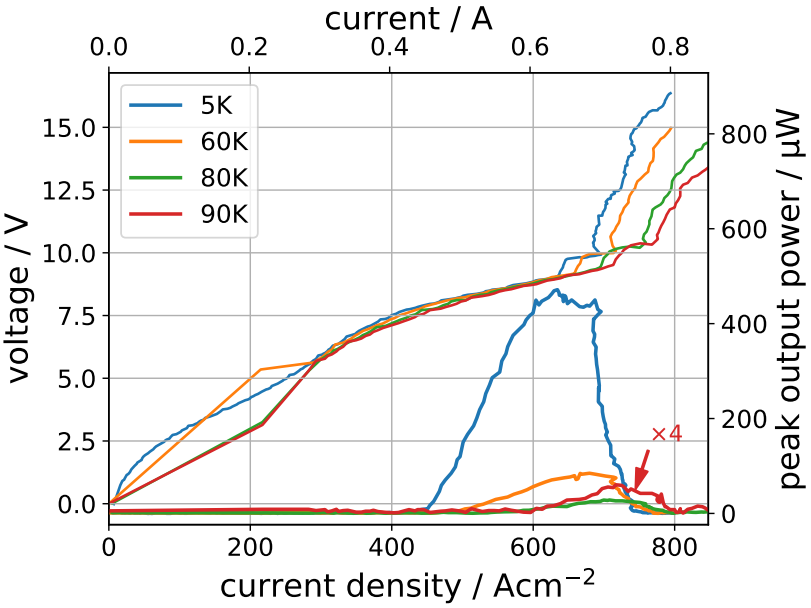

Fig. 3.26 LIV characteristics of the V767 S5 BCB 200 nm device. The hybrid waveguide QCL was measured in pulsed mode, with 10 kHz pulses and 2% duty cycle, with a Golay cell detector. The threshold current density of this device at 5 K is 430 A cm^{-2}, and it lases up to 90 K.

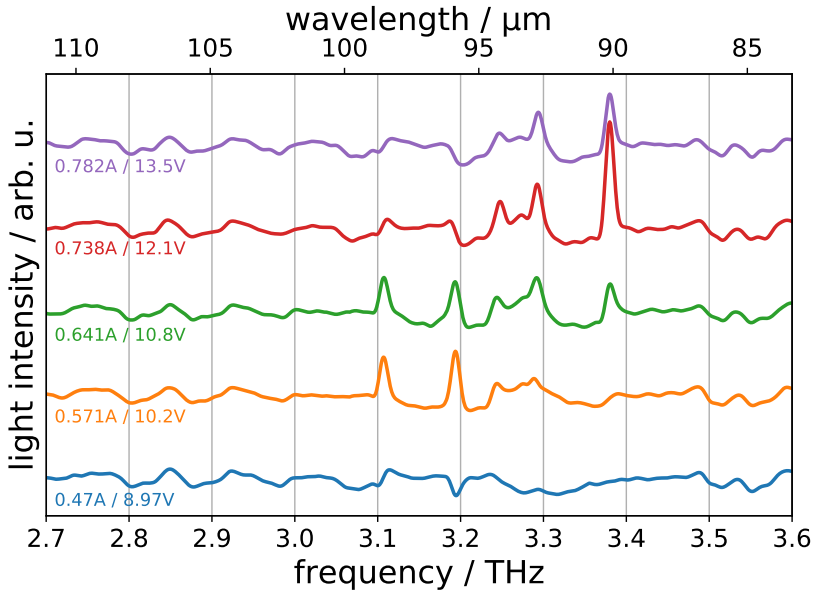

Fig. 3.27 Spectral characteristics of V767 S5 with a 200 nm metal layer. The device was measured in pulsed mode, with 10 kHz pulses and 2% duty cycle. It exhibited a broad emission between 3.1 THz and 3.4 THz, with four clearly distinguishable modes.

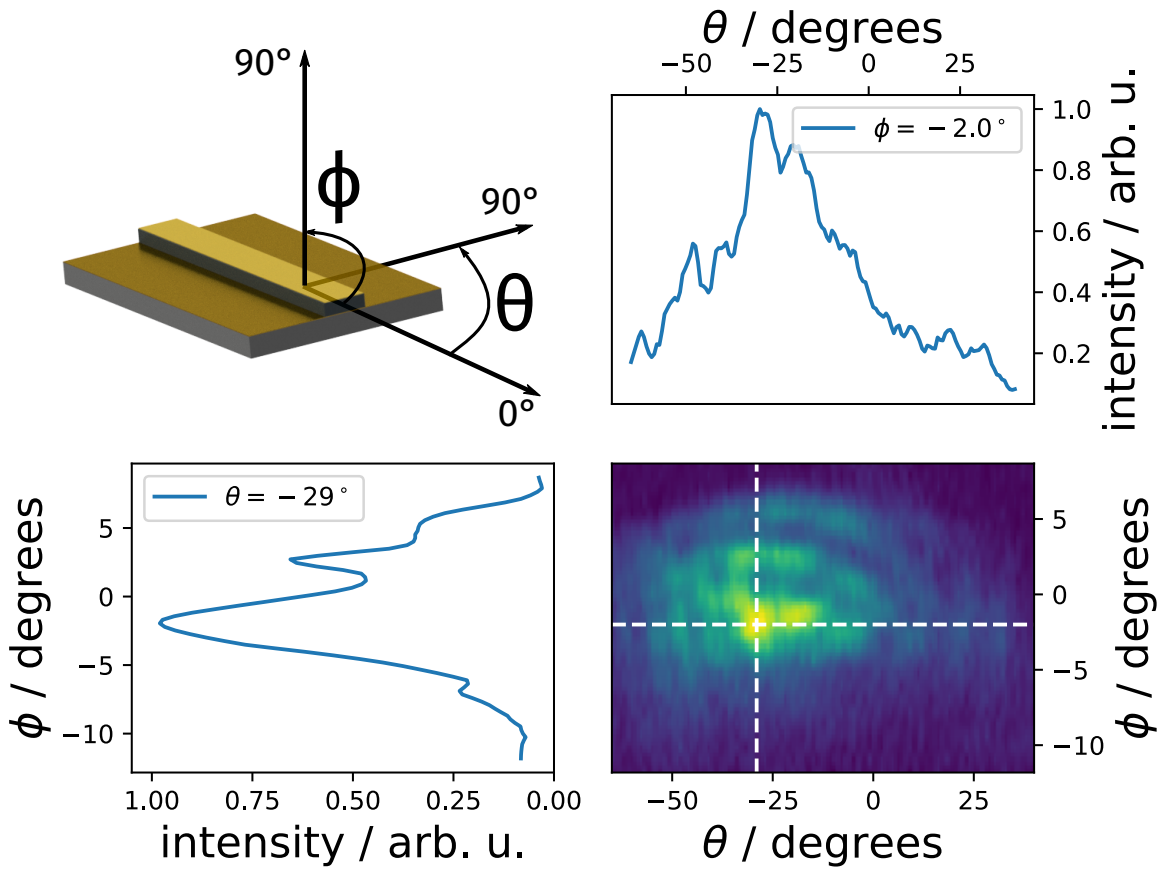

Fig. 3.28 Measured beam intensity from V767 S5 BCB sample with 200 nm thick metal layer at 9.7 V bias. The Golay cell detector (with a 2 mm aperture in front) was placed at 16 mm from the facet. There is one prominent emission peak at $(\theta = -29°, \phi = -2°)$. 1D intensity scans through the maximum are shown to the left and above the surface plot.

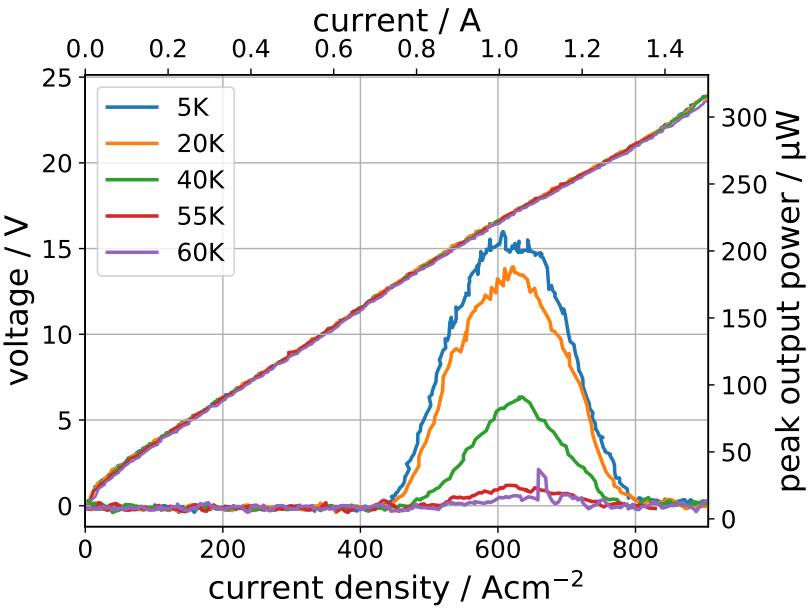

Fig. 3.29 LIV characteristics of the V767 S6 BCB 320 nm device. The hybrid waveguide QCL was measured in pulsed mode, with 10 kHz pulses and 2% duty cycle, with a Golay cell detector. The threshold current density of this device at 5 K is 430 A cm^{-2}, and it lases up to 60 K.

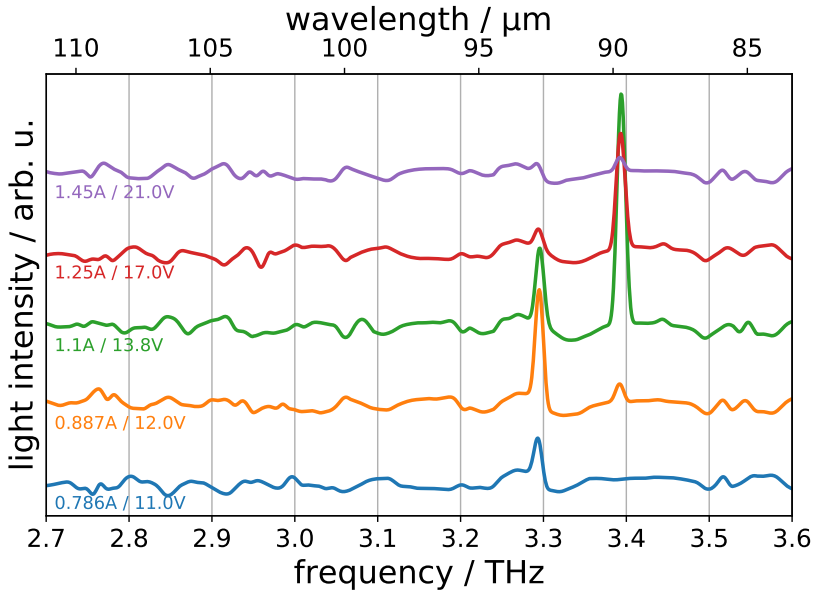

Fig. 3.30 Spectral characteristics of V767 S6 with a 320 nm metal layer. The device was measured in pulsed mode, with 10 kHz pulses and 2% duty cycle. It emitted a single frequency peak at 3.3 THz until $\sim$ 14 V bias, and switched to emitting at 3.4 for higher bias.

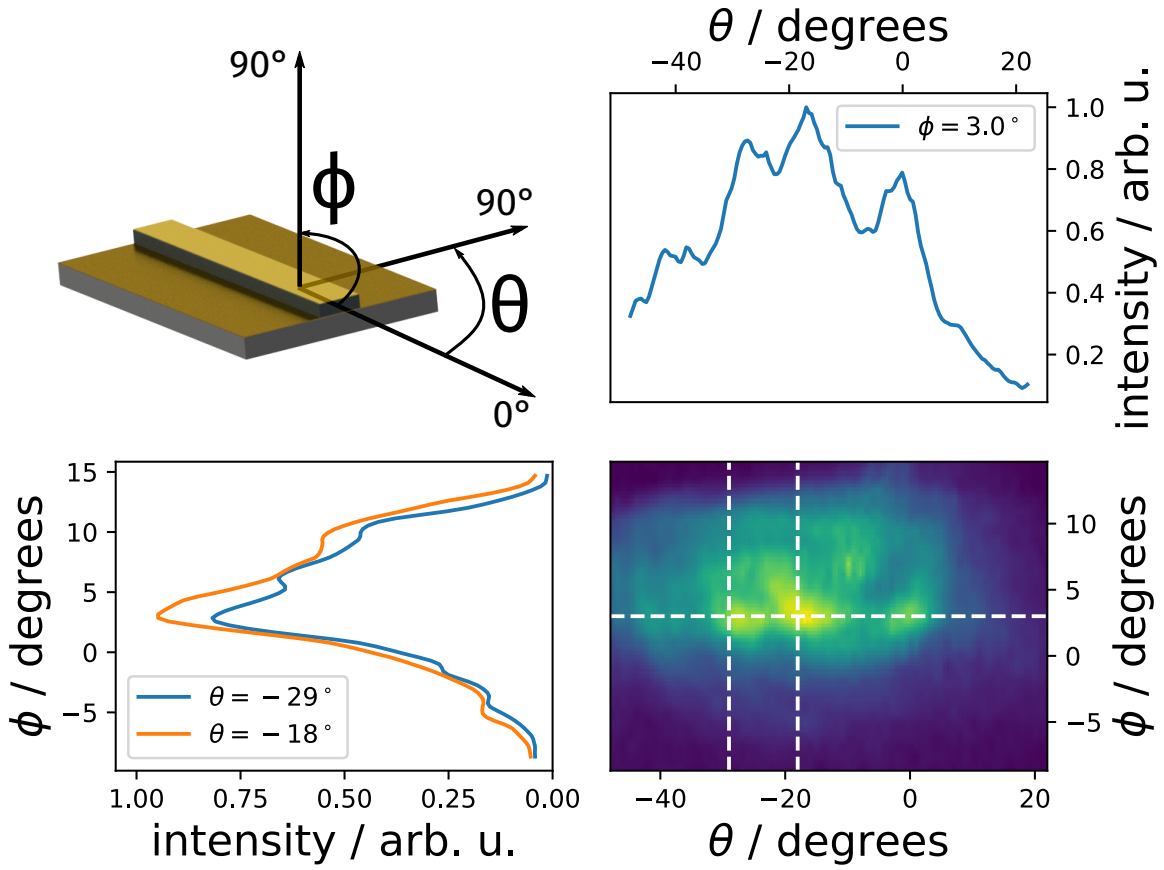

Fig. 3.31 Measured beam intensity from V767 S6 BCB sample with 320 nm thick metal layer at 15.8 V bias. The Golay cell detector (with a 2 mm aperture in front) was placed at 16 mm from the facet. There are two prominent intensity peaks, at $(\theta = -29°, \phi = 3°)$ and at $(\theta = -18°, \phi = 3°)$. 1D intensity scans through the maxima are shown to the left and above the surface plot.

3.3 THz, and at 3.4 THz. The operating frequency seems to switch from the former to the latter at $\sim$ 14 V bias. This is commensurate with the LIV light intensity peak, which is wide at its peak. On its left, the 3.3 THz emission dominates. Throughout the plateau the dominant mode switches to 3.4 THz, and it is the only emitted mode on the right of the device's dynamic range.

Figure 3.31 shows the emission beam pattern of this device. Its FWHM in the angular direction (50°) is smaller than that of the MM device (75°) and it is comparable in the vertical direction (12° BCB vs. 10° MM). It exhibits two prominent intensity peaks, at $(\theta = -29°, \phi = 3°)$ and at $(\theta = -18°, \phi = 3°)$.

Finally, the LIV curves of the BCB QCL with 70 nm of metal below the AR are reported in Figure 3.32. This device exhibited a very high threshold current density ($J_{th} = 680\,\mathrm{A\,cm^{-2}}$)

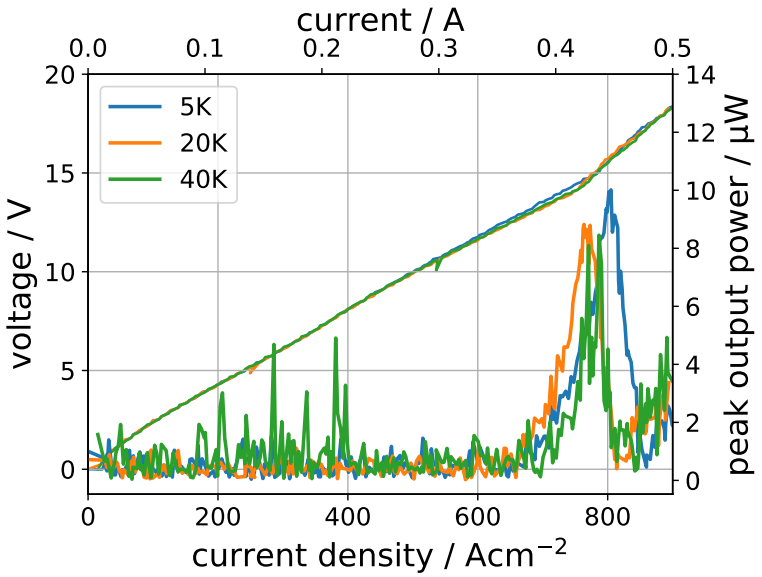

Fig. 3.32 LIV characteristics of the V767 S2 BCB 70 nm device. The hybrid waveguide QCL was measured in pulsed mode, with 10 kHz pulses and 2% duty cycle, with a Golay cell detector. The threshold current density of this device at 5 K is 680 A cm^{-2}, and it lases up to 40 K.

and a narrow dynamic range (150 A cm^{-2}). We confirmed its low temperature performance — both in the original paper and here T_{max} did not exceed 40 K. We attribute the bad performance to too much leakage of the mode from the AR through the thin layer of gold and hence low overlap with the AR. The signal from this sample was also very weak compared to other hybrid BCB QCLs (0.01 mW vs. $>$ 0.2 mW). Due to the very low output power, we were unable to acquire this device's spectra and far-field emission pattern.

In summary, we presented measurement data from five devices fabricated from another BtC active region, in order to further compare hybrid BCB waveguides to MM devices. The temperature performance, as well as the output power, were lower than the reference MM, but only by 20% in the best hybrid devices. This is likely due to BCB's lower thermal conductivity, which we will discuss in Section 3.7.3 along with the threshold current density. Emitted frequency varied between hybrid BCB devices, pointing to possible variability in fabrication. The far-field emission patterns were MM-like, i.e. wide and exhibiting multiple intensity maxima (except for one device, V767 S5). This result confirmed our interpretation of COMSOL simulations in Section 3.6, that gold layers thicker than the skin depth should not allow for mode leakage and improved far-field patterns.

3.7.2 An optimised active region

In the original paper, as discussed in Section 3.4, we attributed the better beam pattern of BCB bonded QCLs to a more uniform mode distribution across the AR and the BCB, and the resulting lower impedance mismatch at the facet. We hypothesise that a thicker active region would lead to better output power (due to higher overlap with the AR) without sacrificing the beam profile — the bonding interface would remain the same, i.e. a thin gold layer and a BCB layer below it. To this end, we fabricated three QCLs from the V773 wafer, which comprised the same AR as V767, but with 230 period repeats times instead of 160. This resulted in the total thickness of 15.6 µm, as opposed to 11.2 µm in V767. It should be noted that the top GaAs layer of V773 had an increased thickness of 300 nm (100 nm in V767) and decreased doping density of $1 \times 10^{17}\,\mathrm{cm}^{-3}$ ($5 \times 10^{18}\,\mathrm{cm}^{-3}$ in V767). The standard values were changed in order to allow more leakage into the BCB layer by reducing the strength of the plasmon, thus allowing for a potentially better output beam pattern. The design and growth of this AR wafer had been carried out before V767 measurements presented above, which disproved the hypothesis about mode leakage for thick Au layers.

The LIV characteristics of the optimised active region reference MM QCL are reported in Figure 3.33. It is a high bias ($V_{\mathrm{th}} \simeq 27\,\mathrm{V}$), high threshold ($J_{\mathrm{th}} \simeq 780\,\mathrm{A\,cm}^{-2}$), and high

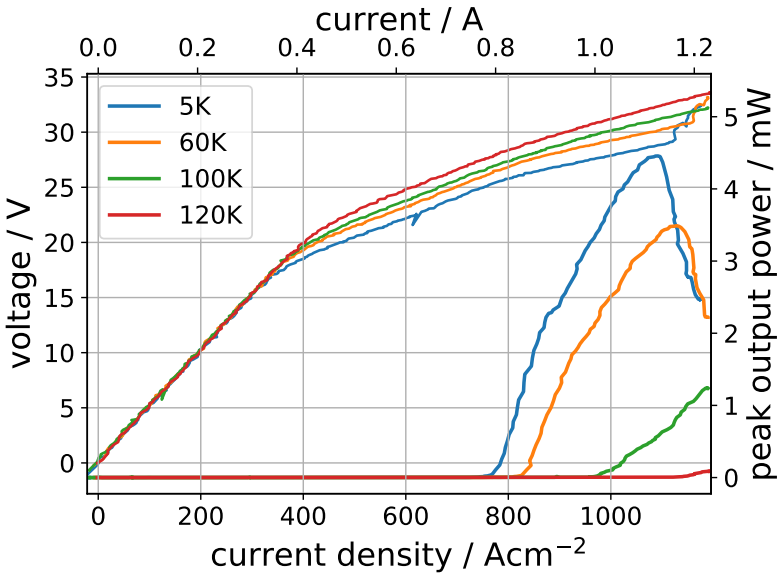

Fig. 3.33 LIV characteristics of a V773 (optimised AR) MM reference device. The device was measured in pulsed mode, with 100 kHz pulses and 2% duty cycle, with a Golay cell detector. The threshold current density of this device at 5 K is $780\,\mathrm{A\,cm}^{-2}$, and it lases up to 120 K.

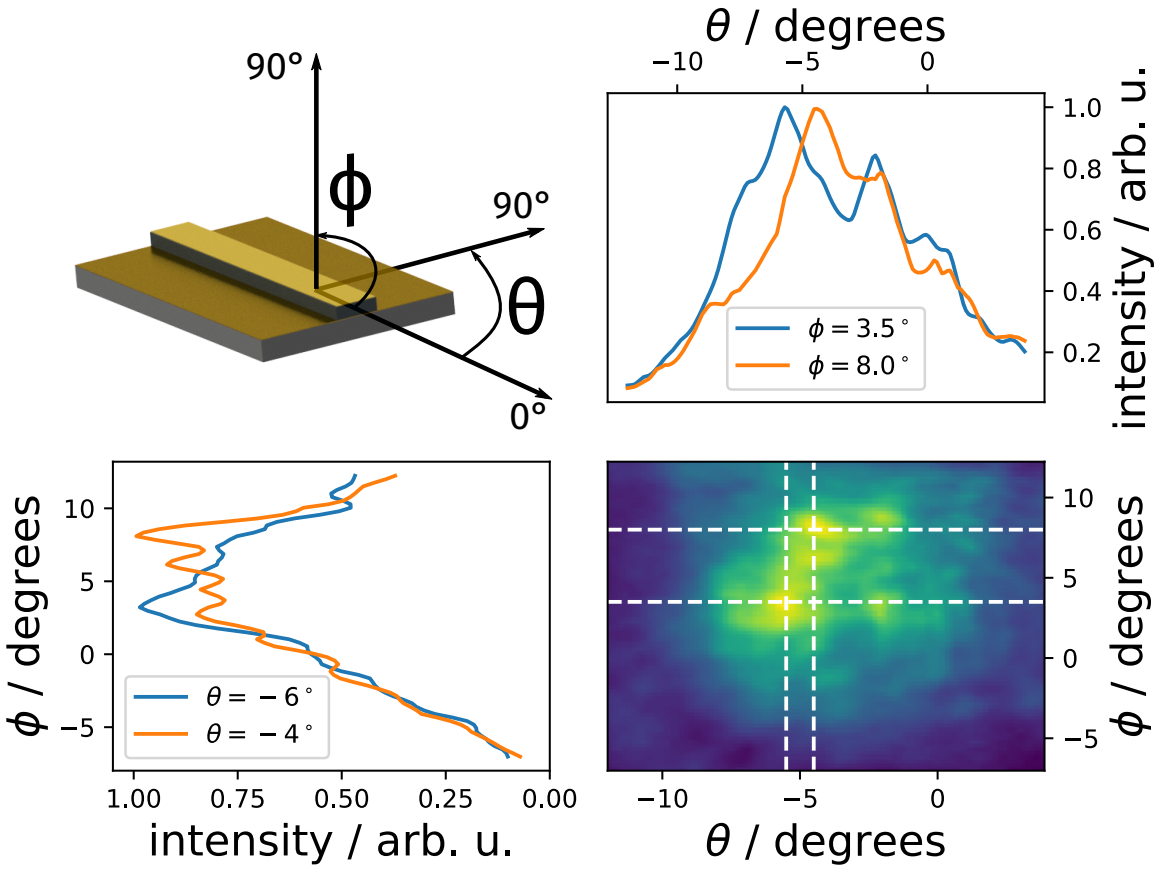

Fig. 3.34 Measured beam intensity from the reference V773 (optimised AR) MM sample at 29.8 V bias. The Golay cell detector (with a 2 mm aperture in front) was placed at 20 mm from the facet. The pattern is highly divergent, with two distinguishable maxima at $(\theta = -6°, \phi = 3.5°)$, and at $(\theta = -4°, \phi = 8°)$. 1D intensity scans through the maxima are shown to the left and above the surface plot.

dynamic range (over 400 A cm^{-2}) device. Its maximum operating temperature was 120 K. We could not measure the laser across its full dynamic range at elevated temperatures because of the high current required to drive the device. Figure 3.34 shows the emission beam pattern of this device. It is a dispersive pattern typical for MM waveguides, without a single sharp emission peak, albeit its FWHM is relatively low in both directions (10° and 15°).

LIV characteristics of V773 S10 are shown in Figure 3.35. It is a hybrid BCB 320 nm device. Its threshold current density was 950 A cm^{-2}, and the dynamic range was greater than 800 A cm^{-2}. We could not measure the whole dynamic range due to the high current required. Both J_{th} and the dynamic range were higher than in the reference MM QCL, but only by about 20% in the case of J_{th}. The unusually high voltage barrier ($\simeq$ 15 V) suggests that the electrical contact quality in this device is poor — potentially indicative of oxides or

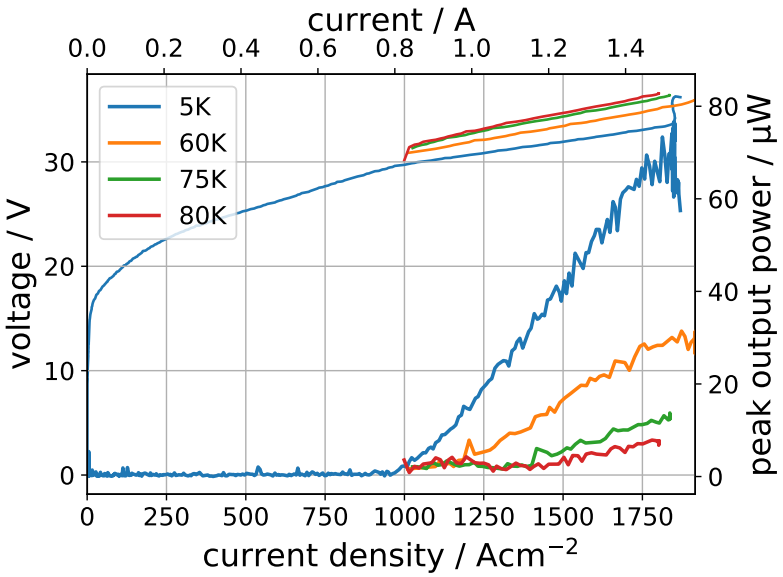

Fig. 3.35 LIV characteristics of V773 S10 (optimised AR). The device was measured in pulsed mode, with 10 kHz pulses and 2% duty cycle, with a Golay cell detector. The threshold current density of this device at 5 K is 950 A cm^{-2}, and it lases up to 80 K. The measurements above 5 K were started at $I = 0.8$ A.

other impurities on the contact surfaces. S10 operated up to 80 K, which is comparable to the earlier devices with a standard 4QW AR, and a good performance given that the AR is 40% thicker. This device attained 0.08 mW peak output power, which again points to fabrication imperfections. Normally, a thicker AR stack would be capable of delivering more power, if efficient cooling is provided.

Figure 3.36 shows the emission beam pattern of S10. It exhibited a Gaussian-like profile, with one central peak at $(\theta = -14°, \phi = 3°)$. Its FWHM was $\simeq 45°$ in one direction (θ) and FWHM$= 8°$ in the other (ϕ). This is another proof (along with V767 S5) that the emission pattern from hybrid BCB waveguides is not inferior to that of MM QCLs.

LIV characteristics of V773 S11 are shown in Figure 3.37. It is a hybrid BCB 320 nm device. Its threshold current density was 1150 A cm^{-2}, and the dynamic range was greater than 800 A cm^{-2}. We could not measure the whole dynamic range due to the high current required. For the same reason, a full temperature sweep was impossible, and we were only able to confirm its operation at 60 K. Both J_{th} and the dynamic range were higher than for S10 and for the reference MM QCL. S11 attained at least 0.01 mW peak output power.

LIV characteristic of V773 S12 at 5 K is shown in Figure 3.37. It is a hybrid BCB 320 nm device. We were only able to carry out a partial measurement at 5 K, after which the ridge

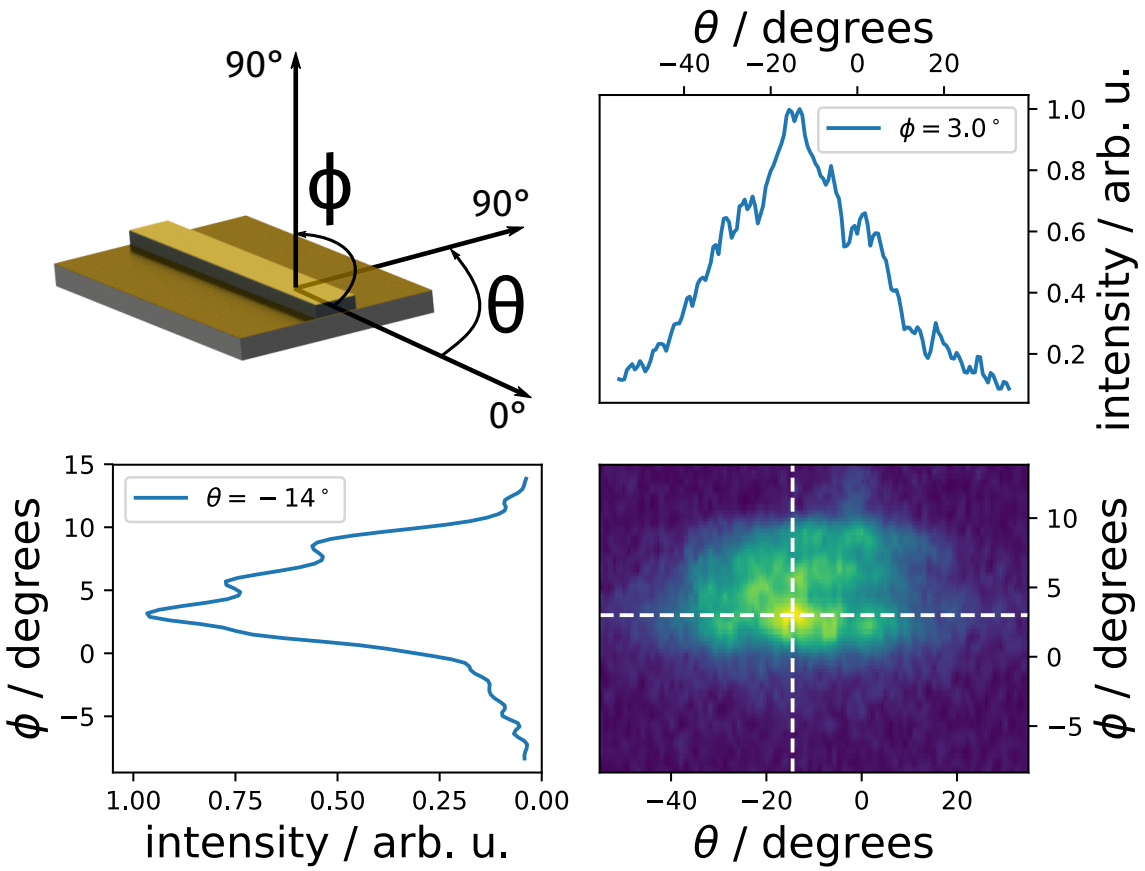

Fig. 3.36 Measured beam intensity from V773 S10 (optimised AR) sample with 320 nm thick layer of metal at 32 V bias. The Golay cell detector (with a 2 mm aperture in front) was placed at 20 mm from the facet. There is one prominent intensity maximum at $(\theta = -14°, \phi = 3°)$. 1D intensity scans through this maximum are shown to the left and above the surface plot.

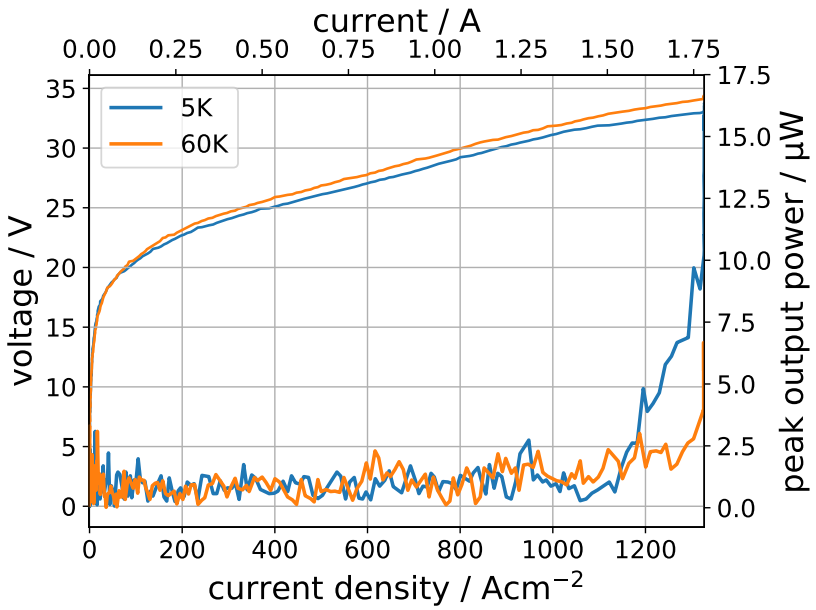

Fig. 3.37 LIV characteristics of V773 S11 (optimised AR). The device was measured in pulsed mode, with 10 kHz pulses and 2% duty cycle, with a Golay cell detector. The threshold current density of this device at 5 K is 1150 A cm^{-2}, and it lases up to 60 K. We were unable to measure the whole dynamic range and operating temperature range due to the limitations of the experimental setup.

delaminated from the substrate. Before it stopped working, S12 attained 1.5 µW peak output power.

In summary, we presented three devices fabricated from an optimised (thicker) 4QW active region. They all had a 320 nm metallic layer below the AR. One device (S10) showed a good temperature performance ($T_{max} = 80$ K) and a far-field emission concentrated in one central peak, which makes it a viable alternative for the MM waveguide. The other two hybrid BCB devices (S11 and S12) did not perform as well, and we were unable to carry out their full characterisation. It should be noted that all three devices were part of fabrication batch II (see Table 3.2), during which we still saw problems with ridge adhesion.

Based on these three devices, it is hard to defend the hypothesis that thicker AR with lowly doped bottom plasmon layer works better in the hybrid BCB waveguide. For Au layers thicker than the skin depth (~ 55 nm) lower doping does not have a beneficial effects, because no mode leakage into the BCB region is expected. The increased AR thickness is likely to be responsible for poorer power performance of the presented lasers, as they require more efficient cooling.

V773 devices also showed that the BCB hybrid waveguide is not optimal for high threshold current active regions. Compared to MM waveguides, BCB samples are more

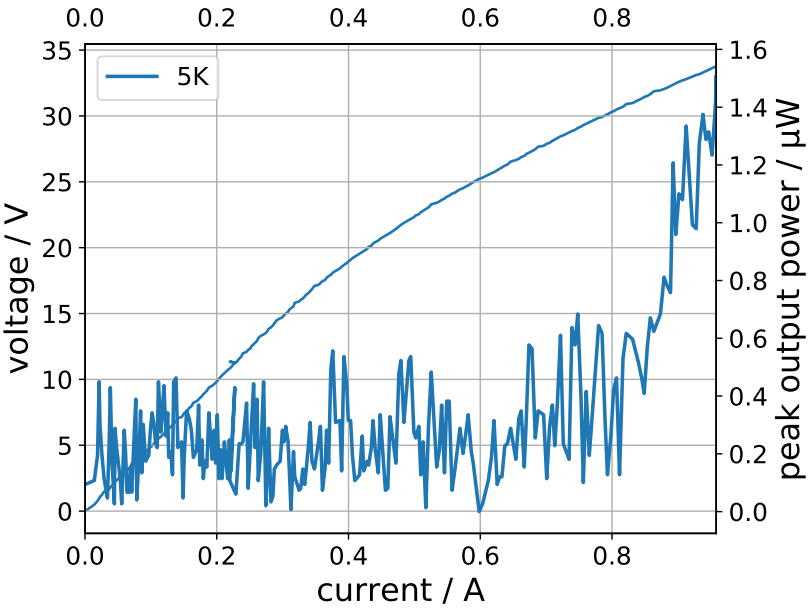

Fig. 3.38 LIV characteristics of V773 S12 (optimised AR). The device was measured in pulsed mode, with 10 kHz pulses and 2% duty cycle, with a Golay cell detector. We only managed to take one measurement at 5 K, after which the ridge delaminated from the substrate.

difficult to cleave cleanly, and obtaining a short ridge is challenging. This in turn puts a minimum driving current requirement on the experimental tools, and requires more wires to be bonded onto the device to sustain high current.

3.7.3 Threshold current density and maximum operating temperature

In the original paper[62], threshold current density of the V706 devices was consistently higher (12–33%) for BCB waveguides than for the MM reference sample, with the exception of the 300 nm Au laser at high temperatures (we reproduced these results in Figure 3.11 in Section 3.4). In Figure 3.39 we present the threshold data for the 4QW AR devices. The lines are least squares fits to $J_{th} = J_0 + A \cdot \exp T/T_0$, where J_0, A, and T_0 are fitting parameters.

The data for V767 QCLs are plotted on the left. All hybrid BCB waveguide devices have a higher threshold (18-40%) than the reference MM across the operating temperature range. On the right, the comparison between V773 MM and V773 S10 device is plotted. In this case, J_{th} of the hybrid BCB QCL was 25% higher than that of MM reference at 5 K. These differences are consistent with the BtC hybrid QCLs from the original paper. The fitted T_0 are between 25 K and 45 K, except for V767 S6 QCL, for which $T_0 = 15$ K. As mentioned earlier, this was generally the poorest performing laser, so it should be considered an outlier.

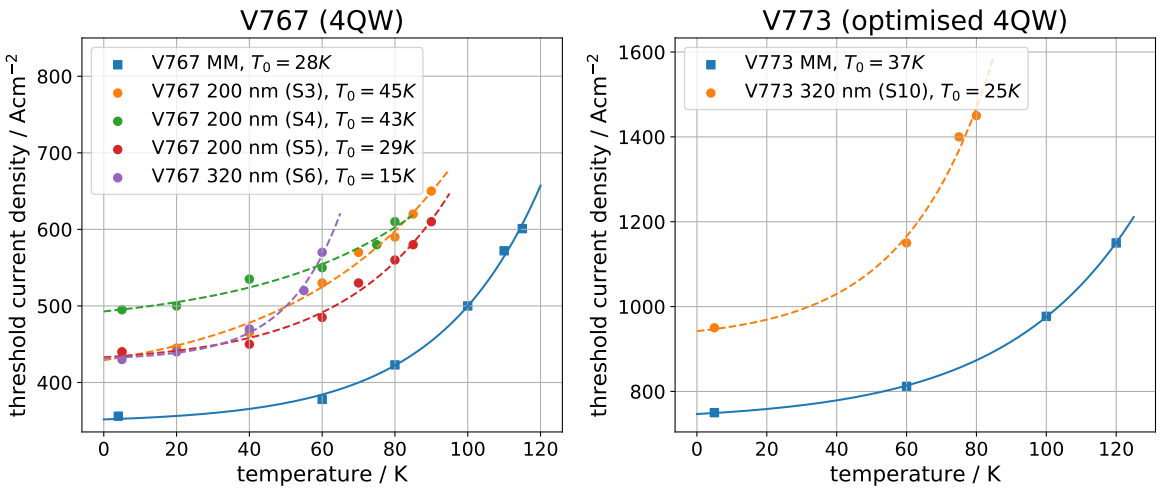

Fig. 3.39 Threshold current density of BCB devices with the 4QW AR. Blue markers and solid lines represent MM references, other colours and dashed lines represent hybrid BCB devices. The lines are least squares fits to $J_{th} = J_0 + A \cdot \exp T/T_0$, where J_0, A, and T_0 are fitting parameters. **Left**: V767 (4QW AR) devices. J_{th} of the hybrid waveguides is 18-40% higher than that of the reference MM waveguide. **Right**: V773 (optimised, thicker 4QW AR) devices. J_{th} of the hybrid waveguide (S10) is 25% higher than that of the reference MM waveguide at 5 K.

Figure 3.40 shows the relationship between the metal layer thickness and threshold current density at 5 K for all discussed hybrid QCLs: V706 from Degl'Innocenti *et al.*[62], as well as V767 and V773 from this work. In case of the BtC AR (V706), J_{th} was higher in all BCB lasers compared to the reference MM device (145 A cm^{-2}). Threshold current density of V767 (4QW AR) lasers varied from 430 A cm^{-2} (the best of 320 nm devices) to 500 A cm^{-2} (S5), compared to 380 A cm^{-2} in the reference MM. Threshold current density of the two measured optimised AR BCB QCLs (V773) was 950 A cm^{-2} and 1150 A cm^{-2}. J_{th} of the reference V773 MM QCL (750 A cm^{-2}) was significantly lower than that of the best performing hybrid waveguide laser. Overall, BCB bonding process seems to have a detrimental effect on J_{th}. We associate higher threshold current with fabrication challenges, for example getting a clean, strong wire bond both on and beside the laser ridge, as well as worse thermal management compared to MM waveguides.

In Figure 3.41 we show the relationship between the metal layer thickness and maximum operating temperature for all discussed hybrid QCLs. V706 lasers showed approximately linear dependence of T_{max} on metal thickness until 300 nm. The device with 300 nm of metal above the BCB attained a higher T_{max} than the reference MM laser (95 K vs. 80 K). Devices with less (40 nm, 150 nm, 220 nm) as well as more metal (420 nm) exhibited lower T_{max} than the reference. In terms of maximum operating temperature, the best V767 (4QW) hybrid

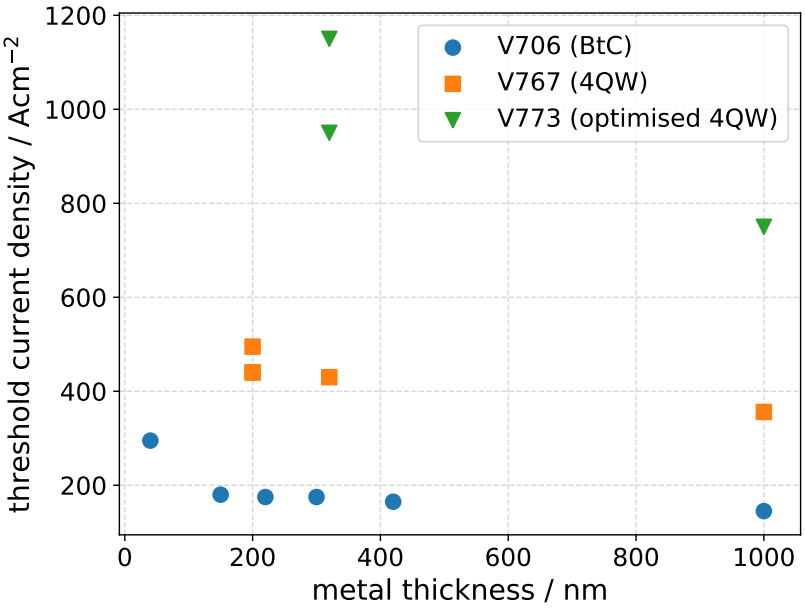

Fig. 3.40 Threshold current density of BCB and reference MM devices at 5 K vs. metal thickness. Blue circles represent the QCLs reported in Degl'Innocenti *et al.*[62], orange squares are the standard thickness 4QW QCLs, and green triangles are the optimised, thicker AR 4QW QCLs.

BCB QCL attained $T_{max} = 90$ K, and the worst operated until 60 K, compared to $T_{max} = 115$ K in the reference MM device. The two thick AR (V773) lasers operated up to 80 K and 60 K respectively, whereas the reference MM device exhibited a maximum operating temperature of 120 K.

The difference in maximum operating temperature in favour of MM waveguides can be qualitatively explained by the difference in thermal conductivity of BCB and GaAs. Dow, the BCB manufacturer, reports the polymer's thermal conductivity to be 0.29 W m^{-1} K^{-1} at 297 K. We were unable to find reported values for lower temperatures, but since it is a dielectric polymer, we assume it is not higher than the value at 297 K. GaAs conductivity varies with temperature, and in the 10-100 K range it takes values between 1000 and 4000 W m^{-1} K^{-1}[61]. It is therefore at least 3 orders of magnitude higher in the operating temperature range of the presented devices. By introducing a more thermally resistive material (BCB) in between the AR and the substrate, a deterioration of thermal sink efficiency is to be expected.

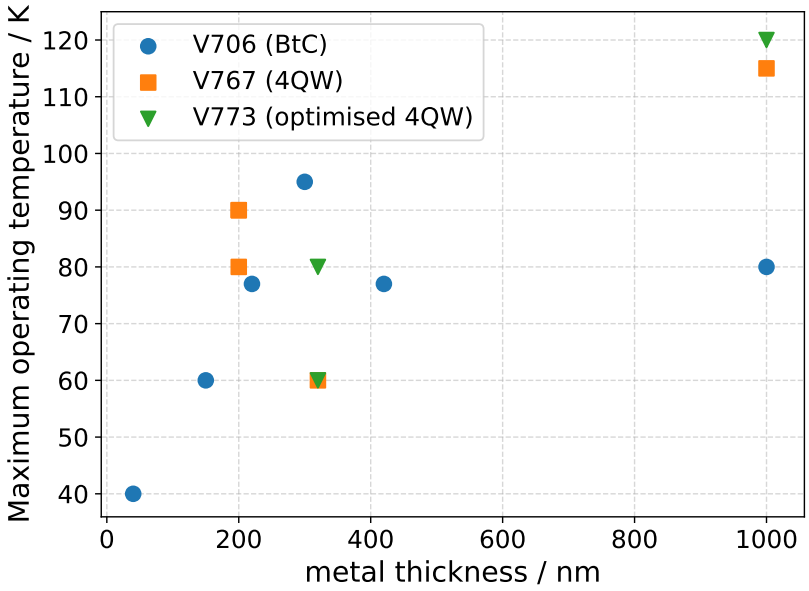

Fig. 3.41 Maximum operating temperature of BCB and reference MM devices vs. metal thickness. Blue circles represent the QCLs reported in Degl'Innocenti *et al.*[62], orange squares are the standard thickness 4QW QCLs, and green triangles are the thick AR 4QW QCLs.

3.7.4 Absolute power

In Table 3.4 we present the absolute peak power of the devices reported in this work as well as in Ref. [62] (absolute power was not published in the paper). In cases where more devices are available (V767 200 nm and V773 320 nm), the device with the highest peak power is reported.

Absolute power was measured as follows. The Golay cell detector was placed as close to the cryostat window as possible, and manually aligned so that its centre was coaxial with the QCL ridge. The distance between the ridge and the entrance cone of the detector was 18-22 mm. A full LIV measurement of the QCL was taken at 5 K. From this measurement, the current corresponding to the maximum output signal was chosen. While the laser was being driven at this current, the position of the detector was adjusted with two micrometre screws in order to find the maximum signal. This value is the absolute power reported below. The detector had been calibrated to an absolute power meter. It should be noted that with an aperture of 11 mm, at 20 mm from the source, the detector captures radiation from $\pm 16°$ from the centre of the sample. As seen in the previous sections, some of the measured lasers were more divergent than that, therefore only a fraction ($\geq 50\%$) of the total power was captured.

Table 3.4 Ridge dimensions of the hybrid BCB lasers along with their size and peak output power.

wafer	metal layer thickness (nm)	dimensions	power
V706	MM	1.79 mm × 140 µm	0.10 mW
V706	420	2.10 mm × 140 µm	0.06 mW
V706	300	1.50 mm × 130 µm	0.06 mW
V706	220	2.05 mm × 130 µm	0.02 mW
V706	150	1.60 mm × 130 µm	0.01 mW
V706	40	1.30 mm × 120 µm	2.50 µW
V767	MM	1.03 mm × 130 µm	1.10 mW
V767	320	1.51 mm × 110 µm	0.20 mW
V767	200	0.82 mm × 110 µm	0.55 mW
V767	70	0.5 mm × 110 µm	0.01 mW
V773	MM	1.29 mm × 80 µm	4.50 mW
V773	320	0.75 mm × 110 µm	0.08 mW

The emitted power from all BCB devices is lower than their reference MM devices. This is likely due to worse thermal management and electrical properties, as explained in the previous section. If mode leakage was a significant factor in hybrid BCB waveguides, we should observe a correlation between metal layer thickness and power, as part of the mode would leak into the BCB or the substrate and the power would be dissipated. Indeed, in the case of BtC V706 devices we can observe this trend. In V767, the 320 nm emits less power than the 200 nm device, but metal thickness in both devices is too high to allow for significant optical mode leakage. Since we were only able to measure BCB V773 waveguides with one metal thickness, we cannot comment on the correlation.

3.8 Conclusions

In this chapter, we investigated an alternative waveguide design for THz QCLs, which employs BCB as the bonding agent in place of thermocompressive metal bonding. We summarised a selection of approaches to improve the beam pattern of MM QCLs reported in literature. We also cited examples of successful employment of BCB in semiconductor processing. The goal of this work was to develop a repeatable fabrication process with a yield higher than in Degl'Innocenti *et al.*[62] (in which the success rate was 10-15%), explain the results from that paper by means of numerical simulations, and reproduce those results with a different QCL AR.

We started by investigating fabrication steps in order to identify the most crucial ones. We developed a process involving dry etching the laser ridges in a reactive ion etching (RIE) tool (waveguides in Reference [62] were wet etched). By improving other fabrication steps (e.g. BCB planarisation, reducing thermal stress) we achieved a much higher yield (100% in our last fabrication batch). We concluded that devices of similar quality to MM can be fabricated using BCB, but great care should be taken in BCB planarisation and its thermal treatment.

We then carried out simulations with an aim to explain qualitatively the two phenomena most likely occurring in hybrid BCB waveguides: the slot effect and mode leakage through a thin metal layer. The simulations suggest that it is very unlikely for the optical mode to leak through layers of gold above 100 nm in thickness.

We characterised various devices with two different active regions and compared them to MM waveguide reference samples, by which we have shown that BCB processing is transferable and not limited to BtC ARs. We were unable to corroborate the hypothesis from Ref. [62] that there is an optimal metal layer thickness at which the beam pattern is less dispersive than in MM waveguides. There are various reasons which could explain the discrepancy between results:

- Change of fabrication operator between the runs. Despite the same protocol, individual skills and habits might have had an influence on results. For example, samples were fabricated at different times of the day, and therefore different air conditions (humidity and temperature).
- Change of cleanroom tools, e.g. hot plates and evaporators.
- Despite dry etching improving yield, it might have introduced other unwanted effects, e.g. QCL ridge walls were smoother when wet etched. This might have influenced the beam shape.
- Finally, the only hybrid waveguide lasers available for comparison were the five reported by Degl'Innocenti *et al.* [62] (there were no repeated devices for the same metal thickness), it is therefore difficult to determine how reproducible those results were.

The temperature performance was worse in all BCB bonded devices as compared to reference samples. This can be explained by lower thermal conductivity of BCB compared to GaAs. The power emitted by the BCB devices was consistently lower than in reference samples, which due to worse thermal management and more difficult facet cleaving. The

usable power can be improved by coupling the lasers to external elements such as lenses or metal waveguides.

Despite its shortcomings, we think that the hybrid BCB waveguide is a viable alternative for the MM waveguide in THz QCLs. It should be noted that the MM waveguide is not a panacea for all THz waveguide difficulties. It has become a standard in literature, but publications rarely report differences between MM devices fabricated from the same AR wafers. Reported performance is often not reproducible in other laboratories, which suggests that the best performing MM waveguides are used in published papers. For example, the Semiconductor Physics group has not been able to achieve $T_{max} = 150\,K$ of the original 4QW laser[30], despite numerous regrowths and fabrication runs.

The most attractive aspect of hybrid BCB waveguides is the possibility of integrating them with other optical elements (e.g. interferometers) in THz circuits. The BCB gives more flexibility than rigid GaAs substrates for placing QCLs and other elements on semiconductor chips. The fact that BCB exhibits low losses in the THz region is a necessary requirement for such a bonding agent. Moreover, the polymer enables MM-like waveguide fabrication without specialised wafer bonders, which might facilitate THz QCL research in some research laboratories.

Chapter 4

Air pocket QCL

4.1 Introduction

In this chapter, we present a modification of the surface plasmon (SP) waveguide with trenches etched at the bottom of the substrate. We will call it the (air) pocket QCL. It is motivated by the need to improve the threshold gain and temperature performance of SP-like waveguides, in order to bridge the gap between SP (high power, low T_{max}) and MM (lower power, higher T_{max}) waveguides.

The efforts to improve operating temperature have been focused on better active region design, magnetic field assisted emission and the use of material systems other than GaAs/AlGaAs[82, 83]. For example, Wade *et al.*[83] employed the then-novel resonant-phonon active region (AR) design and achieved operating temperatures above 200K by applying strong (> 16 T) magnetic fields. They attributed the record-breaking temperature performance to the suppression of inter-Landau-level non-radiative scattering, which helps maintain a population inversion between closely spaced electronic energy levels. See Figure 4.1 for key results from this paper, namely 225 K emission at 3 THz/19.3 T and 215 K emission at 1 THz/31 T.

Valmorra *et al.*[82] reported an InGaAs-based AR design, with quaternary AlInGaAs used for barriers. The latter material was an improvement over the previously used GaAsSb, which is prone to interface asymmetry, which causes strong elastic electron scattering[84]. Because InGaAs/AlInGaAs system is lattice-matched to InP, which has a high conduction band offset, thin barriers are required and therefore interface effects are especially pronounced. By setting the magnetic field to 12 T, where the cyclotron transition is almost resonant with the LO-phonon, the authors achieved an operating temperature of 195 K. See Figure 4.2 for the details of the AR design and the key result.

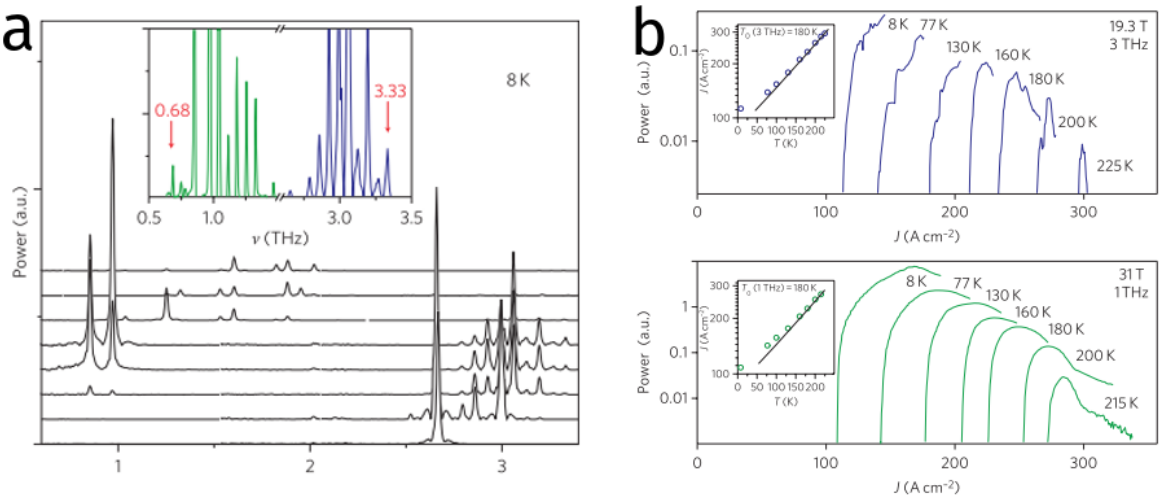

Fig. 4.1 Emission spectra (**a**) and current-intensity curves (**b**) from devices reported by Wade *et al.*[83]. At high magnetic fields ($>$ 19 T), they achieved 225 K lasing at 3 THz and 215 K emission at the very low frequency of 1 THz.

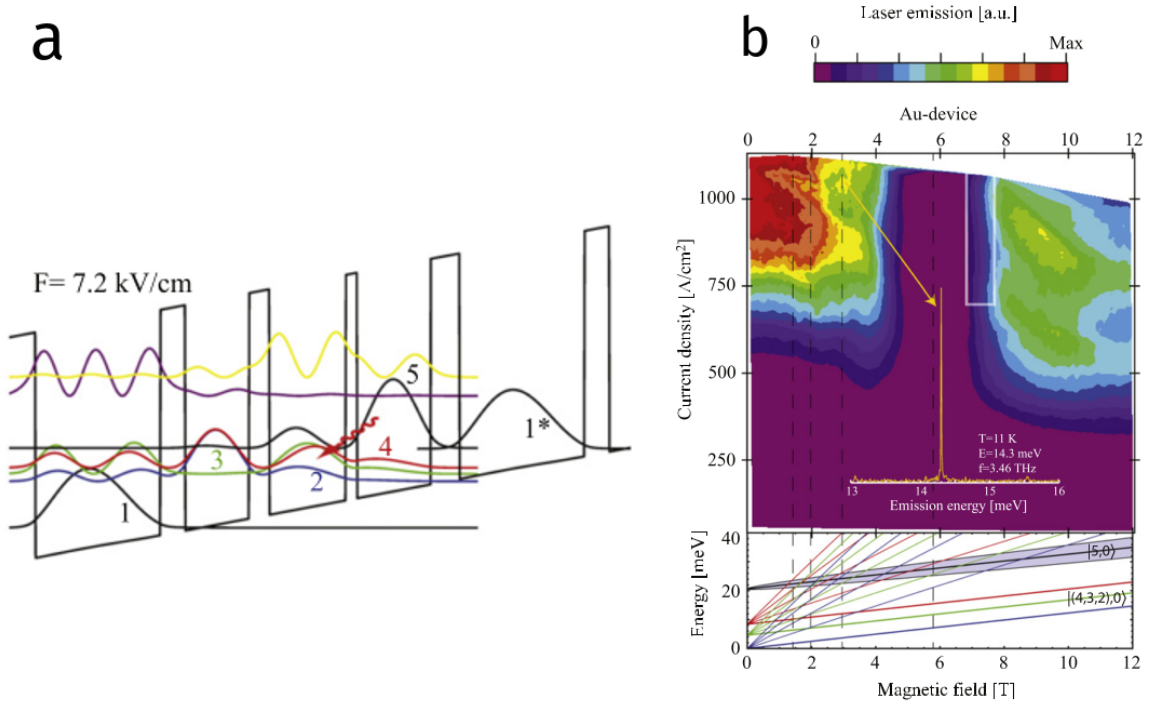

Fig. 4.2 AR design and laser emission intensity as a function of applied magnetic field in InGaAs/AlInGaAs devices by Valmorra *et al.*[82]. **a**: the conduction band diagram of the bound-to-continuum design at the alignment bias. **b**: The emission map shows two regimes of lasing corresponding to Landau levels (mis)alignment. The calculated "Landau fan" of involved levels is shown below. Lasing at $\sim 700\,\mathrm{A\,cm^{-2}}$ prevails up 195 K.

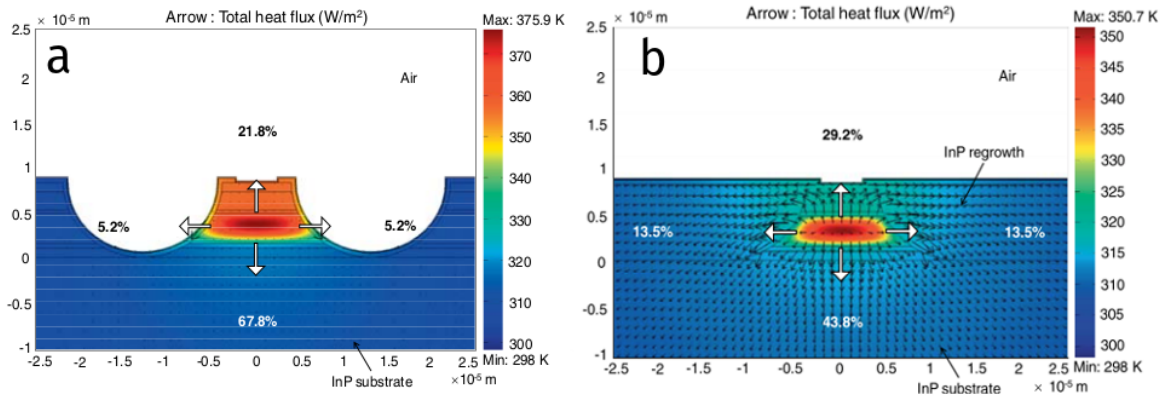

Fig. 4.3 Heat flux simulations for buried mid-infrared QCL waveguides, reproduced from Lee *et al.*[85]. **a**: The laser ridge is exposed to air/vacuum on the sides. Maximum simulated temperature in the AR is 375.9 K. **b**: The laser ridge is fully buried in InP material. Maximum simulated temperature in the AR is 350.7 K.

In mid-infrared QCLs, it has long been standard practice to use buried waveguides. Instead of exposing the laser ridge to air/vacuum on the sides and on the top, a buried ridge is surrounded on all sides with a semiconductor material. This allows for mode confinement in the AR without lossy metallic layers, and improves heat extraction. Thermal properties of buried waveguides were studied by Lee *et al.*[85]. In Figure 4.3, we reproduce their simulated heat flux plots for a waveguide with vacuum on the sides of the ridge (Fig. 4.3a), and for a fully buried InP waveguide (Fig. 4.3). In the fully buried case head extraction is more efficient, which results in lower temperature in the AR (350.7 K vs. 375.9 K in the partially buried case).

Fully buried waveguides are not used in THz QCL because it would involve MBE growth of impractically thick layers (comparable to the emitted wavelength of 50-100 µm). Alton *et al.*[86] reported a partially buried waveguide. In the growth direction it was a typical SP waveguide. However, instead of etching a ridge, the authors defined a metal strip on top of the structure, which confined the plasmonic mode to 100 µm laterally (i.e. similar width to a standard THz ridge). To ensure current flow in the same confined region, they carried out ion implantation to the sides of the metal strips (see Figure 4.4a). Due to reduced losses and improved heat extraction, the buried waveguides achieved better temperature performance than a reference SP QCL (see Figure 4.4b).

We propose a waveguide approach at increasing T_{max}. This is done by reducing waveguide losses, increasing mode overlap with the AR, and improving thermal management of the waveguide. The concept of the pocket QCL is depicted in Figure 4.5. Instead of a uniformly polished substrate, there are three square air "pockets" or "trenches" etched directly below

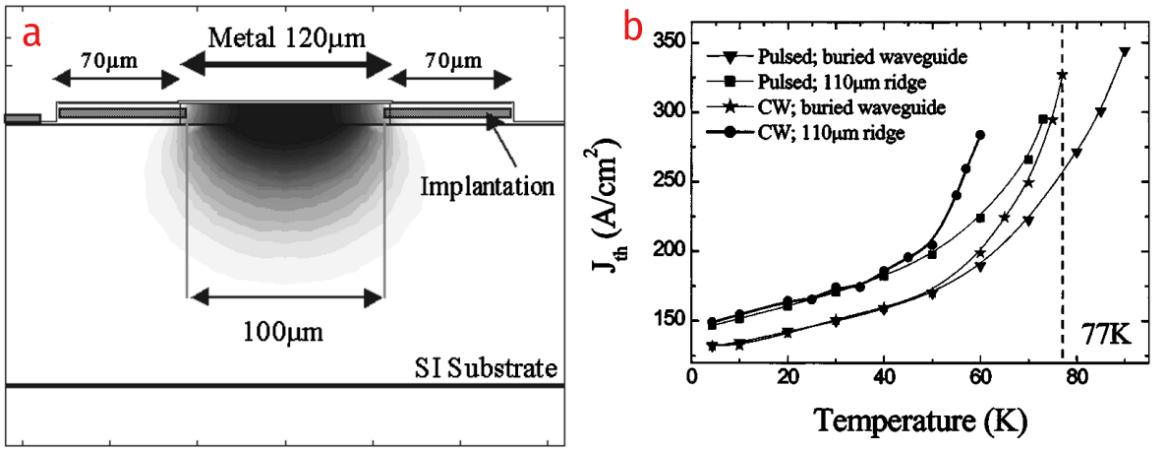

Fig. 4.4 **a**: Schematic of a buried SP waveguide employed by Alton *et al.*[86]. A metal strip was defined on top of the MBE-grown wafer, and the sides of the "virtual ridge" were implanted with ions. **b**: J_{th} and temperature performance comparison between a standard SP and a buried waveguide. J_{th} was lower and T_{max} was higher for the buried structure.

the AR. Their sides (a) are 30-50 μm and their purpose is to push the optical mode up from the metalised back side of the substrate, thus reducing the losses and increasing the overlap with the AR, when compared to a standard SP waveguide. The distance between the centres of adjacent trenches (d) is 55 μm. In order to further reduce losses, the doping of the layer below the AR is reduced from the standard 2×10^{18} cm^{-3}. Thermal management is further improved by reducing the thickness of the substrate (i.e. minimising the distance between the heat sink and the AR).

This chapter has the following structure: first, the role of the bottom plasmon is discussed in Section 4.2. Simulations (which employ the Drude model, described in the previous chapter) are presented and discussed in Section 4.3. Subsequently, we describe the fabrication and process development in Section 4.4, and conclude the chapter in Section 4.5.

4.2 The role of bottom plasmon

All SP THz QCLs have an n-doped layer below the active region. Its function is twofold: to provide an electrical path for electrons through the laser ridge and to help confine the mode inside the AR. The authors of the first THz QCL paper chose the doping density of 2×10^{18} cm^{-3}, which yielded "a good compromise between absorption losses and overlap with the active material"[13]. Let us define the terminology used to describe waveguide simulations, in order to explore this compromise and its possible modifications.

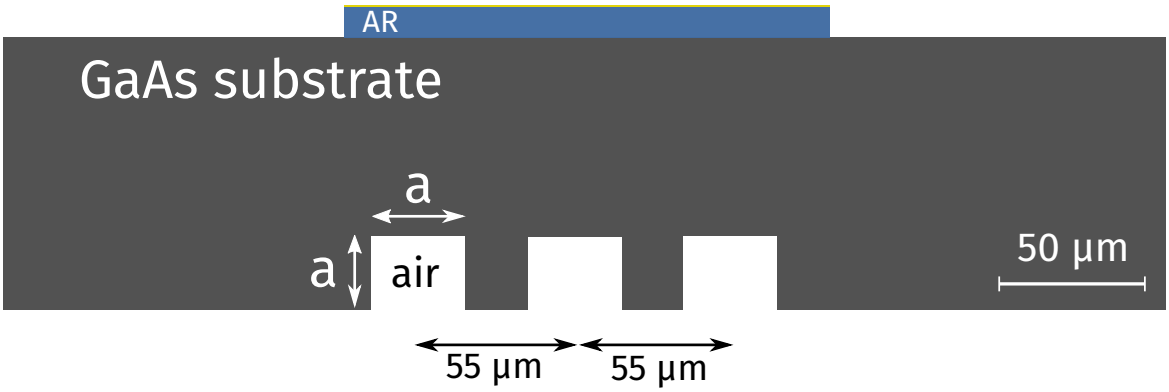

Fig. 4.5 Air pocket QCL concept. The three "pockets" at the bottom of the substrate are meant to push the optical mode up to allow for fabrication of very thin substrates and reduction of bottom plasmon doping.

The figure of merit that we will use in this chapter is the threshold gain:

$$g_{\text{th}} = \frac{\alpha}{\Gamma} = \frac{\alpha_w + \alpha_m}{\Gamma}, \tag{4.1}$$

where α_w are waveguide losses, α_m are mirror losses, and Γ is the overlap of the mode with the active region:

$$\Gamma = \frac{\int_{\text{AR}} \|E\| dV}{\int \|E\| dV}, \tag{4.2}$$

where $\|E\|$ is the norm of the electric field. The integral in the numerator is taken over the active region only, and the denominator is over the whole structure. $\Gamma = 1$ would describe a mode completely confined to the AR. All three parameters in equation 4.1 are determined by the waveguide structure.

In this chapter, we will be mainly focusing on waveguide loss α_w and therefore we define $g_{\text{th}} = \alpha_w/\Gamma$ unless stated otherwise. Mirror loss, α_m, for SP waveguides can be approximated with the effective index method, i.e. the reflectivity R is the Fresnel reflection coefficient of a GaAs/air interface[87]. Numerical finite element method calculations give similar results of $R \simeq 0.32$[77]. The mirror loss is given by

$$\alpha_m = -\frac{\ln R}{L}, \tag{4.3}$$

where L is the length of the cavity. For a typical cavity length of 1.5 mm, $\alpha \simeq 7.6\,\text{cm}^{-1}$. We will assume that the simulated devices have the same lateral dimensions and reflectivity. In fact, as the substrate thickness is significantly reduced in the proposed device, the reflection

coefficient increases (MM waveguides have $R \geq 0.5$ in the THz range)[77]. Therefore α_m should be more favourable (lower) in the air pocket waveguide.

Waveguide losses (α_w) arise mainly from free carrier absorption in metal and semiconductor layers. For wavelengths above 5 THz (equivalent to ~ 20 meV) at elevated temperatures the phonon absorption starts to be significant ($\hbar\omega_{\mathrm{LO}} \simeq 36$ meV in GaAs), but the THz QCLs currently emit at $1.2-5$ THz[64]. The values of α_w presented in this chapter are calculated from the simulated effective mode index

$$n_{\mathrm{eff}} = n + i\kappa = n + i\frac{\lambda\,\alpha_w}{4\pi}. \tag{4.4}$$

In the following simulations we have simplified the calculations by ignoring the lateral metal contacts, which also induce lossy surface plasmons. Firstly, if the contacts are placed far enough from the ridge, the coupling of the lasing mode with the plasmons is minimal. Secondly, the *air pocket* structure proposed in this chapter employs the same contacts, therefore they should neither improve nor deteriorate the performance compared to SP QCLs.

4.3 Waveguide simulations

To simulate air pocket waveguides, we used the same COMSOL module (RF), physics ("Electromagnetic Waves, Frequency Domain") and study ("Mode analysis") as in Section 3.6 in the previous chapter. Refer to Table 3.3 for the list of parameters used in the model. All simulations were carried out for 3 THz. Results should not be significantly different within the THz range.

As already mentioned in Section 4.2, $2\times10^{18}\,\mathrm{cm}^{-3}$ is the widely used doping density of the bottom plasmon layer. Indeed, neither lower nor higher doping lead to better performance. This is illustrated in Figure 4.6 for a typical bottom plasmon layer thickness of 700 nm in a conventional SP waveguide. As the doping decreases, the overlap increases slightly due to a lower strength of the bottom plasmon. The overlap increases from approximately 0.15 at $3\times10^{18}\,\mathrm{cm}^{-3}$ doping to ~ 0.21 at $4\times10^{17}\,\mathrm{cm}^{-3}$ — a difference of 40%. However, the attachment of the mode to either side of the bottom plasmon is weaker, therefore the field overlap with the layer itself is higher. This leads to more free carrier loss and consequently to a higher gain threshold. At its minimum, for $n = 2\times10^{18}\,\mathrm{cm}^{-3}$ the loss is $\sim 5.5\,\mathrm{cm}^{-1}$. This increases to $\sim 14.5\,\mathrm{cm}^{-1}$ for $n = 4\times10^{17}\,\mathrm{cm}^{-3}$ (a 2.6-fold increase). In Figure 4.7, we show cross-sections of the simulated optical mode for three different doping values. If the doping is too high ($4\times10^{18}\,\mathrm{cm}^{-3}$), the mode attachment to the bottom plasmon is more lossy. If the

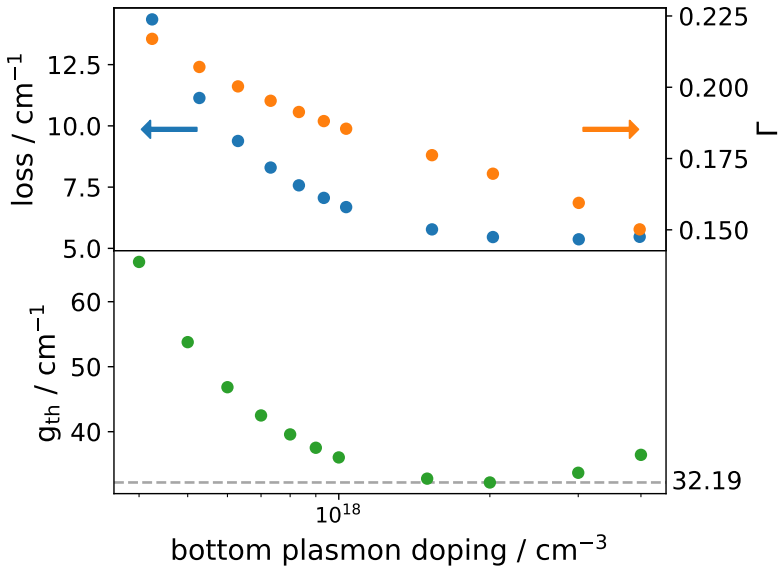

Fig. 4.6 Simulated threshold gain and its constituents for different doping densities of the bottom plasmon layer in a conventional SP waveguide. At the top, loss (blue markers, left axis) and overlap (orange markers, right axis) are plotted. At the bottom, their ratio (figure of merit) is shown in green. In line with the first THz QCL report[13], the minimum is found at $2 \times 10^{18}\,\mathrm{cm}^{-3}$.

doping is too low ($7 \times 10^{17}\,\mathrm{cm}^{-3}$), the mode is not attached well and its overlap with the AR is lower. $2 \times 10^{18}\,\mathrm{cm}^{-3}$ is the optimal trade off between the mode attachment and losses.

For the doping densities lower than $1 \times 10^{17}\,\mathrm{cm}^{-3}$ the real part of the dielectric constant in the bottom layer becomes positive and it loses its plasmonic properties. A slot waveguide emerges, where a mode is confined to a subwavelength region of lower refractive index (bottom plasmon layer) which is sandwiched between regions of higher index (AR and substrate)[68]. This phenomenon is illustrated in Figure 4.8 for a standard SP waveguide with a 200 µm thick substrate and a 700 nm thick bottom plasmon with reduced doping. The slot waveguide effect leads to even larger overlap of the mode with the doped region and more loss — the mode intensity in the doped region is twice as high as in the AR. Most of the mode leaks out into the substrate, hence very low $\Gamma \simeq 0.06$. To the right of the optimal doping from Figure 4.6, for a doping greater than $2 \times 10^{18}\,\mathrm{cm}^{-3}$, the loss due to the bottom plasmon increases again while the overlap further decreases.

SP waveguides usually employ ∼200 µm thick GaAs substrate, plated with gold at the bottom to aid soldering onto a cryostat holder. Because of this metal layer, any thinner substrates allow the bottom surface plasmon to pull the mode down and decrease Γ, which is detrimental to the QCL's performance[77]. This can be seen in Figure 4.9, where we show

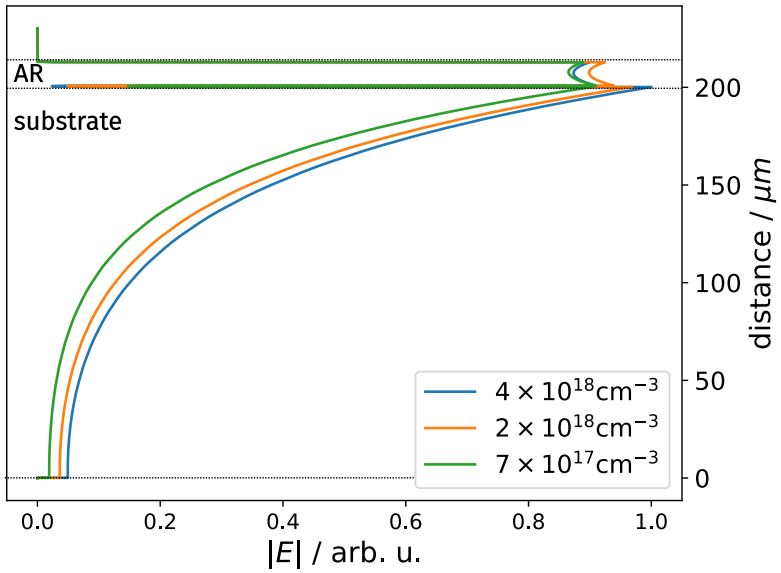

Fig. 4.7 Simulated electric field norm across the device for three different doping densities of the bottom plasmon. The blue line represents the doping which is too high (too strong and lossy attachment to the bottom plasmon), and the green line shows the doping which is too low (too weak attachment to the bottom plasmon). The orange line shows the optimal doping of $2 \times 10^{18}\,\mathrm{cm}^{-3}$.

a simulated SP waveguide with a 80 µm substrate and a standard doping of $2 \times 10^{18}\,\mathrm{cm}^{-3}$. The mode extends to the bottom of the substrate, which reduces the overlap (0.17), and increases the losses ($6\,\mathrm{cm}^{-1}$). This results in $g_{\mathrm{th}} = 35.4\,\mathrm{cm}^{-1}$, which is 10% higher than in a waveguide with 200 µm substrate. Thinning the substrate is advantageous in terms of heat extraction.

The goal of this chapter is to explore an alternative waveguide design in which the doping (and loss) of the bottom layer is lower but the overlap with the active region remains high, while reducing the substrate thickness for better thermal management.

4.3.1 Air pockets

We propose a design with three air "pockets" at the bottom of the substrate. Their function is to push the mode away from the bottom metal layer by means of refractive index contrast (thus increasing the overlap with the AR), while allowing for significant substrate thinning. In our design, there is no metal on the inner walls of the pockets. Figure 4.10 shows waveguide parameters for different substrate thicknesses. We did not simulate below 80 µm as we found this to be the practical limit of handling the chips — thinner samples are too fragile. The

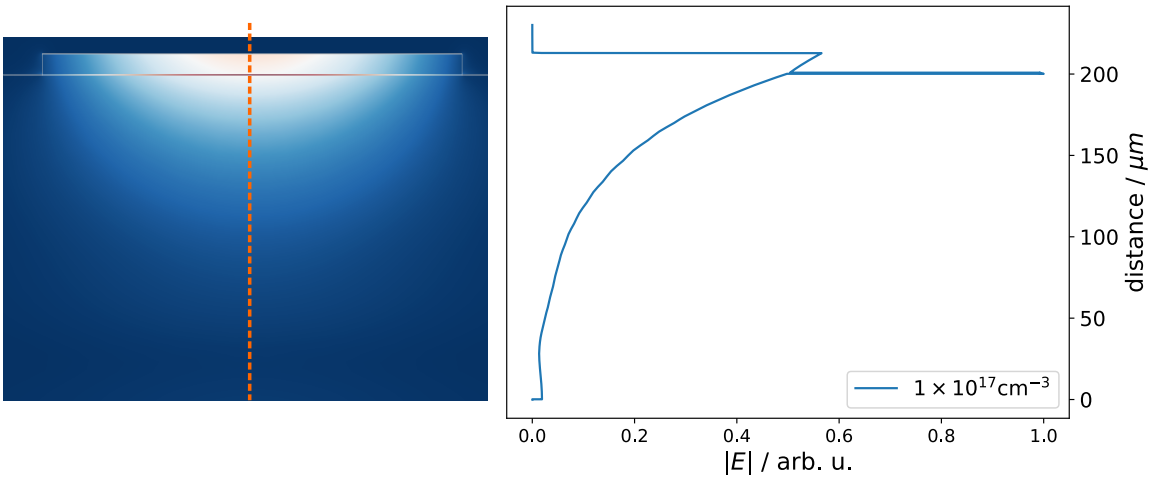

Fig. 4.8 **Left**: 2D plot of the non-plasmonic mode, which arises when the doping of the bottom layer is too low and its dielectric constant becomes positive. The simulated doping density is 1×10^{17} cm^{-3}. **Right**: Cross-section of the same mode along the dashed line in the 2D plot.

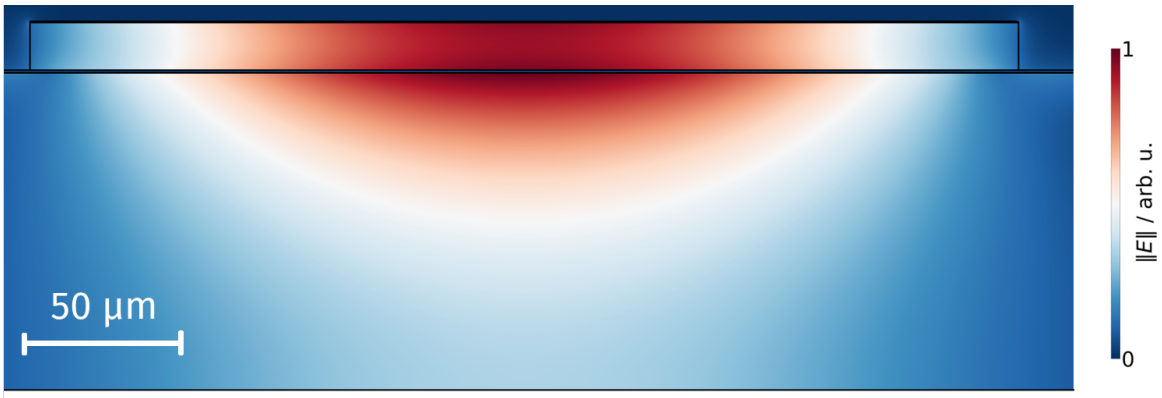

Fig. 4.9 Simulated electric field norm in a conventional SP waveguide with a thin (80 µm) substrate. The optical mode extends to the bottom of the waveguide, thus increasing loss (6 cm^{-1}), and reducing overlap (0.17) compared to a 200 µm waveguide.

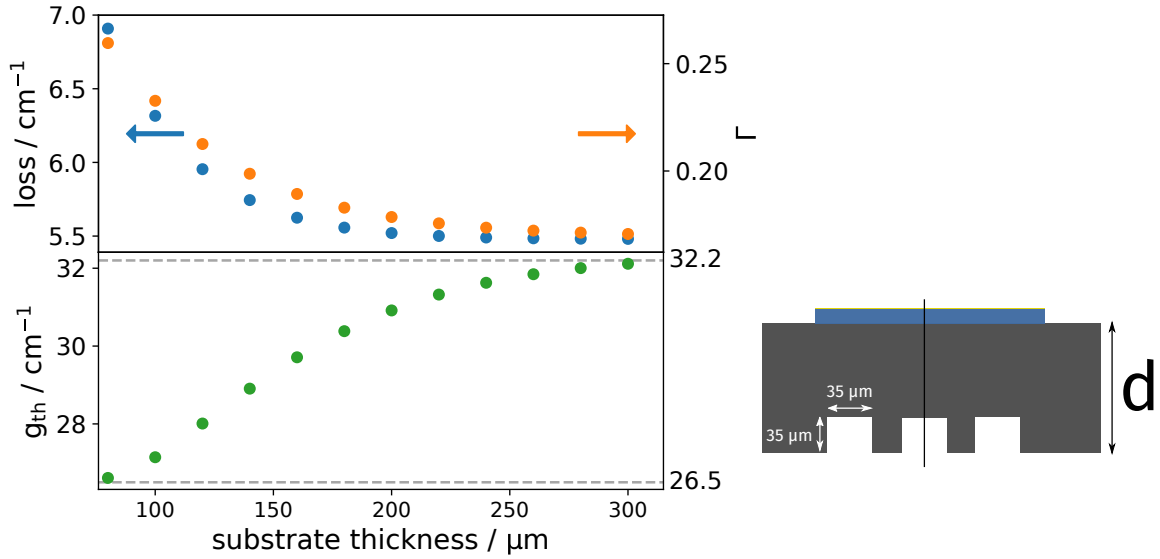

Fig. 4.10 Simulated threshold gain and its constituents for different substrate thicknesses. In the simulation, 3 air pockets were placed at the back side of the substrate. They are 35 µm wide and are placed 55 µm apart. There is a 20% reduction in g_{th} between the commonly employed 200 µm substrate and the proposed 80 µm one. The dashed line at the top of the g_{th} plot marks the best simulated performance of a surface plasmon waveguide, whereas the line at the bottom marks the simulated threshold gain of a 80 µm thick pocket device.

loss still increases with thinner substrates, but it is overcompensated by the increase in Γ. By simply employing the pockets and thinning down the substrate we can expect almost 20% reduction in g_{th}. See Figure 4.11 for the electric field distribution in a waveguide with standard 2×10^{18} cm^{-3} doping density of the plasmon layer, with the substrate thinned to 80 µm and three etched pockets.

We will now explore the effect of the bottom plasmon layer doping for a thin substrate and etched air pockets. We will continue referring to the "bottom plasmon" layer even though below a doping density of 1×10^{17} cm^{-3} a surface plasmon is not supported. Figure 4.12 shows the properties of thinned waveguides for different doping densities. We will focus on the lower end of the doping range scale, where g_{th} drops below the benchmark figure of 26.5 cm^{-1}, which is the threshold gain of a pocket waveguide with the standard doping of 2×10^{18} cm^{-3} and a 80 µm substrate. The peak around $n = 1 \times 10^{17}$ cm^{-3} arises due to the disappearance of the bottom plasmon layer, as discussed in Section 4.3. At its highest, g_{th} is an order of magnitude higher than the benchmark value. This is a result of the sharp drop in mode overlap (leaking out into the substrate) and the strong increase of the losses (slot waveguide). The overlap levels off around the doping density of 5×10^{16} cm^{-3}, and the loss decreases due to fewer free carriers in the bottom layer. These simulations show that the

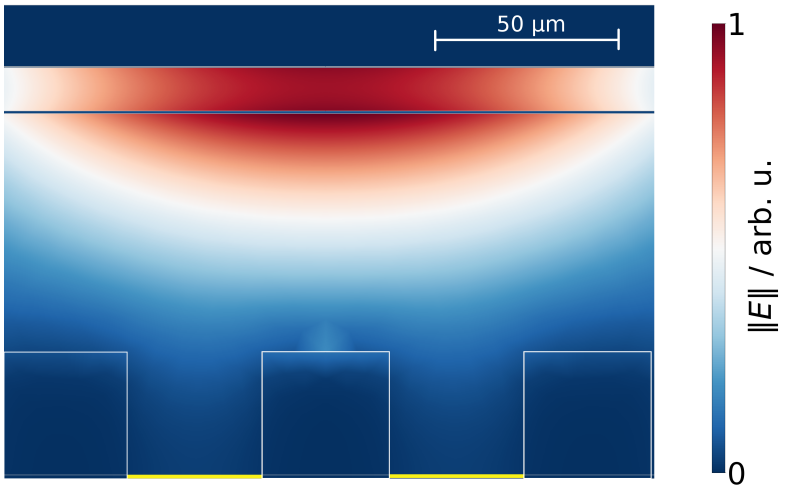

Fig. 4.11 Simulated electric field norm in a waveguide with the bottom layer doped to $2 \times 10^{18}\,\mathrm{cm}^{-3}$ and a 80 µm substrate. The air pockets (35 µm) push the mode up into the AR, therefore reducing the loss arising from the metal at the bottom of the substrate.

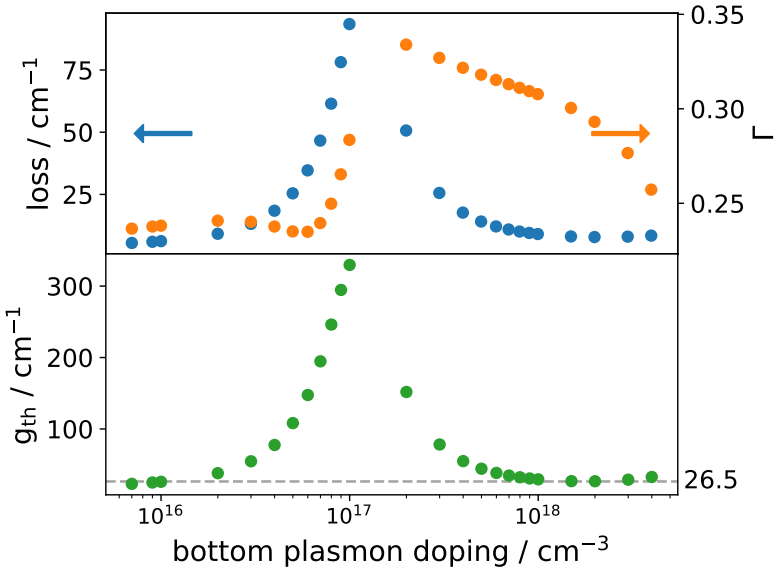

Fig. 4.12 Simulated threshold gain and its constituents for different doping densities of the bottom plasmon in a pocket waveguide. The substrate is 80 µm thick, and the pockets are 35 µm deep and wide. The dashed line marks the best simulated threshold gain from Figure 4.10, i.e. a 80 µm thick waveguide with 35 µm pockets and a doping density of $2 \times 10^{18}\,\mathrm{cm}^{-3}$.

gain performance of the pocket waveguide with low doping in the bottom plasmon could outcompete that of surface plasmon waveguides. From this perspective, the doping of the bottom layer would not be needed whatsoever, but it is still required as the electrical contact layer. This will be further discussed in Section 4.3.3. In Figure 4.13 we show the simulated electric field norm in a pocket waveguide with the same parameters as in Figure 4.11 (80 µm substrate, 35 µm pocket size), but with the bottom layer doping reduced to $1 \times 10^{16}\,\mathrm{cm}^{-3}$. Significant mode leakage into the substrate can be seen (the bottom plasmon does not exist at this low doping), reducing the overlap with the AR, but the air pockets push the mode up, away from the metal below the substrate. This corresponds to the region on the left of Figure 4.12, with g_{th} below $26.5\,\mathrm{cm}^{-1}$.

In order to find the optimal size of the air pockets, we simulated two waveguides with different air pockets width (and height, since they have a square cross-section). Figure 4.14 shows a pocket waveguide with the lower doping in the bottom plasmon layer ($1 \times 10^{16}\,\mathrm{cm}^{-3}$), whereas Figure 4.15 corresponds to the standard $2 \times 10^{18}\,\mathrm{cm}^{-3}$ doping. For the bottom layer with lower doping, the bigger the pocket the lower the gain threshold. The benchmark g_{th} of $26.5\,\mathrm{cm}^{-1}$ ($2 \times 10^{18}\,\mathrm{cm}^{-3}$ doping, three 35 µm pockets, 80 µm substrate) can be improved by pocket sides > 40 µm. In this case, the limitation lies in the fabrication — etching 50 µm squares into the substrate affects the mechanical stability of the sample. For the standard bottom plasmon layer ($2 \times 10^{18}\,\mathrm{cm}^{-3}$) the minimum g_{th} corresponds to square pockets with sides of $\sim$35 µm, i.e. the same waveguide as the optimum found by reducing the substrate thickness to 80 µm in Figure 4.10. The main function of the pockets is to push the mode up into the active region. The drawback of this is an increase of the overlap with

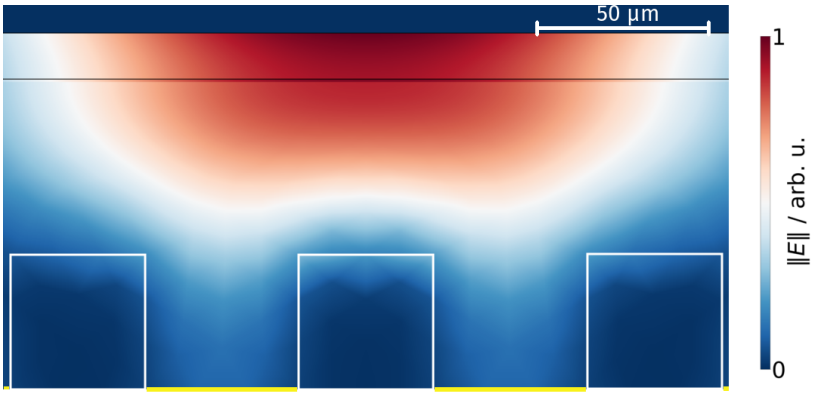

Fig. 4.13 Simulated electric field norm in a waveguide with the bottom layer doped to $1 \times 10^{16}\,\mathrm{cm}^{-3}$, a 80 µm substrate, and 35 µm pockets. Mode leakage into the substrate is significant due to the lack of bottom plasmon. The air pockets push the mode up into the AR, therefore reducing the loss arising from the metal at the bottom of the substrate.

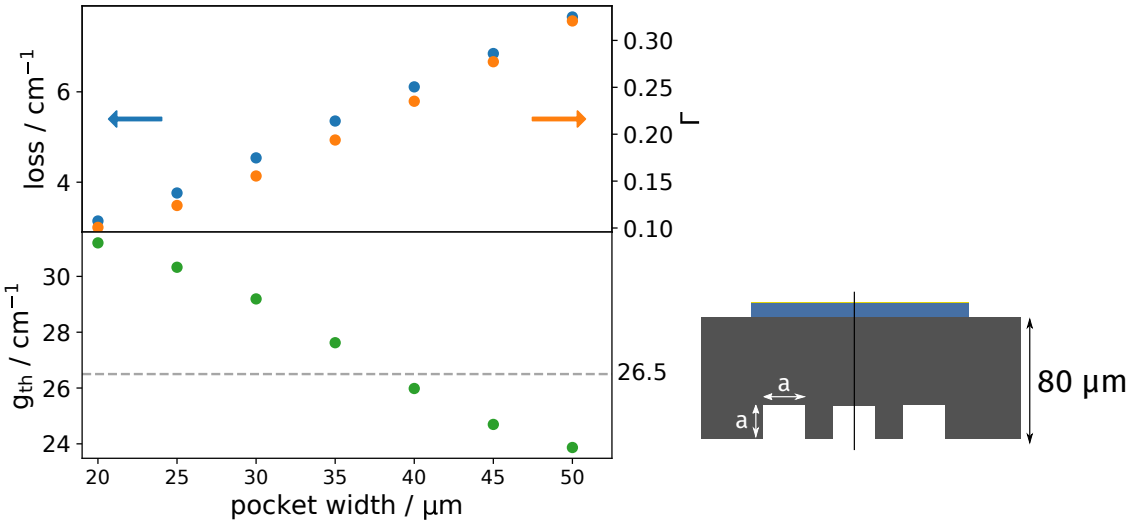

Fig. 4.14 Simulated threshold gain and its constituents for different pocket widths for the bottom plasmon layer doped to $1 \times 10^{16}\,\mathrm{cm}^{-3}$. Both loss and overlap increase with the width, but the overall effect is advantageous as the overlap increases more quickly.

the bottom doped layer, therefore pockets that are too large have a detrimental effect on the waveguide characteristics for higher doping densities.

It should be noted that there might be more advantageous air pocket geometries, e.g. a smaller middle pocket, a different shape of the pockets, or a different number of them. Due to the large parameter space we were not able to simulate all of them. We explored the question of the optimal number of pockets briefly, to conclude that three trenches was the lowest number required to push the mode away from the bottom of the waveguide.

Because the processing of the proposed waveguide requires non-trivial double-side alignment (see Section 4.4), we explored the effect of misalignment of the lithographic features. See Figures 4.16 and 4.17. In the case of the highly doped bottom layer, a misalignment of 15 µm leads only to 1% deterioration in g_{th} (Figure 4.17). For layers with lower doping the effect is much more pronounced: 15 µm misalignment leads to a 6.5% increase in g_{th} (Figure 4.16). This is because the highly doped layer sustains a surface plasmon and the pockets only push the mode up the waveguide. In case of the layers with lower doping, the pockets are crucial to confine the mode in the active region and if they are misaligned, the mode attaches to the metal at the bottom.

What are the consequences of lowering g_{th}? We can consider the threshold current as the current needed to balance loss and gain in a laser:

$$J_{\mathrm{th}} = \frac{\alpha_m + \alpha_w}{g\Gamma} = \frac{g_{\mathrm{th}}}{g}, \tag{4.5}$$

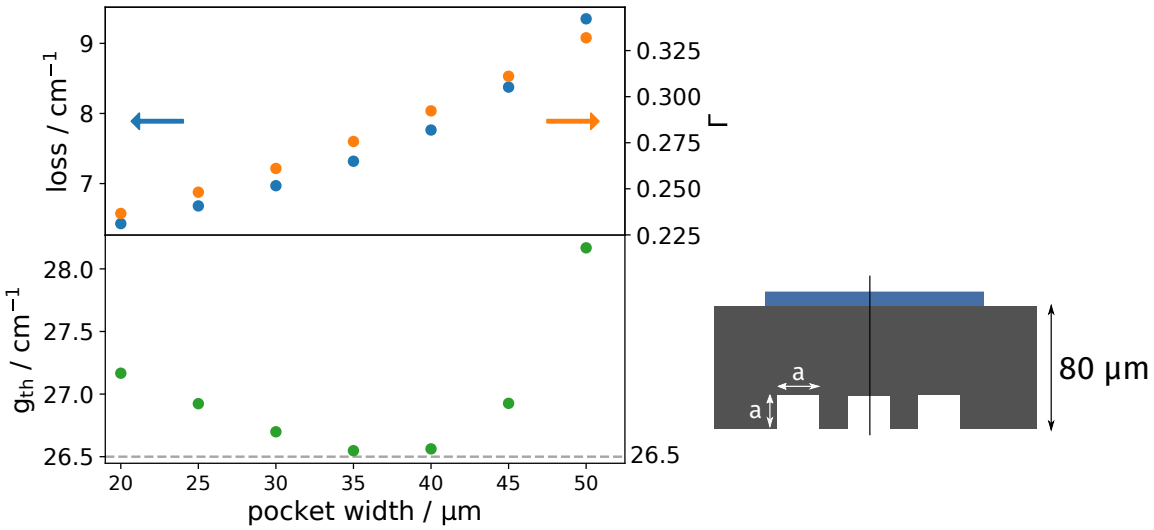

Fig. 4.15 Simulated threshold gain and its constituents for different pocket widths for the bottom plasmon layer doped to 2×10^{18} cm^{-3} and a 80 µm thick substrate. For pockets wider and deeper than 35-40 µm the mode is pushed too much into the doped layer and induces losses.

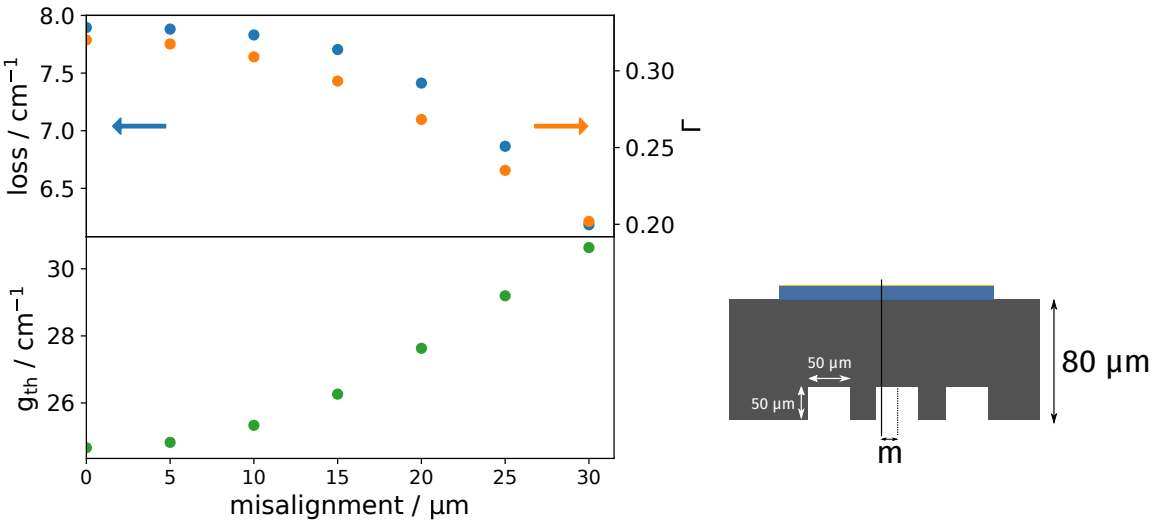

Fig. 4.16 Simulated threshold gain and its constituents for different degrees of pocket misalignment. The bottom plasmon layer in this simulation is doped to 1×10^{16} cm^{-3} and the pockets are 50 µm on each side. A 15 µm misalignment leads to $\sim 8\%$ increase in g_{th}.

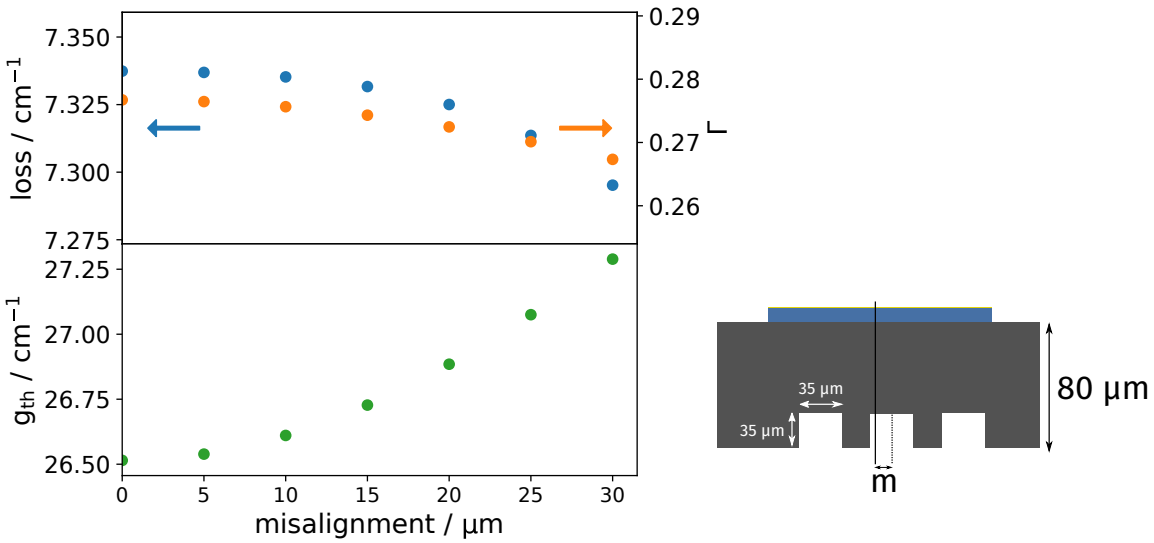

Fig. 4.17 Simulated threshold gain and its constituents for different degrees of pocket misalignment. The bottom plasmon layer in this simulation is doped to 2×10^{18} cm^{-3} and the pockets are 35 µm on each side. A 15 µm misalignment leads to $\sim 1\%$ increase in g_{th}.

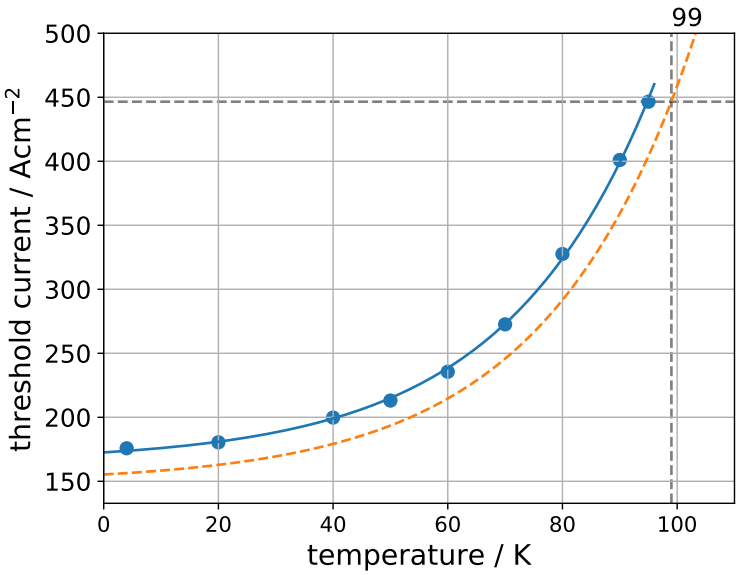

Fig. 4.18 The effect of reduced gain on temperature. The solid line shows experimental results for a typical bound-to-continuum QCL, where $T_{max} = 95$ K. The orange dashed line was obtained by reducing J_{th} by 10%, i.e. the amount the threshold gain could be improved in a pocket QCL. The grey dashed lines indicate the T_{max} the pocket QCL could achieve (99 K), assuming the same maximum J_{th}.

where g is the laser gain. In this picture, threshold current should decrease proportionally to g_{th}. In Figure 4.18 we plotted current threshold density data of a SP QCL. The solid line is a fit to the function:

$$J_{\text{th}} = J_0 + A \exp \frac{T}{T_0}. \tag{4.6}$$

The dashed line is the same function reduced by 10%, i.e. the amount that g_{th} could be reduced according to simulations. Here we do include mirror loss ($\alpha_m \simeq 7.6\,\text{cm}^{-1}$) in g_{th} — it is comparable to simulated $\alpha_w \simeq 7\,\text{cm}^{-1}$, hence the 20% reduction in above simulations translate into 10% reduction in the total loss. The temperature at which the maximum current threshold is achieved would be 99 K in a pocket QCL compared to 95 K in a SP waveguide. The effect would be more pronounced in QCLs where the slope of $J_{th}(T)$ is less steep, i.e. where T_0 is larger.

4.3.2 Temperature simulations

Thermal conductivity of GaAs at cryogenic temperatures is of the order of $\text{W}\,\text{cm}^{-1}\,\text{K}^{-1}$[61], therefore the thinner the substrate below a QCL ridge, the better the heat extraction. In the air pocket waveguide design, the proposed substrate thickness ($<$100 µm) is much smaller than in SP waveguides ($\sim$200 µm). On the other hand, some material (the pockets) is etched away, therefore the heat extraction volume is reduced. In order to quantify this, we simulated the thermal distribution of QCL ridges. We used COMSOL's "Heat Transfer" physics interface, which solves for the following equation:

$$\rho C_p(\vec{u}_{\text{trans}} \cdot \nabla T) + \nabla \cdot (\vec{q} + \vec{q}_r) = Q, \tag{4.7}$$

where ρ is the material density, C_p is the specific heat capacity, $\vec{u}_{\text{trans}}$ is the velocity vector of translational motion, T is the absolute temperature, $\vec{q}$ is the heat flux by conduction, $\vec{q}_r$ is the heat flux by radiation and Q is the heat from the source. To simulate a laser operating in continuous wave at the maximum temperature, we set the temperature of the heat sink to 80 K and the power dissipated in the AR to $1.1 \times 10^7\,\text{W}\,\text{cm}^{-2}$, following Reference [88]. For the thermal conductivity of the substrate we used the values from Reference [61] (k varies between $3 \times 10^2\,\text{W/mK}$ and $4 \times 10^3\,\text{W/mK}$ for $T = 5 - 100\,\text{K}$). Figure 4.19 shows the temperature distribution in a SP waveguide with 200 µm thick substrate, Figure 4.20 — SP waveguide with 100 µm substrate, and Figure 4.21 — the pocket waveguide (35 µm pocket width) with 100 µm thick substrate. The simulated maximum temperatures in the AR are: 174 K (SP 200 µm), 125 K (SP 100 µm), and 139 K (pocket).

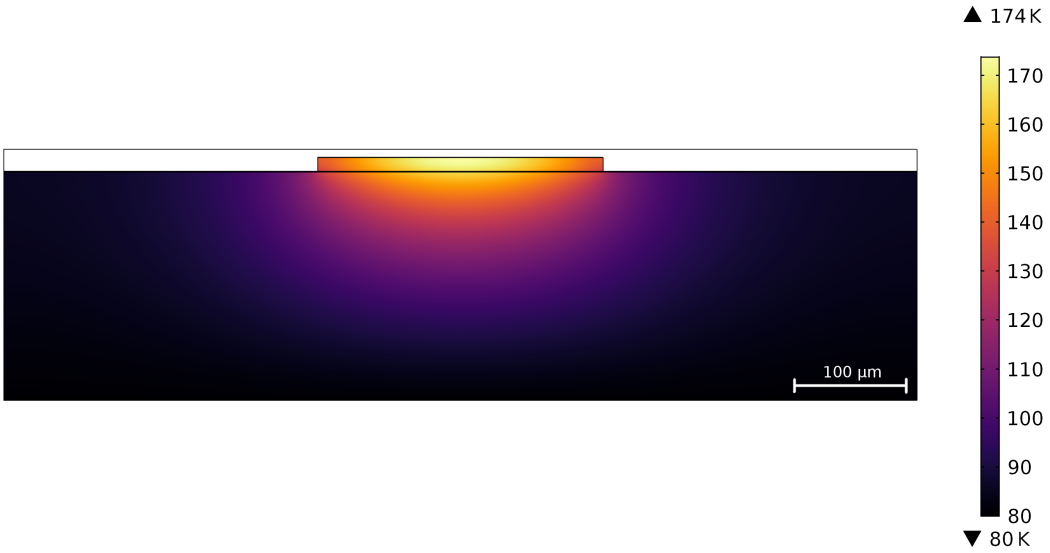

Fig. 4.19 Temperature distribution for 200 µm substrate SP waveguide for a QCL operating in continuous wave mode. The maximum temperature in the AR is 174 K.

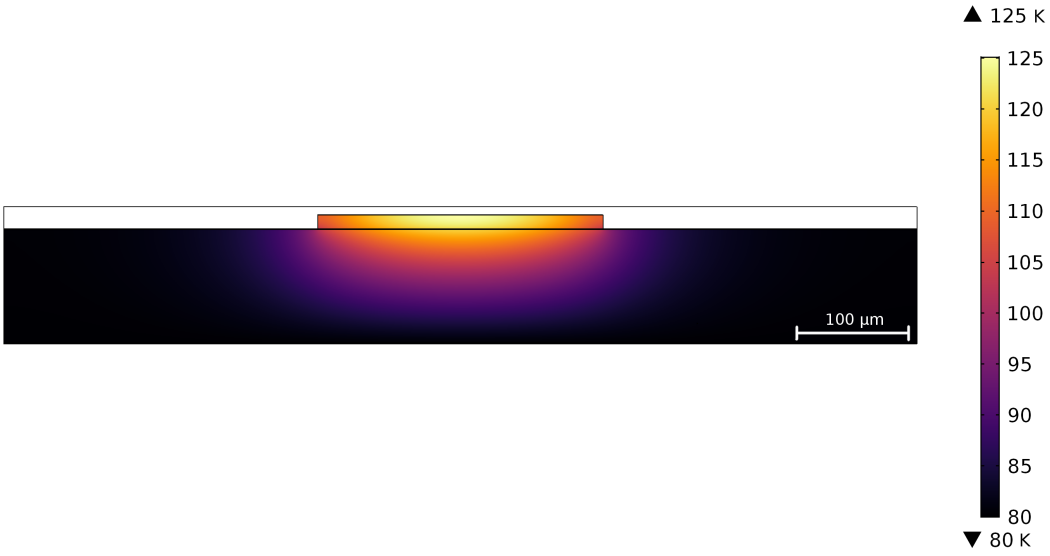

Fig. 4.20 Temperature distribution for 100 µm substrate SP waveguide for a QCL operating in continuous wave mode. The maximum temperature in the AR is 125 K.

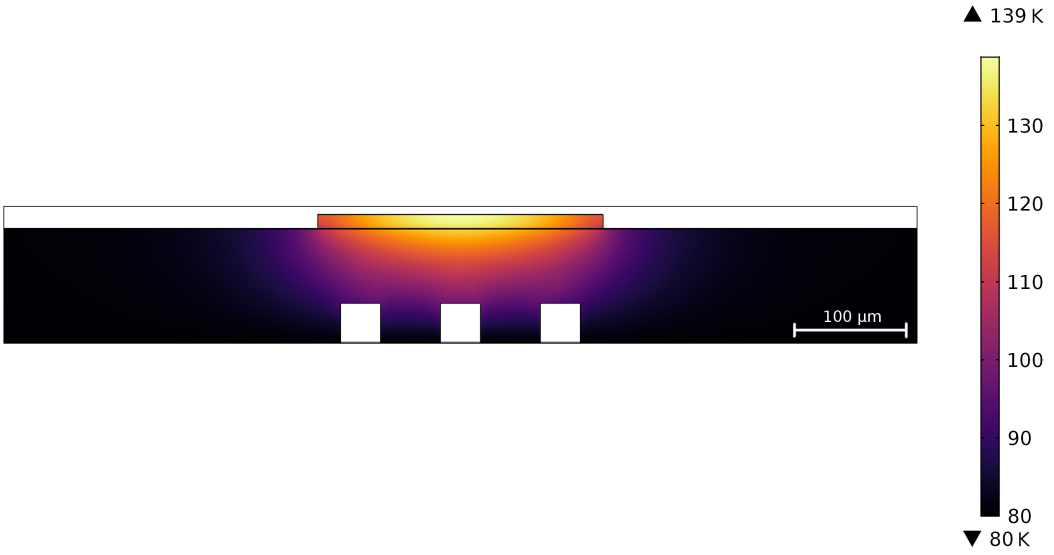

Fig. 4.21 Temperature distribution for the pocket waveguide for a QCL operating in continuous wave mode. The maximum temperature in the AR is 139 K.

In order to simulate possible thermal management improvements from employing the pocket design, we took the maximum temperature from a SP laser operating at 80 K in cw mode (174 K, see Figure 4.19) and searched for a heat sink temperature which would result in the same maximum temperature in a pocket waveguide. The results are shown in Figure 4.22. A pocket QCL operating at 92 K in continuous wave would attain the same maximum temperature in the AR as a SP QCL operating on a 80 K heat sink. This corresponds to a 15% T_{max} increase, which would reinforce the effect of reducing the threshold gain discussed in the previous section.

Thermal management of the pocket waveguide could potentially be improved even more by filling the trenches with a material which is thermally conductive, and has a low refractive index in the THz range. Al_2O_3 would be a good candidate for such filling[89].

4.3.3 Resistivity

Resistivity ρ in semiconductors decreases with increasing doping density, as there are more free electrons available for transport. According to experimental data[90], $\rho(2\times10^{18}\,\mathrm{cm}^{-3})\simeq 9.5\times10^{-4}\,\Omega\mathrm{cm}^{-1}$ and $\rho(1\times10^{16}\,\mathrm{cm}^{-3})\simeq 0.11\,\Omega\mathrm{cm}^{-1}$. Assuming the distance between the lateral contacts and the ridge to be 50 µm, the resistance along the electrical path is $4.75\times10^{-6}\,\Omega$ for the higher doping and $5.5\times10^{-4}\,\Omega$ for the lower one. In a real device, the current path is non-uniform, therefore the above values are only an approximation. Given

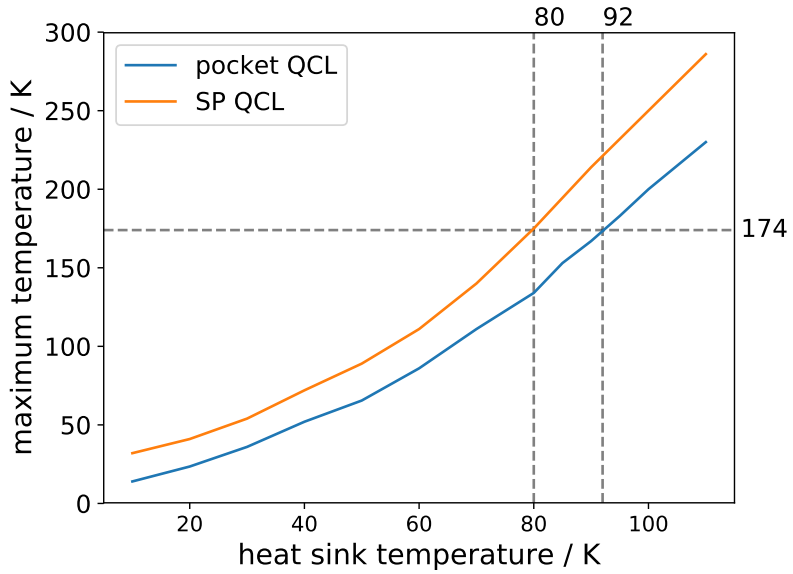

Fig. 4.22 Maximum temperature in the AR as a function of the heat sink temperature, simulated in COMSOL. The blue line represents the simulated pocket QCL device, and the orange line represents a standard SP device. The heat sink temperature of 80 K (3 K above the boiling point of nitrogen, a readily available coolant) corresponds to the maximum temperature of 175 K in a SP device. The same T_{max} would be attained by a pocket device at the heat sink temperature of 92 K.

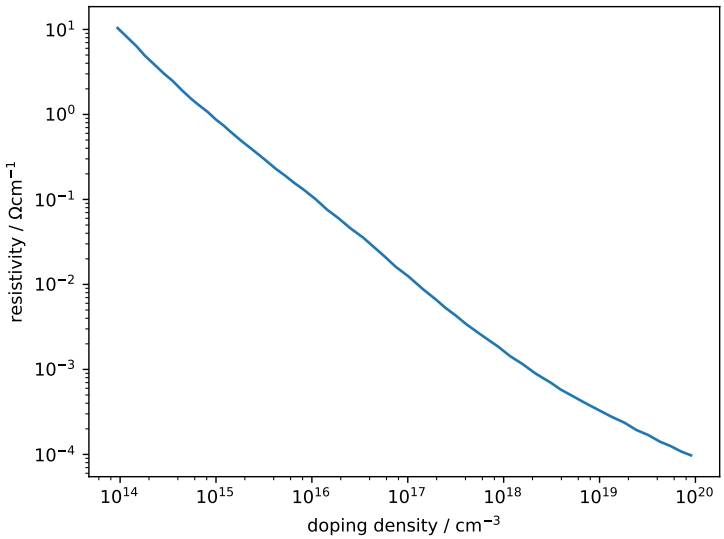

Fig. 4.23 Experimental resistivity data from Reference [90] (at 300K). Resistivity increases linearly as the inverse of doping density, but given the scales involved, higher resistivity in the bottom plasmon layer is not likely to affect the transport between the ridge and bottom contacts.

that the resistivity of the ridge is higher due to lower doping and that the usual resistance at lasing is in the Ω range (e.g. 2 A at 10 V), the effect of lower doping should be negligible.

In order to test this, we MBE-grew a QCL wafer with the doping density of the bottom layer lowered to $1 \times 10^{16}\,\mathrm{cm}^{-3}$. The wafer was then fabricated into a standard SP ridge (see Section 1.5.2), mounted in a cryostat and characterised. The results of these experiments are shown in Figure 4.24a. The lack of lasing was expected due to very low overlap, as discussed in Section 4.3.1.

4.4 Process development

4.4.1 Substrate thinning

QCL chips are usually thinned down to about 200 µm in order to reduce heating in the substrate. According to the simulations presented in Sections 4.3.1 and 4.3.2, thinner substrates are optimal for the pocket waveguide design. We polished a series of test chips to different thicknesses and checked their mechanical stability by handling them with tweezers with a reasonable force. The samples were stuck on a brass block with crystal bond and polished on a rotating polishing machine with the following recipe:

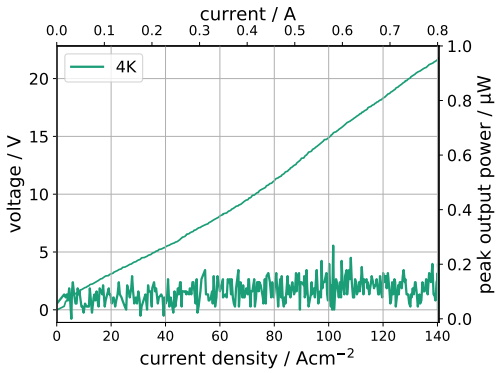

(a) $1 \times 10^{16}\,\mathrm{cm}^{-3}$ bottom plasmon doping (V811).

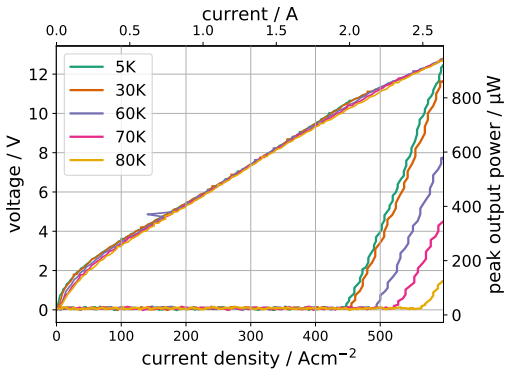

(b) $2 \times 10^{18}\,\mathrm{cm}^{-3}$ bottom plasmon doping (V788).

Fig. 4.24 LIV characteristics of **(a)** a SP QCL fabricated from the pocket wafer and **(b)** a wafer incorporating the same AR design, but with the usual $2 \times 10^{18}\,\mathrm{cm}^{-3}$ doping of the bottom plasmon layer. Despite showing signs of alignment, the device with low doping does not lase. This is expected, as there are no pockets below the ridge, therefore the mode is free to leak out of the AR. The SP device with the standard doping of the bottom plasmon starts lasing at $J_{\mathrm{th}} \simeq 450\,\mathrm{A\,cm}^{-2}$ at 5 K.

1. Grade P800 sand paper, 5 min, 40 rpm
2. Grade P1200 sand paper, 5 min 40 rpm
3. 1 µm alumina powder, 3 min, 40 rpm
4. 0.3 µm alumina powder, 3 min, 40 rpm
5. 0.05 µm alumina powder, 3 min, 40 rpm

80 µm was the lowest thickness at which the samples retained their mechanical stability. Thinner chips were too brittle to handle with tweezers and stick to glass slides. Therefore we used 80 µm thick samples in the process development described below.

4.4.2 Double-sided alignment

QCL waveguides are usually only processed on one side of the wafer, as described in Section 1.5. In order to implement the pocket QCL concept, it was essential to develop a double-sided process which would enable us to align the pockets with the ridge within the tolerance shown in Figure 4.16. We considered several possibilities, outlined below.

Seemingly the simplest processing technique would be to use a double-sided photolithography mask aligner. After fabricating laser ridges and contacts, the chip would be placed in an

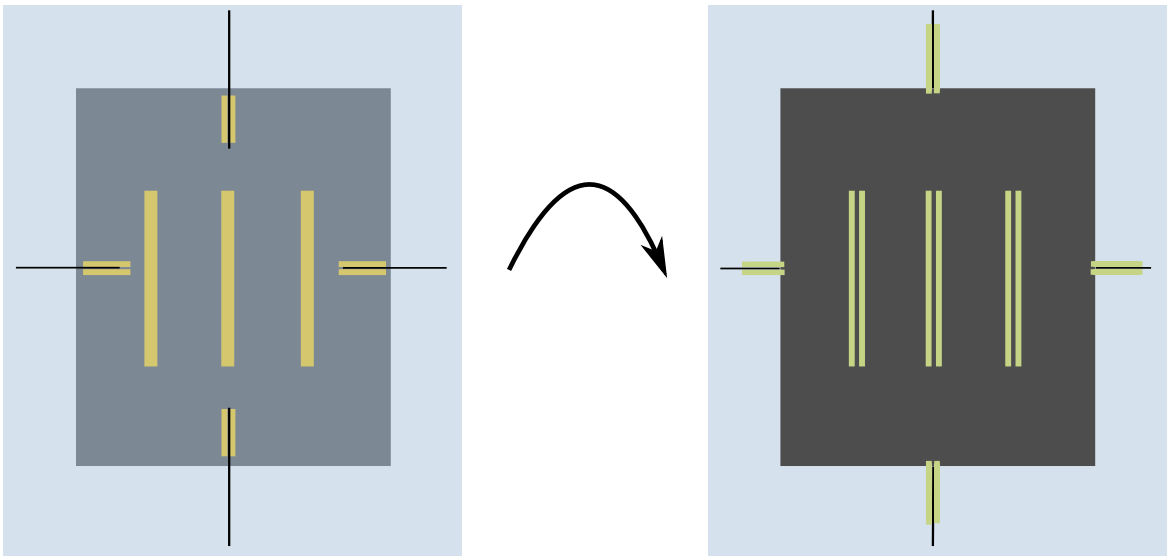

Fig. 4.25 Double side processing of a pocket QCL. A chip with the top side (ridges) fully processed is stuck on to a glass slide and alignment marks are scribed onto the glass substrate in the alignment slit (left drawing; the chip is behind the glass slide). Then the chip is flipped over and the scratches are aligned with the gaps in the metal mask. A standard lift-off process follows. The end result is a chip covered with metal with openings for dry etching of the pockets.

aligner and the pocket pattern for photolithography would be aligned precisely. Unfortunately, a double sided photolithography aligner was not available for this project, therefore another method had to be developed.

One approach would be to fit a single-sided mask aligner with a mid-infrared diode, whose emission would be transmitted by GaAs and seen with a CCD camera fitted in the microscope. Then metal alignment marks could be placed on the top side of the chip and they would be seen in infrared. Unfortunately, it was not possible implement this system in our mask aligners.

We adopted another approach, namely sticking a chip on a glass slide, making alignment scratches on the slide and using those in a traditional one sided mask aligner (see Figure 4.25). We estimate the accuracy of this method to be 5-10 µm.

4.4.3 Pocket etching

We set out to develop a wet etching recipe for the backside pockets. We used negative resist from MicroChemicals, as it results in a satisfactory undercut profile. The recipe was the following:

1. Bake the sample on a 115 °C hot plate.

2. Spin MicroChemicals AZ5214E resist at 5000 rpm for 60 second.
3. Bake at 115 °C for 2 min.
4. Remove edge beads with a wipe soaked in acetone.
5. Align the pattern and expose for 3.4 s in a mask aligner.
6. Bake at 115 °C for 2 min.
7. Expose the whole sample (without a mask) for 30 s.
8. Develop in AZ726 MIF developer for 1 min.

Subsequently the samples were etched in a 1:80:40 ($H_2SO_4 : H_2O_2 : H_2O$) solution — the same as is used for ridge wet etching in SP processing. The etch rate of GaAs is usually $\sim 1\,\mu m/min$. We attempted this etch 10-15 times. The state of one representative sample after a 10 min etch is shown in Figure 4.26. The solution had etched away an undercut below the resist until the "tunnels" from adjacent pockets joined — at this point the resist was washed away. We tried different solution ratios and a positive resist, but we could not successfully etch separate pockets.

In the hope that metal would be a more adhesive and chemically resistant etching mask, we tried using an inverted lithography mask followed by gold evaporation and a lift-off procedure. A 10 nm/100 nm Ti/Au layer was evaporated on the back side of the sample. The pocket rectangles were lifted off and used as a mask for wet etching. The undercut in this case was also significant (see Figure 4.27 for a SEM image after 10 min etching) and eventually led to the metal peeling off and leaving a wide gap where the pockets should be (see Figure 4.28).

We conclude that wet etching is not appropriate for the pocket QCL design. Dry etching would most likely give better results, but a suitable dry etching facility was not available at the time these works were carried out. There are two techniques that we recommend exploring.

An Inductively Coupled Plasma (ICP) tool is capable of fast ($> 100\,nm/min$) etch rates, which would result in almost vertical walls of the pockets. This process requires depositing a dielectric (e.g. SiN) mask on the sample, defining a pattern with photolithography and Al lift-off, and finally etching the substrate in an ICP tool. The advantage of this approach is the fast etch rate. However, the drawback is that the back side of the pocket QCL still requires a metal evaporation for efficient heat extraction. This puts more stress on the thin samples and adds another challenge to protect the etched pockets from gold being evaporated on the inside (which would introduce losses).

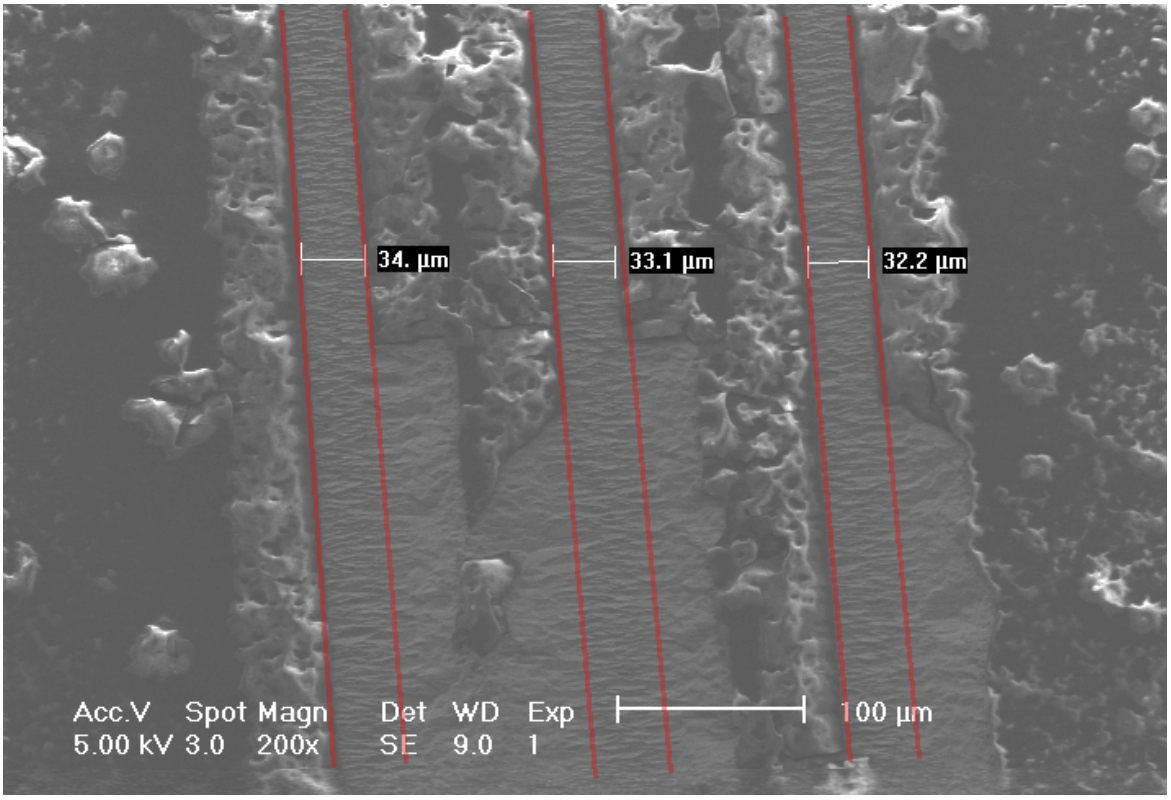

Fig. 4.26 SEM image of wet-etched pockets after 10 min. Resist was used as the etch mask, and 1:80:40 ($H_2SO_4 : H_2O_2 : H_2O$) solution was used as the etchant. The undercut resulted in parts of the resist washing off and therefore joining the adjacent pockets. The red lines indicate where the edges of the etched trenches should be.

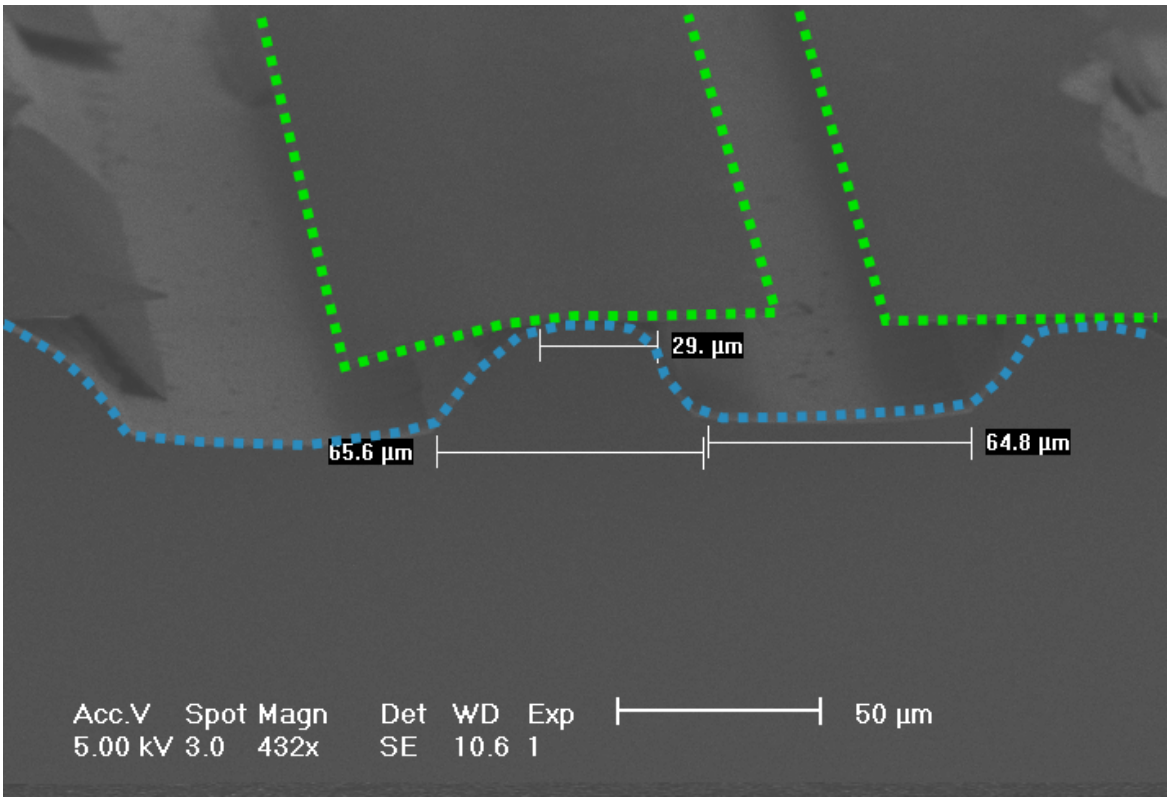

Fig. 4.27 SEM image of wet-etched pockets after 10 min. 10 nm/100 nm Ti/Au layer was used as the etch mask, and 1:80:40 ($H_2SO_4 : H_2O_2 : H_2O$) solution was used as the etchant. Dashed lines mark the metal mask (green), and the semiconductor (blue). The undercut is smaller than in the resist mask case, however it does not allow for etches deeper than about 10 µm.

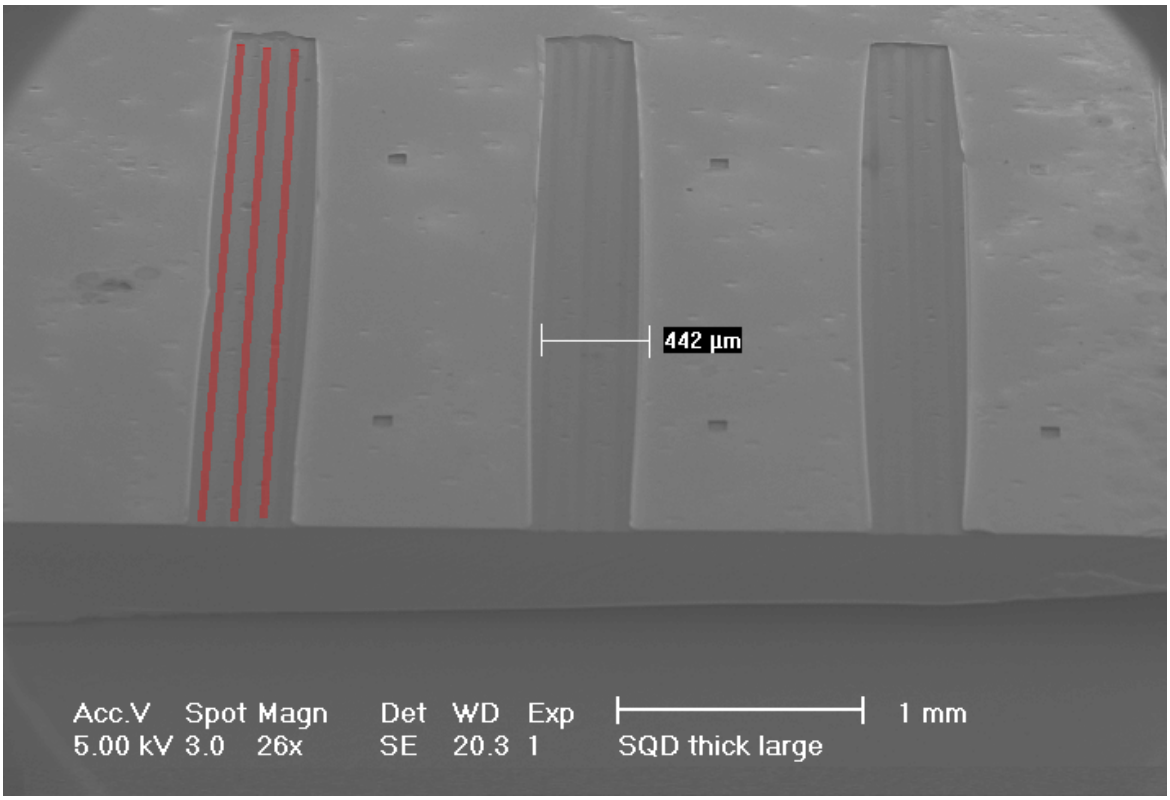

Fig. 4.28 SEM image of wet-etched pockets after 20 min (10 min after the state shown in Figure 4.27). The undercut resulted in the metal lifting off and therefore in joining the adjacent pockets. The red lines indicate where the etched trenches should be.

Another possible etching method would involve a Reactive Ion Etching (RIE) where a metal mask is allowed in the chamber. A similar method to that used in Chapter 2 (a $SiCl_4$ etch with a Ti/Au/Ni mask) could be employed. The defect QCL etches were however much shallower ($\sim 12\,\mu m$) and they allowed for the etched material to be disposed of in the chamber, whereas in the pocket QCL case a trench is etched with no side channels for the residual material to be pumped out. It could be mitigated by stopping the etching process often and pumping out the chamber before continuing.

This project had been suspended due to RIE unavailability. When the dry etching system became available, the defect line QCL project took precedence, and we were unable to resume the work on the pocket QCL.

4.5 Conclusions

In this chapter, we have shown that there is still some room for improvement in QCL waveguide design. We proposed a pocket QCL, which is a derivative of the standard SP waveguide, but with the substrate thinned down for better thermal management, and bottom plasmon doping reduced for lower optical losses. The simulations of an unoptimised pocket QCL show the potential to achieve higher operating temperatures and lower threshold gain. This approach is independent of the AR design and could show the biggest absolute improvement in high-temperature ARs.

We found that the biggest challenge was fabricating the pocket QCLs. We outlined the proposed process, including a few possible approaches to the challenging step of double-side mask alignment. We also tested the lower limit of substrate thickness in QCLs. Although ultra thin ($\leq 50\,\mu m$) silicon wafers are commercially available[91], GaAs is inherently more brittle. We found however that it should be possible to fabricate thin ($80\,\mu m$) GaAs QCLs with appropriate care. Deep GaAs etching with nearly vertical walls is very difficult and rarely done. The development of such a process was not possible due to the RIE system being unavailable. We suggest using a dry etching technique (RIE or ICP), preferably with breaks between etches to allow for the residual material to be pumped out.

Chapter 5

Future work

In this thesis, we explored three different designs for THz QCL waveguides: the photonic crystal defect line, the hybrid BCB waveguide, and the air pocket waveguide.

We confirmed that the defect line waveguides are good candidates for frequency selective, low threshold THz QCLs. We developed a fabrication process which allowed us to test the proof-of-concept devices, but a more precise dry etching tool (ICP) would allow one to systematically explore the frequency tunability of the PhC. In principle, precise tunability is possible throughout the THz range, and only requires micrometer-sized features, readily achievable in modern cleanrooms. We suggest fabricating defect lines of one coupling type (D1, D3, or D5), and varying the defect size. If the pillars' radii are controlled precisely, one should see lasing from different optical modes (hexapole, quadrupole, dipole, and the monopole), and the differences in their output power could be determined experimentally.

We acknowledge the uncertainty of the methods that we used for threshold current density estimation. They set reasonable bounds on J_{th}, but it would be interesting to probe the electrical transport directly and verify which of the methods (area or IV matching) is a closer estimate.

According to the slow light theory, J_{th} is affected by the coupling strength between defects in a line. Our results using IV alignment estimates confirm this, but a systematic study should be done on more samples of D1, D3, and D5 types. This would allow one to find the compromise between J_{th} reduction and the emitted power.

PhC QCLs could also be used to study Purcell enhancement at THz frequencies. For this, a very precise cleaving technique is required, allowing one to isolate one defect in a device, such that differences (in J_{th} and radiative emission lifetimes) between different cavity volumes could be measured.

The defect line allows for waveguide geometries impossible to achieve with ridge QCLs. We presented proof-of-concept *T defect lines*, and characterised them while they were

powered uniformly. It would be interesting to measure the output of each of the branches in isolation, by introducing gaps in the top contacts. When electrically separated, the branches with different defect sizes should emit different frequencies. By switching individual branches on and off, interference effects can be explored.

The defect line also paves the way for QCLs lasing in arbitrary directions, which would be useful in integrated THz systems, such as interferometers. The line direction can be engineered, and an external element (such as a lens or a hollow waveguide) can be used to collimate its divergent output.

In Chapter 3 we have extensively studied the hybrid BCB waveguide. Since publishing the initial work on this novel waveguide[62], we improved the fabrication yield significantly (from 10-15% to above 80%). This is important for the adoption of this technique in the THz QCLs research community, as well as for future commercialisation. It also enables MM-like fabrication in laboratories without the access to thermocompressive bonding facilities.

To research hybrid BCB waveguides in more detail, we suggest investigating thinner layers of metal in between the AR and the BCB layer. We focused on layers above 100 nm in order to reproduce and explain the results from the original paper. For thin layers however, optical mode leakage starts to play a significant role in laser operation. This effect could be studied quantitatively by fabricating and characterising waveguides with 50-100 nm of gold in between the AR and BCB.

Thermal management of hybrid BCB waveguides is slightly worse than their MM counterparts, most likely due to lower thermal conductivity of BCB compared to GaAs. This could be improved upon by investigating thinner layers of BCB (below 10 µm). More thermally conductive metal layers could also be used. We attempted to thermally evaporate copper instead of gold, but the samples suffered from poor adhesion. Using a better adhesive layer than titanium (such as tantalum) could give better results.

Finally, we designed, simulated, and carried out preliminary experiments with a *pocket QCL*, i.e. a thin substrate waveguide with etched trenches below the AR. Due to equipment unavailability, we could not characterise these waveguides, but we outlined the fabrication process and excluded wet etching as a means to define the pockets. The waveguides can be fabricated with an RIE or ICP tool, and with double sided alignment allowing for micrometre precision. Our simulations suggest that the biggest thermal management gains are available in high-T_{max} ARs, therefore a resonant phonon or a 4 quantum well design should be used to study the air pocket waveguide.

The proposed geometry (3 square pockets, each 40 µm deep and wide, substrate thinned down to 80 µm) has not been fully optimised. It would therefore be instructive to fabricate waveguides with other pocket sizes, position, or number. Even though the 2 pocket waveguide

performed worse in simulation, it is possible that in a real device, the increased mechanical stability and better thermal conduction of a two-trench waveguide would lead to better overall performance.

In summary, all three presented waveguide designs pave the way for exciting improvements in long-term THz QCLs goals, namely frequency selectivity, current density reduction, and temperature management. The waveguides, along with developments in active region design, QCL fabrication, and packaging, are important stepping stones towards wide adoption of THz QCL technology.

References

[1] I. Mehdi, G. Chattopadhyay, E. Schlecht, J. Ward, J. Gill, F. Maiwald, and A. Maestrini. Terahertz multiplier circuits. In *IEEE MTT-S International Microwave Symposium Digest*, pages 341–344, 2006.

[2] F. Amir, C. Mitchell, N. Farrington, and M. Missous. Advanced Gunn diode as high power terahertz source for a millimetre wave high power multiplier. *Millimetre Wave and Terahertz Sensors and Technology II*, 7485, 2009. doi: 10.1117/12.830296.

[3] M. Tonouchi. Cutting-edge terahertz technology. *Nature Photonics*, 1(2):97–105, 2007.

[4] B. Ferguson and X. C. Zhang. Materials for terahertz science and technology. *Nature Materials*, 1(1):26–33, 2002. doi: 10.1038/nmat708.

[5] C. Yu, S. Fan, Y. Sun, and E. Pickwell-MacPherson. The potential of terahertz imaging for cancer diagnosis: A review of investigations to date. *Quantitative Imaging in Medicine and Surgery*, 2 (1):33–45, 2012.

[6] D. Dragoman and M. Dragoman. Terahertz fields and applications. *Progress in Quantum Electronics*, 28:1–66, 2004.

[7] D. M. Slocum, E. J. Slingerland, R. H. Giles, and T. M. Goyette. Atmospheric absorption of terahertz radiation and water vapor continuum effects. *Journal of Quantitative Spectroscopy and Radiative Transfer*, 127:49–63, 2013. doi: 10.1016/j.jqsrt.2013.04.022.

[8] R. F. Kazarinov and R. A. Suris. Possibility of the amplification of electromagnetic waves in a semiconductor with a superlattice. *Soviet Physics: Semiconductors*, 5(4): 707–709, 1971.

[9] L. Tsu and R. Esaki. Superlattice and negative differential conductivity in semiconductor. *IBM Journal of Research and Development*, 14(1):61–65, 1970.

[10] F. Capasso, K. Mohammed, and A. Cho. Resonant Tunneling Through Double Barriers, Perpendicular Quantum Transport Phenomena in Superlattics, and Their Device Applications. *IEEE Journal of Quantum Electronics*, 22:1853, 1986.

[11] H. C. Liu. A novel superlattice infrared source. *Journal of Applied Physics*, 63(8): 2856–2858, 1988.

[12] J. Faist, F. Capasso, D. L. Sivco, C. Sirtori, A. L. Hutchinson, and A. Y. Cho. Quantum cascade laser. *Science*, 264(5158):553–6, 1994. doi: 10.1126/science.264.5158.553.

[13] R. Kohler, A. Tredicucci, F. Beltram, H. E. Beere, E. H. Linfield, A. G. Davies, D. A. Ritchie, R. C. Iotti, and F. Rossi. Terahertz semiconductor-heterostructure laser. *Nature*, 417(6885):156–159, 2002.

[14] G. Scalari, C. Walther, M. Fischer, R. Terazzi, H. E. Beere, D. A. Ritchie, and J. Faist. THz and sub-THz quantum cascade lasers. *Laser and Photonics Reviews*, 3(1-2):45–66, 2009. doi: 10.1002/lpor.200810030.

[15] A. W. M. Lee, Q. Qin, S. Kumar, B. S. Williams, Q. Hu, and J. L. Reno. Real-time terahertz imaging over a standoff distance (>25 meters). *Applied Physics Letters*, 89 (14):1–4, 2006. doi: 10.1063/1.2360210.

[16] S. Fathololoumi, E. Dupont, C. W. I. Chan, Z. R. Wasilewski, S. R. Laframboise, D. Ban, A. Mátyás, C. Jirauschek, Q. Hu, and H. C. Liu. Terahertz quantum cascade lasers operating up to $\sim 200\,\mathrm{K}$ with optimized oscillator strength and improved injection tunneling. *Optics express*, 20(4):3866–76, 2012.

[17] M. Wienold, B. Röben, and L. Schrottke. High-temperature, continuous-wave operation of terahertz quantum-cascade lasers with metal-metal waveguides and third-order distributed feedback. *Optics Express*, 22(3), 2014. doi: 10.1364/OE.22.003334.

[18] L. H. Li, L. Chen, J. R. Freeman, M. Salih, P. Dean, A. G. Davies, and E. H. Linfield. Multi-Watt high-power THz frequency quantum cascade lasers. *Electronics Letters*, 53 (12):799–800, 2017. doi: 10.1049/el.2017.0662.

[19] X. Wang, C. Shen, T. Jiang, Z. Zhan, Q. Deng, W. Li, W. Wu, N. Yang, W. Chu, and S. Duan. High-power terahertz quantum cascade lasers with $\sim 0.23\,\mathrm{W}$ in continuous wave mode. *AIP Advances*, 6(7):1–6, 2016. doi: 10.1063/1.4959195.

[20] M. Rösch, G. Scalari, M. Beck, and J. Faist. Octave-spanning semiconductor laser. *Nature Photonics*, 9(1):42–47, 2014. doi: 10.1038/nphoton.2014.279.

[21] J. Faist. *Quantum Cascade Lasers*. Oxford University Press, 2013. ISBN 9780198528241.

[22] E. Dupont, S. Fathololoumi, and H. C. Liu. Simplified density-matrix model applied to three-well terahertz quantum cascade lasers. *Physical Review B*, 81:1–18, 2010. doi: 10.1103/PhysRevB.81.205311.

[23] A. Mátyás, M. A. Belkin, P. Lugli, and C. Jirauschek. Temperature performance analysis of terahertz quantum cascade lasers: Vertical versus diagonal designs. *Applied Physics Letters*, 96:2012–2015, 2010. doi: 10.1063/1.3430741.

[24] A. Wacker, M. Lindskog, and D. O. Winge. Nonequilibrium Green's function model for simulation of quantum cascade laser devices under operating conditions. *IEEE Journal on Selected Topics in Quantum Electronics*, 19(5), 2013. doi: 10.1109/JSTQE.2013.2239613.

[25] L. R. Ram-Mohan. *Finite Element and Boundary Element Applications in Quantum Mechanics*. Oxford University Press, 2002. ISBN 9780198525226.

[26] B. S. Williams. Terahertz quantum-cascade lasers. *Nature Photonics*, 1(9):517–525, 2007.

[27] G. Scalari, L. Ajili, J. Faist, H. E. Beere, E. H. Linfield, D. A. Ritchie, and A. G. Davies. Far-infrared ($\lambda \simeq 87\,\mu$m) bound-to-continuum quantum-cascade lasers operating up to 90 K. *Applied Physics Letters*, 82(19):3165–3167, 2003. doi: 10.1063/1.1571653.

[28] L. Ajili, G. Scalari, J. Faist, H. Beere, E. Linfield, D. Ritchie, and A. G. Davies. High power quantum cascade lasers operating at $\lambda \simeq 87$ and $130\,\mu$m. *Applied Physics Letters*, 85(18):3986–3988, 2004. doi: 10.1063/1.1810217.

[29] C. Worrall, J. Alton, M. Houghton, S. Barbieri, H. E. Beere, D. A. Ritchie, and C. Sirtori. Continuous wave operation of a superlattice quantum cascade laser emitting at 2 THz. *Optics Express*, 14(1):171–181, 2006. doi: 10.1364/OPEX.14.000171.

[30] M. I. Amanti, G. Scalari, R. Terazzi, M. Fischer, M. Beck, J. Faist, A. Rudra, P. Gallo, and E. Kapon. Bound-to-continuum terahertz quantum cascade laser with a single-quantum-well phonon extraction/injection stage. *New Journal of Physics*, 11(12): 125022, 2009. doi: 10.1088/1367-2630/11/12/125022.

[31] S. Barbieri, J. Alton, H. E. Beere, J. Fowler, E. H. Linfield, and D. A. Ritchie. 2.9 THz quantum cascade lasers operating up to 70 K in continuous wave. *Applied Physics Letters*, 85(10):1674, 2004. doi: 10.1063/1.1784874.

[32] B. S. Williams, H. Callebaut, S. Kumar, Q. Hu, and J. L. Reno. 3.4-THz quantum cascade laser based on longitudinal-optical-phonon scattering for depopulation. *Applied Physics Letters*, 82(7):1015–1017, 2003. doi: 10.1063/1.1554479.

[33] S. Kumar, Q. Hu, and J. L. Reno. 186 K operation of terahertz quantum-cascade lasers based on a diagonal design. *Applied Physics Letters*, 94(13), 2009.

[34] L. Li, L. Chen, J. Zhu, and J. Freeman. Terahertz quantum cascade lasers with >1 W output powers. *Electronics letters*, 50(4):309–311, 2014. doi: 10.1049/el.2013.4035.

[35] M. Franckié, L. Bosco, M. Beck, C. Bonzon, E. Mavrona, G. Scalari, A. Wacker, and J. Faist. Two-well quantum cascade laser optimization by non-equilibrium Green's function modelling. *Applied Physics Letters*, 112(2), 2018. doi: 10.1063/1.5004640.

[36] H. E. Beere, J. C. Fowler, J. Alton, E. H. Linfield, D. A. Ritchie, R. Köhler, A. Tredicucci, G. Scalari, L. Ajili, J. Faist, and S. Barbieri. MBE growth of terahertz quantum cascade lasers. *Journal of Crystal Growth*, 278(1-4):756–764, 2005.

[37] Y. Ren, R. Wallis, D. S. Jessop, R. Degl'Innocenti, A. Klimont, H. E. Beere, and D. A. Ritchie. Fast terahertz imaging using a quantum cascade amplifier. *Applied Physics Letters*, 107(1):011107, 2015. doi: 10.1063/1.4926602.

[38] L. Mahler, R. Köhler, A. Tredicucci, F. Beltram, H. E. Beere, E. H. Linfield, D. A. Ritchie, and A. G. Davies. Single-mode operation of terahertz quantum cascade lasers with distributed feedback resonators. *Applied Physics Letters*, 84(26):5446–5448, 2004. doi: 10.1063/1.1767957.

[39] M. I. Amanti, M. Fischer, G. Scalari, M. Beck, and J. Faist. Low-divergence single-mode terahertz quantum cascade laser. *Nature Photonics*, 3(10):586–590, 2009. doi: 10.1038/nphoton.2009.168.

[40] R. Colombelli, K. Srinivasan, M. Troccoli, O. Painter, C. F. Gmachl, D. M. Tennant, A. M. Sergent, D. L Sivco, A. Y. Cho, and F. Capasso. Quantum Cascade Surface-Emitting Photonic Crystal Laser. *Science*, 302:1374–1377, 2003. doi: 10.1117/12.532586.

[41] L. A. Dunbar, V. Moreau, R. Ferrini, R. Houdré, L. Sirigu, G. Scalari, M. Giovannini, N. Hoyler, and J. Faist. Design, fabrication and optical characterization of quantum cascade lasers at terahertz frequencies using photonic crystal reflectors. *Optics Express*, 13(22):8960, 2005. doi: 10.1364/OPEX.13.008960.

[42] H. Zhang, L. A. Dunbar, G. Scalari, R. Houdré, and J. Faist. Terahertz photonic crystal quantum cascade lasers. *Optics Express*, 15(25):16818, 2007. doi: 10.1364/OE.15.016818.

[43] A. Benz, C. Deutsch, G. Fasching, K. Unterrainer, A. M. Andrews, P. Klang, W. Schrenk, and G. Strasser. Active photonic crystal terahertz laser. *Optics Express*, 17(2):941–946, 2009. doi: 10.1364/OE.17.000941.

[44] H. Zhang, G. Scalari, J. Faist, L. A. Dunbar, and R. Houdré. Design and fabrication technology for high performance electrical pumped terahertz photonic crystal band edge lasers with complete photonic band gap. *Journal of Applied Physics*, 108(9):093104, 2010. doi: 10.1063/1.3476565.

[45] L. A. Dunbar, R. Houdré, G. Scalari, L. Sirigu, M. Giovannini, and J. Faist. Small optical volume terahertz emitting microdisk quantum cascade lasers. *Applied Physics Letters*, 90(14):88–91, 2007. doi: 10.1063/1.2719674.

[46] M. Bahriz, V. Moreau, R. Colombelli, O. Crisafulli, and O. Painter. Design of mid-IR and THz quantum cascade laser cavities with complete TM photonic bandgap. *Conference on Lasers and Electro-Optics Europe - Technical Digest*, 15(10):4164–4166, 2007. doi: 10.1109/CLEOE-IQEC.2007.4386025.

[47] O. P. Marshall, V. Apostolopoulos, J. R. Freeman, R. Rungsawang, H. E. Beere, and D. A. Ritchie. Surface-emitting photonic crystal terahertz quantum cascade lasers. *Applied Physics Letters*, 93(17):37–40, 2008. doi: 10.1063/1.3012385.

[48] Y. Chassagneux, R. Colombelli, W. Maineult, S. Barbieri, H. E. Beere, D. A. Ritchie, S. P. Khanna, E. H. Linfield, and A. G. Davies. Electrically pumped photonic-crystal terahertz lasers controlled by boundary conditions. *Nature*, 457(7226):174–178, 2009. doi: 10.1038/nature07636.

[49] R. Degl'Innocenti, Y. D. Shah, L. Masini, A. Ronzani, A. Pitanti, Y. Ren, D. S. Jessop, A. Tredicucci, H. E. Beere, and D. A. Ritchie. Hyperuniform disordered terahertz quantum cascade laser. *Scientific Reports*, 6:19325, 2016. doi: 10.1038/srep19325.

[50] T. Baba, D. Mori, K. Inoshita, and Y. Kuroki. Light localizations in photonic crystal line defect waveguides. *IEEE Journal on Selected Topics in Quantum Electronics*, 10(3):484–491, 2004. doi: 10.1109/JSTQE.2004.829201.

[51] M. Notomi, K. Yamada, A. Shinya, J. Takahashi, C. Takahashi, and I. Yokohama. Extremely large group-velocity dispersion of line-defect waveguides in photonic crystal slabs. *Physical Review Letters*, 87(25):253902–253902–4, 2001. doi: 10.1103/PhysRevLett.87.253902.

[52] H.-W. Hübers, S. G. Pavlov, A. D. Semenov, R. Köhler, L. Mahler, A. Tredicucci, H. E. Beere, D. A. Ritchie, and E. H. Linfield. Terahertz quantum cascade laser as local oscillator in a heterodyne receiver. *Optics Express*, 13(15):5890, 2005. doi: 10.1364/OPEX.13.005890.

[53] J. D. Joannopoulos, S. G. Johnson, J. N. Winn, and R. D. Meade. *Photonic Crystals: Molding the Flow of Light*. Princeton University Press, 2 edition, 2008. ISBN 9780691124568.

[54] S. G. Johnson and J. D. Joannopoulos. Block-iterative frequency-domain methods for Maxwell's equations in a planewave basis. *Optics Express*, 8(3):173–190, 2001.

[55] T. E. Oliphant. *A guide to NumPy*. Trelgol Publishing, 2006.

[56] J. D. Hunter. Matplotlib: A 2D graphics environment. *Computing In Science & Engineering*, 9(3):90–95, 2007. doi: 10.1109/MCSE.2007.55.

[57] S. G. Johnson. MPB user tutorial, 2017. URL http://ab-initio.mit.edu/wiki/index.php/MPB_User_Tutorial.

[58] A. Yariv, Y. Xu, R. K. Lee, and A. Scherer. Coupled-resonator optical waveguide: a proposal and analysis. *Optics Letters*, 24(11):711, 1999. doi: 10.1364/OL.24.000711.

[59] E. M. Purcell. Spontaneous Emission Probabliities at Radio Frequencies. *Physical Review*, 69:674–674, 1946. doi: 10.1103/PhysRev.69.674.2.

[60] C. Walther, G. Scalari, M. Beck, and J. Faist. Purcell effect in the inductor-capacitor laser. *Optics Letters*, 36(14):2623–2625, 2011. doi: 10.1364/OL.36.002623.

[61] R. O. Carlson, G. a. Slack, and S. J. Silverman. Thermal Conductivity of GaAs and GaAs1-xPx Laser Semiconductors. *Journal of Applied Physics*, 36(2):505, 1965. doi: 10.1063/1.1714018.

[62] R. Degl'Innocenti, Y. D. Shah, R. Wallis, A. Klimont, Y. Ren, D. S. Jessop, H. E. Beere, and D. A. Ritchie. A hybrid plasmonic waveguide terahertz quantum cascade laser. *Applied Physics Letters*, 106(8):082101, 2015. doi: 10.1063/1.4913307.

[63] E. Perret, N. Zerounian, S. David, and F. Aniel. Complex permittivity characterization of benzocyclobutene for terahertz applications. *Microelectronic Engineering*, 85(11): 2276–2281, 2008. doi: 10.1016/j.mee.2008.07.008.

[64] A. W. M. Lee, Q. Qin, S. Kumar, B. S. Williams, Q. Hu, and J. L. Reno. High-power and high-temperature THz quantum-cascade lasers based on lens-coupled metal – metal waveguides. *Optics Letters*, 32(19):2840–2842, 2007. doi: 10.1364/OL.32.002840.

[65] R. Degl'Innocenti, Y. D. Shah, D. S. Jessop, Y. Ren, H. E. Beere, and D. A. Ritchie. Hollow metallic waveguides integrated with terahertz quantum cascade lasers. *Optics Express*, 22(20):5051–5055, 2014. doi: 10.1364/OE.22.024439.

[66] I. Christiaens, K. De Mesel, D. Van Thourhout, and R. Baets. Thin-Film Devices Fabricated With Benzocyclobutene Adhesive Wafer Bonding. *Journal of Lightwave Technology*, 23(2):517–523, 2005.

[67] A. Guarino, G. Poberaj, D. Rezzonico, R. Degl'Innocenti, and P. Gu. Electro – optically tunable microring resonators in lithium niobate. *Nature Photonics*, 1:407–410, 2007. doi: 10.1038/nphoton.2007.93.

[68] Q. Xu, V. R. Almeida, R. R. Panepucci, and M. Lipson. Experimental demonstration of guiding and confining light in nanometer-size low-refractive-index material. *Optics Letters*, 29(14):1626–1628, 2004. doi: 10.1364/OL.29.001626.

[69] S. Pandey, G. Kumar, and A. Nahata. Slot waveguide-based splitters for broadband terahertz radiation. *Optics Express*, 18(22):23466–23471, 2010. doi: 10.1364/OE.18.023466.

[70] H. Pahlevaninezhad, B. Heshmat, and T. E. Darcie. Efficient Terahertz Waveguides. *Engineering*, 1(26):25–27, 2011. doi: 10.1364/ECOC.2011.Tu.5.LeSaleve.1.

[71] V. R. Almeida, Q. Xu, C. A. Barrios, and M. Lipson. Guiding and confining light in void nanostructure. *Optics Letters*, 29:1209–1211, 2004.

[72] G. Mehta and S. Kotha. Recent chemistry of benzocyclobutenes. *Tetrahedron*, 57(4):625–659, 2001. doi: 10.1016/S0040-4020(00)00958-3.

[73] D. Burdeaux, P. Townsend, J. Carr, and P. Garrou. Benzocyclobutene (BCB) dielectrics for the fabrication of high density, thin film multichip modules. *Journal of Electronic Materials*, 19(12):1357–1366, 1990. doi: 10.1007/BF02662825.

[74] Y. Shah. *Novel designs and waveguides in THz quantum cascade lasers*. PhD thesis, University of Cambridge, 2017.

[75] M. A Belkin, J. A Fan, S. Hormoz, F. Capasso, S. P Khanna, M. Lachab, A. G. Davies, and E. H. Linfield. Terahertz quantum cascade lasers with copper metal-metal waveguides operating up to 178 K. *Optics Express*, 16(5):3242, 2008. doi: 10.1364/OE.16.003242.

[76] M. Fox. *Optical Properties of Solids*. Oxford University Press, 2 edition, 2010. ISBN 9780199573370.

[77] S. Kohen, B. S. Williams, and Q. Hu. Electromagnetic modeling of terahertz quantum cascade laser waveguides and resonators. *Journal of Applied Physics*, 97(5):053106, 2005. doi: 10.1063/1.1855394.

[78] E. A. Mashkovich, A. I. Shugurov, S. Ozawa, E. Estacio, M. Tani, and M. I. Bakunov. Noncollinear Electro-Optic Sampling of Terahertz Waves in a Thick GaAs Crystal. *IEEE Transactions on Terahertz Science and Technology*, 5(5):732–736, 2015.

[79] M. A. Ordal, R. J. Bell, R. W. Alexander, L. L. J. Long, and R. Marvin. Optical properties of Au, Ni, and Pb at submillimeter wavelengths. *Applied Optics*, 26:744–752, 1987.

[80] N. Laman and D. Grischkowsky. Terahertz conductivity of thin metal films. *Applied Physics Letters*, 93(5):051105, 2008. doi: 10.1063/1.2968308.

[81] D. R. Lide, editor. *CRC Handbook of Chemistry and Physics*. CRC, Boca Raton, FL, 73 edition, 1992.

[82] F. Valmorra, G. Scalari, K. Ohtani, M. Beck, and J. Faist. InGaAs/AlInGaAs THz quantum cascade lasers operating up to 195 K in strong magnetic field. *New Journal of Physics*, 17(2):023050, 2015. doi: 10.1088/1367-2630/17/2/023050.

[83] A. Wade, G. Fedorov, D. Smirnov, S. Kumar, B. S. Williams, Q. Hu, and J. L. Reno. Magnetic-field-assisted terahertz quantum cascade laser operating up to 225 K. *Nature Photonics*, 3(1):41–45, 2009. doi: 10.1038/nphoton.2008.251.

[84] C. Deutsch, H. Detz, M. Krall, M. Brandstetter, T. Zederbauer, A. M. Andrews, W. Schrenk, G. Strasser, and K. Unterrainer. Dopant migration effects in terahertz quantum cascade lasers. *Applied Physics Letters*, 102(20), 2013. doi: 10.1063/1.4805040.

[85] H. K. Lee, K. S. Chung, J. S. Yu, and M. Razeghi. Thermal analysis of buried heterostructure quantum cascade lasers for long-wavelength infrared emission using 2D anisotropic heat-dissipation model. *Physica Status Solidi (a)*, 362(2):356–362, 2009. doi: 10.1002/pssa.200824314.

[86] J. Alton, S. S. Dhillon, C. Sirtori, A. de Rossi, M. Calligaro, S. Barbieri, H. E. Beere, E. H. Linfield, and D. A. Ritchie. Buried waveguides in terahertz quantum cascade lasers based on two-dimensional surface plasmon modes. *Appl. Phys. Lett.*, 86(071109), 2005. doi: 10.1063/1.1866639.

[87] S. L. Chuang. *Physics of Optoelectronic Devices*. Wiley, 1 edition, 1995. ISBN 9780471109396.

[88] B. S. Williams, S. Kumar, Q. Hu, and J. L. Reno. Operation of terahertz quantum-cascade lasers at 164 K in pulsed mode and at 117 K in continuous-wave mode. *Optics Express*, 13(9):3331–3339, 2005. doi: 10.1364/OPEX.13.003331.

[89] K. Z. Rajab, M. Naftaly, E. H. Linfield, J. C. Nino, D. Arenas, D. Tanner, and M. Lanagan. Broadband Dielectric Characterization of Aluminum Oxide (Al_2O_3). *Journal of Microelectronics and Electronic Packaging*, 5(1):2–7, 2008.

[90] S.M. Sze and J.C. Irvin. Resistivity, mobility and impurity levels in GaAs, Ge, and Si at 300°K. *Solid-State Electronics*, 11(6):599–602, 1968. doi: 10.1016/0038-1101(68)90012-9.

[91] University Wafer. Ultrathin silicon wafers, 2017. URL http://ultrathinsilicon.com/.